Analytical and Numerical Modelling of a Compact Catalytic Reformer

Thesis submitted in accordance with the requirements of

the University of Liverpool

for the degree of Doctor in Philosophy

by

Alana Selsil

June 2005

In loving memory of

Anneciğim

Acknowledgements

I would like to express my sincere gratitude to my colleagues, friends and family for everything they have taught me about both mathematics and myself throughout the past three and a half years.

Without any shadow of a doubt, this thesis would not have been possible without the excellent supervision and guidance of Professor A.B. Movchan (Sasha) and Dr Natasha Movchan. They are totally unique in their enthusiasm, mathematical creativity and expertise in this field. Their focus, motivation and academic genius is truly admirable. They are thorough in everything they do, and I am very lucky and privileged to have had the great pleasure of working alongside them.

I would also like to say a huge thank you to Dr John Gracey. This whole academic journey was initiated by him, and for that, I will always be very grateful. He convinced me to do a PhD in the first place, he believed in me, supported me, encouraged me, and above all, became a very good friend.

I would also like to acknowledge the EPSRC studentship (grant GR/R26108/01). Without this funding, it would have been impossible for me to complete this research, or attend and have the experience of presenting work at national and international conferences.

Throughout the project I had the great opportunity to work with many well-respected experts in the fields of mathematics and chemical engineering. Thanks to Professor Stan Kolaczkowski at the University of Bath, for his academic discussions, encouraging comments, excellent physical intuition, and for increasing my interest in practical problems and engineering. Thanks also to Professor Leonid Berlyand and Mrs Yuliya Gorb at Penn State University, for providing me with such a warm welcome to Pennsilvania, for giving me their time and for all the productive discussions we had while I was there.

Special thanks is also given to someone who kept me focused, with his enthusiasm, motivation, encouragement and constant academic, as well as non-academic discussions: 'Knock, knock, Dr Martyn Hughes'. You are a true friend.

Other special friends I wish to mention, people I care about, who are close to me, who kept me sane and who were there to share the experience with me, include: Dr Juan Bercial (a brilliant office mate), Miss Sara Burns (I can see myself so much in you), Dr Steven Platts (I admire the fact that you followed your heart), Mr Stephen Gallagher (I admire your enthusiasm for life), Dr Anwar Hussein, Miss Aoibhinn Bradley, Mr Colin Gallagher, Dr Kieran Sharkey, Miss Rachel Bennett, Dr Damian (Damo) Clancy, Dr Nathan Green, Miss Clare Barber and Mrs Ingrid (Ingy) Harper. For these, and all the other people I have had the pleasure of becoming friends with over my time here, thank you.

The Department of Mathematics has become my second home over the past eight years and I have truly enjoyed the entire experience. I am proud to say that I have studied at this university, and I will always be grateful to each and every person who played a role in making me feel like I belonged here. Thanks to everyone, and a very special thanks goes especially to Mrs Margaret Frazer and Mrs Sue Richardson: thank you for always making me smile; you are two amazing, genuine and really lovely women.

I would also very much like to thank the teachers of Foyle and Londonderry College, in particular Mrs Joy Coskery and Mr Graham Mercer. You convinced me that I could achieve whatever I wanted, you believed in me and you gave me the confidence I needed to get this far. To all my 'Foyle' family, including Miss Ella King (I will cherish our friendship forever): thank you.

I am very lucky to have such loving and caring families, both in Ireland and Turkey. To all the Harkins, Selsils and Cusacks: thanks for all your support and love. To Linda and Terry Harkin, thank you for letting me do things for myself, for never pressurising me, for keeping me grounded and for helping me

realise the priorities in life. Annem Feriha, babam Şeraffetin: Her şey için, çok teşekkürler, bir gün beraber dolma yapacağiz. To Miss Danielle Cusack, you are a true fighter and a model to anyone. Special thanks and love to my brothers and sisters: David, Stephen, Shaun, Nuri, Elika, Buse and above all Melissa (the wee angel Missy).

Finally, and especially, I would like to thank my wonderful husband, Dr Özgür Selsil. This thesis is as much yours as it is mine. I could not have done it without you. You stand by me through everything. You are an inspiration. Your support and love have been unconditional. You are my best friend. Thanks for being there, always.

Alana Selsil

Liverpool, June 2005

Abstract

We develop a mathematical model that describes a new design for an environmentally friendly compact industrial reactor. The reactor consists of long and thin parallel channels, packed with pellets, with exothermic and endothermic reactions taking place alternately. Thin conducting walls separate the channels. A description of the chemical reactions and the heat transfer in this new catalytic reformer is presented. Much of the previous work on this design has been experimental. Until now, there remained the challenge to provide a detailed and accurate theoretical model, which would be used to analyse and develop design alternatives.

We are interested in the coupling of the temperatures between the channels across the thin walls. First, a model example for fluids flowing in unobstructed channels is considered. The temperature in the wall is expanded asymptotically. The coupling in the temperatures is obtained from the solvability conditions. Numerical simulations of the uncoupled and coupled temperature distributions are presented.

We then consider the case when the channels are packed with catalytic pellets. For the conditions between the channels and the wall we take a combination of Newton's law of cooling and Fourier's conduction law. Industrial data taken from experimental literature is used in numerical simulations.

Thermal conductivity of the wall influences the coupling in temperatures. Therefore, layers of different widths and thermal conductivities within the wall are considered. Additionally, the coupling could be controlled by introducing an air gap inside the wall, where heat is also transferred via radiation. A detailed analysis of this case is presented.

Boundary layer solutions near the inlet and outlet of the reactor are constructed and we provide an asymptotic approximation to the solution for both the linear

and nonlinear models along the full length of the reactor.

A detailed model of a fluid flowing through a packed bed channel is given, and we explain the relationship to Darcy's law and Hartmann flow. Analytical expressions for the equations of motion and the effective velocity are derived.

Finally the transient problem is considered. We conclude that the steady state solution, which the transient problem evolves to, is exactly the same as the solution of the corresponding steady state problem.

Contents

List of Figures

List of Tables

List of Notations

a_f = Heat transfer area of the wall of the channel per unit bed volume, m^{-1}

a_v = Surface area of pellets per unit bed volume, m^{-1}

A_c = Cross-sectional area of packed bed, m^2

$\mathcal{A}$ = Pre-exponential factor, $mol/(kg_{cat}\ s)$

C_p = Constant pressure heat capacity, J/(mol K) or J/(kg K)

d = Normalised width of layered wall

D = Diffusion coefficient, m^2/s

D_e = Effective axial dispersion coefficient, m^2/s

D_C = Entire width of channel, m

D_w = Entire width of wall, m

$\mathbf{e}^{(1)}$ = Unit vector parallel to the $x-$axis

$\mathbf{e}^{(2)}$ = Unit vector parallel to the $y-$axis

E = Apparent activation energy, J/mol

F_t = Total molar flowrate, mol/s

G = Pressure gradient, Pa/m

h_{fs} = Heat transfer coefficient between fluid and catalyst pellet, $W/(m^2\ K)$

h_w = Heat transfer coefficient between wall and fluid, $W/(m^2\ K)$

(ΔH_R) = Heat of reaction, J/mol

k = Thermal conductivity, W/(m K)

k_f = Thermal conductivity of fluid, W/(m K)

k_m = Mass transfer coefficient between fluid and catalyst pellet, m/s

k_s = Thermal conductivity of solid, W/(m K)

k_w = Thermal conductivity of wall, W/(m K)

$l_1,\ l_2$ = Normalised widths of outer parts of the wall in the air gap model

L = Length of catalytic reformer, m

r = Radius of pellets, m

N = Number of sub-channels

P = Pressure, Pa

R = Gas constant, J/(mol K)

R_g = Universal gas constant, 8.314 J/(mol K)

$(-R)_s$ = Reaction rate: Rate of disappearance of methane at external surface of catalyst pellet, mol/(kg_{cat} s)

T = Temperature, K

T_* = Outer wall temperature for air gap model, K

U_a = Overall heat transfer coefficient, W/(m^2 K)

v = Velocity, m/s

v_x = Mole average superficial velocity in a packed bed, m/s

Y = Mole fraction of methane

Greek symbols

α = Normalised width of sub-channel

δ = Small dimensionless parameter, 7×10^{-7}

ϵ = Emmisivity

ε = Relative width of wall

η = Viscosity, Pa s

$\mathcal{H}$ = Normalised width of sub-channel

$\mathcal{I}$ = Normalised width of sub-channel

κ = Permeability, m^2

ϕ = Fraction of bed not occupied by catalyst pellet

μ = Thermal diffusivity, m^2/s

Π = Normalised width of sub-channel

Ψ = Nonlinear function in reaction rate

ρ = Mass density, kg/m^3

ρ_f = Density of fluid, mol/m^3

ρ_c = Density of catalyst pellet, kg_{cat}/m^3

σ = Stephan-Boltzman constant, $W/(m^2\ K^4)$

ϱ = Scaled variable for boundary layer at left end, m

φ = Scaled variable for boundary layer at right end, m

$\breve{\varphi}$ = Scaled variable for boundary layer at right end, m

τ = Scaled variable for width, dimensionless or m

ξ = Effectiveness factor of the catalyst

Subscripts

C = Channel, w = Wall,

f = Fluid, s = Solid, cat = Catalyst,

Superscripts

0 = Wall, 1 = Reforming side,

2 = Combustion side

Chapter 1

Introduction

1.1 Motivation

The work presented in this thesis is predominantly motivated by the need for a mathematical model to describe a problem that arises in engineering. The challenge lies in the modelling of a new design for a catalytic reactor (used to make hydrogen). This work is potentially of great importance in industry as it offers the opportunity to design a new, efficient and environmentally friendly compact reactor. The aim of this thesis is to provide a detailed explanation of how one can use the asymptotic method to accurately describe theoretical concepts associated with this new catalytic reactor. Although this work is primarily concerned with mathematical modelling and the use of the asymptotic expansions technique, we believe it is also important to highlight the industrial novelty and the physical background associated with this field of research.

The industrial motivation

The description of the industrial challenges associated with this new design is as follows: Using catalytic combustion to convert natural gas into hydrogen is well established and known as steam reforming. A typical plant could have a capacity of 1000 tonne per day and a heat duty of about 65 MW, with a

volume of over 1000 m^3 (see [25]). Natural gas is burned in a furnace, where the predominant mode of heat transfer is radiation. Then there is a convection chamber, where additional heat is recovered from the hot gas leaving the radiant section. In these large chemical plants the hydrogen produced is mainly used in petroleum refining and also in the petrochemical industries for ammonia and methanol synthesis, see the reviews by Jamal and Wyszynskie [52] and Pigent [76]. A considerable amount of energy is required for the convection section, which is obtained from the combustion of the natural gas in the radiant section. In this radiant section the temperatures are in excess of 1500°C. At such high temperatures the formation of dangerous oxides of nitrogen from the air cause significant pollution, see [25] and [45]. Therefore, the industrial objective is to reduce the production of these pollutants and also reduce the size of the plant. An effective way of doing this is to combine catalytic combustion and catalytic steam reforming in a novel way: the new reactor could be visualised as consisting of a large number of parallel channels with endothermic and exothermic reactions occurring in alternate channels. Each channel is packed with pellets that are covered in an appropriate catalyst (to promote whatever reaction is taking place in that channel). This means that the large radiant 'firebox' is no longer required, which would reduce the size by about 100 to only 11 m^3 (see [25] and [26]). This would allow for a modular structure that could easily be scaled up or down depending on its need. The other major industrial advantage of this design is that the peak temperatures would be reduced to about 1000°C where the polluting nitrogen oxides are no longer formed. Another novelty of the design is that it also tackles the problem of the two balanced reactions being operated in parallel rather than in series: the parallel approach is more efficient, as the method of heat input is at the point where it is required. Much of the previous investigative work has been experimentally led (see, for example, [20], [25], [26], [38], [95] and [96]), but so far there has been a substantial lack of emphasis on understanding the interaction among the physical and chemical processes taking place. Until now,

there still remains the challenge to develop a workable design, paying particular attention to the theoretical concepts associated with the transfer of heat between the parallel channels.

The mathematical motivation

To date, little has been done from a mathematical modelling point of view regarding the description of these types of catalytic reactors, which are complicated due to the nonlinearity of the transient first and second order differential and algebraic equations in the channels. In addition, the heat transfer process also couples the equations across the connecting wall. If a full time-dependent model of this reactor were to be constructed, with highly exothermic reactions balancing highly endothermic reactions in neighbouring channels, then some solutions of the system of nonlinear equations may be unstable. This would result in difficulties in using modelling techniques to identify possible operating conditions and design scenarios. In this thesis we use the asymptotic method as a tool, not only to provide information about the theoretical concepts behind what is physically happening, but also to reduce the complications that numerical packages solving this problem may encounter. The model includes asymptotic analysis of both the fields within the thin interconnecting walls, and also the thermal coupling between the channels. In the physical phenomenon we describe, reactions take place at relatively low temperatures. The mathematical model of such a reactor involves a reaction-diffusion system of nonlinear partial differential equations with algebraic equations. It describes the chemical reactions that take place in the thin channels of the reactor as well as the effect of thermal interaction across the layers. A direct three-dimensional (3D) problem would require enormous computational resources and would probably not provide sufficient accuracy. Our mathematical model incorporates the above-mentioned asymptotic method, which enables us to use a 1D formulation to describe the leading approximation along the channels, and a 2D formulation to describe the temperature and concentration distributions across and along the wall. We take

many of the design and physical properties for the system of interest as fixed values. These are not considered to be absolute values as they could change as the design evolves. Many of these values may also relate to physical, chemical and/or transport properties and therefore could be functions of temperature, pressure, composition of reactants, flow rates in the channels, and properties of the catalyst. They provide an indication of the order of magnitude of the terms that have been calculated for a fixed set of inlet conditions or estimated as a good starting point for a design concept.

Therefore, we need to address the following main issues relating to the design of the new reactor:

- Asymptotic modelling of the coupling in the temperatures across the thin walled structure of the catalytic reactor, and the resulting effect of this coupling on the distributions of the temperatures and concentrations in the adjacent channels.

- Analysis of the effect of varying the resistance (to the transfer of heat) of the wall on the temperature and concentration distributions.

- Analysis of what is needed to avoid failure of the system: understanding how one could prevent the endothermic reaction taking too much heat and consequently extinguishing the exothermic reaction.

- Use of the asymptotic expansions technique to model the flow of a fluid through a packed bed channel.

- Use of the asymptotic expansions technique to analyse boundary layer regions associated with the model.

- The inclusion of transient terms and the stability of the system.

These are the key features in solving the problems that people working in this field have faced so far. An experimental study of this type would be very costly

and time consuming and may even result in the wrong thing being attributed to the breakdown of the process. Consequently, a mathematical model is vital for the progressive development of the work in this field, as it provides detailed information on the necessary operating conditions, and the key theoretical concepts required to meet all of the above challenges.

1.2 Literature review

Review of engineering literature

Hunter and McGuire 1980, [49], give an early application of the reactor discussed in this thesis. They are the first to suggest coupling of chemical reactions, by means of heat transfer, as an improved method for obtaining efficiency in catalytic heat exchangers. They recommend a process in which flameless combustion is involved, and highly exothermic reactions are suggested as a heat source for highly endothermic reactions. Many experimental studies have followed, which include the work by Branch and Tomlinson [20] on the feasibility of coupling methane reforming with catalytic combustion in a catalytic plate reactor. They deduce that the catalyst plays a vital role in the process, and they show how deactivation of this catalyst can have severe consequences on the operation and stability of the reactor. A theoretical and experimental study is given by Charlesworth [25] and Charlesworth *et al.* [26], where steam reforming and combustion of methane on micro-thin catalysts, for use in an industrial reactor, is discussed. They also demonstrate how this new design would make the catalytic reactor substantially smaller than existing conventional reformers. Frauhammer *et al.* [38] present analysis of the coupling of catalytic combustion and steam reforming in counter-current flow, using so-called ceramic honeycomb monolithic reactors. They show that in the middle of the channels there is a high temperature zone leading to a high conversion of heat. They also conclude that the performance of the reactor is affected by the catalyst distribution, the heat

capacity of the flows and the presence of the homogeneous reactions. Recent experimental work includes that of Zanfir [95], and Zanfir *et al.* [96], where a more mathematical study, on the coupling of endothermic and exothermic reactions in a catalytic plate reactor, is presented, and a two-dimensional model is used. They take the reaction rate in the *Arrhenius* form (which is discussed in detail in Section 1.5). Their work explains that the catalyst loading (directly related to the pre-exponential factor in the reaction rate), the thermal conductivity of the wall, and the flow rate between each plate are key parameters, which need careful adjustment, to avoid hotspots or insufficient conversion in the reactor. When heat generated and heat consumed are not balanced locally, hot and cold spots are formed which could potentially damage the reactor. This is also considered in the work by Worth *et al.* [93], where an explanation is given about the validity of the one-dimensional model. Khanna and Seinfeld [53] include a mathematical model of the packed bed reactor in their work, and emphasize why using a heterogeneous model is physically more realistic. These studies (Zanfir, Worth, Khanna and Seinfeld) confirm the importance of mathematical modelling with regards to industrial reactors, and the use of this modelling as a tool to explore design concepts. However, neither transient terms nor diffusion/dispersion terms are included in these models. In general, in the work in this field, there tends to be a lack of emphasis on a thorough understanding of the interaction between physical and chemical processes taking place in the reactor. Other recent work on reactors include the mathematical models presented by Antipov *et al.* [5] and Kolaczkowski *et al.* [54]. In both of these papers a monolithic reactor is described, and asymptotic analysis is used, but their aim is to look at the formation of cracks and the breakdown of the catalysts. Chemical reactions, which would further complicate the problem, are not taken into account.

Stiff systems

In the systems of differential equations that describe catalytic reactors, small coefficients usually multiply the principal derivative terms, giving *stiff systems* of equations. In our particular case we use the numerical package Femlab (which provides an equivalence to the limit solution) and we then construct the boundary layers separately. Stiff systems (characterised by widely varying eigenvalues) are encountered in many areas of applied mathematics. Curtiss [28] and Liniger and Willoughby [61] discuss efficient integration methods for stiff systems of ordinary differential equations. They present numerical examples and discuss the application to nonlinear systems. They analyse the advantages of using methods such as the forward Euler method, Newton's method and implicit integration formulae to solve nonlinear systems. Miranker [64] also discusses numerical methods for systems of differential equations, paying particular attention to methods of the boundary layer type. There is equivalence between singularly perturbed problems and a certain subclass of stiff systems. The small parameter characterising a stiff system as one of the singularly perturbed type is not always identifiable. Miranker presents results showing how boundary layer techniques can be used to obtain numerical approximations, without having to identify this small parameter directly. Similar work, employing singular perturbation methods for stiff systems, is carried out by Aiken and Lapidus [1]. Here, the thickness of the boundary layer is determined, and the numerical integration method presented is shown to be capable of high stability and accuracy. Hayes and Tanguy [47] look specifically at a convection-diffusion system (a stiff, nonlinear problem with chemical reactions) and present a modified form of what is known as the *Marquardt's method.* This is an implicit finite difference method and it provides an effective process for predicting the behaviour of the system. Other examples of work on stiff systems in packed bed reactor models includes that of Blouza and Coquel [17], Foss and Wasbo [36] and Iordanidis *et al.* [51].

Sandwich structures

In our work we consider a sandwich structure - three layers corresponding to the two channels of the reactor, with a thin wall between them. There is a vast amount of literature available on sandwich structures. Here we present a few examples of the on-going work in this field. Designers of composite structures need to assess decay effects associated with loading, and consequently, there is a lot of research being carried out on what is known as St. Venant end effects. A simple explanation of this is as follows: if a force acting on a small portion of an elastic body is replaced by another force (with the same resulting force and momentum), the redistribution of loading produces substantial changes in stress in the close neighbourhood of the loading. The stresses on the parts of the body that are far away from this portion essentially remain the same. The work by Baxter and Horgan [10] and Choi and Horgan [27] discusses the decay length of the St. Venant end effects with perfect and imperfect bonding for isotropic (has the same properties in all directions) and anisotropic (properties differ according to direction of measurement) sandwich structures. The main results include the fact that these end effects for an isotropic structure, with a soft middle layer, decay slower (have longer decay lengths) than those for a homogeneous isotropic strip. Also, the decay length is much longer for an anisotropic strip than for an isotropic strip, and for imperfect bonding rather than perfect bonding. The work presented by Benveniste and Miloh [13] is of a different nature: they study composites with highly conducting interfaces. They describe in detail the interface conditions and they derive a definition for the effective (averaged) conductivity of these composites. The modelling of steady-state heat conduction in an anisotropic layered sandwich is the focus of other work by Baxter and Horgan [9]. They consider the effect of increasingly imperfect thermal contact on the deformations of the sandwich structure. The main objective of the thesis by Avila-Pozos [7] is to apply mathematical models to problems of layered structures with imperfect interfaces. The application of the work in [7] is to increase the

performance of adhesive joints used in the design of aeroplane wing structures.

Homogenisation and porous media

The idea of averaging and homogenisation of porous media began in the second half of the 19th century with work by Maxwell, Rayleigh and then Einstein in 1905 (see the references given in the book by Hornung [50]). Since then it has been a very active field of research in civil engineering, chemical engineering, mathematics and theoretical physics. In our work we consider a packed bed reactor - a structure consisting of parallel channels, which are packed with fixed spherical solid pellets. We model fluids flowing through this porous network. Because of the complicated nature of the microscopic boundaries, a rigorous solution to this problem is practically impossible. Usually an averaging process or a conceptual continuum model is used for problems involving a porous media. Many important examples of the applications of transport phenomena (transport of mass, momentum, energy etc.) in porous media are given in the detailed works of Dullien [34], Hornung [50] and Polubarinova-Kochina and Falkovich [75], to name but a few. Allaire [3] and [4] considers the homogenisation of the Navier-Stokes equation in a domain containing many tiny periodically distributed solid particles. He shows the convergence of the homogenisation process to what is known as a *Brinkman law*, when a linear term for the velocity is added to the Navier-Stokes equation. He also derives Darcy's law for the limiting behaviour when the holes are large. Other work of this type is carried out by Bear and Bachmat [11] and [12]. They discuss transport phenomena in porous media and analyse the processes occurring in the solid-void interfaces. The work by Berlyand and colleagues [14], [15] and [40] looks at high contrast composites. The emphasis is on obtaining the effective properties (for example, the effective conductivity) associated with the random location of the inclusions and the small interparticle distances. In [18] and [19] Borcea gives additional results on what is known as the *resistor-capacitor network approximation*, to obtain the effective transport properties. The work of Brezis and Lions [21] explains the additional

'strange' term that is added to the equations of motion. This appears when the holes are of a critical size depending on their number and distribution. Prieur Du Plessis and Masliyah [77] consider a laminar flow through a rigid anisotropic porous media with varying permeability. Other work includes that of Kvernfold and Tyvand [56], Hayes, Afacan and Boulanger [44] and Slattery [85], in which heat transfer in reactors, flow through channels, and the prediction of the pressure drop in packed beds, can be found.

Exponential nonlinearities and transient problems

Our work studies the coupling of temperatures across the thin wall of a packed bed reactor. The transient problem we present confirms that the steady state solution discussed in the main part of the thesis is stable. There is extensive literature on the stability of solutions of problems in reactor design. Those with reaction rates of a similar form to the one we take include the work on non-adiabatic tubular reactor models (non-adiabatic means that heat exchange with the surroundings is taken into account), for example, Hawkings and Spence [43], Heinemann and Poore [48], Uppal, Ray and Poore [88] and [89]. The work of Hawkings and Spence [43] is concerned with the steady states of a system of nonlinear partial differential equations. The eigenvalues of a Jacobian matrix are compared with the eigenvalues of a corresponding preconditioned Jacobian matrix, to detect Hopf bifurcations and analyse the stability of the solutions. Heinemann and Poore [48] study the multiplicity and stability of steady states, and the oscillatory dynamics of the system. They use numerical procedures to present Hopf bifurcation formulae, which determine stability and location of the Hopf points. Heinemann and Poore also present numerical simulations, which show how temperature changes with the parameter known as the *Damköhler number*. In [88] the types of dynamic behaviour are also classified, and the existence and stability of limit cycles is predicted. Uppal, Ray and Poore [89] present a system of first order differential equations for the reactor, and analyse the evolution of multiple steady states and limit cycles over time. Plots of the

Damköhler number against temperature are given, to show the effect of certain parameters on the behaviour. The work on unsteady fronts by Balmforth *et al.* [8] suggests that travelling waves, in some models for catalytic reactions, lose stability, and the authors also demonstrate the similarity to combustion systems with Arrhenius kinetics. They employ the method of matched asymptotic expansions to find the asymptotic speed of the front of the chemical reaction. Needham and colleagues [59], [63], [68] and [69] also consider wave fronts in chemical reactions. Chapter 1 of Needham's book [59], and the paper [69] refer to what is known as the *Fisher equation* and they discuss the position of bifurcation points and their relation to reaction-diffusion type wave fronts. McCabe, Leach and Needham [63] examine a coupled system of singular reaction-diffusion equations, with the objective being to predict when travelling waves are most likely to arise. The paper [68] is associated with the accelerating wave fronts for a system of reaction-diffusion equations, and matched asymptotic expansions are used to obtain a complete solution over a large time.

1.3 Structure of the thesis

Throughout the thesis we use the asymptotic expansions technique, discussed in detail in the next section, to model the transfer of heat between the channels of the catalytic reactor. Our first aim is to present an illustrative example showing how an asymptotic method is used to model heat transfer between fluids in two adjacent channels, where the channels are separated by a thin conducting wall. This is the objective of Chapter 2. Our model consists of a two-dimensional (2D) problem with nonhomogeneous equations in the channels and homogeneous equations in the wall. We introduce a small parameter and expand the temperatures asymptotically. Consequently, this allows us to obtain a set of solvability conditions for a set of boundary value problems, which contains a *coupling term*, that is, the difference between the leading order temperatures in the two channels. We

consider a particular example showing how this difference in temperatures affects the temperature distributions along the channels. We then extend this analysis to the more physical problem where we consider the case when we have two homogeneous 2D steady state chemical reactions taking place in the channels, one that gives out heat and the other that consumes heat. We follow the asymptotic method described in the first part of the chapter, expanding the functions that denote temperature and concentration of a particular reactant, and, as before, we obtain the coupling terms from the solvability conditions. Solving the system numerically for a set of model parameters, we present the results of coupled and uncoupled temperature and concentration distributions along a channel of fixed length.

Chapter 3 looks in more detail at the model for the industrial packed bed catalytic reformer. We explain the novelty of the design. We describe the geometry of the multi-channel reactor and the formulation of the problem, specifying the endothermic and exothermic reactions that occur, as well as the non-dimensional parameter associated with the geometry. The equations for molar and energy balances, with a detailed explanation of the coefficients and the reaction rates we take, are explained in the next section. Our aim is to study how heat is transferred across the thin conducting wall between the two channels of this chemical reactor and how temperature and concentration distributions are effected as a result. We expand the temperature in the wall asymptotically as before and using the conditions between the wall and the channels we obtain the coupling terms which relate the fluid temperatures in the two channels. The full well posed system of equations is then solved numerically for both a set of model parameters and a set of industrial parameters taken from the appropriate literature. Uncoupled and coupled graphs are presented in both cases to show the effect of this coupling on temperature and concentration distributions along the channels. A note is made in this chapter about the fact that the numerical package does not solve the system precisely: the numerical solution does not satisfy the zero-flux

conditions that are set at the outlet of the reactor. Chapter 3 focuses on the analysis of the main trends of the temperature and concentration distributions: more detail on boundary layer regions near the ends of the channels is given in Chapter 5. We also discuss the effect of the geometry of the pellets inside the channel on the overall temperature distributions and we show that if the volume fraction of the pellets remains constant, the graphs do not change significantly as the surface area is increased. In the last section of Chapter 3 we explore the effect of changing the wall: the wall is constructed of layers of different widths and thermal conductivities. We assume ideal thermal contact between the layers. As a result, the forms of the coupling terms and the overall heat transfer coefficient change. Three examples with their corresponding numerical simulations are discussed in detail.

In Chapter 4 we extend the ideas developed in Chapter 3 and focus on the concept of having an air gap inside the wall: the wall is made up of three layers where two of those layers are some conducting material and the layer between them is filled with air. As a consequence, there is an additional transfer of heat via radiation across the air gap, resulting in the conditions within the wall changing significantly. The radiation condition contains nonlinear terms (only linear terms appeared in the conditions in Chapter 3), which means that the coupling terms cannot be written analytically. Nevertheless, we construct the asymptotic expansion for the temperature in the wall as before and obtain the coupling terms numerically using Femlab. Temperature and concentration distributions are presented, to show the effect on the coupling when the parameters associated with the air gap are changed. One conclusion is that for this particular set of industrial data, there is no significant change in the graphs when the width of the air gap is changed slightly. The explanation for this is given in detail in the last section of Chapter 4. Additionally we consider the sensitivity to certain boundary conditions and plot the corresponding cases for the air gap, together with uncoupled and coupled cases for comparison. The final section is associated

with the limiting air gap case, when no physical air gap exists. We show that, in order to obtain accurate and physically realistic results, conduction as well as radiation needs to be considered.

Chapter 5 includes an analytical analysis of the equations and conditions in the previous chapters. We present a detailed explanation of the full solution satisfying all the boundary conditions. We first normalise the nonlinear differential system. The problem is then written in the form of a singularly perturbed boundary value problem, with small coefficients multiplying the second order derivatives for the vector $\mathbf{Z}$, whose six components are unknown functions. The first half of this chapter deals with the linear case: we linearise the problem by taking the solid temperature upon which the reaction rate is exponentially dependent as the solid temperature at the inlet. Since the coefficient in front of the second order derivative is small, we first consider the limit case: we set this coefficient equal to zero. We compute the eigenvalues and corresponding eigenvectors of the limiting differential system, and the constants associated with the boundary conditions. However, some inlet conditions are not satisfied, which implies that the corresponding functions change rapidly near this region. We therefore construct boundary layers for these functions: we consider the full differential system, which contains the small coefficient, and we obtain the eigenvalues, eigenvectors and constants associated with this full system. The solution obtained from this process gives small discrepancies in all the conditions at the outlet. This implies that all six components of the vector $\mathbf{Z}$ have boundary layer regions at the outlet and these are constructed accordingly to compensate for any errors in the conditions. The full asymptotic solution is a combination of the solution of the limit problem and the boundary layers at both the inlet and outlet. We also present the numerical results showing the magnified regions near the inlet and outlet.

The second part of Chapter 5 deals with an approximation to the nonlinear problem. We assume that the problem can be solved in three steps for three regions that make up the length of the channel. The three solutions are 'matched'

to give the overall solution. In the first region we solve the nonlinear equations for the functions that change rapidly near the inlet. The second region is one in which the nonlinearity does not play a significant role in the distributions of temperature and concentration and therefore, we take a modified form of the solution for the linearised system in this region. The third region, associated with the outlet proves to be the most difficult. The solution for the region at the outlet is made up of two parts: one that depends on a slow variable, and the other that depends on fast variables. The boundary layer region for the fluid temperatures starts closer to the right end than the boundary layer regions for the other four functions. We solve the equations for these fluid temperatures separately and then substitute these into the remaining four equations. The solutions in the three regions of the channel for the nonlinear case are consequently matched. The results of the temperature and the concentration distributions are presented for the full solution and for the magnified regions near the inlet and outlet.

Our objective in Chapter 6 differs from the previous chapters in the fact that the main emphasis shifts slightly from the transfer of heat between the fluids in the channels to the specific case of a fluid flow in a channel which is packed with pellets obstructing the flow. Previously we used constant values for the coefficients, and we took 1D equations in the channels of the catalytic reformer. This chapter focuses more on how one could model the flow of fluid through a channel that is randomly packed with pellets. We compare two 2D models: the first assumes a certain arrangement of the pellets and the second looks at what is known in the literature as a *homogenised* channel. In Model 2 the governing equations contain an additional term that accounts for the fact that we have obstructions in the flow. Our aim in this chapter is to write the governing equations for the homogenised fluid and the solution for the homogenised velocity in terms of the properties of the real fluid described in Model 1. We expand the velocity and the pressure asymptotically and from the leading order terms for the velocity we derive what is known in the literature as Darcy's law. We also

show the similarity to Hartmann flow, which is known for problems involving magnetic fluids. Both Darcy's law and Hartmann flow are discussed in detail in the next section. We then write the full analytical representation of the average velocity, across any cross-section of the homogenised channel, in terms of known quantities. The idea of the pellets being arranged in a certain way is extended to more complicated arrangements, and similar analysis is carried out for these cases.

In the final chapter, Chapter 7, we return to the idea of the full catalytic reactor with exothermic and endothermic reactions taking place in adjacent channels, although this time the emphasis is on the transient problem. We expand the temperature in the wall asymptotically. We follow the methods used in Chapter 3 to find the coupling terms and then solve the problem numerically for a certain time interval. We show that the results for the steady state case are exactly those that the solution of the transient problem converges to over time. This emphasizes that the steady state case described in the previous chapters is physically valid. We also explore the sensitivity of the boundary conditions and the initial conditions on the temperature and concentration distributions. We provide a detailed summary of the effect on the graphs when these conditions are slightly perturbed.

1.4 Mathematical background

1.4.1 Asymptotics in thin domains

The main feature of the asymptotic technique used here is to present solutions of problems as series in powers of a small parameter, say ϵ. These expansions are asymptotic and give a sufficiently accurate approximation to the solution, see [55] and [70].

The analysis of laminar flow of a fluid through a thin domain is known in the

theory of hydrodynamics as the lubrication theory, see, for example [70], [72] and [87]. This theory assumes that the viscous term of the Navier-Stokes equation is much greater than the inertia term, and therefore, the inertia term can be neglected. Here we present a detailed explanation of this lubrication theory, using asymptotic expansions for the velocity and the pressure, and we show how the 2D problem can be reduced to the 1D problem for the leading order term of the velocity.

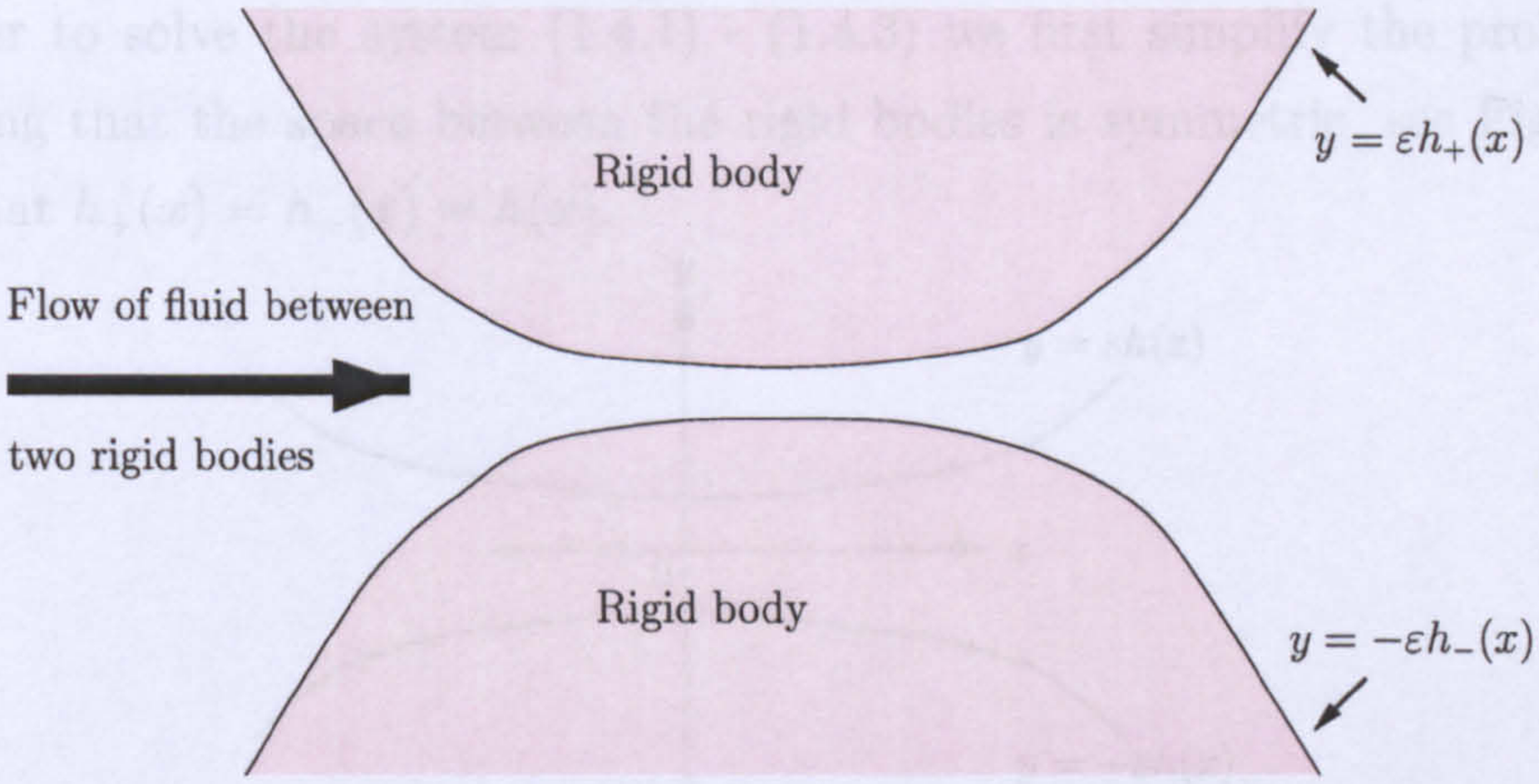

Figure 1.1: The flow of fluid through a thin domain.

Consider an incompressible fluid flowing through a thin space between two fixed rigid bodies as shown in Figure 1.1, where $h_\pm(x)$ are some given functions of the space parameter x, and ε is a small parameter, $0 < \varepsilon \ll 1$. The 2D governing equations, relating the velocity and the pressure, are the steady state Navier-Stokes equation and the continuity equation given by

$$-(\mathbf{v}(x,y)\cdot\nabla)\mathbf{v}(x,y) + \eta^*\nabla^2\mathbf{v}(x,y) - \frac{\nabla P}{\rho}(x,y) = 0, \tag{1.4.1}$$

$$\nabla\cdot\mathbf{v} = 0, \tag{1.4.2}$$

$$-\infty < x < \infty, \quad -\varepsilon h_-(x) < y < \varepsilon h_+(x).$$

Here, $\mathbf{v}$ is the velocity, η^* is the viscosity, ρ is the density, and P is the pressure.

We consider the case when the velocity increases as the distance between the rigid bodies decreases, that is, we assume that the viscosity is small, $\eta^* = \varepsilon^2\eta$, where η is of order $O(1)$. The governing equations above contain the nonlinear term $(\mathbf{v}(x,y)\cdot\nabla)\mathbf{v}(x,y))$, and the rigid bodies are assumed to be fixed, so we have the non-slip boundary conditions

$$\mathbf{v}(x, \pm\varepsilon h_{\pm}(x)) = 0. \tag{1.4.3}$$

In order to solve the system (1.4.1) - (1.4.3) we first simplify the problem by assuming that the space between the rigid bodies is symmetric, see Figure 1.2, such that $h_+(x) = h_-(x) = h(x)$.

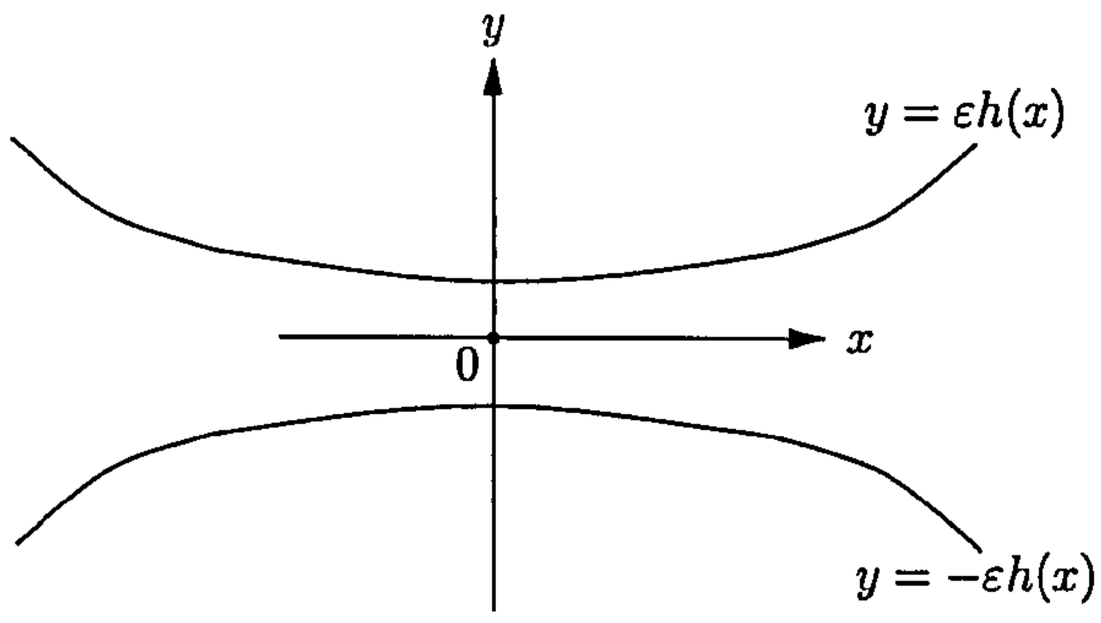

Figure 1.2: A simplified model of a fluid flow through a thin symmetric domain.

We also introduce a scaled coordinate τ such that

$$\tau = \frac{y}{\varepsilon h(x)}, \quad \tau \in (-1,1).$$

Conditions (1.4.3) then imply that $\mathbf{v}(x, \pm 1) = 0$.
The formal asymptotic expansions for the pressure and the velocity are given by

$$P(x,\tau) = P^{(0)}(x,\tau) + \varepsilon P^{(1)}(x,\tau) + \varepsilon^2 P^{(2)}(x,\tau) + ..., \tag{1.4.4}$$

$$\mathbf{v}(x,\tau) = \mathbf{v}^{(0)}(x,\tau) + \varepsilon \mathbf{v}^{(1)}(x,\tau) + \varepsilon^2 \mathbf{v}^{(2)}(x,\tau) + \dots . \tag{1.4.5}$$

Rewriting the continuity equation (1.4.2) in terms of the scaled coordinate, and substituting the expansion for the velocity given in (1.4.5), we obtain the follow-

ing, where $\tau = \tau(x)$:

$$\begin{aligned} 0 = \nabla \cdot \mathbf{v}(x,\tau) &= \Big(\frac{\partial}{\partial x}, \frac{1}{\varepsilon h(x)}\frac{\partial}{\partial \tau}\Big) \cdot (v_1(x,\tau),\ v_2(x,\tau)) \\ &= \frac{\partial v_1}{\partial x}(x,\tau) + \frac{\partial v_1}{\partial \tau}(x,\tau)\frac{\partial \tau}{\partial x}(x) + \frac{1}{\varepsilon h(x)}\frac{\partial v_2}{\partial \tau}(x,\tau) \\ &= \frac{\partial v_1}{\partial x}(x,\tau) - \tau\frac{h'(x)}{h(x)}\frac{\partial v_1}{\partial \tau}(x,\tau) + \frac{1}{\varepsilon h(x)}\frac{\partial v_2}{\partial \tau}(x,\tau). \end{aligned} \tag{1.4.6}$$

From the leading order term of (1.4.6), we find that $v_2^{(0)} = A(x)$, where A is some function of x. However, the non-slip conditions at $\tau = \pm 1$ imply that

$$v_2^{(0)} \equiv 0. \tag{1.4.7}$$

The next term in the asymptotic expansion given by (1.4.5) is the following:

$$h(x)\frac{\partial v_1^{(0)}}{\partial x}(x,\tau) - \tau h'(x)\frac{\partial v_1^{(0)}}{\partial \tau}(x,\tau) + \frac{\partial v_2^{(1)}}{\partial \tau}(x,\tau) = 0. \tag{1.4.8}$$

Now, rewriting the momentum equation (1.4.1) in terms of the scaled coordinate, and substituting the expansions for $\mathbf{v}$ and P we have

$$\begin{aligned} -\Big[(\mathbf{v}^{(0)}(x,\tau)+\varepsilon\mathbf{v}^{(1)}(x,\tau)+\ldots)\cdot\Big(\frac{\partial}{\partial x}, \frac{1}{\varepsilon h(x)}\frac{\partial}{\partial \tau}\Big)\Big](\mathbf{v}^{(0)}(x,\tau)+\varepsilon\mathbf{v}^{(1)}(x,\tau)+\ldots) \\ +\varepsilon^2\eta\Big(\frac{\partial^2}{\partial x^2} + \frac{1}{\varepsilon^2(h(x))^2}\frac{\partial^2}{\partial \tau^2}\Big)(\mathbf{v}^{(0)}(x,\tau) + \varepsilon\mathbf{v}^{(1)}(x,\tau) + \ldots) \\ -\frac{1}{\rho}\Big(\frac{\partial}{\partial x}, \frac{1}{\varepsilon h(x)}\frac{\partial}{\partial \tau}\Big)(P^{(0)}(x,\tau) + \varepsilon P^{(1)}(x,\tau) + \ldots) = 0. \end{aligned}$$

Due to (1.4.7), the leading order term from the momentum equation above gives

$$P^{(0)} = P^{(0)}(x),$$

that is, the leading order pressure does not depend on the scaled coordinate. The

problem for the next term (of order $O(1)$) is given by

$$\Big(-v_1^{(0)}(x,\tau)\frac{\partial v_1^{(0)}}{\partial x}(x,\tau)-\frac{v_2^{(1)}(x,\tau)}{h(x)}\frac{\partial v_1^{(0)}}{\partial \tau}(x,\tau)+\frac{\eta}{(h(x))^2}\frac{\partial^2 v_1^{(0)}}{\partial \tau^2}(x,\tau)\Big)\mathbf{e}^{(1)}$$

$$-\frac{1}{\rho}\frac{dP^{(0)}}{dx}(x)\mathbf{e}^{(1)}-\frac{1}{\rho h(x)}\frac{\partial P^{(1)}}{\partial \tau}(x,\tau)\mathbf{e}^{(2)}=0, \qquad (1.4.9)$$

where $\mathbf{e}^{(j)}$, $j=1,2$, are unit vectors parallel to the $x-$ and $y-$ axes, respectively. Equation (1.4.9) implies that

$$P^{(1)}=P^{(1)}(x),$$

and

$$-v_1^{(0)}(x,\tau)\frac{\partial v_1^{(0)}}{\partial x}(x,\tau)-\frac{v_2^{(1)}(x,\tau)}{h(x)}\frac{\partial v_1^{(0)}}{\partial \tau}(x,\tau)+\frac{\eta}{(h(x))^2}\frac{\partial^2 v_1^{(0)}}{\partial \tau^2}(x,\tau)-\frac{1}{\rho}\frac{dP^{(0)}}{dx}(x)=0.$$

Stokes flow

We assume that the velocity and its derivative are small so that any product of the two is significantly smaller than any other term in equation (1.4.1). Therefore, the term $(\mathbf{v}(x,y)\cdot\nabla)\mathbf{v}(x,y))$ may be neglected. As a consequence, the equations for the system become

$$h(x)\frac{\partial v_1^{(0)}}{\partial x}(x,\tau)-\tau h'(x)\frac{\partial v_1^{(0)}}{\partial \tau}(x,\tau)+\frac{\partial v_2^{(1)}}{\partial \tau}(x,\tau)=0. \qquad (1.4.10)$$

$$\frac{\partial^2 v_1^{(0)}}{\partial \tau^2}(x,\tau)-\frac{(h(x))^2}{\rho\eta}\frac{dP^{(0)}}{dx}(x)=0, \qquad (1.4.11)$$

with $$v_1^{(0)}(x,\pm 1)=v_2^{(1)}(x,\pm 1)=0.$$

Equations (1.4.10) and (1.4.11) are what is known in the literature as the lubrication model. Examples when the thin domain is of a constant thickness are considered by Ockendon and Ockendon [70], Parker, Boggs and Blick [72], and

Streeter and Wylie [87]. Here, when $h(x)$ is constant, h say, solving (1.4.11) for $v_1^{(0)}$, we obtain the following quadratic equation in the scaled coordinate τ:

$$v_1^{(0)} = C(x)(\tau^2 - 1), \quad C(x) = \frac{h^2}{2\rho\eta}\frac{dP^{(0)}}{dx}. \tag{1.4.12}$$

This implies that, for any given x, to leading order, the horizontal component of the velocity has a parabolic profile in the thin domain and from (1.4.7) the vertical component is zero.

In Chapter 6 we model the flow of fluid through a packed bed channel. We compare the results of two cases. The first is when we assume the pellets can be arranged in such a way that the fluid flows through the thin spaces between the layers of pellets, and in this case we show that the horizontal component of the velocity has a parabolic profile, in the same way as above. The second model describes a homogenised channel and we show that, in this channel, the velocity distribution is flat across the main section but decays exponentially near the walls. This effect is similar to the model of Hartmann flow (described in the following section) which is used to model magnetic fluids.

1.4.2 Hartmann flow

In this section we present a classical model for what is known in the theory of magneto fluid dynamics as Hartmann flow (see, for example, [22], [42], [57] and [66]). For a fluid moving in a magnetic field between parallel plates, where the

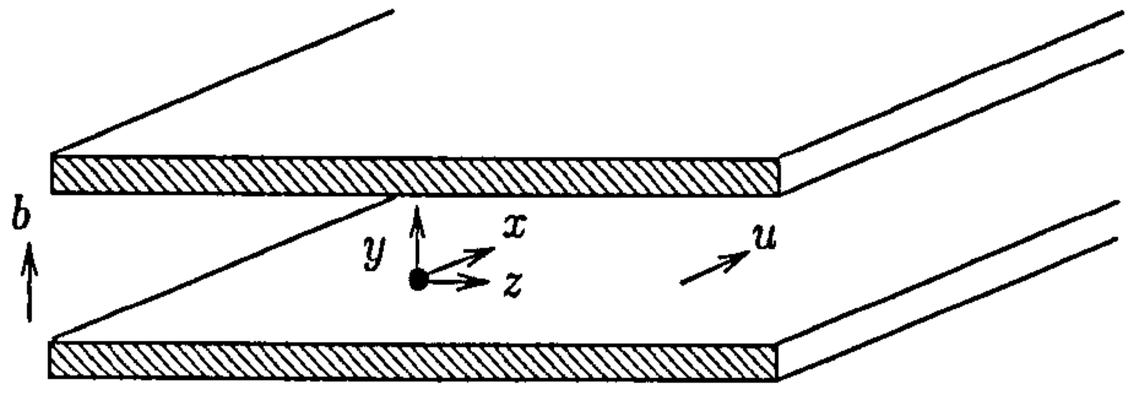

Figure 1.3: An infinite channel formed by two parallel plates.

magnetic field b is perpendicular to the plates as shown in Figure 1.3, and the space between the parallel plates is long and thin (so we assume that the velocity and the magnetic fields are one-dimensional (1D)), the governing equations can be reduced to give

$$\frac{\partial^2 u}{\partial y^2}(y) + H_a \frac{\partial b}{\partial y}(y) = -1,$$

$$\frac{\partial^2 b}{\partial y^2}(y) + H_a \frac{\partial u}{\partial y}(y) = 0 \quad \text{for} \quad -1 < y < 1, \tag{1.4.13}$$

where H_a is known as the Hartmann number. The conditions on the velocity $u(y)$ and the induced magnetic field $b(y)$ are

$$u = 0, \quad \frac{b}{c} \pm \frac{\partial b}{\partial y} = 0 \quad \text{at} \quad y = \pm 1, \tag{1.4.14}$$

where c is a constant associated with the conductance of the walls. The solution (see [66] for relevant details) of system (1.4.13) with conditions (1.4.14) is

$$u(y) = u^* \Big(1 - \frac{\cosh(H_a y)}{\cosh(H_a)}\Big); \quad b(y) = -\frac{y}{H_a} + u^* \frac{\sinh(H_a y)}{\cosh(H_a)}, \tag{1.4.15}$$

where the constant u^* is the characteristic magnitude of the velocity, specified in [22], [42], [57] and [66]. The solution for the velocity in equation (1.4.15) corresponds exactly to the solution we derive for the velocity in the homogenised channel in Chapter 6. For Hartmann flow, an increase in the Hartmann number corresponds to a flattened velocity profile in the main part of the channel, but produces boundary layers called Hartmann layers, near the plates. For large H_a there is an exponential decay in the velocity near the plates. We show that a similar concept holds in our model for a fluid flowing through a packed bed. Darcy's law, discussed in the following section, gives a relationship between the velocity and the pressure. In Chapter 6 we derive Darcy's law for our particular case of a fluid flowing through a packed bed channel of a catalytic reactor.

1.4.3 Darcy's law

Darcy's law is used widely in the literature for predicting velocities and flow rates through porous media (see, for example, [11], [12], [16], [44], [62] and [72]). It states that, for zero body force, the velocity of a fluid flowing through a porous media is of the form

$$u = -\frac{\kappa}{\eta}\frac{dP}{dx},$$

where u is the velocity, κ is the permeability, η is the viscosity, and P is pressure. In Chapter 6, we model a homogenised channel with effective properties and derive an expression for the effective velocity of a fluid flowing through a packed bed reactor, where the coefficient $1/a$ multiplies the second order derivative. When a is large, we have a singularly perturbed problem, whose limit solution relates the velocity and the pressure gradient in exactly the same way as in Darcy's law. We show that away from the boundaries of the channel, to leading order, we have a flat velocity profile, in accordance with Darcy's law. However, close to the boundaries the velocity changes exponentially; the corresponding details are given in Chapter 6.

1.4.4 Singular perturbation

Singularly perturbed boundary value problems are usually characterised by a small coefficient multiplying the highest order derivative. They differ from regularly perturbed boundary value problems in that the asymptotic solution is not a smooth function of the small parameter, and as a consequence, boundary layer terms need to be constructed. We use the technique of compound asymptotic expansions (see, for example, [7], [55], [65], [67], [70], [83] and [90]), in the first part of Chapter 5, for the full linear system of differential and algebraic reaction-diffusion equations associated with the catalytic reactor.

Figure 1.4: A thin rod connecting two bodies, which are maintained at constant temperatures.

To illustrate the technique, we present a simple example, see Figure 1.4, where a thin rod connects two large bodies, which are maintained at constant temperatures (for a similar example see [55]). We allow the thermal conductivity of the rod to be a function of x, and we allow the temperature of the surrounding medium to vary in x. We consider a Dirichlet boundary value problem for a second order differential equation where the small coefficient multiplies the highest order derivative:

$$\begin{aligned} \varepsilon^2 T''(x,\varepsilon) - r(x)T(x,\varepsilon) = p(x),\ 0 \le x \le 1, \\ T(0) = q_0,\ \ T(1) = q_1, \end{aligned} \tag{1.4.16}$$

where T is temperature, r and p are smooth, q_0 and q_1 are given constants, and $r(x) > 0$ for $x \in [0,1]$.

Limit solution

The limit solution (when $\varepsilon = 0$) is

$$T_0(x) = -\frac{p(x)}{r(x)}.$$

The above solution may not necessarily satisfy the boundary conditions; this implies that we need to construct boundary layers near the left and right ends.

Boundary layers

In order to compensate for the discrepancies in the boundary conditions left by the limit solution, $T_0(x)$, we approximate the solution for the function $T(x,\varepsilon)$ as

$$T(x,\varepsilon) \backsimeq T_0(x) + \mathcal{V}(X) + \mathcal{W}(Y),$$

where $\mathcal{V}$ is a boundary layer function, which compensates for the error at the left end, and $\mathcal{W}$ is a boundary layer function compensating for the error at the right end. The independent variables, X and Y, are scaled coordinates in magnified regions near the ends, such that,

$$X = \frac{x}{\varepsilon} \quad \text{and} \quad Y = \frac{1-x}{\varepsilon}.$$

The boundary layers decay as we move away from the end regions.

Boundary layer at the left end

The model problem (independent of the small parameter) for $\mathcal{V}$ is

$$\mathcal{V}_0''(X) - r(0)\mathcal{V}_0(X) = 0, \quad X > 0,$$

where we have fixed the function r at $x = 0$. The corresponding boundary conditions are

$$\mathcal{V}_0(0) = T(0) - T_0(0) = q_0 - T_0(0),$$
$$\text{and} \qquad \mathcal{V}_0(X) \to 0 \ \text{ as } \ X \to \infty.$$

The solution for the above problem for $\mathcal{V}_0$ is given by

$$\mathcal{V}_0(X) = (q_0 - T_0(0))e^{-\sqrt{r(0)}X}.$$

Boundary layer at the right end

The model problem (independent of the small parameter) for $\mathcal{W}$ is

$$\mathcal{W}_0''(Y) - r(1)\mathcal{W}_0(Y) = 0, \quad Y > 0,$$

where we have fixed the function r at $x = 1$. The corresponding boundary conditions are

$$\mathcal{W}_0(0) = T(1) - T_0(1) = q_1 - T_0(1),$$
$$\text{and} \qquad \mathcal{W}_0(Y) \to 0 \ \text{ as } \ Y \to \infty.$$

The solution for $\mathcal{W}_0$ is given by

$$\mathcal{W}_0(Y) = (q_1 - T_0(1))e^{-\sqrt{r(1)}Y}.$$

Consequently, to leading order, the solution of (1.4.16) is the sum

$$\begin{aligned} T(x,\varepsilon) &= T_0(x) + \mathcal{V}_0(X) + \mathcal{W}_0(Y) \\ &= -\frac{p(x)}{r(x)} + (q_0 - T_0(0))e^{-\sqrt{r(0)}X} + (q_1 + T_0(1))e^{-\sqrt{r(1)}Y} \\ &= -\frac{p(x)}{r(x)} + \left(q_0 + \frac{p(0)}{r(0)}\right)e^{-\sqrt{r(0)}\frac{x}{\varepsilon}} + \left(q_1 - \frac{p(1)}{r(1)}\right)e^{-\sqrt{r(1)}\frac{1-x}{\varepsilon}}. \end{aligned}$$

Similar analysis is carried out in Chapter 5 for the model describing the exothermic and endothermic reactions taking place in the adjacent channels of an industrial reactor. We explain how the numerical solution corresponds to the limit problem, and we construct asymptotic approximations for the boundary layers in a similar way to what is presented here.

The second part of Chapter 5 is associated with a nonlinear problem. We approximate the solution by taking three separate regions along the length of the channel, and we then use a certain matching procedure, sometimes called "the method of inner and outer expansions" (see, for example, [59], [68] and [90]), to join the solutions in the three regions. For our particular case of the catalytic reactor, the 'outer' region is the main part of the channel, and the 'inner' regions are associated with magnified areas at the ends of the channels.

1.5 Physical and engineering background

1.5.1 Packed bed reactors and balance equations in the channels

Packed bed reactors, of the type we consider in the present work, usually consist of parallel channels filled with pellets, which are covered in a catalyst that

promotes the chemical reactions taking place inside the channels. The velocity profile in a packed bed is quite complex as the fluid must pass through the pore network formed by usually randomly packed particles. The average velocity profile at a macroscopic level is approximately flat in the main central portion of the bed but changes rapidly near the walls of the reactor (see, for example, [30], [45], [60], [71] and [80]). In the previous section we explained how this relates to the theoretical concepts known in the literature as Darcy's law and Hartmann flow. Usually in applications, the profile is considered to be flat along the entire cross-section of the bed, and the changes that occur near the walls are ignored (see, for example, [23], [29], [45], [53] and [91]). In the literature on chemical engineering there are three types of reactors discussed. The first is the homogeneous reactor in which a single phase, i.e. only the fluid phase, is modelled; this is usually in cases when there is no packed bed. For cases when there is a packed bed, one model is for the pseudo-homogeneous reactor and the other is for the heterogeneous reactor. In the pseudo-homogenous reactor, the solid and fluid temperatures are the same at any given point. In the heterogeneous reactor, which is the most physically realistic (see, for example, [45] and [53]), the fluid and solid phases are accounted for separately, with heat and mole balance equations written for each phase. For the model considered in this thesis we derive the equations for a non-adiabatic heterogeneous packed bed reactor. Other work on steady state dispersion models for packed bed reactors and the kinetics of catalytic reactions can be found in the work by Hayes and Kolaczkowski [45], Hayes *et al.* [46], Slattery [85] and Spence *et al.* [86].

For our model, dispersion is included in the fluid phase balance equation only. In the energy balance equations diffusion is taken into account in both phases, since they both can conduct heat.

Consider the reactor volume element shown in Figure 1.5 (a similar description of the equations can be found in [23] and [45]), where H denotes the enthalpy (heat) of reaction and F is the molar flow rate.

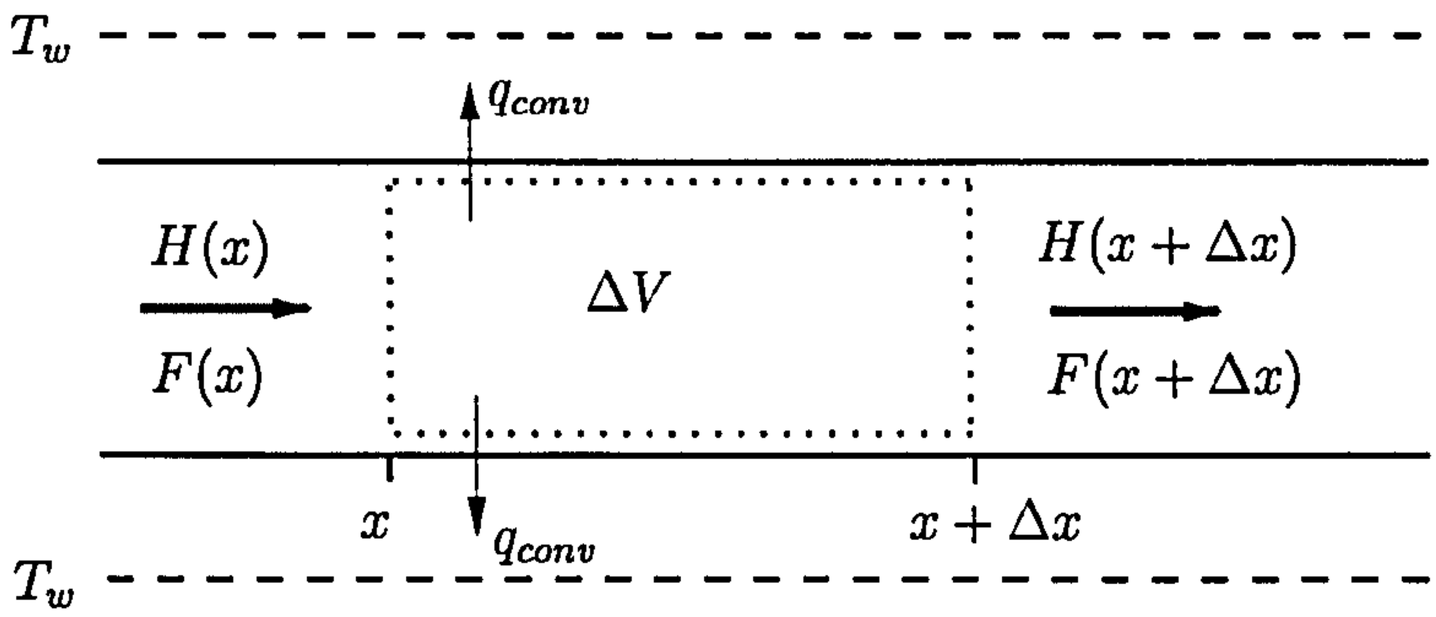

Figure 1.5: Differential volume element used to obtain molar and energy balances for the non-adiabatic packed bed reactor.

Fluid mole balance

(without superimposed dispersion term)

$$\Big[\text{Moles in}\Big] - \Big[\text{Moles out}\Big] - \Big[\text{Moles transported to cat. surface}\Big] = 0.$$

where

$$\Big[\text{Moles in}\Big] - \Big[\text{Moles out}\Big] = \Big[F\Big]_x - \Big[F\Big]_{x+\Delta x} = -\Delta F$$

and

$$\Big[\text{Moles transported to cat. surface}\Big] =$$

$$\Big[\text{mass transfer coeff.}\Big] \times \Big[\text{cat. surf. area}\Big] \times \Big[\text{mean conc.}\Big] \times \Big[\text{mole frac.}\Big]$$

$$= k_m \Delta S C_f (Y_f - Y_s),$$

giving

$$0 = -\Delta F - k_m \Delta S C_f (Y_f - Y_s). \tag{1.5.17}$$

The solid particle surface area per unit bed volume, denoted by a_v, is given by

$$a_v = \frac{\Delta S}{\Delta V} \quad \text{where} \quad \Delta V = A_c \Delta x,$$

and the molar flow rate F is related to the mole average velocity v_x as follows:

$$F = v_x A_c C_f Y_f.$$

Here A_c is the cross-sectional area of the packed bed, and C_f is the mean fluid concentration. Dividing (1.5.17) by $A_c \Delta x$ and considering the case when the volume element becomes small (when it approaches its differential volume element), we have

$$0 = -v_x \frac{dY_f}{dx} - k_m a_v (Y_f - Y_s).$$

Superimposing the dispersion term, the steady state fluid mole balance equation becomes

$$0 = D_e \frac{d^2 Y_f}{dx^2} - v_x \frac{dY_f}{dx} - k_m a_v (Y_f - Y_s).$$

Solid mole balance

Similarly for the solid mole balance equation we have

$$\Big[\text{Moles transported to cat. surface}\Big] = \Big[\text{Moles reacted in cat. reaction}\Big].$$

$$k_m \Delta S C_f (Y_f - Y_s) = \xi (-R)_s (1 - \phi) \Delta V \rho_c,$$

where ξ is the effectiveness factor of the catalyst, $(-R)_s$ is the reaction rate, $(1 - \phi)$ is the fraction of bed occupied by the catalyst pellets, and ρ_c is the solid density. Dividing through by ΔV we obtain the algebraic steady state solid mole balance equation,

$$k_m a_v C_f (Y_f - Y_s) = \xi (-R)_s (1 - \phi) \rho_c.$$

Fluid energy balance

(without superimposed diffusion term)

$$\Big[\text{Enthalpy increase as a result of temperature rise and heat added from surroundings}\Big] = \Big[\text{Heat added to fluid from surface}\Big],$$

$$-v_x A_c \rho_f C_p \Delta T_f + a_f A_c \Delta x U_a (T_w - T_f) = -h_{fs} \Delta S (T_s - T_f),$$

where ρ_f is the fluid density, C_p is the specific heat capacity, a_f is the heat transfer area of the wall of the channel per unit bed volume, U_a is the overall heat transfer coefficient, and h_{fs} is the heat transfer coefficient between the solid and the fluid. Dividing through by ΔV, assuming that the volume element is small, and superimposing the diffusion term, the steady state fluid energy balance equation becomes

$$k_f \frac{d^2T_f}{dx^2} - v_x \rho_f C_p \frac{dT_f}{dx} + h_{fs} a_v (T_s - T_f) + a_f U_a (T_w - T_f) = 0.$$

Solid energy balance

(with superimposed diffusion term)

$$\begin{aligned} \left[\text{Diffusion term}\right] \quad &+ \quad \left[\text{Heat released by reaction}\right] \\ &- \quad \left[\text{Heat transferred from solid}\right] = 0, \end{aligned}$$

giving the steady state solid energy balance equation as

$$k_s \frac{d^2T_s}{dx^2} - \xi(-R)_s \rho_c (1-\phi) \Delta H_R - h_{fs} a_v (T_s - T_f) = 0.$$

1.5.2 Explanation of industrial constants

In this thesis we consider the following catalytic combustion and steam reforming reactions:

$CH_4 + H_2O$	$\rightleftharpoons$	$3H_2 + CO$	Steam reforming reaction (simplified)
$CH_4 + 2O_2$	$\rightarrow$	$2H_2O + CO_2$	Catalytic combustion reaction.

There is extensive literature on the steam reforming and combustion of methane (see, for example, [2], [35], [45], [74], [78] and [96]). We give a detailed explanation

below of the industrial data associated with these chemical reactions, which we use in Chapters 3 to 7:

The mass transfer coefficient k_m is given in [45] as

$$k_m = \frac{D_{iff}}{D_p}\Big(2 + 1.1(Sc)^{\frac{1}{2}}(Re)^{\frac{3}{5}}\Big), \tag{1.5.18}$$

where Sc and Re are the Schmidt number and Reynolds number respectively, such that

$$Sc = \frac{\eta}{\rho_m D_{iff}}, \quad Re = \frac{D_p v_x \rho}{\eta},$$

D_{iff} is the diffusion of methane into water, D_p is the diameter of the pellets, η is the viscosity, ρ is the mass density, and the mole average superficial velocity v_x is given by

$$v_x = \frac{F_t}{A_c \rho_f},$$

with F_t being the total molar flow rate. For the above-mentioned coefficients we take the values given in Table 1.1.

The dispersion coefficient D_e is related to the velocity as follows:

$$D_e = \frac{D_B v_x}{Pe_R}, \tag{1.5.19}$$

where D_B is associated with the specific geometry, and Pe_R is the Peclet number, which describes the flow of the fluid in the channel (see, for example, [45]).

The heat transfer coefficient between the solid and the fluid, denoted by h_{fs}, is computed using the following relation (see, for example, [45]),

$$h_{fs} = \frac{k_f}{D_p}\Big(2 + 1.1(Pr)^{\frac{1}{3}}(Re_p)^{\frac{3}{5}}\Big), \tag{1.5.20}$$

where Pr is the Prandtl number, which describes the flow of the fluid in the channel, and it is given by

$$Pr = \frac{C_p \eta}{k_f},$$

Constant	Units	Reformer side	Combustion side
D_{iff}	m^2/s	5.3×10^{-6}	4.2×10^{-6}
D_p	m	0.0174	0.0174
η	Pa s	3.6×10^{-5}	3.4×10^{-5}
ρ	kg/m^3	7.076	11.2
F_T	mol/s	6.25	5.66
A_c	m^2	0.00632	0.00632
ρ_f	mol/m^3	400.4	400.4
v_x	m/s	2.47	2.24
Sc	-	0.9599	0.7228
Re_p	-	8447	12839
k_m	m/s	0.0794	0.070

Table 1.1: Values taken from [2], [6], [35] and [45] to compute the mass transfer coefficient k_m, given by (1.5.18).

Constant	Units	Reformer side	Combustion side
D_B	m	0.0214	0.0214
Pe_R	–	10	10
D_e	m^2/s	0.0053	0.0048
C_p	J/(kg K)	2490.1	1147.78
k_f	W/(m K)	0.061	0.054
Pr	-	1.47	0.723
h_{fs}	$W/(m^2 K)$	1002.4	900.34

Table 1.2: Values taken from [32], [45] and [60] to compute the dispersion coefficient D_e, given by (1.5.19) and the heat transfer coefficient h_{fs}, given by (1.5.20).

k_f is the thermal conductivity of the fluid, and C_p is the mass heat capacity. For the dispersion coefficient D_e and the heat transfer coefficient h_{fs}, we take the values given in Table 1.2.

The heat transfer coefficient between the wall and the fluid, denoted by h_w is computed from the following relation

$$h_w = \frac{k_f Nu}{D_p},$$

where Nu is known as the Nusselt number (see, for example, [45]), which is a dimensionless parameter describing the flow of the fluid in the channel, and it is given by

$$Nu = 0.17(Re_p)^{0.79},$$

The reaction rate is expressed as the moles of methane reacting per unit area of catalyst per unit time. It is the product of the concentration and a factor containing the solid temperature, the second of which is denoted here by Ψ and is known in the literature as the reaction velocity function, (see, for example, [2]

Constant	Units	Description	Reformer side	Combustion side
Nu	–	Nusselt number	215.06	299.36
h_w	W/(m^2 K)	Heat transfer between wall and fluid	753.95	929.05
a_v	1/m	(Surface area)/volume	76.33	76.33
ξ	–	Effectiveness factor of catalyst	0.65	0.65
ρ_c	kg/m^3	Catalyst density	2355.2	2355.2
ϕ	–	Bed porosity	0.605	0.605
k_s	W/(m K)	Solid thermal conductivity	0.22	0.22
(ΔH_R)	J/mol	Heat of reaction	206000	−802000
$\mathcal{A}$	mol/(kg$_{\text{cat}}$ s)	Pre-exponential factor	0.778	0.0794
E	J/(mol K)	Activation energy	36720	1100
R_g	J/(mol K)	Universal gas constant	8.314	8.314
L	m	Length of channel	12	12

Table 1.3: Description and values of industrial data taken from [6], [23], [35], [45], [74], [78], [94] and [96].

and [45]). This second factor can be expressed using the Arrhenius equation

$$\frac{d\ \ln\Psi}{dT_s^2}(x) = \frac{E}{R_g T_s(x)},$$

where E is the apparent activation energy, R_g is a universal gas constant, and T_s is the solid temperature. Integrating gives the more common form of the temperature dependent factor of what is known as the Arrhenius reaction rate:

$$\Psi = \mathcal{A} e^{-\frac{E}{R_g T_s(x)}},$$

where $\mathcal{A}$ is the pre-exponential factor. For the constants involved in this reaction rate, and the remaining industrial data, we use the values given in Table 1.3, which have been taken from the extensive literature on experimental studies of reactors (see, for example, [6], [23], [35], [45], [74], [78], [94] and [96]). For the numerical simulations of the industrial examples in this thesis we take Dirichlet conditions at the inlet of the reactor, with the Dirichlet data taken from the above literature. The conditions at the outlet of the reactor are the zero-flux conditions for all the functions. Examples by Hayes and Kolaczkowsi [45], Parulekar and Ramkrishna [73], Wehner and Wilhelm [92] and Zanfir [95] and [96] show that the zero-flux condition is the usual assumption for models of reactors of this type.

Chapter 2

Asymptotic analysis of heat transfer in a system of channels connected by thin conducting walls

2.1 Introduction

The aim of this chapter is to present an illustrative example showing how we use an asymptotic method to analyse the thermal interaction between fluids in adjacent channels which are connected by thin walls of low thermal conductivity. The model we investigate is a system of n thin channels of normalised thickness ε $(0 < \varepsilon \ll 1)$ separated by thin conducting walls of normalised thickness ε^2. We consider a two-dimensional problem, where we allow for heat sources in the channels and assume there is no heat sources in the wall, that is, we have non-homogeneous heat equations in the channels and homogeneous heat equations in the walls. Neumann boundary conditions are set on the upper and lower horizontal parts of the external boundary of the system, and ideal thermal contact

(continuity in temperature and heat flux) is assumed between each layer. Using an asymptotic method we reduce the dimensions of the leading order problem by obtaining a set of solvability conditions which lead to a coupling between the temperatures in the channels. This asymptotic model enables us to accurately describe the thermal interaction between the channels across the thin wall. A particular example incorporating chemical reactions inside the channels highlights possible industrial applications.

A model asymptotic problem where the heat source density is independent of the temperature is considered in the next section of this chapter. We present results that show the coupling in the temperatures between the adjacent channels. In Section 2.3 we relate the asymptotic algorithm to two steady state chemical reactions, one of which generates heat and the other consumes heat. The numerical results for a simple illustrative example showing the coupling in temperature between these chemical reactions are also presented in this chapter. This chapter is partially based on Selsil, Movchan and Movchan [81].

2.2 Formulation of a model problem

Consider the system shown in Figure 2.1, which consists of two channels Ω_1 and Ω_2 of normalised[1] width ε, separated by a thin conducting wall Ω_0 of normalised width ε^2, where ε is a small positive parameter, $0 < \varepsilon \ll 1$. Assume that each channel Ω_j, $j = 1, 2$, is filled with a fluid whose temperature $T^{(j)}$ satisfies a nonhomogeneous heat equation

$$\mu_j \nabla^2 T^{(j)}(x, y, t) - \frac{\partial T^{(j)}}{\partial t}(x, y, t) + f^{(j)}(x, y, t) = 0 \ \text{ in } \Omega_j, \quad j = 1, 2, \quad (2.2.1)$$

[1]Throughout this thesis we assume that the ratio of the width D_C of the channel to its length L is small, and we denote this dimensionless quantity by ε, that is, $\varepsilon = D_C/L$, $0 < \varepsilon \ll 1$. In this chapter we are interested in the temperature and concentration distributions in the middle regions of the channels (away from the ends).

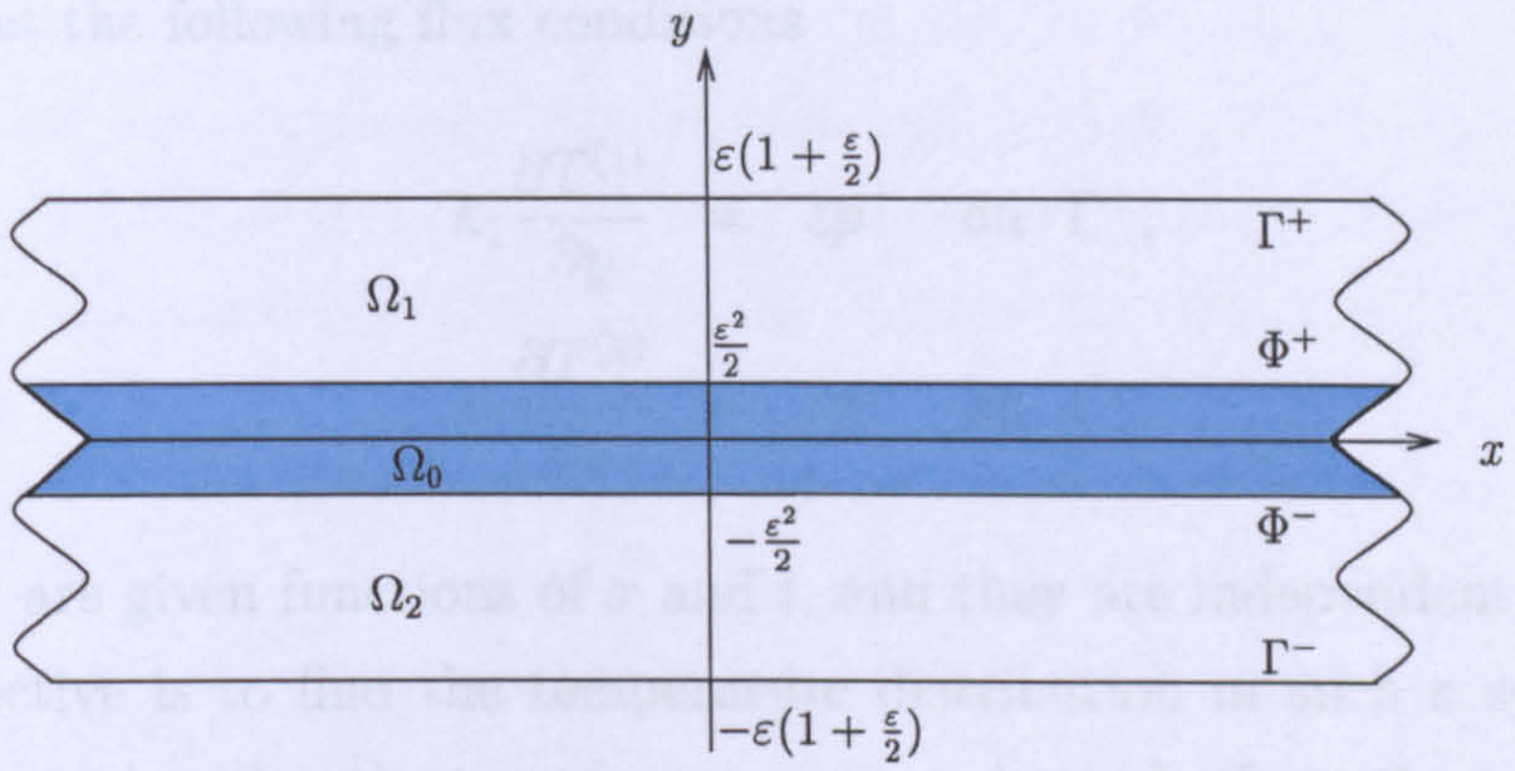

Figure 2.1: Two infinite channels separated by a thin conducting wall.

where t is time, μ_j denotes the thermal diffusivity[2], and $f^{(j)}$ is the heat source density, which is independent of ε and $T^{(j)}$, $j = 1, 2$.

The distribution of the temperature $T^{(0)}$ within the wall Ω_0 is described by a homogeneous heat equation

$$\mu_0 \nabla^2 T^{(0)}(x, y, t) - \frac{\partial T^{(0)}}{\partial t}(x, y, t) = 0 \ \text{ in } \Omega_0, \tag{2.2.2}$$

where μ_0 is the thermal diffusivity of the wall.

We assume that the temperatures $T^{(1)}$, $T^{(2)}$ and $T^{(0)}$ satisfy the ideal thermal contact conditions (continuity in temperature and heat flux) on the surfaces Φ^+ and Φ^- of the wall Ω_0, that is,

$$T^{(1)} = T^{(0)}, \ k_1 \frac{\partial T^{(1)}}{\partial y} = k_0 \frac{\partial T^{(0)}}{\partial y} \ \text{ on } \Phi^+, \tag{2.2.3}$$

$$T^{(2)} = T^{(0)}, \ k_2 \frac{\partial T^{(2)}}{\partial y} = k_0 \frac{\partial T^{(0)}}{\partial y} \ \text{ on } \Phi^-. \tag{2.2.4}$$

[2]Thermal diffusivity is proportional to thermal conductivity: $\mu_i = \frac{k_i}{\rho_f^{(i)} C_p^{(i)}}$, $i = 0, 1, 2$, where k_i is the thermal conductivity, $\rho_f^{(i)}$ is the fluid density, and $C_p^{(i)}$ is the constant pressure heat capacity.

On the upper and lower horizontal external boundaries Γ^+ and Γ^- (see Figure 2.1) we set the following flux conditions

$$k_1 \frac{\partial T^{(1)}}{\partial y} = \varepsilon p^+ \quad \text{on} \quad \Gamma^+, \tag{2.2.5}$$

$$k_2 \frac{\partial T^{(2)}}{\partial y} = \varepsilon p^- \quad \text{on} \quad \Gamma^-, \tag{2.2.6}$$

where $p^{\pm}$ are given functions of x and t, and they are independent of ε.
Our objective is to find the temperature distribution in such a system and to analyse how changing the temperature in one channel affects the temperature in the other channel.
We assume that the thermal conductivity k_0 of the wall is small compared to the thermal conductivities k_1 and k_2 of the channels, that is, k_0 is taken in the form

$$k_0 = \varepsilon^3 k^*, \tag{2.2.7}$$

where k^* has the same order of magnitude as k_1 and k_2.

2.2.1 Scaled variables and asymptotic approximations

Using an asymptotic technique similar to those described in [7], [55], [65], [67], [70], [83] and [90], we construct asymptotic expansions for the temperatures $T^{(j)}$ in the following form

$$T^{(j)}(x,y,t) = T_0^{(j)}(x,y,t) + \varepsilon T_1^{(j)}(x,y,t) + \varepsilon^2 T_2^{(j)}(x,y,t) + \ldots, \qquad j = 0,1,2. \tag{2.2.8}$$

We use expansions (2.2.8) to derive a set of conditions which 'couple' the leading order temperatures $T_0^{(1)}$ and $T_0^{(2)}$ in the two channels. A 'coupled' system is one in which the differential equation for the temperature in one channel contains the function for the temperature from the other channel, that is, the differential

equation for $T_0^{(1)}$ contains the function $T_0^{(2)}$ via a term of the form $T_0^{(1)} - T_0^{(2)}$, and vice versa. An 'uncoupled' system is one in which the two reactions in the channels are completely independent and changing the temperature in one channel will have no effect on the temperature in the other channel.

Since the channels are thin, we introduce new scaled variables, such that

$$\tau_j = \frac{y_j}{\varepsilon} \text{ in } \Omega_j, \quad j = 1,2, \quad \tau_0 = \frac{y}{\varepsilon^2} \text{ in } \Omega_0, \tag{2.2.9}$$

where

$$\tau_i \in \Big(-\frac{1}{2}, \frac{1}{2}\Big),\ i = 0,1,2;\ y_j = y + \frac{(-1)^j \varepsilon(1+\varepsilon)}{2},\ j = 1,2.$$

In these new variables, the conditions (2.2.3) - (2.2.6) can be rewritten as follows:

$$T^{(1)}\Big|_{\tau_1=-\frac{1}{2}} = T^{(0)}\Big|_{\tau_0=\frac{1}{2}},\ \frac{k_1}{\varepsilon}\frac{\partial T^{(1)}}{\partial \tau_1}\Big|_{\tau_1=-\frac{1}{2}} = \frac{k_0}{\varepsilon^2}\frac{\partial T^{(0)}}{\partial \tau_0}\Big|_{\tau_0=\frac{1}{2}}, \tag{2.2.10}$$

$$T^{(2)}\Big|_{\tau_2=\frac{1}{2}} = T^{(0)}\Big|_{\tau_0=-\frac{1}{2}},\ \frac{k_2}{\varepsilon}\frac{\partial T^{(2)}}{\partial \tau_2}\Big|_{\tau_2=\frac{1}{2}} = \frac{k_0}{\varepsilon^2}\frac{\partial T^{(0)}}{\partial \tau_0}\Big|_{\tau_0=-\frac{1}{2}}, \tag{2.2.11}$$

$$\frac{k_1}{\varepsilon}\frac{\partial T^{(1)}}{\partial \tau_1}\Big|_{\tau_1=\frac{1}{2}} = \varepsilon p^+,\quad \frac{k_2}{\varepsilon}\frac{\partial T^{(2)}}{\partial \tau_2}\Big|_{\tau_2=-\frac{1}{2}} = \varepsilon p^-. \tag{2.2.12}$$

Substituting (2.2.8) into equations (2.2.1) and (2.2.2), for the first two terms of each expansion we obtain

$$\frac{\partial^2 T_0^{(j)}}{\partial \tau_j^2} = 0,\ \frac{\partial^2 T_1^{(j)}}{\partial \tau_j^2} = 0,\ \tau_j \in \Big(-\frac{1}{2}, \frac{1}{2}\Big),\ j = 0,1,2.$$

This implies that $T_0^{(j)}$ and $T_1^{(j)}$, $j = 0,1,2$, are linear in τ_j, that is,

$$T_i^{(j)}(x, \tau_j, t) = \beta_1^{(i,j)}(x,t) + \beta_2^{(i,j)}(x,t)\tau_j,\ i = 0,1,\ j = 0,1,2, \tag{2.2.13}$$

where $\beta_1^{(i,j)}$ and $\beta_2^{(i,j)}$, $i = 0,1$, $j = 0,1,2$, are functions that we find from the boundary conditions. By substituting (2.2.7) into the flux conditions in (2.2.10)

- (2.2.12), it follows that

$$\frac{\partial T_i^{(1)}}{\partial \tau_1}\Big|_{\tau_1=\pm 1/2} = 0, \quad \frac{\partial T_i^{(2)}}{\partial \tau_2}\Big|_{\tau_2=\pm 1/2} = 0, \ i = 0, 1,$$

and therefore, the functions $T_0^{(1)}, T_0^{(2)}, T_1^{(1)}$, and $T_1^{(2)}$ are independent of the scaled variable τ_j, $j = 1, 2$.

The remaining two Dirichlet conditions in (2.2.10) and (2.2.11), together with (2.2.13), give

$$T_0^{(0)}\left(x, \frac{1}{2}, t\right) = \beta_1^{(0,0)}(x,t) + \frac{\beta_2^{(0,0)}(x,t)}{2} = T_0^{(1)}(x,t),$$

$$T_0^{(0)}\left(x, -\frac{1}{2}, t\right) = \beta_1^{(0,0)}(x,t) - \frac{\beta_2^{(0,0)}(x,t)}{2} = T_0^{(2)}(x,t).$$

Thus, eliminating the functions $\beta_1^{(0,0)}(x,t)$ and $\beta_2^{(0,0)}(x,t)$, for the leading term of the temperature in the wall, we obtain

$$\begin{aligned} T_0^{(0)}(x, \tau_0, t) &= \frac{T_0^{(1)}(x,t) + T_0^{(2)}(x,t)}{2} \\ &+ (T_0^{(1)}(x,t) - T_0^{(2)}(x,t))\tau_0, \quad \tau_0 \in \left(-\frac{1}{2}, \frac{1}{2}\right). \end{aligned}$$

In order to find the unknown functions $T_0^{(1)}(x,t)$ and $T_0^{(2)}(x,t)$, we derive a set of boundary value problems for the next terms $T_2^{(j)}$, $j = 1, 2$, in the asymptotic representations (2.2.8) in the two channels:

$$\frac{\partial^2 T_2^{(j)}}{\partial \tau_j^2} = -\frac{\partial^2 T_0^{(j)}}{\partial x^2} + \frac{1}{\mu_j}\left(\frac{\partial T_0^{(j)}}{\partial t} - f^{(j)}\right), \ \tau_j \in \left(-\frac{1}{2}, \frac{1}{2}\right), \quad (2.2.14)$$

$$\frac{\partial T_2^{(1)}}{\partial \tau_1}\Big|_{\tau_1=1/2} = \frac{p^+}{k_1}, \qquad \frac{\partial T_2^{(1)}}{\partial \tau_1}\Big|_{\tau_1=-1/2} = \frac{k^*}{k_1}(T_0^{(1)} - T_0^{(2)}), \quad (2.2.15)$$

$$\frac{\partial T_2^{(2)}}{\partial \tau_2}\Big|_{\tau_2=-1/2} = \frac{p^-}{k_2}, \qquad \frac{\partial T_2^{(2)}}{\partial \tau_2}\Big|_{\tau_2=1/2} = \frac{k^*}{k_2}(T_0^{(1)} - T_0^{(2)}). \quad (2.2.16)$$

The functions $T_2^{(1)}$ and $T_2^{(2)}$ satisfy Neumann boundary conditions at $\tau_1 = \pm\frac{1}{2}$ and $\tau_2 = \pm\frac{1}{2}$, respectively. The system of equations (2.2.14) - (2.2.16) is solvable if and only if

$$-\frac{\partial^2 T_0^{(1)}}{\partial x^2} + \frac{1}{\mu_1}\frac{\partial T_0^{(1)}}{\partial t} - \frac{1}{\mu_1}\int_{-\frac{1}{2}}^{\frac{1}{2}} f^{(1)} d\tau_1 = \frac{p^+}{k_1} - \frac{k^*}{k_1}(T_0^{(1)} - T_0^{(2)}), \qquad (2.2.17)$$

and

$$-\frac{\partial^2 T_0^{(2)}}{\partial x^2} + \frac{1}{\mu_2}\frac{\partial T_0^{(2)}}{\partial t} - \frac{1}{\mu_2}\int_{-\frac{1}{2}}^{\frac{1}{2}} f^{(2)} d\tau_2 = \frac{k^*}{k_2}(T_0^{(1)} - T_0^{(2)}) - \frac{p^-}{k_2}. \qquad (2.2.18)$$

The solvability conditions (2.2.17) and (2.2.18) can be rearranged to give the following system of equations for $T_0^{(1)}$ and $T_0^{(2)}$:

$$\mu_1\frac{\partial^2 T_0^{(1)}}{\partial x^2} - \frac{\partial T_0^{(1)}}{\partial t} - \frac{k^*}{\rho_{f1}C_{p1}}(T_0^{(1)} - T_0^{(2)}) = -\frac{p^+}{\rho_{f1}C_{p1}} - \int_{-\frac{1}{2}}^{\frac{1}{2}} f^{(1)} d\tau_1, \qquad (2.2.19)$$

$$\mu_2\frac{\partial^2 T_0^{(2)}}{\partial x^2} - \frac{\partial T_0^{(2)}}{\partial t} + \frac{k^*}{\rho_{f2}C_{p2}}(T_0^{(1)} - T_0^{(2)}) = \frac{p^-}{\rho_{f2}C_{p2}} - \int_{-\frac{1}{2}}^{\frac{1}{2}} f^{(2)} d\tau_2. \qquad (2.2.20)$$

Equations (2.2.19) and (2.2.20) are coupled via the term $(T_0^{(1)} - T_0^{(2)})$ which characterises the jump in temperature across the wall. The system (2.2.19) and (2.2.20), together with the initial conditions at $t = 0$ and conditions as $x \to \pm\infty$ (or $x = 0$, $x = L$ for channels of finite length L), can then be solved (analytically or numerically) for the given source densities $f^{(1)}$, $f^{(2)}$ and the fluxes p^+, p^-.

As a particular example, we consider the case when there is no dependence on time and each channel is of length $L = 1$ m. The fluxes p^+, p^-, and the source densities $f^{(1)}$ and $f^{(2)}$, are given by

$$p^+ = -10 \text{ (K m)/s}, \quad p^- = 4 \text{ (K m)/s},$$

$$\int_{-1/2}^{1/2} f^{(1)} d\tau_1 = 0 \text{ K/s}, \quad \int_{-1/2}^{1/2} f^{(2)} d\tau_2 = 12 \text{ K/s}.$$

The temperatures $T_0^{(1)}$ and $T_0^{(2)}$ satisfy the following boundary conditions

$$T_0^{(1)}(0) = 760 \text{ K}, \; T_0^{(2)}(0) = 730 \text{ K}, \; \frac{dT_0^{(1)}}{dx}(1) = 0, \; \frac{dT_0^{(2)}}{dx}(1) = 0.$$

For the fluid densities, the heat capacities and the thermal conductivities we take the values

$$\rho_f^{(1)} = 0.5 \text{ mol/m}^3, \; C_p^{(1)} = 2 \text{ J/(mol K)}, \; \rho_f^{(2)} = 0.2 \text{ mol/m}^3, \; C_p^{(2)} = 5 \text{ J/(mol K)},$$
$$k_1 = 0.2 \text{ W/(m K)}, \quad k_2 = 0.1 \text{ W/(m K)}, \quad k^* = 18 \text{ W/(m K)}.$$

The temperature distribution in each channel[3], for the uncoupled ($k^* = 0$ W/(m K)) and coupled ($k^* = 18$ W/(m K)) cases, is presented in Figures 2.2(a) and 2.2(b).

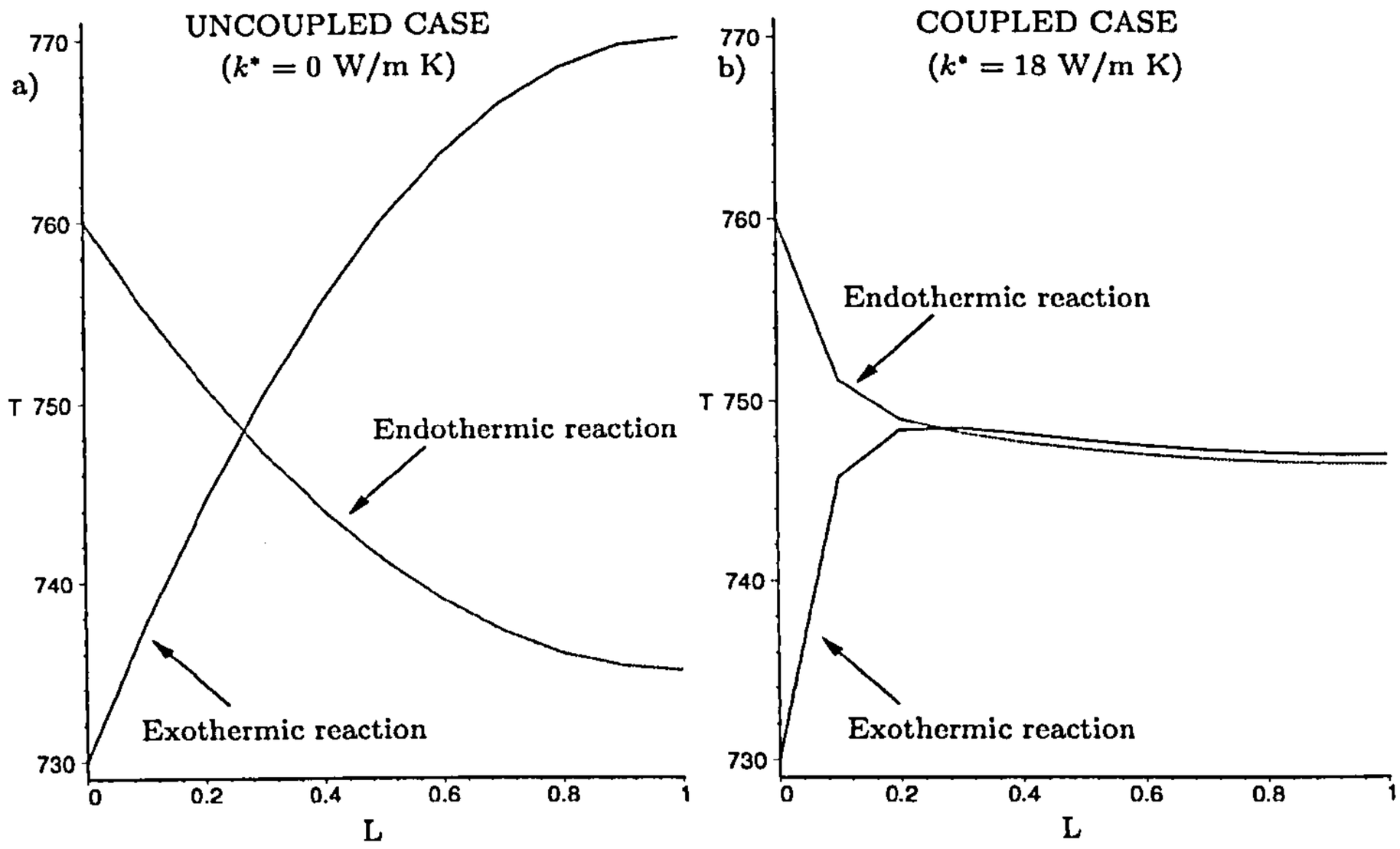

Figure 2.2: Temperature distribution along the channels. (a) Uncoupled temperature distribution (with $k^* = 0$ W/(m K)), (b) Coupled temperature distribution (with k^*=18 W/(m K)).

[3]In the figures presented in this thesis the temperature T is measured in Kelvins (^{o}K) and the length L is measured in metres (m).

For a non-conducting wall, the two reactions are uncoupled, see Figure 2.2(a). In the channel Ω_1, we assume that the temperature decreases along the channel, i.e. we have an endothermic reaction where heat is consumed. In the channel Ω_2 we assume that the temperature increases along the channel, i.e. we have an exothermic reaction where heat is generated. However, when the wall does conduct heat, we have a coupling in the temperatures, and, as a consequence, the reactions balance each other: the heat generated by the exothermic reaction is consumed by the endothermic reaction, see Figure 2.2(b). Consequently, the two temperatures approach a certain value and then remain close to this value for the rest of the channel.

2.3 Illustrative example

Assume now that a steady state chemical reaction takes place in each channel, and the fluid, which, for convenience, is assumed to be Newtonian and incompressible, moves steadily in the horizontal direction with a nonzero velocity $\mathbf{v}^{(j)}$, $j = 1, 2$. In this case the temperatures $T^{(1)}$ and $T^{(2)}$ satisfy the following 2D equations in Ω_1 and Ω_2 respectively (see Chapter 3 of [45] on 2D steady state models of laminar flow in catalytic reactors):

$$\mu_j \nabla^2 T^{(j)} - \mathbf{v}^{(j)} \cdot \nabla T^{(j)} - \frac{(\Delta H_R^{(j)})}{\rho_f{}^{(j)} C_p^{(j)}} (-R)_s^{(j)} = 0, \ j = 1, 2, \tag{2.3.21}$$

where $\rho_f{}^{(j)}$ is the fluid density, $C_p^{(j)}$ is the constant pressure heat capacity, $(-R)_s^{(j)}$ is the reaction rate, and $(\Delta H_R^{(j)})$ is the heat of the reaction. A positive value of $(\Delta H_R^{(j)})$ corresponds to an endothermic reaction, and a negative value corresponds to an exothermic reaction.

For this example we shall take the reaction rates $(-R)_s^{(j)}$ in the Arrhenius form

(see, for example, [2], [45] and [79]):

$$(-R)_s^{(j)} = \mathcal{A}^{(j)} e^{-\frac{E^{(j)}}{RT^{(j)}(x)}} Y^{(j)}, \ j = 1, 2,$$

where $\mathcal{A}^{(j)}$ are constants known as pre-exponential factors, $E^{(j)}$ is the activation energy, R is a gas constant, and $Y^{(j)}$ is the concentration of a certain reactant in the channel Ω_j, $j = 1, 2$, which satisfies the equation (see [45]):

$$\rho_f{}^{(j)} D^{(j)} \nabla^2 Y^{(j)} - \rho_f{}^{(j)} \mathbf{v}^{(j)} \cdot \nabla Y^{(j)} - (-R)_s^{(j)} = 0, \ j = 1, 2. \tag{2.3.22}$$

In equation (2.3.22) $D^{(j)}$ is the diffusion coefficient. For the remainder of this chapter, we shall use a simplified version of the above reaction rate. We shall neglect the nonlinearity by replacing the temperature function in the exponential term by the temperature $T^{(j)}(0)$ at the inlet, that is, we shall take the reaction rate in the form:

$$(-R)_s^{(j_0)} = \mathcal{A}^{(j)} e^{-\frac{E^{(j)}}{RT^{(j)}(0)}} Y^{(j)}, \ j = 1, 2.$$

We take equations (2.3.21) and (2.3.22) for the temperature and concentration in the channels and the homogeneous heat equation (2.2.2) for the temperature $T^{(0)}$ inside the wall. The boundary conditions we set are ideal thermal contact conditions (2.2.3) and (2.2.4) with the flux conditions (2.2.5) and (2.2.6), when $p^{\pm} = 0$, for the temperatures $T^{(j)}$, $j = 0, 1, 2$, the non-slip conditions for the velocities

$$\mathbf{v}^{(j)} = \mathbf{0} \ \text{ on } \ \Phi^{\pm} \cup \Gamma^{\pm}, \tag{2.3.23}$$

and for the concentrations we have

$$\frac{\partial Y^{(1)}}{\partial y} = 0 \ \text{ on } \ \Gamma^{+} \cup \Phi^{+}, \ \ \frac{\partial Y^{(2)}}{\partial y} = 0 \ \text{ on } \ \Gamma^{-} \cup \Phi^{-}. \tag{2.3.24}$$

Due to the fact that we have an incompressible Newtonian fluid, with the flow in one direction only, it follows that

$$\mathbf{v}^{(j)} = (v^{(j)}(y_j), 0), \ j = 1, 2.$$

The first component of this velocity satisfies the equation (see, for example, [16])

$$\nabla^2 v^{(j)} = G^{(j)}/\eta^{(j)}, \tag{2.3.25}$$

where $G^{(j)}$ denotes the pressure gradient, and $\eta^{(j)}$, $j = 1, 2$, is the viscosity. Equation (2.3.25) implies that the velocity distribution in each channel has the form

$$\mathbf{v}^{(j)} = ((G^{(j)}/2\eta^{(j)})y_j^2 + b_1^{(j)}y_j + b_2^{(j)}, 0),\ j = 1, 2, \tag{2.3.26}$$

where the constants $b_1^{(j)}$ and $b_2^{(j)}$ are obtained from the boundary conditions on $\Gamma^{\pm}$ and $\Phi^{\pm}$,

$$b_1^{(j)} = 0,\ b_2^{(j)} = -\frac{G^{(j)}\varepsilon^2}{8\eta^{(j)}},\ j = 1, 2.$$

Using the coordinate transformation (2.2.9) and the representations (2.3.26) for the velocities $\mathbf{v}^{(j)}$ in each channel, we rewrite the system (2.3.21), (2.3.22) in the form

$$\begin{aligned} \mu_j\Big(\frac{\partial^2 T^{(j)}}{\partial x^2} + \frac{1}{\varepsilon^2}\frac{\partial^2 T^{(j)}}{\partial \tau_j^2}\Big) &- \Upsilon^{(j)}(4\tau_j^2 - 1)\frac{\partial T^{(j)}}{\partial x} \\ &- \frac{(\Delta H_R^{(j)})}{\rho_f{}^{(j)}C_p^{(j)}}(-R)_s^{(j_0)} = 0, \end{aligned} \tag{2.3.27}$$

$$\begin{aligned} \rho_f{}^{(j)}D^{(j)}\Big(\frac{\partial^2 Y^{(j)}}{\partial x^2} + \frac{1}{\varepsilon^2}\frac{\partial^2 Y^{(j)}}{\partial \tau_j^2}\Big) &- \Upsilon^{(j)}\rho_f{}^{(j)}(4\tau_j^2 - 1)\frac{\partial Y^{(j)}}{\partial x} \\ &- (-R)_s^{(j_0)} = 0, \end{aligned} \tag{2.3.28}$$

where $\Upsilon^{(j)} = \dfrac{\varepsilon^2 G^{(j)}}{8\eta^{(j)}}$, $j = 1, 2$, and for convenience, we assume that this quantity is of order $O(1)$.

We shall take the asymptotic expansions for the temperatures $T^{(j)}$ and the concentrations $Y^{(j)}$ in the form

$$T^{(j)} = T_0^{(j)} + \varepsilon T_1^{(j)} + \varepsilon^2 T_2^{(j)} + \ldots,\ j = 0, 1, 2, \tag{2.3.29}$$

$$Y^{(j)} = Y_0^{(j)} + \varepsilon Y_1^{(j)} + \varepsilon^2 Y_2^{(j)} + \ldots, \ j = 1, 2. \tag{2.3.30}$$

Substituting these expansions into equations (2.2.2), (2.3.27) and (2.3.28), and the boundary conditions (2.2.3) - (2.2.6), with $p^{\pm} = 0$, (2.3.23) and (2.3.24), we obtain, in the same way as in the previous case, that the functions $T_0^{(j)}, T_1^{(j)}, Y_0^{(j)}$ and $Y_1^{(j)}$, $j = 1, 2$, are independent of the scaled variable τ_j, and the functions $T_2^{(j)}$ and $Y_2^{(j)}$ solve the following problems:

$$\mu_j \frac{\partial^2 T_2^{(j)}}{\partial \tau_j^2} = \frac{(\Delta H_R^{(j)})}{\rho_f{}^{(j)} C_p^{(j)}} \mathcal{A}^{(j)} e^{-\frac{E^{(j)}}{RT_0^{(j)}(0)}} Y_0^{(j)} + \Upsilon^{(j)}(4\tau_j^2 - 1)\frac{dT_0^{(j)}}{dx} - \mu_j \frac{d^2 T_0^{(j)}}{dx^2},$$

$$k_1 \frac{\partial T_2^{(1)}}{\partial \tau_1}\Big|_{\tau_1 = -1/2} = k^*(T_0^{(1)} - T_0^{(2)}), \qquad \frac{\partial T_2^{(1)}}{\partial \tau_1}\Big|_{\tau_1 = 1/2} = 0,$$

$$\frac{\partial T_2^{(2)}}{\partial \tau_2}\Big|_{\tau_2 = -1/2} = 0, \qquad k_2 \frac{\partial T_2^{(2)}}{\partial \tau_2}\Big|_{\tau_2 = 1/2} = k^*(T_0^{(1)} - T_0^{(2)}); \tag{2.3.31}$$

$$\rho_f^{(j)} D^{(j)} \frac{\partial^2 Y_2^{(j)}}{\partial \tau_j^2} = \mathcal{A}^{(j)} e^{-\frac{E^{(j)}}{RT_0^{(j)}(0)}} Y_0^{(j)} + \Upsilon^{(j)} \rho_f{}^{(j)} (4\tau_j^2 - 1)\frac{dY_0^{(j)}}{dx} - \rho_f^{(j)} D^{(j)} \frac{d^2 Y_0^{(j)}}{dx^2},$$

$$\frac{\partial Y_2^{(j)}}{\partial \tau_j}\Big|_{\tau_j = \pm 1/2} = 0, \ j = 1, 2. \tag{2.3.32}$$

The solvability conditions for (2.3.31) and (2.3.32) give a system of coupled differential equations for the leading terms $T_0^{(j)}$ and $Y_0^{(j)}$,

$$\mu_1 \frac{d^2 T_0^{(1)}}{dx^2} + \frac{2}{3}\Upsilon^{(1)} \frac{dT_0^{(1)}}{dx} - \frac{k^*}{\rho_f^{(1)} C_p^{(1)}}(T_0^{(1)} - T_0^{(2)}) = \frac{(\Delta H_R^{(1)})}{\rho_f{}^{(1)} C_p^{(1)}} \mathcal{A}^{(1)} e^{-\frac{E^{(1)}}{RT_0^{(1)}(0)}} Y_0^{(1)},$$

$$\mu_2 \frac{d^2 T_0^{(2)}}{dx^2} + \frac{2}{3}\Upsilon^{(2)} \frac{dT_0^{(2)}}{dx} + \frac{k^*}{\rho_f^{(2)} C_p^{(2)}}(T_0^{(1)} - T_0^{(2)}) = \frac{(\Delta H_R^{(2)})}{\rho_f{}^{(2)} C_p^{(2)}} \mathcal{A}^{(2)} e^{-\frac{E^{(2)}}{RT_0^{(2)}(0)}} Y_0^{(2)},$$

$$\rho_f{}^{(j)} D^{(j)} \frac{d^2 Y_0^{(j)}}{dx^2} + \frac{2}{3}\Upsilon^{(j)} \rho_f{}^{(j)} \frac{dY_0^{(j)}}{dx} - \mathcal{A}^{(j)} e^{-\frac{E^{(j)}}{RT_0^{(j)}(0)}} Y_0^{(j)} = 0, \ j = 1, 2. \tag{2.3.33}$$

We solve system (2.3.33) numerically, using Maple, for the following values of the parameters (the parameters are chosen in such a way that we have an endothermic reaction in channel 1 and an exothermic reaction in channel 2):

$$D^{(1)} = D^{(2)} = 2 \text{ m}^2/\text{s}, \quad \Upsilon^{(1)} = \Upsilon^{(2)} = 3 \text{ (m s)}^{-1}, \quad R = 3 \text{ J/(mol K)},$$
$$C_p^{(1)} = C_p^{(2)} = 0.5 \text{ J/(mol K)}, \quad k_1 = k_2 = 0.15 \text{ W/(m K)}, \quad k^* = 1.5 \text{ W/(m K)},$$
$$\mathcal{A}^{(1)} = \mathcal{A}^{(2)} = 3 \text{ mol/(m}^3 \text{ s)}, \quad E^{(1)} = E^{(2)} = 2 \text{ J/mol},$$
$$(\Delta H_R^{(1)}) = 2 \text{ J/mol}, \quad (\Delta H_R^{(2)}) = -2 \text{ J/mol}, \quad {\rho_f}^{(1)} = {\rho_f}^{(2)} = 1 \text{ mol/m}^3,$$

assuming that both channels are of finite length L ($L = 1$ m). The temperatures $T_0^{(1)}$, $T_0^{(2)}$ and the concentrations $Y_0^{(1)}$, $Y_0^{(2)}$ satisfy the following boundary conditions:

$$Y_0^{(1)}(0) = 0.3, \quad \frac{dY_0^{(1)}}{dx}(1) = 0, \quad Y_0^{(2)}(0) = 0.1, \quad \frac{dY_0^{(2)}}{dx}(1) = 0,$$

$$T_0^{(1)}(0) = 800 \text{ K}, \quad T_0^{(2)}(0) = 700 \text{ K}, \quad \frac{dT_0^{(1)}}{dx}(1) = 0, \quad \frac{dT_0^{(2)}}{dx}(1) = 0.$$

2.3.1 Numerical results and discussion

The results of numerical calculations are presented in Figures 2.3(a) - 2.3(d). To highlight the effect of coupling, the graphs for the uncoupled ($k^* = 0$ W/m K) case are given in Figures 2.3(a) and 2.3(c). The graphs with the higher inlet conditions represent the endothermic reaction whereas the graphs with the lower inlet conditions represent the exothermic reaction. Comparing Figures 2.3(a) and 2.3(b) for the temperature, it is clear that in the coupled ($k^* = 1.5$ W/m K) case, the temperature generated by the exothermic reaction is consumed by the endothermic reaction. Figures 2.3(c) and 2.3(d) show that the coupling effect on the concentrations is not as significant as that for the temperatures.

In this chapter we analysed the effect of heat transfer across a thin conducting wall on the temperature and concentration distributions in adjacent channels.

Using an asymptotic technique we derived the system of differential equations that couples the temperatures in the two channels. In the next chapter we extend this analysis to the case when more complicated heterogeneous reactions take place in thin channels of a packed bed industrial reactor. Similar to the present chapter, the main emphasis is on understanding the theoretical concepts associated with heat transfer and the coupling of the temperatures in the channels across the thin wall.

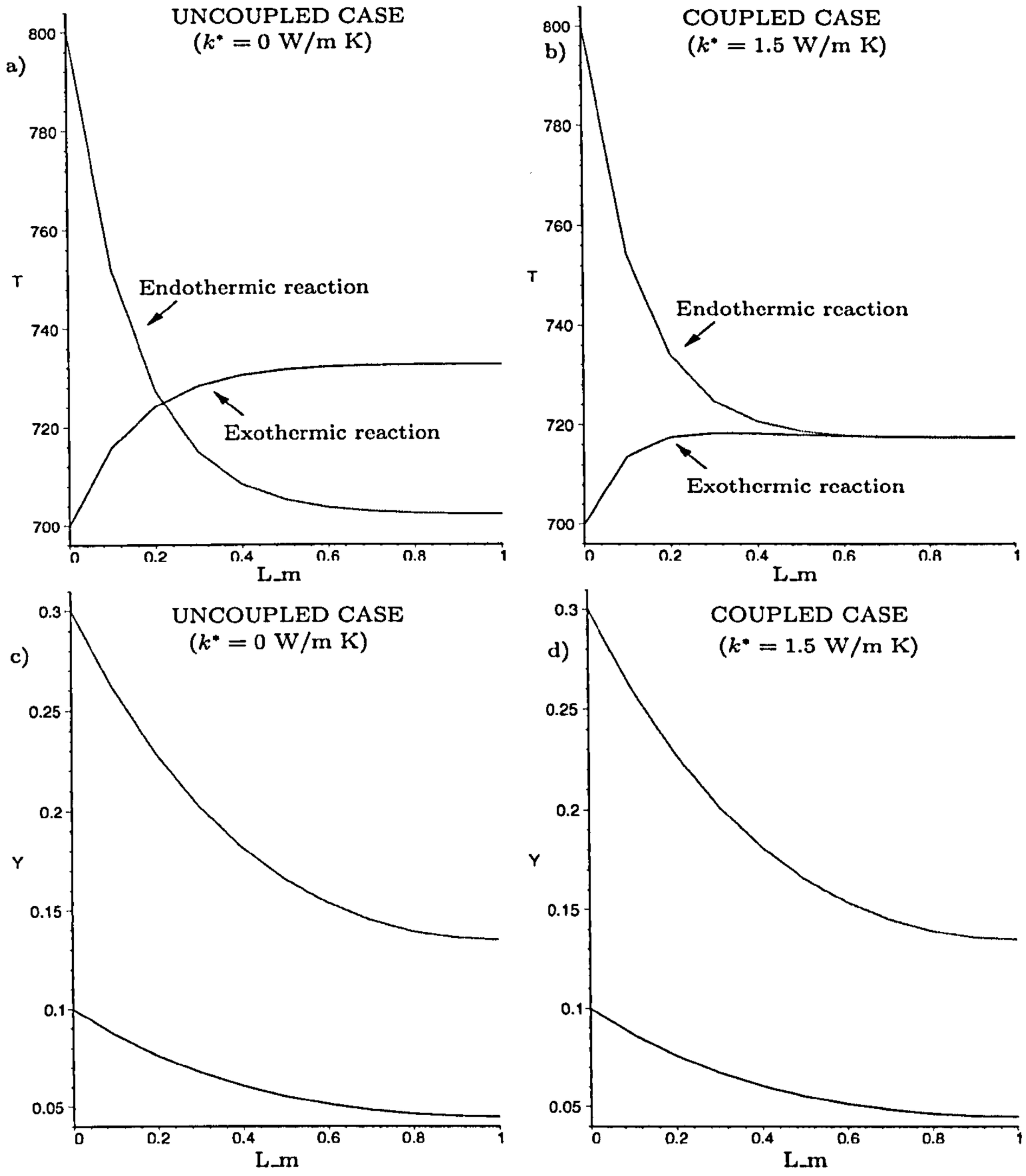

Figure 2.3: Graphs showing the temperature and concentration distributions along the channels for the exothermic and the endothermic reactions. (a) Temperature distribution for non-conducting wall; (b) Temperature distribution for conducting wall; (c) Concentration distribution for non-conducting wall; (d) Concentration distribution for conducting wall.

Chapter 3

Mathematical modelling of heat transfer in a catalytic reformer

3.1 Introduction

In this chapter we analyse heat transfer in a catalytic reformer - a chemical reactor used in industry to produce hydrogen for fuel cells. The novelty, as explained in the thesis introduction, lies in the fact that the reactor itself is made up of adjacent channels connected by thin conducting walls, and it combines exothermic and endothermic reactions in the alternating channels. The channels are packed with catalytic pellets, which promote both the catalytic combustion reactions and the steam reforming reactions. A model is developed in which the thermal conductivity and the thickness of the interconnecting wall can be used as control parameters characterising the heat exchange between the neighbouring channels. The important part of this model includes the asymptotic analysis of the fields within the interconnecting walls between the channels and the thermal coupling between the neighbouring channels. Similar to the previous chapter, our main objective is to study how the heat is transferred across the conducting walls and how this influences the temperature distribution in the channels.

The physical phenomenon discussed is known in the engineering literature as catalytic combustion/reforming, where the reactions take place at relatively low temperatures.

We organise the chapter as follows: first we formulate the problem - present the physical details, describe the geometry of the multi-channel reactor, set the system of governing equations - and discuss the asymptotic features of the model. The set of parameters characterising the model is given in Section 3.3, accompanied by test numerical simulations that show temperature versus longitudinal distance along the channels of the reactor. Finally Section 3.4 deals with the modelling of the temperature distribution within a composite (layered) wall separating the channels, and numerical results are presented.

This chapter is partially based on Selsil *et al.* [82].

3.2 Formulation of the problem

We start by analysing the simplest case, when there are two channels of equal width D_C connected by a thin wall of width D_w, see Figure 3.1. Inside the channels there are chemical reactions taking place - a steam reforming reaction in one channel and a catalytic combustion reaction in the other. We investigate how the energy transfers from one channel to the other via a thin conducting wall.

The full time dependent set of equations that describes the reactions taking place in a catalytic reformer forms a system of three-dimensional (3D) nonlinear singularly perturbed reaction-diffusion partial differential equations and algebraic equations. Due to the complications of the full problem, we consider a simplified model, which involves 1D equations describing the behaviour of the temperatures and the concentrations along the channels, and 2D equations describing the temperature distribution across as well as along the wall. We denote the

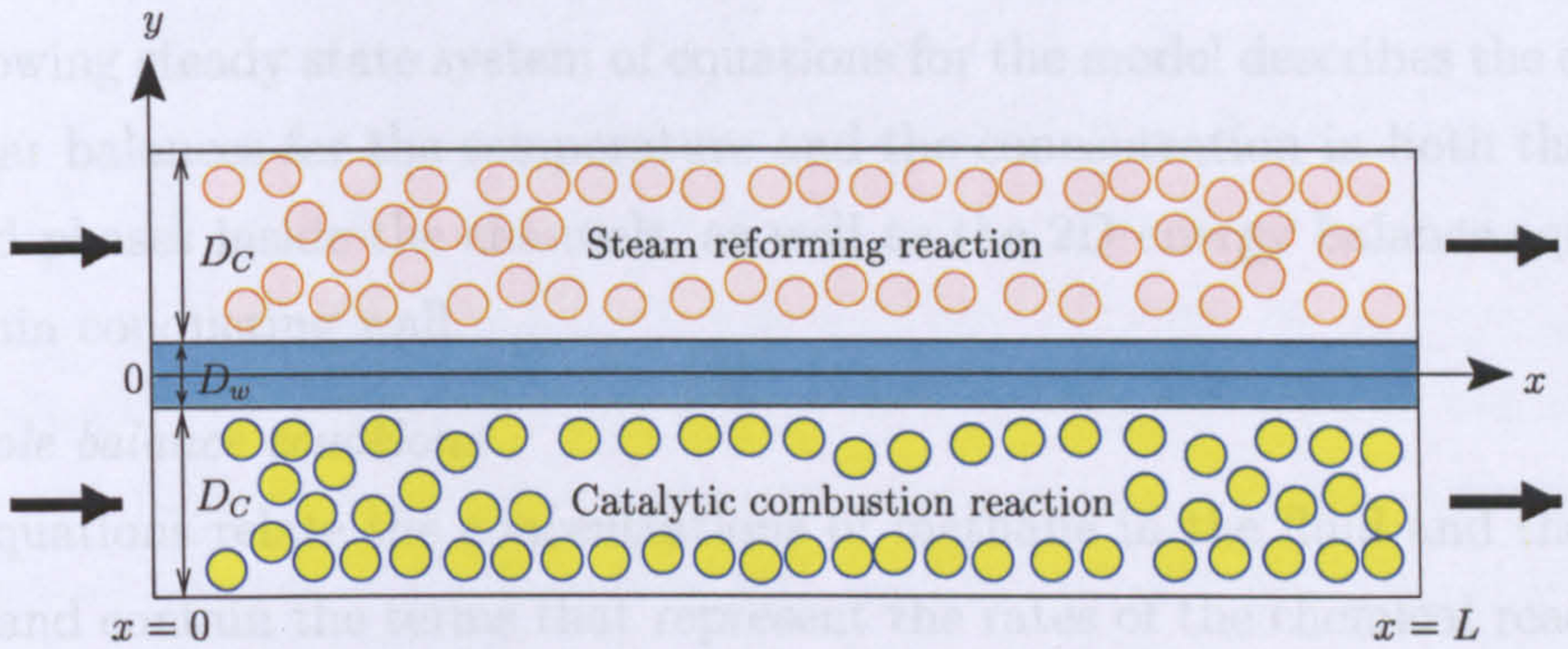

Figure 3.1: Simplified model - two adjacent channels connected by a thin wall.

temperatures[1] of the fluid and the solid by $T_f(x)$ and $T_s(x)$ and the concentrations of methane (represented as mole fractions) by $Y_f(x)$ and $Y_s(x)$, respectively. The reactions that take place are (see, for example, [2], [35], [45], [74] and [78]):

$$CH_4 + H_2O \rightleftharpoons 3H_2 + CO \qquad \text{Steam reforming reaction (simplified),}$$

$$CH_4 + 2O_2 \rightarrow 2H_2O + CO_2 \qquad \text{Catalytic combustion reaction.}$$

Our aim is to study the effect of the thin conducting wall on how the temperatures in the channels influence each other. The asymptotic technique is used to analyse the temperature distribution within the wall, exploiting the fact that the ratio of the entire width of the wall to the entire width of the channel is small. This enables us to introduce a small nondimensional parameter ε (where $0 < \varepsilon \ll 1$), representing the normalised width of the wall, $\varepsilon = D_w/D_C$. The steady state equations for the mass and energy balances in the channels (see, for example, [45], [46], [85] and [86]) are given in the next section. The equations have the same form in both channels, with the differences occuring in the coefficients. (These equations and coefficients are described in detail in Section 1.5 on the theoretical background.) The boundary conditions are prescribed at the inlet, $x = 0$, and the outlet, $x = L$, of the catalytic reformer.

[1]All temperatures are measured in Kelvins, °K =°C+273

3.2.1 Full system of equations

The following steady state system of equations for the model describes the energy and molar balances for the temperature and the concentration in both the fluid and solid phases inside the channels, as well as the 2D energy balance equation in the thin conducting wall.

Solid mole balance equations

These equations relate the concentrations of methane in the fluid and the solid phases, and contain the terms that represent the rates of the chemical reactions. They are given by

$$a_1^{(i)}(Y_f^{(i)}(x) - Y_s^{(i)}(x)) - a_2^{(i)}(-R)_s^{(i)} = 0, \quad i = 1, 2. \tag{3.2.1}$$

Here, $(-R)_s^{(i)}$ denotes the reaction rate, that is, the rate of disappearance of methane at the external surfaces of the catalyst pellets, with $i = 1$ for the reformer side and $i = 2$ for the combustion side. In both of the channels we assume that the reaction rate takes the following form

$$(-R)_s^{(i)} = \Psi^{(i)}\mathcal{M}^{(i)}, \quad i = 1, 2, \tag{3.2.2}$$

where, $\mathcal{M}^{(i)}$ is a function of the concentrations $Y_f^{(i)}$ and $Y_s^{(i)}$, $i = 1, 2$, and, as in the thesis introduction and Chapter 2, the term obtained from the Arrhenius equation is

$$\Psi^{(i)} = \mathcal{A}^{(i)} e^{\left(\frac{-E^{(i)}}{R_g T_s^{(i)}(x)}\right)}, \; i = 1, 2.$$

The pre-exponential factors $\mathcal{A}^{(1)}$ and $\mathcal{A}^{(2)}$ are positive constants, $E^{(1)}$ and $E^{(2)}$ are the apparent activation energies, R_g is the universal gas constant, 8.314 J/mol K, and $T_s^{(1)}(x)$ and $T_s^{(2)}(x)$ are the temperatures of the catalyst pellets. The coefficients $a_1^{(i)}$ and $a_2^{(i)}$, $i = 1, 2$, are independent of the temperature and the concentration and have the following representations:

$$a_1^{(i)} = \frac{k_m^{(i)} a_v^{(i)} F_t^{(i)}}{A_c^{(i)} v_x^{(i)}}, \quad a_2^{(i)} = \xi^{(i)} \rho_c^{(i)} (1 - \phi^{(i)}), \; i = 1, 2,$$

where all the physical parameters are assumed to be constant and are explained in detail in Section 1.5.

Similar to Chapter 2 we deal with a simplified version of the reaction rate, denoted by $(-R)_s^{(i_0)}$, $i = 1, 2$, that is, we set the temperature in $\Psi^{(i)}$, $i = 1, 2$, as the temperature at the inlet, resulting in temperature independent reaction rates in both channels. (We accept that this may appear to be an oversimplification, for an industrial reactor, as intrinsic rate expressions of this type are exponentially dependent on temperature. However, this assumption is acceptable within the range of inlet conditions adopted in the present model. It is assumed that the catalyst is operating above a temperature at which it is very active; in this case the overall effect would be to produce relatively small changes in the reaction rate with changing temperature, and hence the inlet values of temperature can be used in overall calculations). In Chapter 5.4 we return to this point and deal in more detail with this nonlinearity, and the construction of boundary layers, showing that this assumption regarding temperature independent reaction rates holds for the main part of the channel.

The remaining three mass and energy balance equations, and the equation inside the wall are given below.

Fluid mole balance equations

$$a_3^{(i)} \frac{d^2 Y_f^{(i)}}{dx^2}(x) - a_4^{(i)} \frac{dY_f^{(i)}}{dx}(x) - a_5^{(i)}(Y_f^{(i)}(x) - Y_s^{(i)}(x)) = 0, \quad i = 1, 2. \tag{3.2.3}$$

Fluid energy balance equations

$$\begin{aligned} a_6^{(i)} \frac{d^2 T_f^{(i)}}{dx^2}(x) \quad - \quad & a_7^{(i)} \frac{dT_f^{(i)}}{dx}(x) + a_8^{(i)}(T_s^{(i)}(x) - T_f^{(i)}(x)) \\ + \quad & a_9^{(i)}(T_w^{(i)}(x) - T_f^{(i)}(x)) = 0, \ i = 1, 2. \end{aligned} \tag{3.2.4}$$

Solid energy balance equations

$$a_{10}^{(i)} \frac{d^2 T_s^{(i)}}{dx^2}(x) - a_2^{(i)} a_{11}^{(i)} \Psi^{(i)} Y_s^{(i)}(x) - a_8^{(i)}(T_s^{(i)}(x) - T_f^{(i)}(x)) = 0, \quad i = 1, 2. \tag{3.2.5}$$

Equation for the temperature inside the wall

$$\nabla^2 T^{(0)}(x,y) = \frac{\partial^2 T^{(0)}}{\partial x^2}(x,y) + \frac{\partial^2 T^{(0)}}{\partial y^2}(x,y) = 0. \tag{3.2.6}$$

At the inlet $(x = 0)$:

$$Y_f^{(1)}(0) = Y_{f0}^{(1)}, \quad T_f^{(1)}(0) = T_{f0}^{(1)}, \quad T_s^{(1)}(0) = T_{s0}^{(1)},$$
$$Y_f^{(2)}(0) = Y_{f0}^{(2)}, \quad T_f^{(2)}(0) = T_{f0}^{(2)}, \quad T_s^{(2)}(0) = T_{s0}^{(2)}.$$

At the outlet $(x = L)$:

$$\frac{dY_f^{(i)}}{dx}(L) = \frac{dT_f^{(i)}}{dx}(L) = \frac{dT_s^{(i)}}{dx}(L) = 0, \quad i = 1,2. \tag{3.2.7}$$

The coefficients $a_3^{(i)}$ to $a_{11}^{(i)}$, $i = 1,2$, are assumed to be constant (independent of temperature and concentration) and are given by

$$a_3^{(i)} = D_e^{(i)}, \quad a_4^{(i)} = v_x^{(i)}, \quad a_5^{(i)} = k_m^{(i)} a_v^{(i)}, \quad a_6^{(i)} = k_f^{(i)}, \quad a_7^{(i)} = \rho_f^{(i)} C_p^{(i)} v_x^{(i)},$$
$$a_8^{(i)} = h_{fs}^{(i)} a_v^{(i)}, \quad a_9^{(i)} = U_a^{(i)} a_f^{(i)}, \quad a_{10}^{(i)} = k_s^{(i)}, \quad a_{11}^{(i)} = (\Delta H_R^{(i)}), \; i = 1,2. \tag{3.2.8}$$

Similar to $a_1^{(i)}$ and $a_2^{(i)}$, $i = 1,2$, all the industrial parameters are explained in detail in Section 1.5. Equations (3.2.3) to (3.2.5) are second order differential equations for $T_f^{(i)}$, $T_s^{(i)}$ and $Y_f^{(i)}$, $i = 1,2$. An algebraic relationship between $Y_f^{(i)}$ and $Y_s^{(i)}$, $i = 1,2$, is given by (3.2.1). In the fluid energy balance equation (3.2.4) we also have the terms $T_w^{(1)}(x)$ and $T_w^{(2)}(x)$ which are the temperatures at the reformer and combustion sides of the wall, respectively; $T_w^{(1)}(x)$ is the temperature of the wall where the wall touches the channel with the reforming reaction and $T_w^{(2)}$ is the temperature of the wall where the wall touches the channel with the combustion reaction. In order to find these functions, we analyse the temperature distribution within the wall using an asymptotic expansions technique.

3.2.2 Scaled variable and asymptotic approximations

First, we introduce a new dimensionless scaled variable, $\tau_0 = y/(\varepsilon D_C)$. Then equation (3.2.6) can be written as

$$\nabla^2 T^{(0)}(x,\tau_0) = \frac{\partial^2 T^{(0)}}{\partial x^2}(x,\tau_0) + \frac{1}{\varepsilon^2 D_C^2}\frac{\partial^2 T^{(0)}}{\partial \tau_0^2}(x,\tau_0) = 0, \qquad (3.2.9)$$

$$x \in (0,L), \quad \tau_0 \in \Big(-\frac{1}{2},\frac{1}{2}\Big).$$

We assume ideal thermal contact between the wall and the channels. In the new variable, we have

$$\text{at } \tau_0 = \frac{1}{2}: \qquad T^{(0)}\Big(x,\frac{1}{2}\Big) = T_w^{(1)}(x), \qquad (3.2.10)$$

$$k_w \frac{\partial T^{(0)}}{\partial n}\Big(x,\frac{1}{2}\Big) = h_w^{(1)}(T_f^{(1)}(x) - T_w^{(1)}(x)), \qquad (3.2.11)$$

$$\text{at } \tau_0 = -\frac{1}{2}: \qquad T^{(0)}\Big(x,-\frac{1}{2}\Big) = T_w^{(2)}(x), \qquad (3.2.12)$$

$$k_w \frac{\partial T^{(0)}}{\partial n}\Big(x,-\frac{1}{2}\Big) = h_w^{(2)}(T_f^{(2)}(x) - T_w^{(2)}(x)), \qquad (3.2.13)$$

where k_w is the thermal conductivity of the wall, $h_w^{(i)}$, $i = 1,2$, is the heat transfer coefficient between the fluid and the wall, and n is the outward normal. Conditions similar to (3.2.11) and (3.2.13), which represent a combination of Newton's law of cooling and Fourier's conduction law, can be found in the literature (see, for example, [16], [24], [29], [30], [32], [33], [39], [45], [53] and [91]).

The coefficients $a_9^{(i)}$, $i = 1,2$, are proportional to the overall heat transfer coefficients $U_a^{(i)}$, which depend on the thermal conductivity of the wall k_w, the half-thickness $D_w/2$ of the wall, and the heat transfer coefficients $h_w^{(i)}$, $i = 1,2$, in the following way (see, for example, [24], page 53):

$$U_a^{(i)} = \Big(\frac{D_w}{2k_w} + \frac{1}{h_w^{(i)}}\Big)^{-1}, \ i = 1,2. \qquad (3.2.14)$$

We would like to emphasize that the flow in both channels is described using a heterogeneous 1D axial dispersion model. The concentration, temperature and velocity may have nonzero gradients in the x-direction but do not vary in the y-direction. (More details on heterogeneous axial dispersion models can be found in [16], [24], [39], [45] and [53].)
Inside the wall the temperature $T^{(0)}$ satisfies equation (3.2.9) and can be expanded asymptotically in the following way

$$T^{(0)}(x,\tau_0) = T_0^{(0)}(x,\tau_0) + \varepsilon T_1^{(0)}(x,\tau_0) + \varepsilon^2 T_2^{(0)}(x,\tau_0) + \dots .$$

From (3.2.9) it follows that

$$\frac{\partial^2 T_0^{(0)}}{\partial \tau_0^2}(x,\tau_0) = 0, \quad x \in (0,L), \quad \tau_0 \in \Big(-\frac{1}{2},\frac{1}{2}\Big),$$

which implies that $T_0^{(0)}$ is linear in τ_0. Using conditions (3.2.10) and (3.2.12) we find that the leading order term for the temperature can be written as

$$T_0^{(0)}(x,\tau_0) = \frac{1}{2}(T_w^{(1)}(x) + T_w^{(2)}(x)) + (T_w^{(1)}(x) - T_w^{(2)}(x))\tau_0. \tag{3.2.15}$$

Rearranging (3.2.11) and (3.2.13) gives

$$\frac{\partial T_0^{(0)}}{\partial n} = \frac{1}{\varepsilon D_C}\frac{\partial T_0^{(0)}}{\partial \tau_0} = \frac{h_w^{(1)}}{k_w}(T_f^{(1)} - T_w^{(1)}) \quad \text{at} \quad \tau_0 = \frac{1}{2},$$
$$\frac{\partial T_0^{(0)}}{\partial n} = -\frac{1}{\varepsilon D_C}\frac{\partial T_0^{(0)}}{\partial \tau_0} = \frac{h_w^{(2)}}{k_w}(T_f^{(2)} - T_w^{(2)}) \quad \text{at} \quad \tau_0 = -\frac{1}{2}.$$

Using (3.2.15) we can then write

$$\gamma^{(1)}(T_f^{(1)} - T_w^{(1)}) = T_w^{(1)} - T_w^{(2)} \quad \text{and} \quad -\gamma^{(2)}(T_f^{(2)} - T_w^{(2)}) = T_w^{(1)} - T_w^{(2)}, \tag{3.2.16}$$

where $$\gamma^{(i)} = \frac{h_w^{(i)}\varepsilon D_C}{k_w} = \frac{h_w^{(i)} D_w}{k_w}.$$

We assume that the dimensionless quantity $\gamma^{(i)},\ i = 1, 2$, is of order $O(1)$. From equations (3.2.16) we can write $T_w^{(1)}$ and $T_w^{(2)}$ in terms of $T_f^{(1)}$ and $T_f^{(2)}$, that is,

$$T_w^{(1)} = \frac{T_f^{(1)}\gamma^{(1)} + T_f^{(1)}\gamma^{(1)}\gamma^{(2)} + T_f^{(2)}\gamma^{(2)}}{\gamma^{(1)} + \gamma^{(2)} + \gamma^{(1)}\gamma^{(2)}}, \tag{3.2.17}$$

$$T_w^{(2)} = \frac{T_f^{(1)}\gamma^{(1)} + T_f^{(2)}\gamma^{(1)}\gamma^{(2)} + T_f^{(2)}\gamma^{(2)}}{\gamma^{(1)} + \gamma^{(2)} + \gamma^{(1)}\gamma^{(2)}}. \tag{3.2.18}$$

Equations (3.2.17) and (3.2.18) can then be rearranged to give the following coupling terms[2]

$$T_f^{(1)} - T_w^{(1)} = \frac{\gamma^{(2)}(T_f^{(1)} - T_f^{(2)})}{\gamma^{(1)} + \gamma^{(2)} + \gamma^{(1)}\gamma^{(2)}},$$

$$T_f^{(2)} - T_w^{(2)} = -\frac{\gamma^{(1)}(T_f^{(1)} - T_f^{(2)})}{\gamma^{(1)} + \gamma^{(2)} + \gamma^{(1)}\gamma^{(2)}}.$$

These coupling terms are substituted back into the fluid energy balance equations (3.2.4) giving

$$a_6^{(1)}\frac{d^2T_f^{(1)}}{dx^2} - a_7^{(1)}\frac{dT_f^{(1)}}{dx} + a_8^{(1)}(T_s^{(1)} - T_f^{(1)}) - \frac{a_9^{(1)}\gamma^{(2)}(T_f^{(1)} - T_f^{(2)})}{\gamma^{(1)} + \gamma^{(2)} + \gamma^{(1)}\gamma^{(2)}} = 0, \tag{3.2.19}$$

$$a_6^{(2)}\frac{d^2T_f^{(2)}}{dx^2} - a_7^{(2)}\frac{dT_f^{(2)}}{dx} + a_8^{(2)}(T_s^{(2)} - T_f^{(2)}) + \frac{a_9^{(2)}\gamma^{(1)}(T_f^{(1)} - T_f^{(2)})}{\gamma^{(1)} + \gamma^{(2)} + \gamma^{(1)}\gamma^{(2)}} = 0. \tag{3.2.20}$$

[2]The *coupling terms* are the terms containing both the fluid temperature $T_f^{(1)}$ on the reformer side and the fluid temperature $T_f^{(2)}$ on the combustion side. They replace the terms $T_w^{(i)} - T_f^{(i)},\ i = 1, 2$, in equations (3.2.4).

We now have a system of eight equations (3.2.1), (3.2.3), (3.2.5), (3.2.19), and (3.2.20) for the eight unknown quantities $T_f^{(i)}$, $T_s^{(i)}$, $Y_f^{(i)}$, and $Y_s^{(i)}$, $i = 1, 2$. This system is solved numerically using Femlab. Results of numerical calculations are presented in the next section.

3.3 Numerical simulations

3.3.1 Model parameters

We use the following set of model parameters for the reaction rate and the constants (3.2.8) in the equations (3.2.1), (3.2.3), (3.2.5), (3.2.19) and (3.2.20) in the channels:

$$
\begin{aligned}
a_1^{(1)} &= a_1^{(2)} = 2.5 \text{ mol}/(\text{m}^3 \text{ s}), \quad a_2^{(1)} = a_2^{(2)} = 0.5 \text{ kg}_{\text{cat}}/\text{m}^3, \\
a_3^{(1)} &= a_3^{(2)} = 0.3 \text{ m}^2/\text{s}, \quad a_4^{(1)} = a_4^{(2)} = 2 \text{ m/s}, \\
a_5^{(1)} &= a_5^{(2)} = 2 \text{ s}^{-1}, \quad a_6^{(1)} = a_6^{(2)} = 3 \text{ W}/(\text{m K}), \\
a_7^{(1)} &= a_7^{(2)} = 0.4 \text{ W}/(\text{m}^2 \text{ K}), \quad a_8^{(1)} = a_8^{(2)} = 2 \text{ W}/(\text{m}^3 \text{ K}), \\
a_9^{(1)} &= 5.5 \text{ W}/(\text{m}^3 \text{ K}), \quad a_9^{(2)} = 2 \text{ W}/(\text{m}^3 \text{ K}), \\
a_{10}^{(1)} &= a_{10}^{(2)} = 0.7 \text{ W}/(\text{m K}), \quad a_{11}^{(1)} = -a_{11}^{(2)} = 430 \text{ J/mol}, \\
\Psi^{(1)} &= \Psi^{(2)} = 1 \text{ mol}/(\text{kg}_{\text{cat}} \text{ s}), \\
\gamma^{(1)} &= 0.375, \quad \gamma^{(2)} = 1.091,
\end{aligned}
$$

$$
\begin{aligned}
T_f^{(1)}(0) &= T_s^{(1)}(0) = 800 \text{ K}, \quad T_f^{(2)}(0) = T_s^{(2)}(0) = 700 \text{ K}, \\
Y_f^{(1)}(0) &= 0.3, \quad Y_f^{(2)}(0) = 0.1, \quad L = 20 \text{ m}, \\
(-R)_s^{(i)} &= \Psi^{(i)} \mathcal{M}^{(i)} = \Psi^{(i)} Y_f^{(i)} Y_s^{(i)}, \ i = 1, 2, \ \text{mol}/(\text{kg}_{\text{cat}} \text{ s}).
\end{aligned}
$$

The reaction rate given above implies that the solid mole balance equations (3.2.1) can be rewritten as

$$Y_s^{(i)} = \frac{a_1^{(i)} Y_f^{(i)}}{a_1^{(i)} + a_2^{(i)} \Psi^{(i)} Y_f^{(i)}}, \ i = 1, 2.$$

This representation is substituted into equations (3.2.3) and (3.2.5) and the system of six differential equations with the above constants is solved numerically.

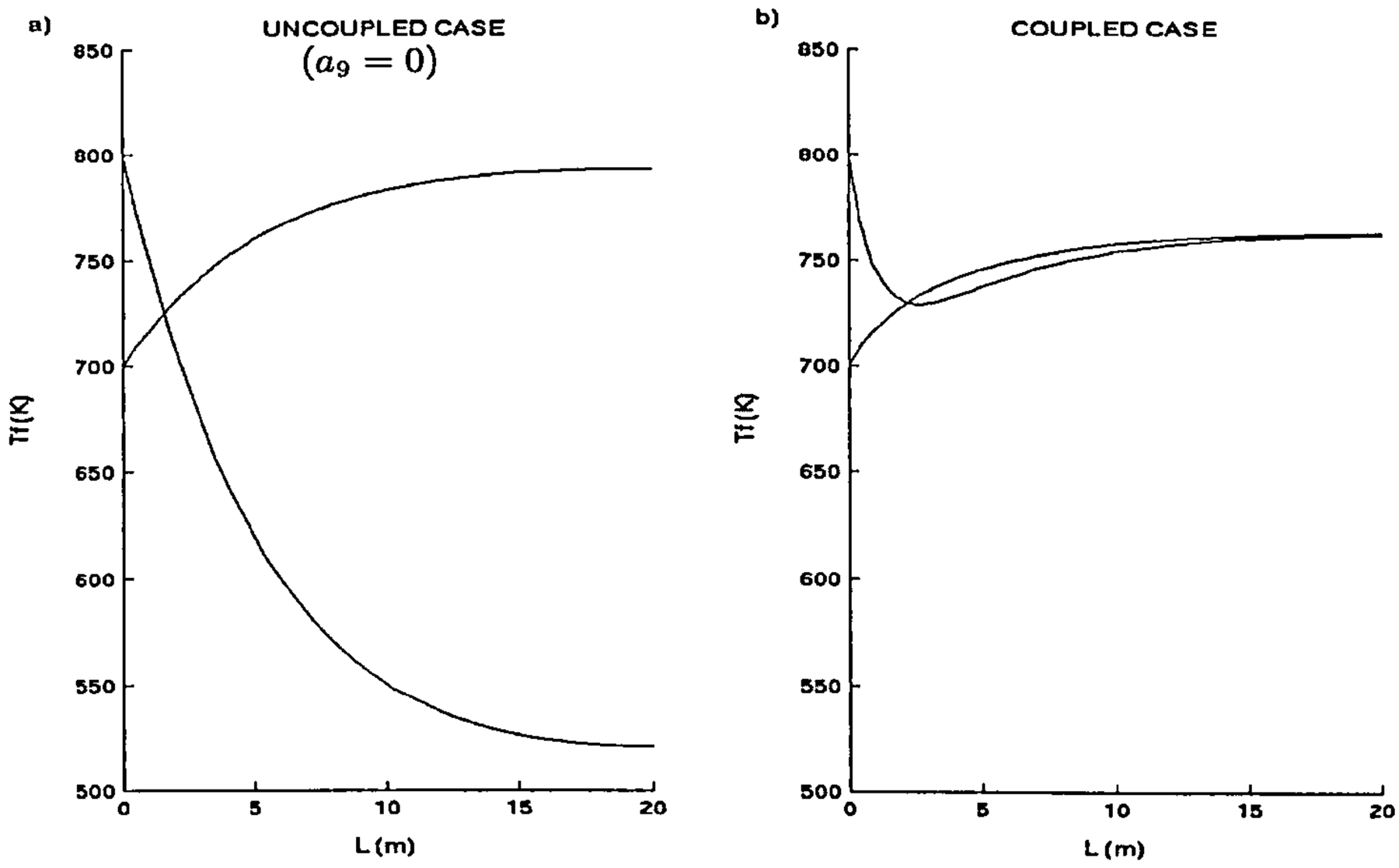

Figure 3.2: Fluid temperature distributions along the channels for model parameters. (Higher inlet condition = Reformer side, Lower inlet condition = Combustion side.)

The graphs for the fluid temperatures are presented in Figures 3.2(a) and 3.2(b). For both Figures the graphs with the higher inlet conditions correspond to the reforming reaction whereas the graphs with the lower inlet conditions correspond to the combustion reaction. We present the results for the fluid temperatures only. The solid temperature distributions follow the same trends and therefore

are not given here. The uncoupled case ($a_9^{(i)} = 0,\ i = 1, 2$, in each channel) is given for comparison. In the uncoupled case the temperature on the reformer side decreases and the temperature on the combustion side increases along the channels. In the coupled case, both temperatures quickly reach a similar value and continue close to this value throughout the channels.

3.3.2 Industrial parameters

We use the following set of industrial parameters[3] for the reaction rate and the constants (3.2.8) in the equations (3.2.1), (3.2.3), (3.2.5), (3.2.19) and (3.2.20) in the channels:

$$
\begin{aligned}
D_C &= 0.0795 \text{ m}, & D_w &= 0.00159 \text{ m},\\
k_m^{(1)} &= 0.0794 \text{ m/s}, & k_m^{(2)} &= 0.070 \text{ m/s},\\
F_T^{(1)} &= 6.25 \text{ mol/s}, & F_T^{(2)} &= 5.66 \text{ mol/s},\\
a_v^{(1)} = a_v^{(2)} &= 76.33 \text{ m}^{-1}, & v_x^{(1)} &= 2.47 \text{ m/s},\\
v_x^{(2)} &= 2.24 \text{ m/s}, & A_c^{(1)} = A_c^{(2)} &= 0.00632 \text{ m}^2\\
\mathcal{A}^{(1)} &= 0.778 \text{ mol/(kg}_{\text{cat}} \text{ s)}, & \mathcal{A}^{(2)} &= 0.0794 \text{ mol/(kg}_{\text{cat}} \text{ s)},\\
\xi^{(1)} = \xi^{(2)} &= 0.65, & R_g &= 8.314 \text{ J/(mol K)},\\
\rho_c^{(1)} = \rho_c^{(2)} &= 2355.2 \text{ kg}_{\text{cat}}/\text{m}^3, & (1-\phi^{(1)}) = (1-\phi^{(2)}) &= 0.395,
\end{aligned}
$$

$$
\begin{aligned}
E^{(1)} &= 36720 \text{ J/mol}, & E^{(2)} &= 1100 \text{ J/mol},\\
D_e^{(1)} &= 0.0053 \text{ m}^2/\text{s}, & D_e^{(2)} &= 0.0048 \text{ m}^2/\text{s},\\
C_p^{(1)} &= 44 \text{ J/(mol K)}, & C_p^{(2)} &= 32 \text{ J/(mol K)},\\
k_f^{(1)} &= 0.061 \text{ W/(m K)}, & k_f^{(2)} &= 0.054 \text{ W/(m K)},
\end{aligned}
$$

[3]This list of parameters is based on experimental data taken from the literature. The details are given in Section 1.5.2.

$$\rho_f^{(1)} = \rho_f^{(2)} = 400.4 \text{ mol/m}^3, \quad k_s^{(1)} = k_s^{(2)} = 0.22 \text{ W/(m K)},$$
$$h_{fs}^{(1)} = 1002.4 \text{ W/(m}^2 \text{ K)}, \quad h_{fs}^{(2)} = 900.34 \text{ W/(m}^2 \text{ K)},$$
$$(\Delta H_R^{(1)}) = 206,000 \text{ J/mol}, \quad (\Delta H_R^{(2)}) = -802,000 \text{ J/mol},$$
$$\varepsilon = 0.02, \qquad a_f^{(1)} = a_f^{(2)} = 12.58 \text{ m}^{-1},$$

$$h_w^{(1)} = 753.95 \text{ W/(m}^2 \text{ K)}, \quad h_w^{(2)} = 929.05 \text{ W/(m}^2 \text{ K)},$$
$$U_a^{(1)} = 538.73 \text{ W/(m}^2 \text{ K)}, \quad U_a^{(2)} = 622.78 \text{ W/(m}^2 \text{ K)},$$
$$k_w = 1.5 \text{ W/(m K)}, \qquad L = 12 \text{ m},$$

$$Y_f^{(1)}(0) = 0.163, \quad Y_f^{(2)}(0) = 0.0836,$$
$$T_f^{(1)}(0) = T_f^{(2)}(0) = 733 \text{ K}, \quad T_s^{(1)}(0) = T_s^{(2)}(0) = 733 \text{ K},$$
$$(-R)_s^{(i)} = \Psi^{(i)} \mathcal{M}^{(i)} = \Psi^{(i)} Y_s^{(i)}, \; i = 1, 2 \text{ mol/(kg}_{\text{cat}} \text{ s)}.$$

From the above data we obtain the following

$$a_1^{(1)} = 2426.51 \text{ mol/(m}^3 \text{ s)}, \quad a_2^{(1)} = 604.70 \text{ kg}_{\text{cat}}/\text{m}^3,$$
$$a_3^{(1)} = 0.0053 \text{ m}^2/\text{s}, \quad a_4^{(1)} = 2.47 \text{ m/s}, \quad a_5^{(1)} = 6.06 \text{ s}^{-1},$$
$$a_6^{(1)} = 0.061 \text{ W/(m K)}, \quad a_7^{(1)} = 43515.47 \text{ W/(m}^2 \text{ K)},$$
$$a_8^{(1)} = 76513.19 \text{ W/(m}^3 \text{ K)}, \quad a_9^{(1)} = 6777.22 \text{ W/(m}^3 \text{ K)},$$
$$a_{10}^{(1)} = 0.22 \text{ W/(m K)}, \quad a_{11}^{(1)} = 206000 \text{ J/mol}, \quad \gamma^{(1)} = 0.799,$$

$$a_1^{(2)} = 2136.21 \text{ mol/(m}^3 \text{ s)}, \quad a_2^{(2)} = 604.70 \text{ kg}_{\text{cat}}/\text{m}^3,$$
$$a_3^{(2)} = 0.0048 \text{ m}^2/\text{s}, \quad a_4^{(2)} = 2.24 \text{ m/s}, \quad a_5^{(2)} = 5.34 \text{ s}^{-1},$$
$$a_6^{(2)} = 0.054 \text{ W/(m K)}, \quad a_7^{(2)} = 28700.67 \text{ W/(m}^2 \text{ K)},$$
$$a_8^{(2)} = 68722.95 \text{ W/(m}^3 \text{ K)}, \quad a_9^{(2)} = 7834.57 \text{ W/(m}^3 \text{ K)},$$
$$a_{10}^{(2)} = 0.22 \text{ W/(m K)}, \quad a_{11}^{(2)} = -802000 \text{ J/mol}, \quad \gamma^{(2)} = 0.985.$$

Here we use the Arrhenius reaction rate, in the form introduced in Section 2.3, that is,

$$(-R)_s^{(i_0)} = \Psi^{(i_0)} Y_s^{(i)} = \mathcal{A}^{(i)} e^{\left(\frac{-E^{(i)}}{R_g T_s^{(i)}(0)}\right)} Y_s^{(i)}, \ i = 1, 2,$$

which consequently means that the solid mole balance equations (3.2.1) can be rewritten as

$$Y_s^{(i)} = \frac{a_1^{(i)} Y_f^{(i)}}{a_1^{(i)} + a_2^{(i)} \Psi^{(i)}}, \ i = 1, 2. \tag{3.3.21}$$

This relationship (3.3.21) between the concentrations is substituted into the fluid mole balance equation (3.2.3) and the solid energy balance equation (3.2.5), and the linear system is then solved numerically. The results for the fluid temperature

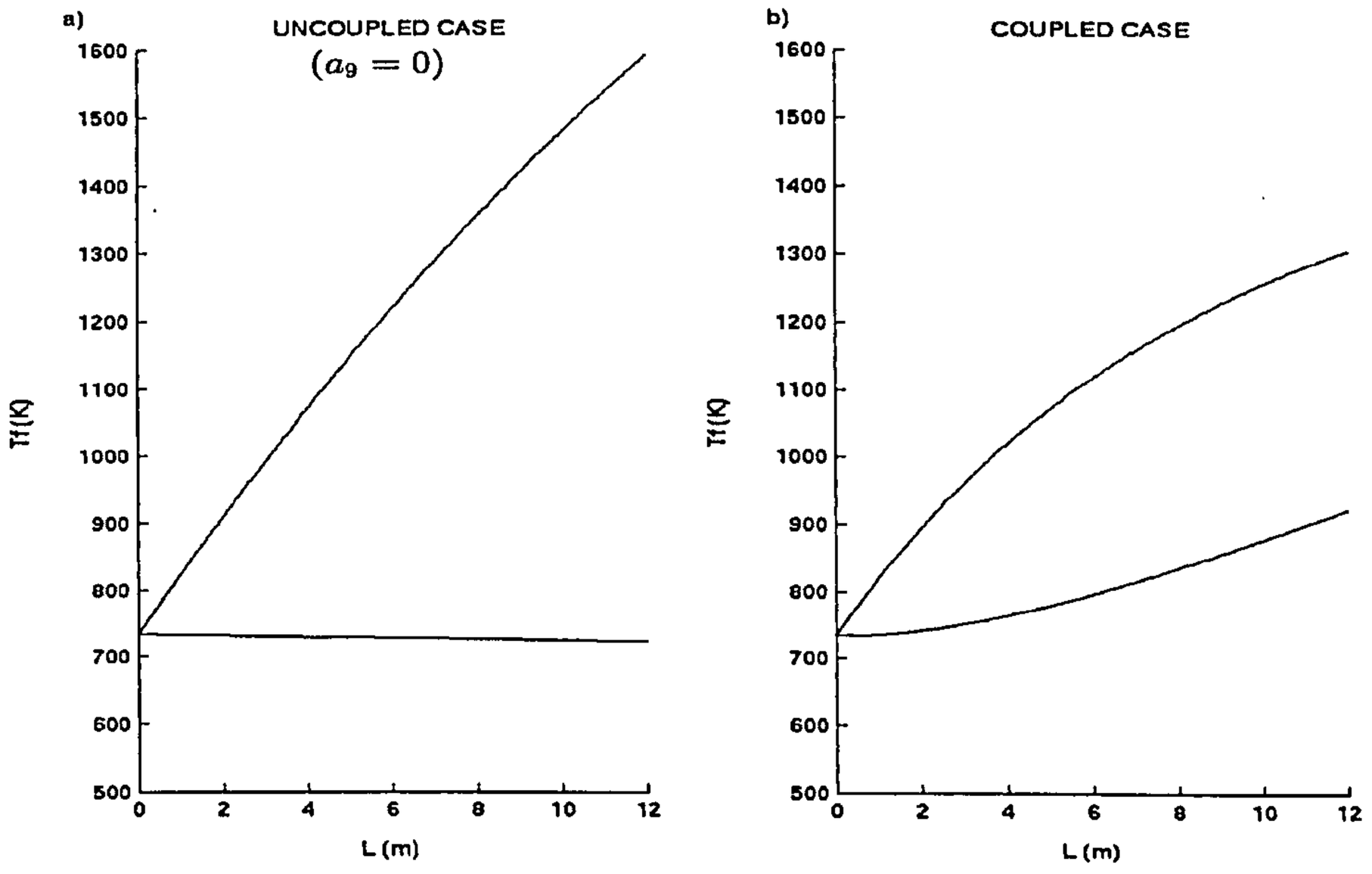

Figure 3.3: Fluid temperature distributions along the channels for industrial parameters. (Upper plot = Combustion side, Lower plot = Reformer side.)

as a function of x are presented in Figures 3.3(a) and 3.3(b). We can clearly see the effect of coupling on the temperature distributions along the channels for this

particular set of industrial parameters. It is also worth noting that due to the large difference in magnitudes of the coefficients calculated from the industrial data, a boundary layer effect is produced near the outlet of the reactor, where the zero heat flux conditions are not satisfied. In order to compensate for this discrepancy one needs to construct boundary layers at the outlet. This present chapter is concerned with the main trends of the temperature distributions along the channels. The construction and detailed discussion of the boundary layer effects is given in Chapter 5.

For this industrial case, by substituting (3.3.21) into (3.2.3) and (3.2.5), it is possible to obtain the exact solution for the concentration $Y_f^{(i)}(x)$, $i = 1, 2$. This implies that the forcing term, $a_2^{(i)} a_{11}^{(i)} \Psi^{(i)} Y_s^{(i)}$, $i = 1, 2$, in equations (3.2.5) is a constant multiplied by a known function of x. One possible way of changing the temperature distributions shown in Figures 3.3(a) and 3.3(b) is to change this forcing term. The equations to solve for $Y_f^{(i)}(x)$ have the form

$$a_3^{(i)} \frac{d^2 Y_f^{(i)}}{dx^2}(x) - a_4^{(i)} \frac{dY_f^{(i)}}{dx}(x) - \left(\frac{a_5^{(i)} a_2^{(i)} \Psi^{(i)}}{a_1^{(i)} + a_2^{(i)} \Psi^{(i)}} \right) Y_f^{(i)}(x) = 0, \quad i = 1, 2. \quad (3.3.22)$$

We assume, for convenience, that the pellets are spherical.
The coefficients $a_1^{(i)}$ and $a_5^{(i)}$, $i = 1, 2$, depend upon the radius of the pellets r, that is,

$$a_1^{(i)} = \frac{k_m^{(i)} a_v^{(i)} F_T^{(i)}}{v_x^{(i)} A_c^{(i)}}, \qquad a_5^{(i)} = k_m^{(i)} a_v^{(i)}, \ i = 1, 2,$$

where $k_m^{(i)}$, the mass transfer coefficient between the fluid and the catalyst, and $a_v^{(i)}$, $i = 1, 2$, the surface area of pellets per unit bed volume, have the following representations (see Section 1.5 and Chapter 3 of [45]):

$$k_m^{(i)} = \frac{D_{iff}^{(i)}}{2r^{(i)}} \left(2 + 1.1 (Sc^{(i)})^{\frac{1}{3}} \left(2 \frac{v_x^{(i)} \rho^{(i)}}{\eta^{(i)}} r^{(i)} \right)^{\frac{3}{5}} \right),$$

$$a_v^{(i)} = 4\pi (r^{(i)})^2 n^{(i)} = 4\pi n^{(i)} \left(\frac{3(1 - \phi^{(i)})}{4\pi n^{(i)}} \right)^{\frac{2}{3}}, \ i = 1, 2,$$

where $(1-\phi^{(i)})$ is the fraction of bed occupied by the catalyst pellet (the volume fraction of pellets), $n^{(i)}$ is the number of pellets in the bed, $\rho^{(i)}$ is the mass density, and $D_{iff}^{(i)}$ and $Sc^{(i)}$, $i = 1, 2$, are the diffusion of methane and the Schmidt number, both discussed in detail in Section 1.5. To investigate the effect of changing the radius of the pellets on the solution $Y_f^{(i)}(x)$, we shall assume that the volume fraction of the pellets remains constant but the surface area varies together with the radius. This implies that, for this particular set of industrial parameters, on the reformer side we have,

$$k_m^{(1)} = \frac{2.65 \times 10^{-6}}{r^{(1)}}(2 + 4244.2\ (r^{(1)})^{\frac{3}{5}}), \quad a_v^{(1)} = \frac{1.185}{r^{(1)}}. \tag{3.3.23}$$

The last coefficient in (3.3.22), for the reformer side, can be written as a function of the radius of the pellets $r^{(1)}$ such that,

$$a_5^{(1)}\left(\frac{a_2^{(1)}\Psi^{(1)}}{a_1^{(1)} + a_2^{(1)}\Psi^{(1)}}\right)Y_f^{(1)}(x) = N^{(1)}(r^{(1)})Y_f^{(1)}(x),$$

where $k_m^{(1)}$ and $a_v^{(1)}$ from (3.3.23) are substituted into $a_1^{(1)}$ and $a_5^{(1)}$ to give the exact representation of $N^{(1)}(r^{(1)})$ for the reformer side

$$N^{(1)}(r^{(1)}) = \frac{7.215 \times 10^{-6} + 0.0153(r^{(1)})^{\frac{3}{5}}}{2.52 \times 10^{-3} + 5.348(r^{(1)})^{\frac{3}{5}} + 1.14893\ (r^{(1)})^2}.$$

As the radius tends to zero, $N^{(1)}(r^{(1)})$ can be approximated by

$$N^{(1)}(r^{(1)}) \approx 0.002863095238 - 0.004695765873\ (r^{(1)})^{\frac{3}{5}}.$$

This implies that the concentration $Y_f^{(1)}$ will not change significantly as the radius decreases and the surface area increases because $N^{(1)}(r^{(1)})$ is almost constant for small $r^{(1)}$. This, in turn, shows that the forcing term in equation (3.2.5), and therefore the graphs for the temperatures, will not change significantly as the surface area of the catalytic pellets is increased, provided the volume fraction of the pellets remains constant. Similar work was carried out for the combustion side and the same result was obtained.

3.4 Layered wall

3.4.1 Geometry and governing equations

In this section we look at the case when the wall consists of layers of different widths and different thermal conductivities. As an example, the three layered wall shown in Figure 3.4 is studied. The middle layer is introduced to model an additional thermal barrier between the two processes. This could be used as a device to reduce interactions between the channels in a sensitive region, for example, when endothermic reactions are high and remove too much heat from the catalytic combustion side, extinguishing the combustion reactions. The equations in the channels remain the same as before, namely (3.2.1) - (3.2.5), with the scaling given in Section 3.2.2, that is, $\tau_0 = y/(\varepsilon D_C)$. The boundary conditions (3.2.10) - (3.2.13) are set on $\tau_0 = \pm\frac{1}{2}$. The equations inside the wall are

$$\begin{aligned}
\nabla^2 T^{(01)}(x,\tau_0) &= 0, \qquad x \in (0,L),\ \tau_0 \in (d_1, 1/2),\\
\nabla^2 T^{(00)}(x,\tau_0) &= 0, \qquad x \in (0,L),\ \tau_0 \in (d_2, d_1),\\
\nabla^2 T^{(02)}(x,\tau_0) &= 0, \qquad x \in (0,L),\ \tau_0 \in (-1/2, d_2). \qquad (3.4.24)
\end{aligned}$$

Here d_1 and d_2 are such that $-\frac{1}{2} < d_2 \leq d_1 < \frac{1}{2}$, see Figure 3.4. At the interfaces $\tau_0 = d_1$ and $\tau_0 = d_2$ inside the wall we pose the ideal thermal contact conditions,

$$\begin{aligned}
T^{(0j)}(x,\tau_0) &= T^{(00)}(x,\tau_0), \quad \tau_0 = d_j,\\
k_w^{(j)} \frac{\partial T^{(0j)}}{\partial \tau_0}(x,\tau_0) &= k_w^{(0)} \frac{\partial T^{(00)}}{\partial \tau_0}(x,\tau_0), \quad \tau_0 = d_j, \quad j = 1,2,
\end{aligned}$$

where $k_w^{(j)}$, $j = 1,2$, denote the thermal conductivities of each layer within the wall. Substituting the scaled coordinate into equations (3.4.24) gives

$$\begin{aligned}
T_0^{(01)}(x,\tau_0) &= F_1^{(1)}(x) + F_2^{(1)}(x)\tau_0, \quad \tau_0 \in (d_1,\ 1/2),\\
T_0^{(00)}(x,\tau_0) &= F_1^{(0)}(x) + F_2^{(0)}(x)\tau_0, \quad \tau_0 \in (d_2,\ d_1),\\
T_0^{(02)}(x,\tau_0) &= F_1^{(2)}(x) + F_2^{(2)}(x)\tau_0, \quad \tau_0 \in (-1/2,\ d_2),
\end{aligned}$$

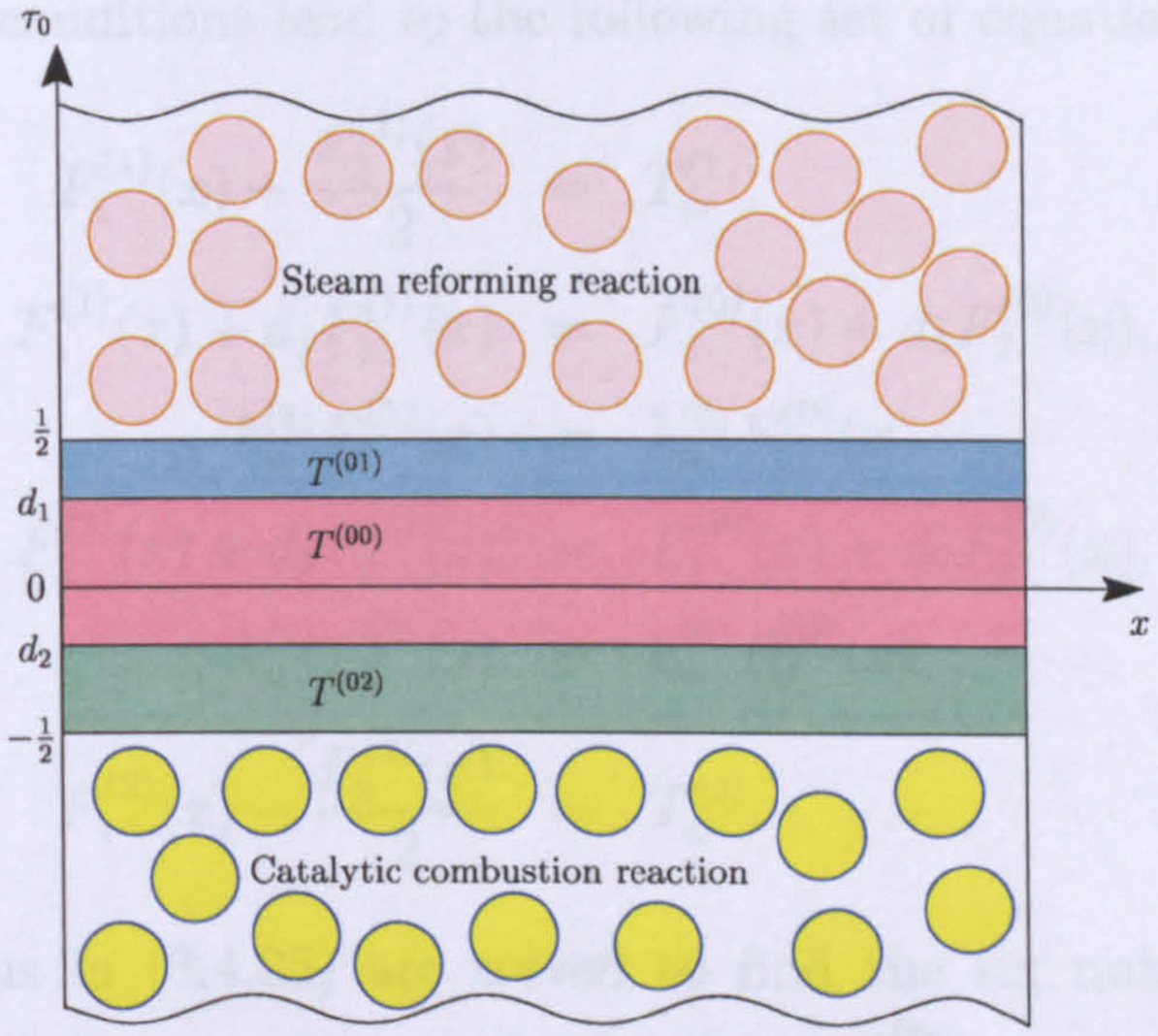

Figure 3.4: Wall consisting of 3 layers of different widths and different thermal conductivities.

where $F_i^{(j)}$, $i = 1, 2$, $j = 0, 1, 2$, are functions of x, which are determined from the boundary conditions. The boundary conditions associated with these three equations are

$$\begin{aligned}
&\text{at } \tau_0 = 1/2: && T^{(01)} = T_w^{(1)}, \\
&\text{at } \tau_0 = d_1: && T^{(01)} = T^{(00)}, \quad k_w^{(1)} \frac{\partial T^{(01)}}{\partial \tau_0} = k_w^{(0)} \frac{\partial T^{(00)}}{\partial \tau_0}, \\
&\text{at } \tau_0 = d_2: && T^{(02)} = T^{(00)}, \quad k_w^{(2)} \frac{\partial T^{(02)}}{\partial \tau_0} = k_w^{(0)} \frac{\partial T^{(00)}}{\partial \tau_0}, \\
&\text{at } \tau_0 = -1/2: && T^{(02)} = T_w^{(2)}.
\end{aligned}$$

These boundary conditions lead to the following set of equations:

$$\begin{aligned}
F_1^{(1)}(x) + \frac{F_2^{(1)}(x)}{2} &= T_w^{(1)}, \\
F_1^{(1)}(x) + d_1 F_2^{(1)}(x) &= F_1^{(0)}(x) + d_1 F_2^{(0)}(x), \\
k_w^{(1)} F_2^{(1)}(x) &= k_w^{(0)} F_2^{(0)}(x), \\
F_1^{(2)}(x) + d_2 F_2^{(2)}(x) &= F_1^{(0)}(x) + d_2 F_2^{(0)}(x), \\
k_w^{(2)} F_2^{(2)}(x) &= k_w^{(0)} F_2^{(0)}(x), \\
F_1^{(2)}(x) - \frac{F_2^{(2)}(x)}{2} &= T_w^{(2)}.
\end{aligned} \tag{3.4.25}$$

The six equations in (3.4.25) are solved to find the six unknowns, $F_i^{(j)}$, $i = 1, 2$, $j = 0, 1, 2$, and consequently, the functions $T_0^{(0j)}$, $j = 0, 1, 2$. In order to eliminate $T_w^{(1)}$ and $T_w^{(2)}$ we analyse the remaining Neumann boundary conditions at $\tau_0 = \pm\frac{1}{2}$. From the flux conditions given by equations (3.2.11) and (3.2.13), it follows that

$$\gamma^{(1)}(T_f^{(1)} - T_w^{(1)}) = F_2^{(1)} \quad \text{and} \quad -\gamma^{(2)}(T_f^{(2)} - T_w^{(2)}) = F_2^{(2)},$$

where

$$F_2^{(1)} = P_*(T_w^{(1)} - T_w^{(2)}), \quad F_2^{(2)} = Q_*(T_w^{(1)} - T_w^{(2)}), \tag{3.4.26}$$

$$P_* = \frac{2k_w^{(0)}k_w^{(2)}}{2d_1k_w^{(2)}(k_w^{(1)} - k_w^{(0)}) + 2d_2k_w^{(1)}(k_w^{(0)} - k_w^{(2)}) + k_w^{(0)}(k_w^{(1)} + k_w^{(2)})},$$

$$Q_* = \frac{2k_w^{(0)}k_w^{(1)}}{2d_1k_w^{(2)}(k_w^{(1)} - k_w^{(0)}) + 2d_2k_w^{(1)}(k_w^{(0)} - k_w^{(2)}) + k_w^{(0)}(k_w^{(1)} + k_w^{(2)})},$$

$$\text{and} \qquad \gamma^{(i)} = \frac{h_w^{(i)}\varepsilon D_C}{k_w^{(i)}} = \frac{h_w^{(i)} D_w}{k_w^{(i)}}, \quad i = 1, 2.$$

Here D_w, D_C are the thicknesses in metres of the wall and the channels, respectively. Equations (3.4.26) can be rewritten in the form

$$T_f^{(1)} - T_w^{(1)} = \frac{P_*}{\gamma^{(1)}}(T_w^{(1)} - T_w^{(2)}), \quad T_f^{(2)} - T_w^{(2)} = -\frac{Q_*}{\gamma^{(2)}}(T_w^{(1)} - T_w^{(2)}),$$

from which we obtain

$$T_w^{(1)} = \frac{(Q_* + \gamma^{(2)})\gamma^{(1)} T_f^{(1)} + P_* \gamma^{(2)} T_f^{(2)}}{\gamma^{(1)}\gamma^{(2)} + P_*\gamma^{(2)} + Q_*\gamma^{(1)}}, \tag{3.4.27}$$

$$T_w^{(2)} = \frac{Q_*\gamma^{(1)} T_f^{(1)} + (\gamma^{(1)} + P_*)\gamma^{(2)} T_f^{(2)}}{\gamma^{(1)}\gamma^{(2)} + P_*\gamma^{(2)} + Q_*\gamma^{(1)}}. \tag{3.4.28}$$

Subtracting (3.4.28) from (3.4.27) and rearranging gives

$$T_f^{(1)} - T_w^{(1)} = \frac{k_w^{(2)}\gamma^{(2)}(T_f^{(1)} - T_f^{(2)})}{J\gamma^{(1)}\gamma^{(2)} + k_w^{(2)}\gamma^{(2)} + k_w^{(1)}\gamma^{(1)}},$$

$$T_f^{(2)} - T_w^{(2)} = -\frac{k_w^{(1)}\gamma^{(1)}(T_f^{(1)} - T_f^{(2)})}{J\gamma^{(1)}\gamma^{(2)} + k_w^{(2)}\gamma^{(2)} + k_w^{(1)}\gamma^{(1)}},$$

where J is the only quantity which depends on the scaled widths of the layers and the thermal conductivity of the middle section of the wall, and it is given by

$$J = \frac{k_w^{(0)}(k_w^{(1)} + k_w^{(2)}) - 2d_2 k_w^{(1)}(k_w^{(2)} - k_w^{(0)}) - 2d_1 k_w^{(2)}(k_w^{(0)} - k_w^{(1)})}{2k_w^{(0)}}.$$

In what follows we investigate how changing the structure of the layered wall affects the temperature distributions along the channels. We focus specifically on the coefficients multiplying the coupling term $(T_f^{(1)} - T_f^{(2)})$. These coefficients have the following form

$$[R]: \quad -\frac{a_9^{(1)} k_w^{(2)}\gamma^{(2)}}{J\gamma^{(1)}\gamma^{(2)} + k_w^{(2)}\gamma^{(2)} + k_w^{(1)}\gamma^{(1)}}, \qquad [C]: \quad \frac{a_9^{(2)} k_w^{(1)}\gamma^{(1)}}{J\gamma^{(1)}\gamma^{(2)} + k_w^{(2)}\gamma^{(2)} + k_w^{(1)}\gamma^{(1)}},$$

where $[R]$ denotes the reformer side and $[C]$ denotes the combustion side. For the layered wall shown in Figure 3.4, the overall heat transfer coefficient has the following form, (compare with (3.2.14) for the unlayered wall),

$$U_a^{(i)} = \left(\frac{D_w^{(i)}}{k_w^{(i)}} + \frac{D_w^{(0)}}{2k_w^{(0)}} + \frac{1}{h_w^{(i)}}\right)^{-1}, \; i = 1, 2,$$

where $D_w^{(i)}$, $i = 0, 1, 2$, denotes the width of each layer within the wall (in metres), and $U_a^{(1)}$ and $U_a^{(2)}$ are the overall heat transfer coefficients between the reformer channel and the middle of the adjacent wall and the combustion channel and the middle of the adjacent wall, respectively. The results of numerical calculations are presented in Figures 3.5 to 3.7. The aim is to show how the structure of the wall affects the coupling between the temperatures in the channels. We analyse three cases and the details are given in Sections 3.4.2 to 3.4.4.

One particular feature of the present combustion/reforming system is that the temperature is obtained as a monotonic function of the distance parameter (see Figures 3.5 to 3.7). The same applies to the temperatures shown in Figure 3.3 in Section 3.3.2. By no means does this characterise a general feature of conventional combustion systems, where critical points would be expected should similar experiments be carried out. In our particular case of combining catalytic combustion and steam reforming in a multi-channel reactor, the temperature-versus-distance behaviour is consistent with the results of the earlier published work (see, for example, [23], [45], [74], [78], [86], [94] and [96]).

3.4.2 Three layers of equal widths but different thermal conductivities

$$d_1 = -d_2 = \frac{1}{6}, \quad k_w^{(1)} \neq k_w^{(0)} \neq k_w^{(2)}$$

In this case the wall consists of 3 layers of the same width but different thermal conductivities. The quantities $\gamma^{(1)}, \gamma^{(2)}$ and J have the form

$$\gamma^{(1)} = \frac{h_w^{(1)} \varepsilon D_C}{k_w^{(1)}} = \frac{1.199}{k_w^{(1)}}, \quad \gamma^{(2)} = \frac{h_w^{(2)} \varepsilon D_C}{k_w^{(2)}} = \frac{1.477}{k_w^{(2)}},$$

$$J = \frac{1}{3k_w^{(0)}} \left(k_w^{(0)} k_w^{(1)} + k_w^{(0)} k_w^{(2)} + k_w^{(1)} k_w^{(2)} \right).$$

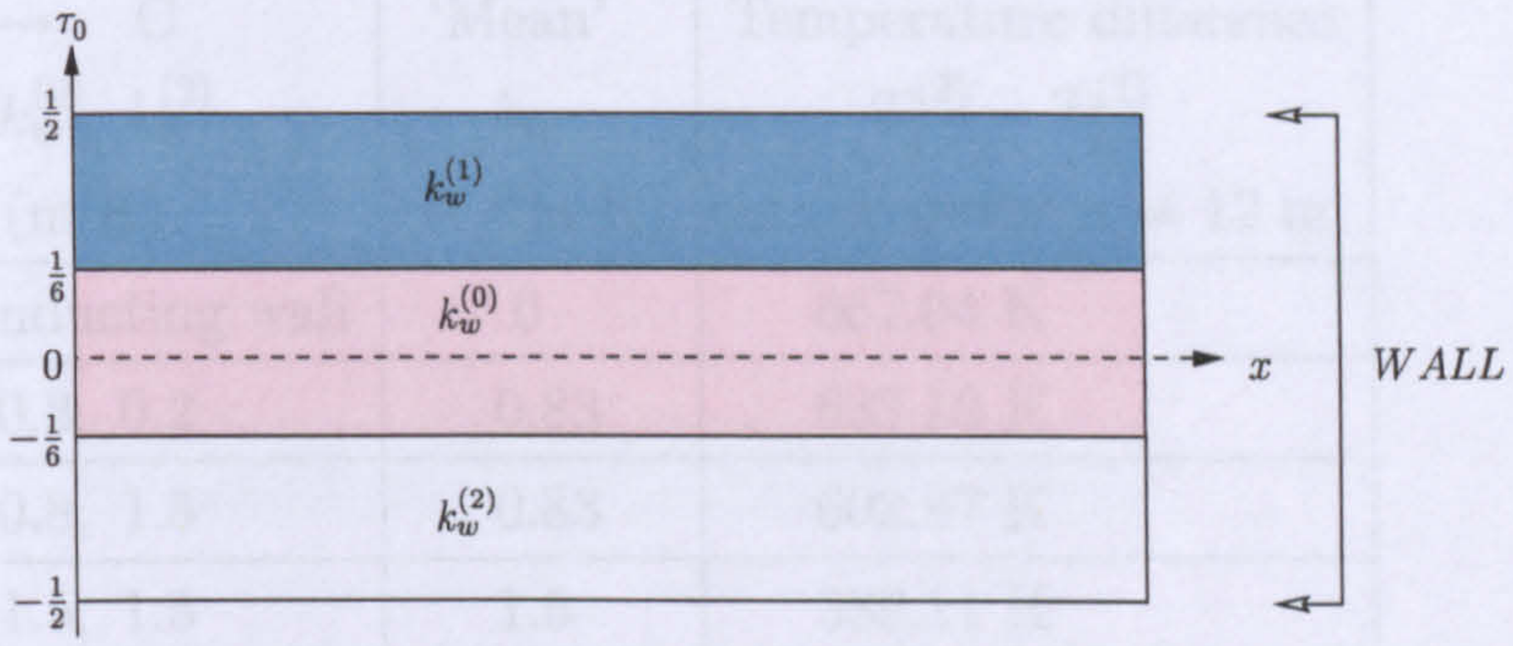

c) $k_w^{(1)} = 1.5\ W/mK,\ \ k_w^{(0)} = 5\ W/mK,\ \ k_w^{(2)} = 10\ W/mK$

d) $k_w^{(1)} = 1.5\ W/mK,\ \ k_w^{(0)} = 0.8\ W/mK,\ \ k_w^{(2)} = 0.2\ W/mK$

e) $k_w^{(1)} = 10\ W/mK,\ \ k_w^{(0)} = 5\ W/mK,\ \ k_w^{(2)} = 1.5\ W/mK$

f) $k_w^{(1)} = 0.2\ W/mK,\ \ k_w^{(0)} = 0.8\ W/mK,\ \ k_w^{(2)} = 1.5\ W/mK$

Diagram 1 : Geometry of the wall for Figures 3.5(c) to 3.5(f).

The graphical results are displayed in Figure 3.5. The geometry and corresponding thermal conductivities for the graphs shown in Figures 3.5(c) to 3.5(f) are described in Diagram 1. Figures 3.5(a) and 3.5(b) correspond to the uncoupled and coupled cases for the unlayered wall, with $k_w = 1.5$ W/(m K), and they are given here for comparison. Figures 3.5(c) and 3.5(d) show the temperature distribution when the layer next to the reformer side has the same conductivity as the unlayered wall. Figures 3.5(e) and 3.5(f) show the temperature distribution when the layer next to the combustion side has the same conductivity as the unlayered wall. The difference in fluid temperatures $T_f^{(2)} - T_f^{(1)}$ at the outlet, for different 'mean' thermal conductivities, is given in Table 3.1. From Figure 3.5 and Table 3.1 we conclude that an increase in 'mean' thermal conductivity leads to an increase in the coupling between the channels, that is, a decrease in the difference between the outlet temperatures $T_f^{(2)} - T_f^{(1)}$. From Table 3.1 we can also see that, for the cases when the 'mean' thermal conductivity is kept the same, if the layer next to the combustion side has the largest thermal conductivity, then we have an increase in the coupling. This is due to the fact that the heat transfer coefficient on the combustion side is larger than that on the reformer side.

R → C $k_w^{(1)}$, $k_w^{(0)}$, $k_w^{(2)}$ W/(m K)	'Mean' k_w W/(m K)	Temperature difference $T_f^{(2)} - T_f^{(1)}$ at the outlet $x = 12$ m
Non-conducting wall	0	867.04 K
1.5, 0.8, 0.2	0.83	633.13 K
0.2, 0.8, 1.5	0.83	602.87 K
1.5, 1.5, 1.5	1.5	383.11 K
10, 5, 1.5	5.5	297.69 K
1.5, 5, 10	5.5	282.74 K

Table 3.1: Results corresponding to Figure 3.5, which show the difference in the outlet fluid temperatures in the two channels when the wall has the geometry (3 layers of equal width) and thermal conductivity as described in Diagram 1.

3.4.3 Outside layers of equal widths and equal thermal conductivities

$$\frac{1}{2} - d_1 = d_2 + \frac{1}{2} = \mathcal{D}, \quad \mathcal{D} \neq d_1 - d_2, \quad k_w^{(1)} = k_w^{(2)} \neq k_w^{(0)}$$

In this case the layer next to the reformer side and the layer next to the combustion side have the same widths and the same thermal conductivities. The width and thermal conductivity of the middle layer differs from those for the two outside layers. The thermal conductivity of the outside layers, $k_w^{(1)}$ and $k_w^{(2)}$ are such that $k_w^{(1)} = k_w^{(2)} = k_w = 1.5$ W/(m K), the thermal conductivity of the unlayered wall. The quantities $\gamma^{(1)}, \gamma^{(2)}$ and J then have the form

$$\gamma^{(1)} = \frac{h_w^{(1)} \varepsilon D_C}{k_w^{(1)}} = \frac{1.199}{k_w}, \quad \gamma^{(2)} = \frac{h_w^{(2)} \varepsilon D_C}{k_w^{(2)}} = \frac{1.477}{k_w}, \quad J = \frac{k_w}{k_w^{(0)}} \Big(2\mathcal{D} k_w^{(0)} + k_w (1 - 2\mathcal{D}) \Big).$$

The graphical results are displayed in Figure 3.6. The geometry and the corresponding thermal conductivities for the graphs shown in Figures 3.6(c) to 3.6(f) are described in Diagram 2.

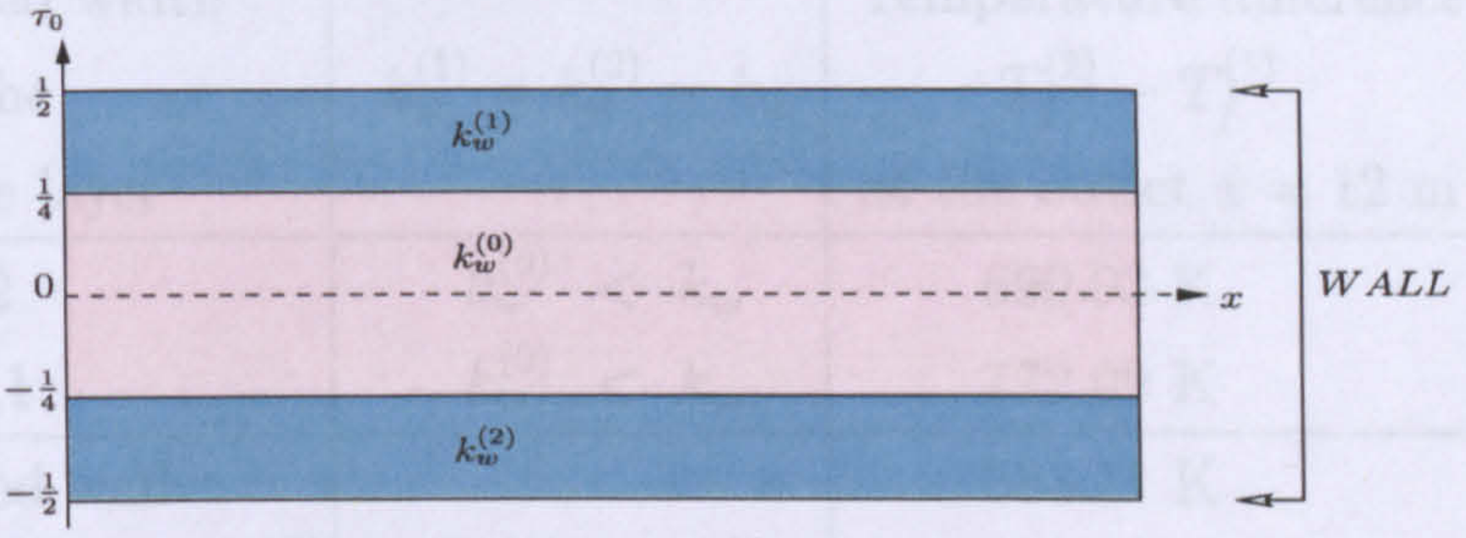

c) $k_w^{(0)} = 10\ W/mK$ d) $k_w^{(0)} = 0.2\ W/mK$

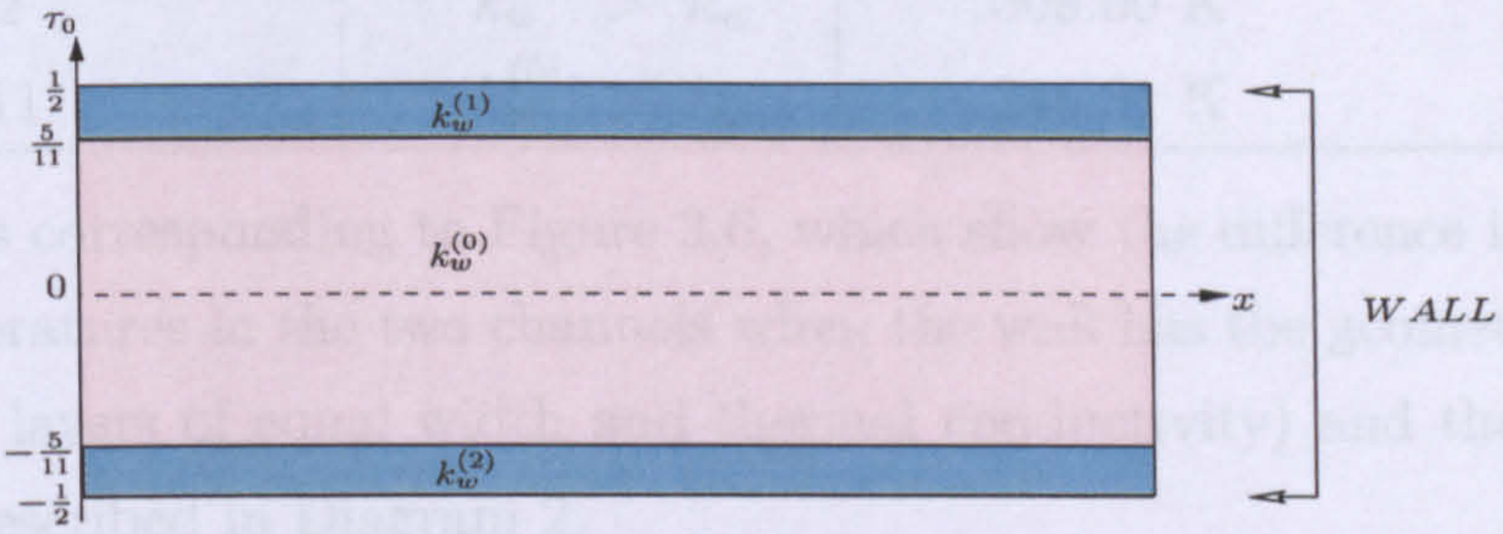

e) $k_w^{(0)} = 10\ W/mK$ f) $k_w^{(0)} = 0.2\ W/mK$

Diagram 2 : Geometry of the wall for Figures 3.6(c) to 3.6(f).
(For Figure 3.6, $k_w^{(1)} = k_w^{(2)} = 1.5$ W/(m K), the same as for the unlayered wall.)

Figures 3.6(a) and 3.6(b) correspond to the uncoupled and coupled cases for the unlayered wall, with $k_w = 1.5$ W/(m K), and they are given here for comparison. Figures 3.6(c) and 3.6(e) show the temperature distribution when $k_w^{(0)}$ is larger than $k_w^{(1)}$ and $k_w^{(2)}$. Figures 3.6(d) and 3.6(f) show the temperature distribution when $k_w^{(0)}$ is smaller than $k_w^{(1)}$ and $k_w^{(2)}$. Figures 3.6(c) and 3.6(d) are for the case when the middle layer is of normalised width 1/2, whereas Figures 3.6(e) and 3.6(f) are for the case when the middle layer is of normalised width 10/11. The difference in fluid temperatures $T_f^{(2)} - T_f^{(1)}$ at the outlet, for each of the cases described in Diagram 2, is given in Table 3.2. From Figure 3.6 and Table 3.2 it follows that the coupling effect is less pronounced when the thermal conductivity of the middle layer is smaller than that of the outer layers and more pronounced

Normalised width of the middle layer	$k_w^{(1)} = k_w^{(2)} = k_w$	Temperature difference $T_f^{(2)} - T_f^{(1)}$ at the outlet $x = 12$ m
1/2	$k_w^{(0)} < k_w$	690.93 K
10/11	$k_w^{(0)} < k_w$	772.09 K
Unlayered wall (of normalised width 1)		383.11 K
1/2	$k_w^{(0)} > k_w$	309.00 K
10/11	$k_w^{(0)} > k_w$	245.31 K

Table 3.2: Results corresponding to Figure 3.6, which show the difference in the outlet fluid temperatures in the two channels when the wall has the geometry (3 layers with outer layers of equal width and thermal conductivity) and thermal conductivity as described in Diagram 2.

when the middle layer has a higher thermal conductivity than the outer layers. Also, from Table 3.2 and Figure 3.6 we conclude that if the middle layer has a lower thermal conductivity than the outer layers, increasing its width decreases the coupling. However, if the middle layer has a higher thermal conductivity than the outer layers, then increasing its width increases the coupling.

3.4.4 Two-layered wall, both layers of equal widths but different thermal conductivities

$$d_1 = d_2 = 0, \quad k_w^{(1)} \neq k_w^{(2)}$$

In this case the wall consists of two layers that have equal widths but different thermal conductivities. For the following numerical experiments we assume that the layer next to the reformer side has the same conductivity as the unlayered wall, that is, $k_w^{(1)} = 1.5$ W/(m K).

The quantities $\gamma^{(1)}, \gamma^{(2)}$ and J have the form

$$\gamma^{(1)} = \frac{h_w^{(1)} \varepsilon D_C}{k_w^{(1)}} = \frac{1.199}{k_w^{(1)}}, \quad \gamma^{(2)} = \frac{h_w^{(2)} \varepsilon D_C}{k_w^{(2)}} = \frac{1.477}{k_w^{(2)}}, \quad J = \frac{1}{2}\left(k_w^{(1)} + k_w^{(2)}\right).$$

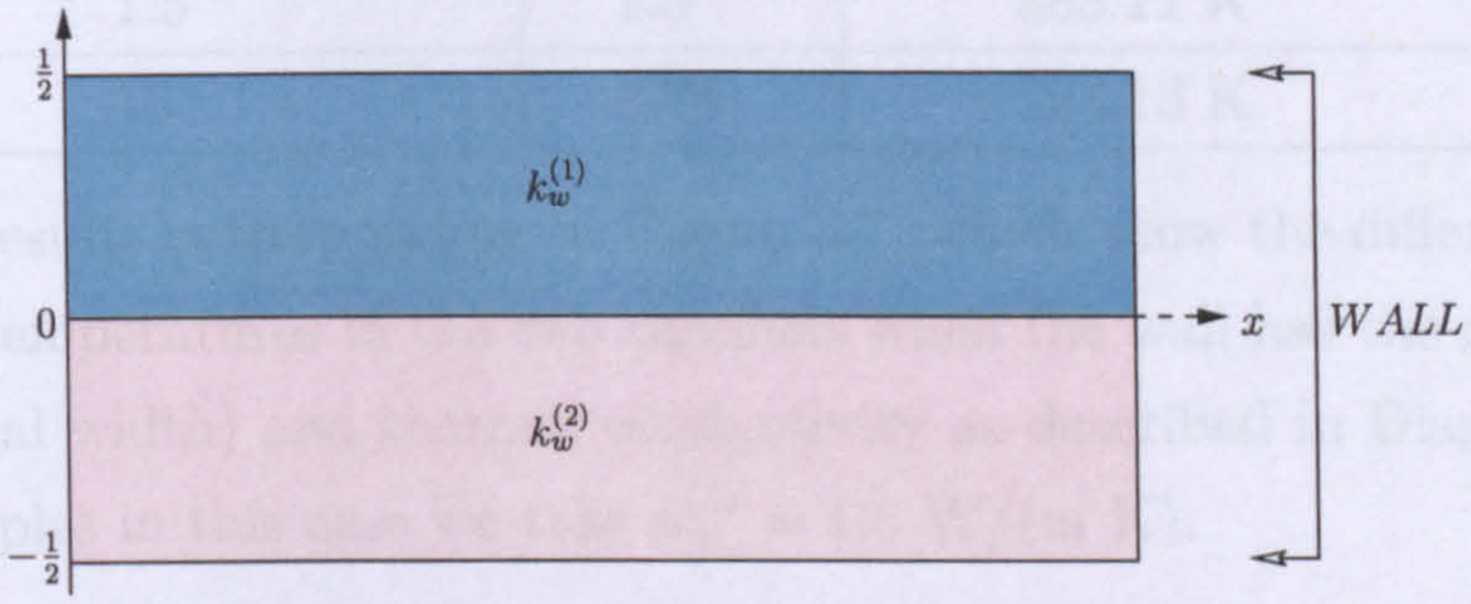

c) $k_w^{(2)} = 10\ W/mK$ *d)* $k_w^{(2)} = 0.2\ W/mK$

Diagram 3 : Geometry of the wall for Figures 3.7(c) and 3.7(d).
(In Figure 3.7, $k_w^{(1)} = 1.5$ W/(m K), the same as for the unlayered wall.)

The graphical results are displayed in Figure 3.7. The geometry and the corresponding thermal conductivities for the graphs shown in Figures 3.7(c) and 3.7(d) are described in Diagram 3. Figures 3.7(a) and 3.7(b) are the uncoupled and coupled cases for the unlayered wall, with $k_w = 1.5$ W/(m K), and they are given here for comparison. In Figure 3.7(c) the layer next to the reformer side has a higher thermal conductivity than the layer next to the combustion side and vice versa for Figure 3.7(d). The difference in fluid temperatures $T_f^{(2)} - T_f^{(1)}$ at the outlet, for different 'mean' thermal conductivities, is given in Table 3.3. From Figure 3.7 and Table 3.3 we conclude that an increase in the 'mean' thermal conductivity leads to an increase in the coupling between the channels, that is, a decrease in the difference between the outlet temperatures $T_f^{(2)} - T_f^{(1)}$.

$k_w^{(2)}$ W/(m K)	'Mean' k_w W/(m K)	Temperature difference $T_f^{(2)} - T_f^{(1)}$ at the outlet $x = 12$ m
Non-conducting wall	0	867.04 K
0.2	0.85	660.56 K
1.5	1.5	383.11 K
10	5.75	293.13 K

Table 3.3: Results corresponding to Figure 3.7, which show the difference in the outlet fluid temperatures in the two channels when the wall has the geometry (2 layers of equal width) and thermal conductivity as described in Diagram 3. For all the examples in this case we take $k_w^{(1)} = 1.5$ W/(m K).

3.5 Discussion of the results

In this chapter we have analysed, using an accurate asymptotic technique, how the temperatures in the channels of a catalytic reformer are coupled across the thin conducting wall between the channels. We have described in detail how we obtain the coupling terms analytically, expanding the temperature in the wall asymptotically, and we have presented two numerical examples with the corresponding coupled and uncoupled cases for each example. The first example was for a set of model parameters with a model reaction rate, and the second example was for a set of industrial parameters, taken from previously published work on reactors of this type. We have also considered how the geometry and thermal conductivity of the wall affects the coupling between the channels. We have presented several numerical examples which show that an increase in the 'mean' thermal conductivity across the wall results in a more pronounced coupling of the fluid temperatures, as expected. We have also shown that, if we keep the 'mean' thermal conductivity the same, the coupling between the channels is increased

when the layer next to the combustion side has the highest thermal conductivity. Finally, for the case of a three-layered wall, we have shown that if the middle layer has a lower thermal conductivity than the outer layers, increasing its width decreases the coupling between the channels. However, if the middle layer has a higher thermal conductivity than the outer layers, increasing its width increases the coupling between the channels.

In the next chapter we extend this technique and explore in more detail the effect of changing the properties of the connecting wall by including an air gap. Consequently, heat transfer via radition is also taken in account. We find the nonlinear coupling terms (nonlinear in $T_0^{(1)}(x)$ and $T_0^{(2)}(x)$) and we solve the coupled system numerically, presenting several examples.

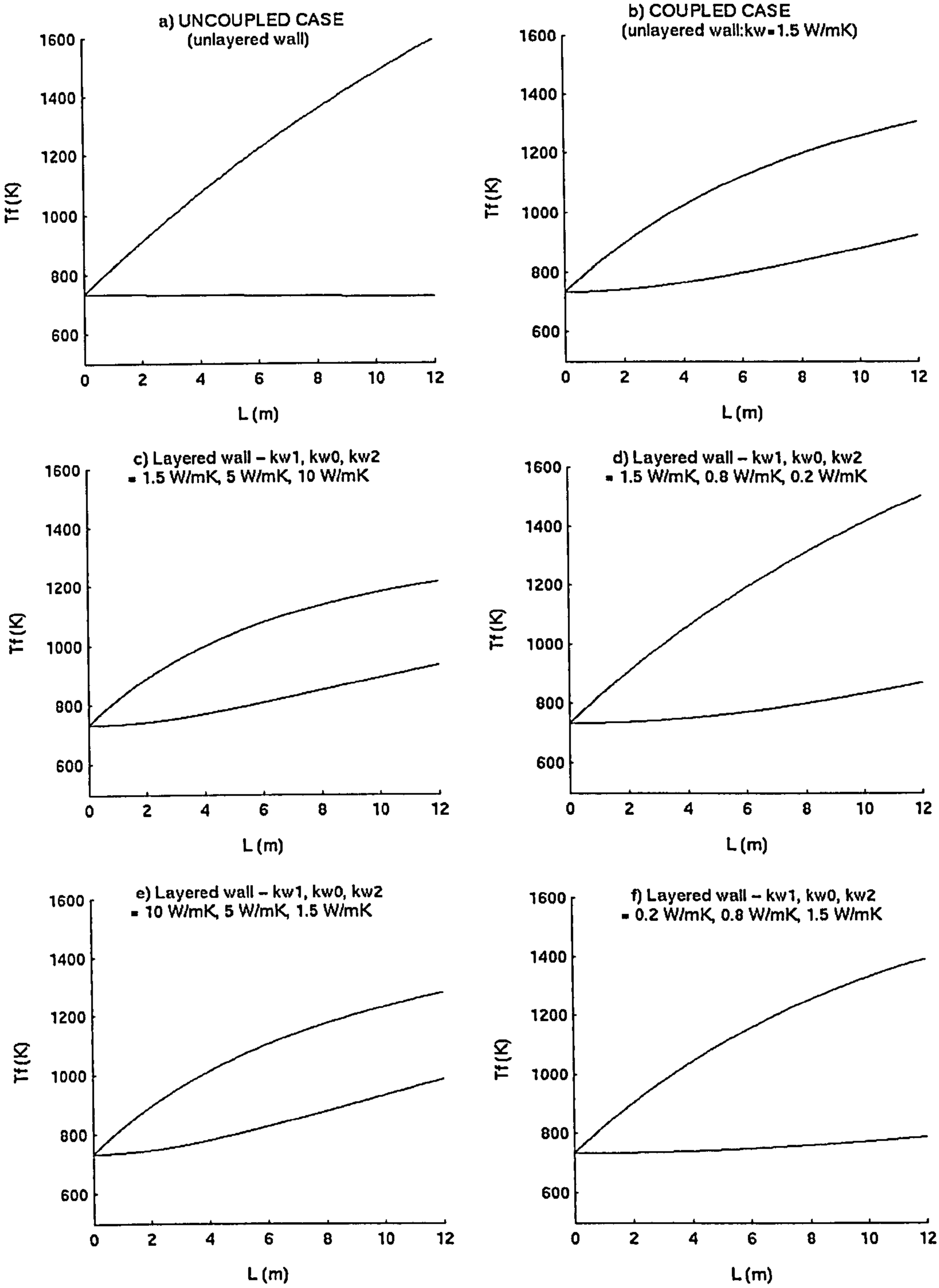

Figure 3.5: The distribution of the fluid temperatures along the channels with the geometry and thermal conductivities described in Diagram 1. (Upper plot = Combustion side, Lower plot = Reformer side.)

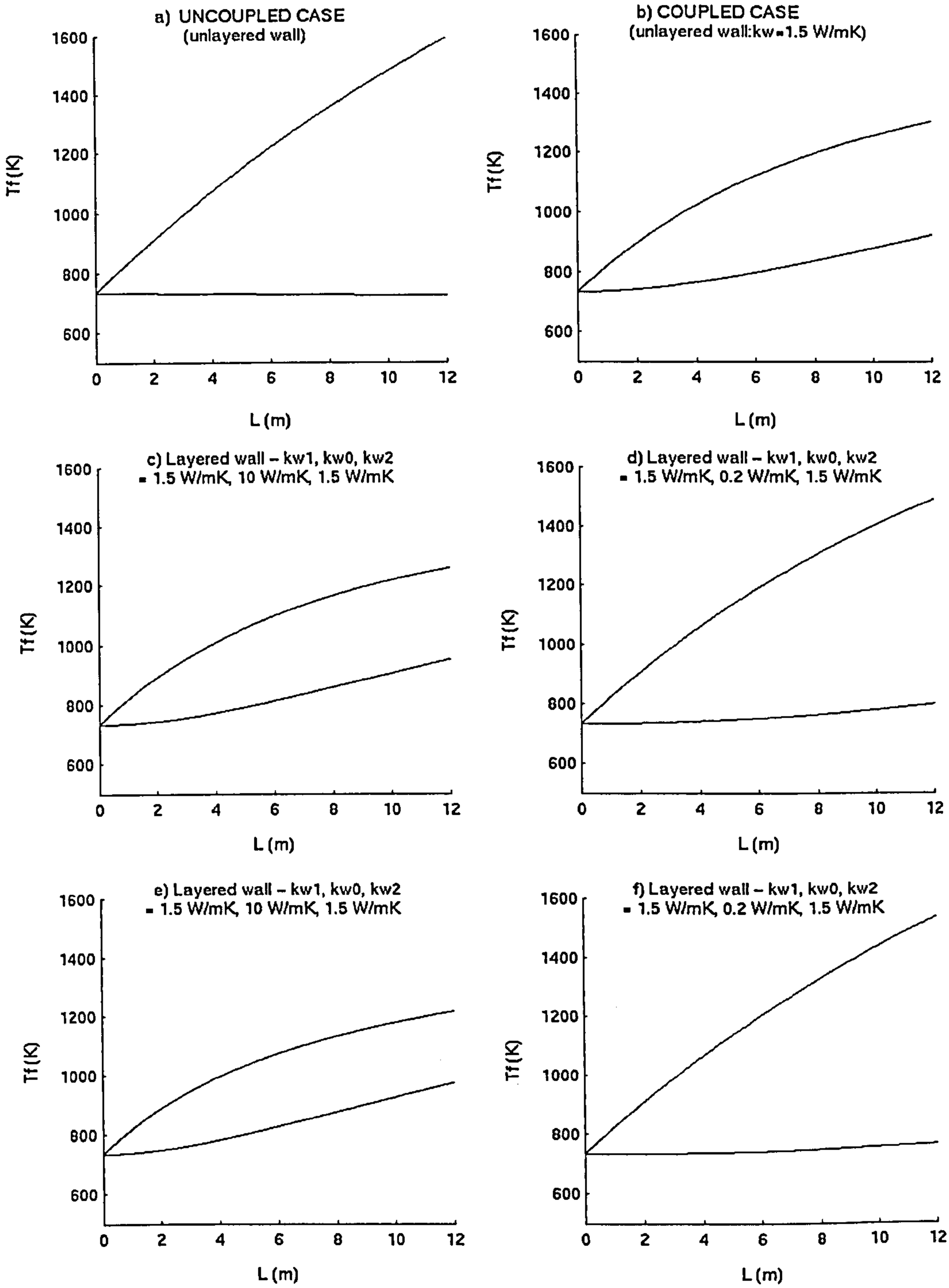

Figure 3.6: The distribution of the fluid temperatures along the channels with the geometry and thermal conductivities described in Diagram 2. (Upper plot = Combustion side, Lower plot = Reformer side.)

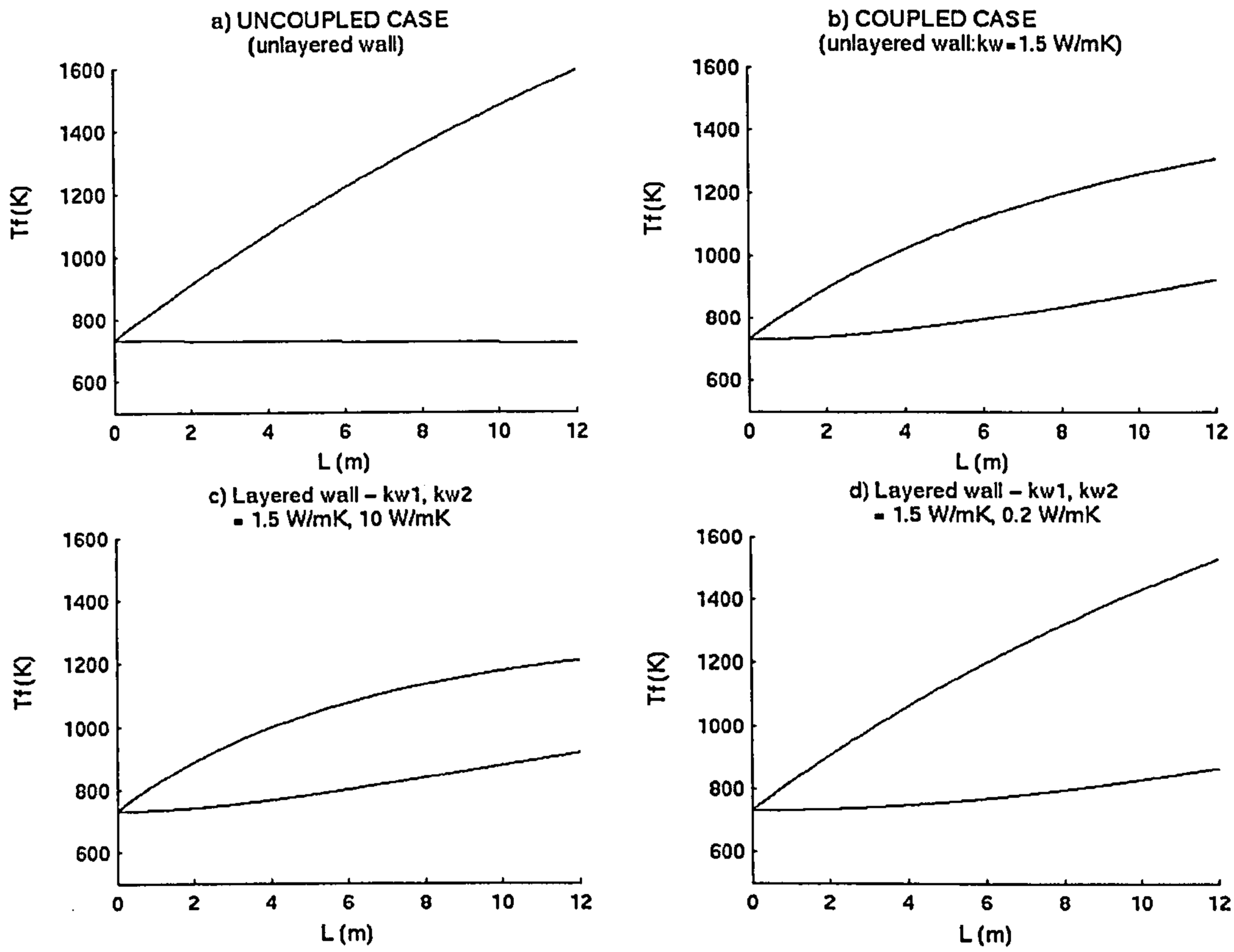

Figure 3.7: The distribution of the fluid temperatures along the channels with the geometry and thermal conductivities described in Diagram 3. (Upper plot = Combustion side, Lower plot = Reformer side.)

Chapter 4

Air gap in the wall

4.1 Introduction

It is of great importance to understand what would happen, not only if the wall connecting the channels where the reactions are taking place was layered, but also if there was a thin air gap inside the wall, see Figure 4.1. The air gap could be used to shift the main mechanism of heat transfer from conduction to radiation and thereby raise temperatures on the combustion side. This could be used as a self-regulating method of temperature control, which could be exploited to ensure that the reforming side does not act too much as a heat sink, which could in turn extinguish the combustion reaction. If too much heat is being transferred, then the surface temperature on the combustion side will fall and heat transfer by radiation would rapidly decrease. However, the combustion reactions would still be sustained. In the examples illustrated here the simulations are performed at higher temperatures to illustrate this principle. This chapter comprises of two parts: in the first part we assume that heat transfers across the air gap via radiation only. In the second part we then consider the 'limit' case, as the width of the air gap approaches zero, and we include heat transfer via conduction, as well as radiation, across the air gap. In the remaining parts of the wall, the *outer*

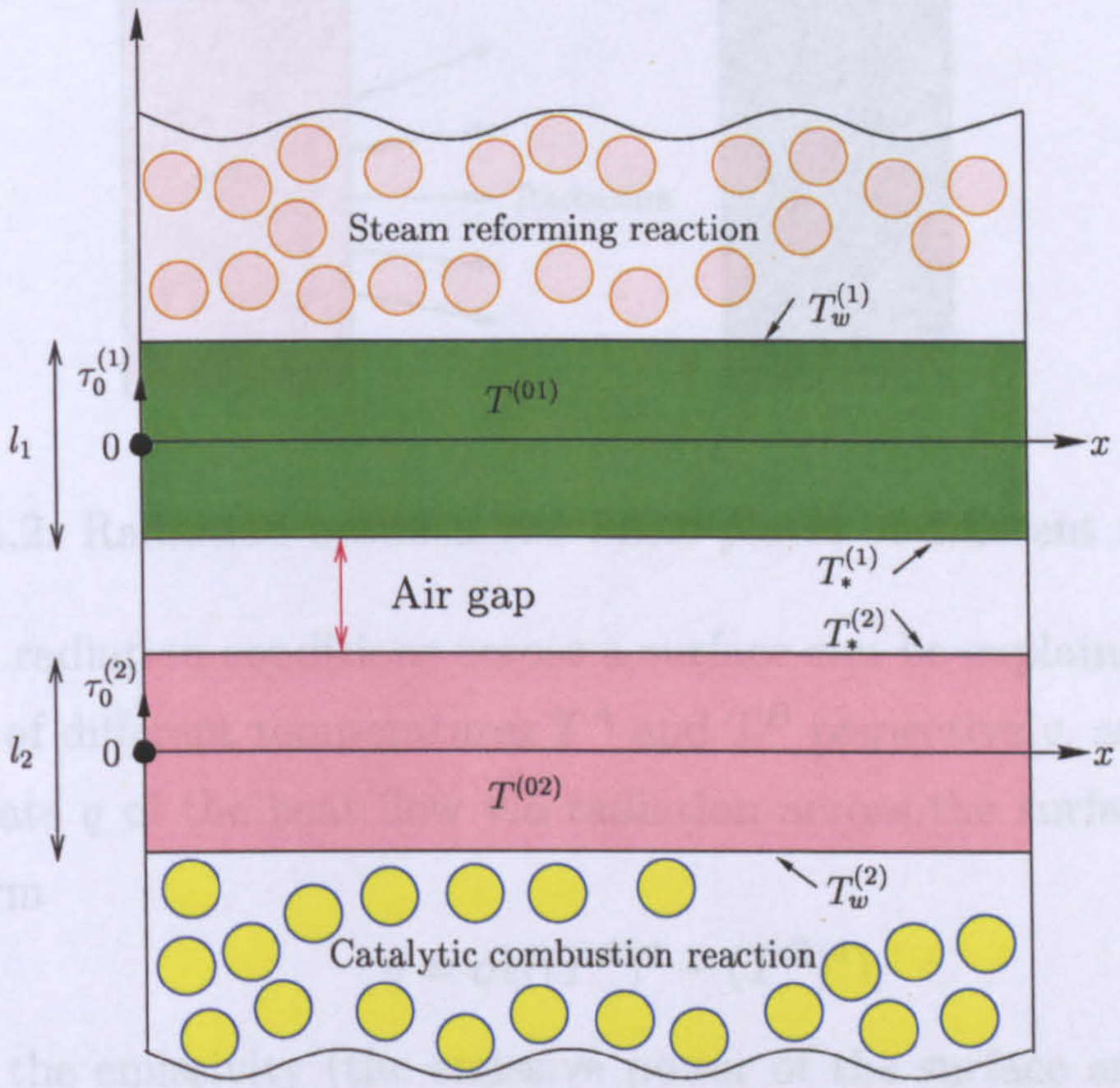

Figure 4.1: An air gap inside the wall.

layers, heat transfers via conduction as before. We introduce local coordinates such that

$$\tau_0^{(i)} \in \Big(-\frac{l_i}{2}, \frac{l_i}{2}\Big),\ i = 1, 2,$$

i.e. the outer layers of the wall are of dimensionless width l_1 and l_2 as shown in Figure 4.1. The specific temperatures, at the interfaces between the air gap and the outer layers of the wall are denoted by $T_*^{(1)}$ and $T_*^{(2)}$ respectively, see Figure 4.1, and at these interfaces, we set the radiation conditions, which are discussed in the following section.

4.2 Formulation of the problem

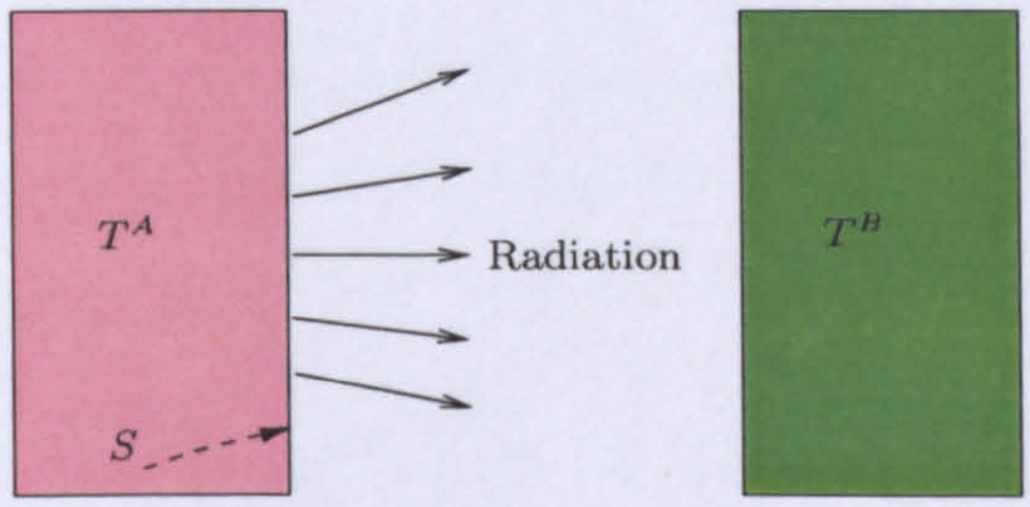

Figure 4.2: Radiation between two finite plates of different temperatures.

In general, radiation conditions across a surface can be explained by considering two plates of different temperatures T^A and T^B respectively, as shown in Figure 4.2. The rate q of the heat flow via radiation across the surface S on plate T^A has the form

$$q = \sigma\epsilon((T^A)^4 - (T^B)^4),$$

where ϵ is the emissivity (the emissive power of the surface emitting radiation) $0 < \epsilon < 1$, and σ is the Stephan-Boltzman constant, $\sigma = 5.670 \times 10^{-8}$ W/(m^2 K^4) (see, for example, [23], [45] and [46]).

Similar radiation conditions are posed at $\tau_0^{(1)} = -l_1/2$ and $\tau_0^{(2)} = l_2/2$. In the outer layers of the wall the temperatures $T^{(0i)}$, $i = 1, 2$, satisfy the steady state heat equation which, in the new local coordinates, takes the form

$$\nabla^2 T^{(0i)}(x, \tau_0^{(i)}) = \frac{\partial^2 T^{(0i)}}{\partial x^2} + \frac{1}{\varepsilon^2 D_C^2} \frac{\partial^2 T^{(0i)}}{\partial \tau_0^{(i)2}} = 0, \ i = 1, 2, \qquad (4.2.1)$$

where, as before, ε denotes the ratio of the width of the wall to the width of the channel, $\varepsilon = D_w/D_C$.

The temperatures $T^{(0i)}$, $i = 1, 2$, are expanded asymptotically in the following way:

$$T^{(0i)}(x,\tau_0^{(i)}) = T_0^{(0i)}(x,\tau_0^{(i)}) + \varepsilon T_1^{(0i)}(x,\tau_0^{(i)}) + \varepsilon^2 T_2^{(0i)}(x,\tau_0^{(i)}) + \ldots, \ i=1,2. \quad (4.2.2)$$

4.2.1 Part 1: Heat transfer across the air gap via radiation only

Similar to the previous chapters we assume ideal thermal contact between the wall and the channels. Therefore, considering heat transfer across the air gap via radiation only, the full set of boundary conditions associated with the wall is

$$T^{(01)} = T_w^{(1)}, \; k_w^{(1)} \frac{\partial T^{(01)}}{\partial n} = h_w^{(1)} (T_f^{(1)} - T_w^{(1)}), \quad \text{at} \quad \tau_0^{(1)} = \frac{l_1}{2}; \tag{4.2.3}$$

$$T^{(01)} = T_*^{(1)}, \; k_w^{(1)} \frac{\partial T^{(01)}}{\partial n} = \sigma \epsilon ((T_*^{(2)})^4 - (T_*^{(1)})^4), \quad \text{at} \quad \tau_0^{(1)} = -\frac{l_1}{2}; \tag{4.2.4}$$

$$T^{(02)} = T_*^{(2)}, \; k_w^{(2)} \frac{\partial T^{(02)}}{\partial n} = \sigma \epsilon ((T_*^{(1)})^4 - (T_*^{(2)})^4), \quad \text{at} \quad \tau_0^{(2)} = \frac{l_2}{2}; \tag{4.2.5}$$

$$T^{(02)} = T_w^{(2)}, \; k_w^{(2)} \frac{\partial T^{(02)}}{\partial n} = h_w^{(2)} (T_f^{(2)} - T_w^{(2)}), \quad \text{at} \quad \tau_0^{(2)} = -\frac{l_2}{2}, \tag{4.2.6}$$

where $k_w^{(i)}$ and $h_w^{(i)}$, $i = 1, 2$, are the thermal conductivities and the heat transfer coefficients associated with the two outer layers of the wall, respectively. Substituting (4.2.2) into (4.2.1) we find that the leading terms $T_0^{(0i)}$, $i = 1, 2$, of the temperatures are linear in $\tau_0^{(i)}$, that is,

$$T_0^{(0i)}(x, \tau_0^{(i)}) \;\; = \;\; F_3^{(i)}(x) + F_4^{(i)}(x) \tau_0^{(i)}, \; i = 1, 2, \tag{4.2.7}$$

where $F_3^{(i)}$ and $F_4^{(i)}$, $i = 1, 2$, are functions of x which are obtained from the boundary conditions (4.2.3) and (4.2.6), giving

$$F_3^{(1)} = T_w^{(1)} - \frac{l_1}{2} \gamma^{(1)} H^{(1)}, \quad F_4^{(1)} = \gamma^{(1)} H^{(1)},$$

$$F_3^{(2)} = T_w^{(2)} - \frac{l_2}{2} \gamma^{(2)} H^{(2)}, \quad F_4^{(2)} = -\gamma^{(2)} H^{(2)},$$

where, as before,

$$\gamma^{(i)} = \frac{D_w h_w^{(i)}}{k_w^{(i)}}, \; i = 1, 2,$$

and

$$H^{(i)}(x) = T_f^{(i)}(x) - T_w^{(i)}(x),\ i = 1, 2.$$

Substituting $F_3^{(i)}$ and $F_4^{(i)}$, $i = 1, 2$, into (4.2.7) and rearranging, we obtain the following expressions for $T_0^{(01)}$ and $T_0^{(02)}$:

$$T_0^{(01)}(x, \tau_0^{(1)}) \ = \ T_f^{(1)} - H^{(1)}\Big[1 + \gamma^{(1)}\Big(\frac{l_1}{2} - \tau_0^{(1)}\Big)\Big], \tag{4.2.8}$$

$$T_0^{(02)}(x, \tau_0^{(2)}) \ = \ T_f^{(2)} - H^{(2)}\Big[1 + \gamma^{(2)}\Big(\frac{l_2}{2} + \tau_0^{(2)}\Big)\Big]. \tag{4.2.9}$$

The Dirichlet conditions in (4.2.4) and (4.2.5) are substituted into (4.2.8) and (4.2.9) to give

$$T_*^{(1)}(x) \ = \ T_f^{(1)} - H^{(1)}(1 + \gamma^{(1)} l_1), \tag{4.2.10}$$

$$T_*^{(2)}(x) \ = \ T_f^{(2)} - H^{(2)}(1 + \gamma^{(2)} l_2). \tag{4.2.11}$$

Comparing the Neumann conditions in (4.2.3) and (4.2.4) and then in (4.2.5) and (4.2.6), we obtain the following

$$-h_w^{(1)} H^{(1)} \ = \ \sigma\epsilon((T_*^{(2)})^4 - (T_*^{(1)})^4), \tag{4.2.12}$$

$$h_w^{(2)} H^{(2)} \ = \ \sigma\epsilon((T_*^{(2)})^4 - (T_*^{(1)})^4), \tag{4.2.13}$$

which gives a relationship between $H^{(1)}$ and $H^{(2)}$, that is,

$$H^{(2)} = -\frac{h_w^{(1)}}{h_w^{(2)}} H^{(1)}. \tag{4.2.14}$$

Using this relationship along with the substitution of (4.2.10) and (4.2.11) into (4.2.12) gives the following fourth order equation for the function $H^{(1)}$:

$$0 = \sigma\epsilon((T_f^{(1)} - H^{(1)} B^{(1)})^4 - (T_f^{(2)} + H^{(1)} B^{(2)})^4) - h_w^{(1)} H^{(1)}, \tag{4.2.15}$$

where the coefficients $B^{(1)}$ and $B^{(2)}$ are given by

$$B^{(1)} = (1 + \gamma^{(1)} l_1), \quad B^{(2)} = \frac{h_w^{(1)}}{h_w^{(2)}}\Big(1 + \gamma^{(2)} l_2\Big). \tag{4.2.16}$$

4.2.2 Full system of equations

For the numerical simulations in this chapter we again use the simplified form of the Arrhenius reaction rate as discussed in Chapters 2 and 3, that is,

$$(-R)_s^{(i_0)} = \Psi^{(i_0)} Y_s^{(i)} = \mathcal{A}^{(i)} e^{\left(\frac{-E^{(i)}}{R_g T_s^{(i)}(0)}\right)} Y_s^{(i)}, \ i = 1, 2.$$

This implies that the solid mole balance equation (3.2.1) can be written as

$$Y_s^{(i)} = \frac{a_1^{(i)} Y_f^{(i)}}{a_1^{(i)} + a_2^{(i)} \Psi^{(i)}}, \ i = 1, 2. \tag{4.2.17}$$

Therefore, the full system of equations for the temperatures and the concentrations describing the mass and energy balances in the fluid and the solid phases, is

$$a_3^{(i)} \frac{d^2 Y_f^{(i)}}{dx^2}(x) - a_4^{(i)} \frac{dY_f^{(i)}}{dx}(x) - \left(\frac{a_5^{(i)} a_2^{(i)} \Psi^{(i)}}{a_1^{(i)} + a_2^{(i)} \Psi^{(i)}}\right) Y_f^{(i)}(x) = 0,$$

$$a_6^{(i)} \frac{d^2 T_f^{(i)}}{dx^2}(x) - a_7^{(i)} \frac{dT_f^{(i)}}{dx}(x) + a_8^{(i)} (T_s^{(i)}(x) - T_f^{(i)}(x)) - a_9^{(i)} g^{(i)} H^{(1)} = 0, \tag{4.2.18}$$

$$a_{10}^{(i)} \frac{d^2 T_s^{(i)}}{dx^2}(x) - \left(\frac{a_1^{(i)} a_2^{(i)} a_{11}^{(i)} \Psi^{(i)}}{a_1^{(i)} + a_2^{(i)} \Psi^{(i)}}\right) Y_f^{(i)}(x) - a_8^{(i)} (T_s^{(i)}(x) - T_f^{(i)}(x)) = 0, \ i = 1,2,$$

where

$$H^{(1)} = (T_f^{(1)} - T_w^{(1)}), \quad g^{(1)} = 1, \quad g^{(2)} = -\frac{h_w^{(1)}}{h_w^{(2)}}.$$

For the purpose of the numerical simulations in this chapter only, the value of the parameter $\mathcal{A}^{(1)}$ (the pre-exponential factor on the reformer side), provided

by our colleagues in chemical engineering, was changed to 1832.35 mol/(kg_{cat} s). This was to give a clear indication of the effect on the temperature distributions of changing the parameters associated with the air gap. All other constants in $\Psi^{(i)}$, $a_1^{(i)}$ to $a_{11}^{(i)}$, $i = 1, 2$, and the boundary conditions at the inlet and the outlet are those given in Section 3.3.2.

Equation (4.2.15) and system (4.2.18), together with the inlet and outlet boundary conditions, and industrial data for the coefficients $B^{(i)}$, $g^{(i)}$ and $a_j^{(i)}$, $i = 1, 2$, $j = 1, ..., 11$, is solved numerically to find the temperature and the concentration distributions along the channels. We also obtain the results for the function $H^{(1)}$, which show how the difference between the temperature of the fluid in the reformer channel and the temperature of the wall on the reformer side changes. (The graph for $H^{(2)}$ - the difference between the temperature of the fluid in the combustion channel and the temperature of the wall on the combustion side - is similar and therefore, we do not include it here.)

4.2.3 Numerical results and discussion

Figures 4.3 - 4.6 show the numerical simulations for the temperature and concentration distributions in the case when there is an air gap inside the wall (across the air gap we consider heat transfer via radiation only). The corresponding coupled and uncoupled cases are presented for comparison. For each case, we also present the graph of the function $H^{(1)}$ which is monotonically decreasing. For each numerical simulation we notice that the graph for the temperature distribution in the case when there is an air gap always lies between the coupled and the uncoupled graphs, as expected. Also, higher emissivity of the surfaces leads to a significant increase in the coupling between the channels (compare Figure 4.3(a) and Figure 4.3(b)), whereas decreasing the width of the air gap shows only a very slight increase in the coupling (compare Figures 4.4(a) and 4.4(b)). This second observation can be explained as follows.

The function $H^{(1)}$, which appears in the last term of the fluid energy balance equation, the second equation in (4.2.18), drives the coupling between the two channels. When the width of the air gap is changed, i.e. when l_1 and l_2 are changed, the coefficients $B^{(1)}$ and $B^{(2)}$ (which depend linearly on l_1 and l_2), also change. Our aim is to show that small perturbations in the widths l_1 and l_2 (which result in small perturbations in $B^{(1)}$ and $B^{(2)}$) give a small perturbation in the function $H^{(1)}$. This would explain why the graphs in Figure 4.4(a) and 4.4(b) look similar for different values of l_1 and l_2. We can write equation (4.2.15) as a function, M say, of $B^{(1)}$, $B^{(2)}$ and $H^{(1)}$, such that

$$0 = M(B^{(1)},\ B^{(2)},\ H^{(1)}), \tag{4.2.19}$$

where the function M is nonlinear in the three independent variables. We slightly perturb each of these variables and assume that at this perturbed point the solution still satisfies equation (4.2.19). Denoting the perturbations in $B^{(1)}$, $B^{(2)}$ and $H^{(1)}$ as $\hat{\varepsilon}B^{(1)}$, $\hat{\varepsilon}B^{(2)}$ and $\hat{\varepsilon}H^{(1)}$ respectively, we have

$$0 = M(B^{(1)} + \hat{\varepsilon}B^{(1)},\ B^{(2)} + \hat{\varepsilon}B^{(2)},\ H^{(1)} + \hat{\varepsilon}H^{(1)}).$$

Expanding about the original point $(B^{(1)}, B^{(2)}, H^{(1)})$, up to and including terms of the order $O(\hat{\varepsilon})$, gives

$$\begin{aligned} &M(B^{(1)}, B^{(2)}, H^{(1)}) + \hat{\varepsilon}B^{(1)}\frac{\partial M}{\partial B^{(1)}}(B^{(1)}, B^{(2)}, H^{(1)}) \\ &+\hat{\varepsilon}B^{(2)}\frac{\partial M}{\partial B^{(2)}}(B^{(1)}, B^{(2)}, H^{(1)}) + \hat{\varepsilon}H^{(1)}\frac{\partial M}{\partial H^{(1)}}(B^{(1)}, B^{(2)}, H^{(1)}) = 0. \end{aligned} \tag{4.2.20}$$

Computing the derivatives in equation (4.2.20) and rearranging we obtain the following expression for the perturbation in $H^{(1)}$

$$\hat{\varepsilon}H^{(1)} = \frac{4H^{(1)}\sigma\epsilon(\hat{\varepsilon}B^{(1)}(T_f^{(1)} - H^{(1)}B^{(1)})^3 + \hat{\varepsilon}B^{(2)}(T_f^{(2)} + H^{(1)}B^{(2)})^3)}{-4\sigma\epsilon(B^{(1)}(T_f^{(1)} - H^{(1)}B^{(1)})^3 + (T_f^{(2)} + H^{(1)}B^{(2)})^3) - h_w^{(1)}}. \tag{4.2.21}$$

From (4.2.21) we deduce that if the changes in $B^{(1)}$ and $B^{(2)}$ are small, (if the widths of the outer layers l_1 and l_2 are changed slightly) then consequently the

change in $H^{(1)}$ is also small and this is why we do not see a significant change in the graphs shown in Figures 4.4(a) and 4.4(b).

In addition, we present the graphs for the fluid concentrations in all the figures. These contain the uncoupled and coupled fluid concentrations as well as their corresponding distributions for the air gap cases. We see from these graphs that, due to the particular physical parameters used in these numerical simulations, there is no significant difference between the results for the uncoupled and coupled fluid concentration distributions, which, in turn, leads to the conclusion that we do not notice a significant difference in the graphs for the concentrations when either the width or the emissivity of the air gap are changed. (Compare with the case shown in Figure 2.3, which was for the illustrative example with simple chemical reactions taking place in the channels. A similar effect was observed, that the coupling is more pronounced for the temperature distributions than for the concentration distributions.)

Figure 4.5 is presented to show what happens to the uncoupled, coupled and air gap cases for the temperature distributions when the inlet boundary conditions (in this case the conditions for $T_f^{(1)}$ and $T_s^{(1)}$) are changed slightly. We set the modified conditions on the reformer side to be

$$T_f^{(1)}(0) = T_s^{(1)}(0) = 500 \text{ K}.$$

Comparing Figure 4.4(a) and Figure 4.5(a) we see that the temperature distribution on the reformer side changes significantly as we lower the inlet condition. The same is true for the concentration distributions, which can be seen by comparing Figure 4.4(c) and Figure 4.5(c).

In addition, Figures 4.6 is presented to show what happens to the temperature and concentration distributions when the inlet boundary values for $T_f^{(1)}, T_s^{(1)}$ and $Y_f^{(2)}$ are all decreased, that is

$$T_f^{(1)}(0) = T_s^{(1)}(0) = 500 \text{ K}, \; Y_f^{(2)}(0) = 0.06.$$

Conclusions this time are that for the coupled, uncoupled and all the air gap cases, the temperatures on the reformer side and the combustion side are closer together in all the graphs and the concentration distributions on the combustion side all have a lower gradient than those in the cases with the original boundary conditions. This can be seen by comparing Figures 4.3 and 4.4 with Figure 4.6.

Another important point to note here is that in this chapter on the air gap, we are introducing a new concept, different from those in the previous chapter where we had different layers of different widths and thermal conductivities within the wall. In all of the previous cases, the temperature distribution across each layer of the wall, to leading order, was linear in the scaled coordinate, i.e. in the layered wall in Section 3.4 we had

$$\begin{aligned} T_0^{(01)}(x,\tau_0) &= F_1^{(1)}(x) + F_2^{(1)}(x)\tau_0, \quad \tau_0 \in (d_1,\ 1/2), \\ T_0^{(00)}(x,\tau_0) &= F_1^{(0)}(x) + F_2^{(0)}(x)\tau_0, \quad \tau_0 \in (d_2,\ d_1), \\ T_0^{(02)}(x,\tau_0) &= F_1^{(2)}(x) + F_2^{(2)}(x)\tau_0, \quad \tau_0 \in (-1/2,\ d_2), \end{aligned}$$

where $F_i^{(j)},\ i = 1, 2,\ j = 0, 1, 2$, were determined from the boundary conditions. This lead to the coupling terms being of the form

$$\begin{aligned} T_f^{(1)} - T_w^{(1)} &= \frac{k_w^{(2)}\gamma^{(2)}(T_f^{(1)} - T_f^{(2)})}{J\gamma^{(1)}\gamma^{(2)} + k_w^{(2)}\gamma^{(2)} + k_w^{(1)}\gamma^{(1)}}, \\ T_f^{(2)} - T_w^{(2)} &= -\frac{k_w^{(1)}\gamma^{(1)}(T_f^{(1)} - T_f^{(2)})}{J\gamma^{(1)}\gamma^{(2)} + k_w^{(2)}\gamma^{(2)} + k_w^{(1)}\gamma^{(1)}}, \end{aligned}$$

with

$$J = \frac{k_w^{(0)}(k_w^{(1)} + k_w^{(2)}) - 2d_2k_w^{(1)}(k_w^{(2)} - k_w^{(0)}) - 2d_1k_w^{(2)}(k_w^{(0)} - k_w^{(1)})}{2k_w^{(0)}}.$$

For the case when $d_1 = d_2 = 0$, that is, when the wall only consisted of two layers, setting the thermal conductivities of the layers to be the same lead to the

modified coupling terms having the form

$$T_f^{(1)} - T_w^{(1)} = \frac{\gamma^{(2)}(T_f^{(1)} - T_f^{(2)})}{\gamma^{(1)} + \gamma^{(2)} + \gamma^{(1)}\gamma^{(2)}}, \quad T_f^{(2)} - T_w^{(2)} = -\frac{\gamma^{(1)}(T_f^{(1)} - T_f^{(2)})}{\gamma^{(1)} + \gamma^{(2)} + \gamma^{(1)}\gamma^{(2)}}.$$

These coupling terms are identical to the coupling terms obtained for the unlayered wall discussed in Sections 3.2.1 - 3.3.2. For the air gap case, if we neglect heat transfer by conduction across the air gap, and assume heat transfer by radiation only, the coupling terms for the limit case (as the width of the air gap approaches zero) are obtained from the following nonlinear equation

$$0 = \sigma\epsilon((T_f^{(1)} - H^{(1)}B^{(1)})^4 - (T_f^{(2)} + H^{(1)}B^{(2)})^4) - h_w^{(1)}H^{(1)},$$

where the coefficients $B^{(1)}$ and $B^{(2)}$ are given by

$$B^{(1)} = (1 + \frac{\gamma^{(1)}}{2}), \quad B^{(2)} = \frac{h_w^{(1)}}{h_w^{(2)}}\left(1 + \frac{\gamma^{(2)}}{2}\right).$$

Consequently, the coupling terms obtained from the limiting air gap case differ significantly from the coupling terms obtained for the case when there is no air gap, as discussed in Sections 3.2.1 - 3.3.2. This implies that, as the width of the air gap approaches zero, both conduction and radiation become important. Heat transfer via both radiation and conduction across the air gap is discussed in Part 2.

4.2.4 Part 2: Heat transfer across the air gap via radiation and conduction

As the distance between the outer layers approaches zero, heat will also be transferred via conduction in the air gap. For conduction as well as radiation across the air gap, the model in Part 1 is modified as follows:

We denote by $T^{(03)}$ the temperature in the air gap, which satisfies the steady state heat equation, and we introduce local coordinates

$$\tau_0^{(3)} = \frac{y}{\varepsilon^\alpha D_C}, \qquad \tau_0^{(3)} \in \Big(-\frac{l_3}{2}, \frac{l_3}{2}\Big), \quad \alpha \geq 1,$$

where l_3 is the width of the air gap, which is of the order $O(\varepsilon^\alpha)$. Conditions (4.2.3) and (4.2.6) remain the same as before, on $\tau_0^{(1)} = l_1/2$ and $\tau_0^{(2)} = -l_2/2$, respectively. However, due to heat transfer via conduction, conditions (4.2.4) and (4.2.5), on $\tau_0^{(1)} = -l_1/2$ and $\tau_0^{(2)} = l_2/2$, respectively, become

$$T^{(01)} = T_*^{(1)} = T^{(03)}, \quad k_w^{(1)} \frac{\partial T^{(01)}}{\partial n} = \sigma\epsilon((T_*^{(2)})^4 - (T_*^{(1)})^4) + k_w^{(3)} \frac{\partial T^{(03)}}{\partial n};$$

$$T^{(02)} = T_*^{(2)} = T^{(03)}, \quad k_w^{(2)} \frac{\partial T^{(02)}}{\partial n} = \sigma\epsilon((T_*^{(1)})^4 - (T_*^{(2)})^4) + k_w^{(3)} \frac{\partial T^{(03)}}{\partial n}.$$

Here $k_w^{(3)}$ is the thermal conductivity of the wall, where $k_w^{(3)} = \varepsilon k^{(*)}$ and $k^{(*)}$ is the same order of magnitude as $k_w^{(1)}$ and $k_w^{(2)}$. Similar to Section 4.2, we find that

$$\begin{aligned} T_*^{(1)}(x) &= T_f^{(1)} - H^{(1)}(1 + \gamma^{(1)} l_1), \\ T_*^{(2)}(x) &= T_f^{(2)} - H^{(2)}(1 + \gamma^{(2)} l_2), \end{aligned}$$

and

$$H^{(2)} = -\frac{h_w^{(1)}}{h_w^{(2)}} H^{(1)}.$$

The following modified fourth order equation (compare with (4.2.15)) is used to find the function $H^{(1)}$:

$$\begin{aligned} 0 &= \sigma\epsilon((T_f^{(1)} - H^{(1)}B^{(1)})^4 - (T_f^{(2)} + H^{(1)}B^{(2)})^4) - h_w^{(1)} H^{(1)} \\ &+ \frac{k^{(*)}}{\varepsilon^{\alpha-1} D_C}\Big((T_f^{(1)} - B^{(1)}H^{(1)}) - (T_f^{(2)} + B^{(2)}H^{(1)})\Big), \ \alpha \geq 1. \quad (4.2.22) \end{aligned}$$

The last term on the right hand side of equation (4.2.22) becomes increasingly significant as the value of α increases, that is, as the width of that air gap

decreases. Therefore, as the distance between the outer layers approaches zero, heat transfer by conduction, as well as radiation, must also be taken into account.

4.2.5 Numerical results and discussion

Figure 4.7 is presented to show the effect on the solution $H^{(1)}$, from equation (4.2.22), as the distance between the outer layers is decreased. On each graph we have presented two solutions for $H^{(1)}$: the upper graph is for the case when we consider radiation only across the air gap, and the lower graph is for the case when we include conduction as well as radiation. It is clear from Figure 4.7 that as the width of the air gap approaches zero, the effect of heat transfer via conduction becomes more significant and consequently must be taken into account. We emphasize this in Figures 4.8 and 4.9. Figure 4.8 shows the temperature distribution for the case when the width of the air gap is of the same order of magnitude as the widths of the outer layers. The difference between the cases when radiation only and when conduction and radiation are considered, is small, i.e. there is an error of approximately 4% in the outlet temperature. However, Figure 4.9 shows the temperature distributions in the limit case, as the width of the air gap approaches zero, for the two cases when radiation only and when conduction and radiation are taken into account. In the limit case, when the outer layers have the same width and thermal conductivity, we expect to obtain the same results as those for the unlayered wall (no air gap). Figure 4.9 shows that this is indeed the case: the temperature distributions, for the coupled (no air gap) case and that for the case when conduction and radiation across the limiting air gap are taken into account, are almost identical. If radiation only is considered, the error in the outlet temperature is significant, approximately 45%, which shows that, as the width of the air gap approaches zero, for an accurate analysis of the air gap, we must include heat transfer by conduction as well as radiation.

In the next chapter we return to the points raised in Chapter 3 about why it appears that the numerical solutions for the temperature distributions do not satisfy the zero flux condition at the outlet. In Chapters 2 to 4 we analysed the heat transfer across the wall, the coupling effect and the effect on the temperature and concentration distributions of changing the resistance (to the transfer of heat) of the wall. We also discussed the graphical representations of the solutions. In the following chapter we consider the full analytical solution in more detail, by constructing boundary layers near the inlet and outlet. We show that the numerical package used in Chapters 2 to 4 gives the limit solution, which holds for the main part of the channel. We also introduce the nonlinearity in the reaction rate term and construct the boundary layers accordingly.

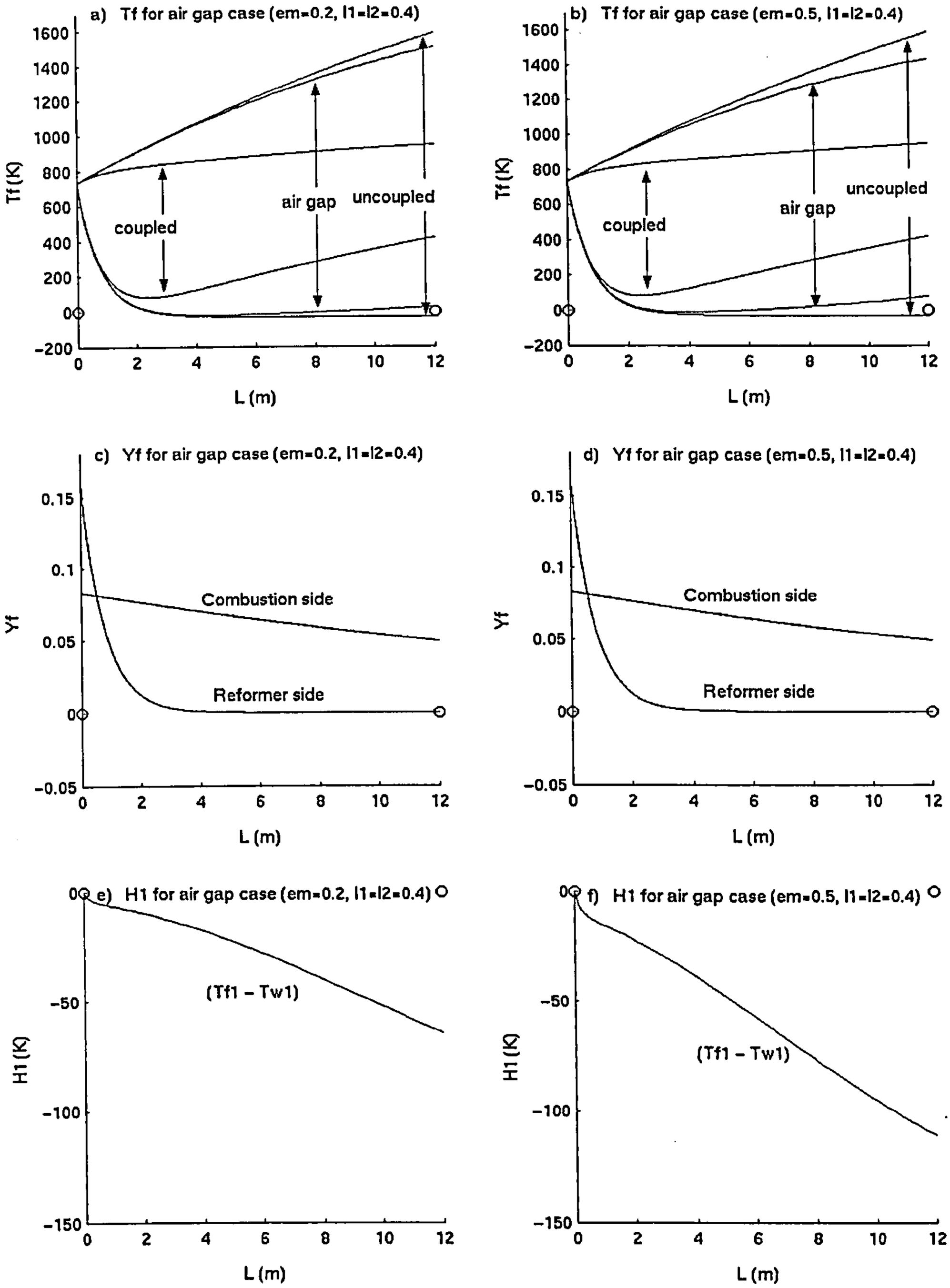

Figure 4.3: Graphs showing the fluid temperature and concentration distributions when the emissivity of the surfaces of the wall is changed. (Top two graphs: Upper plots = Combustion side, Lower plots = Reformer side.)

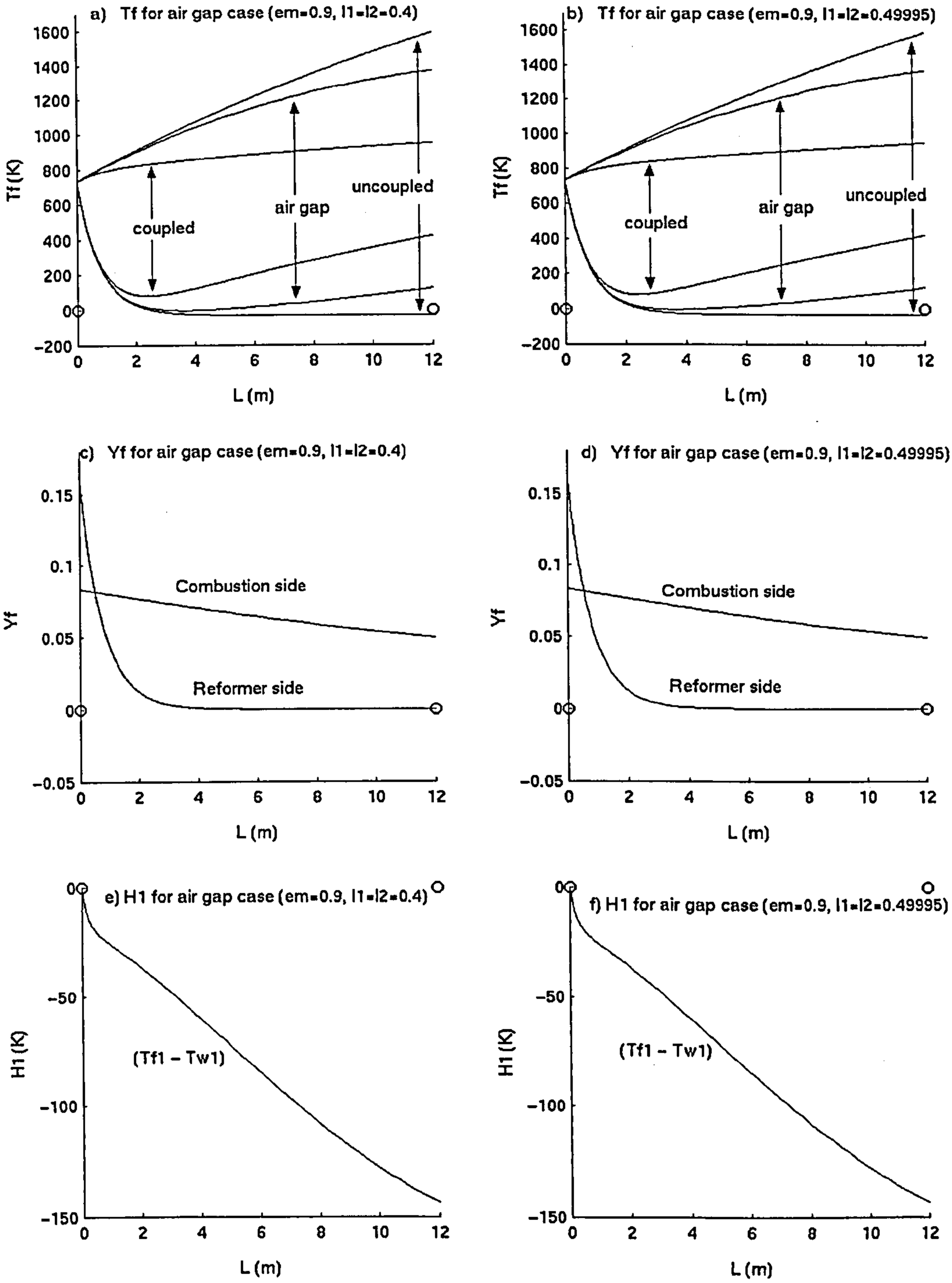

Figure 4.4: Graphs showing the fluid temperature and concentration distributions when the width of the air gap is changed. (Top two graphs: Upper plots = Combustion side, Lower plots = Reformer side.)

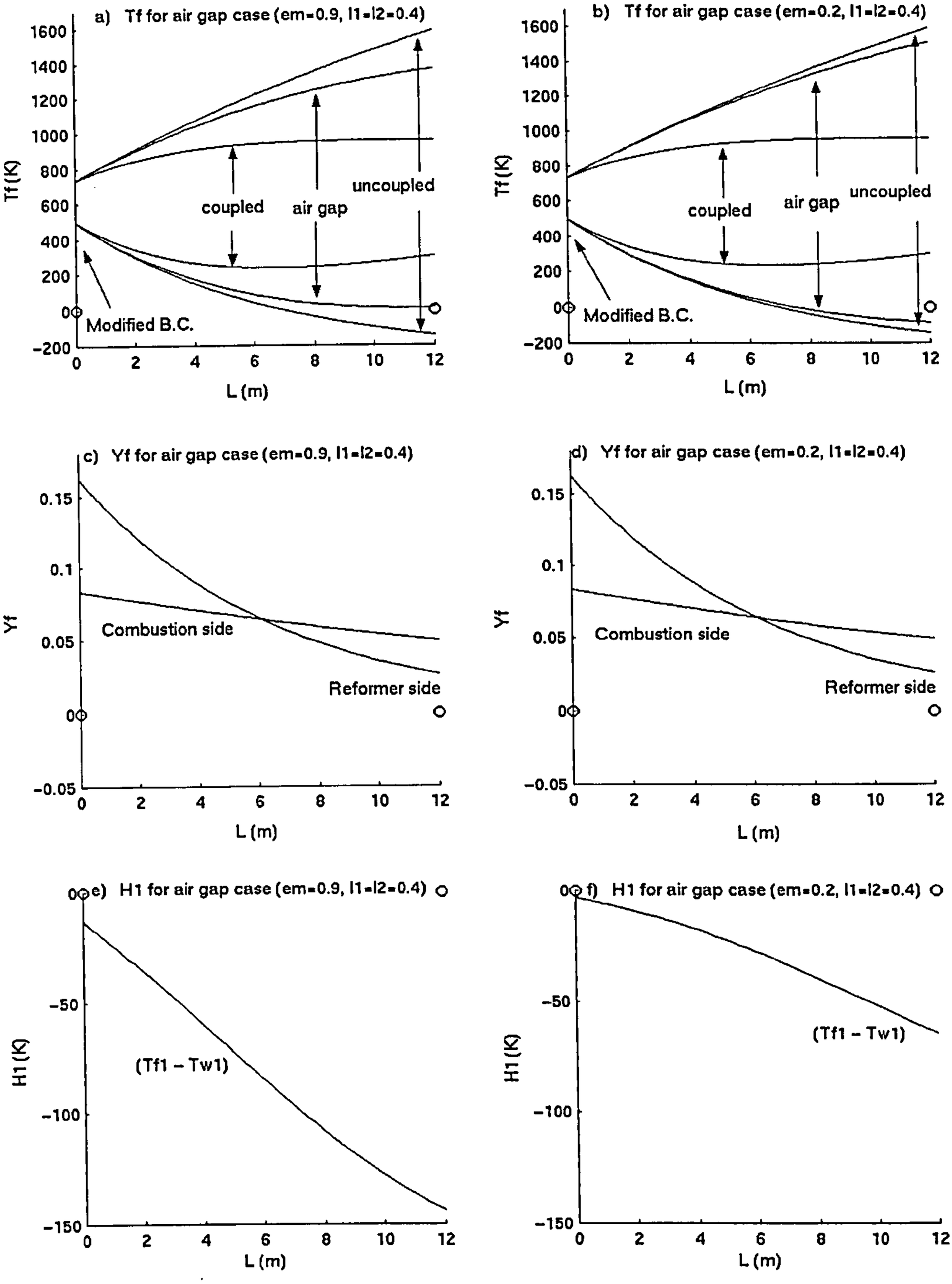

Figure 4.5: Graphs showing the fluid temperature and concentration distributions when $T_f^{(1)}(0)$ and $T_s^{(1)}(0)$ are changed to 500 K. (Top two graphs: Upper plots = Combustion side, Lower plots = Reformer side.)

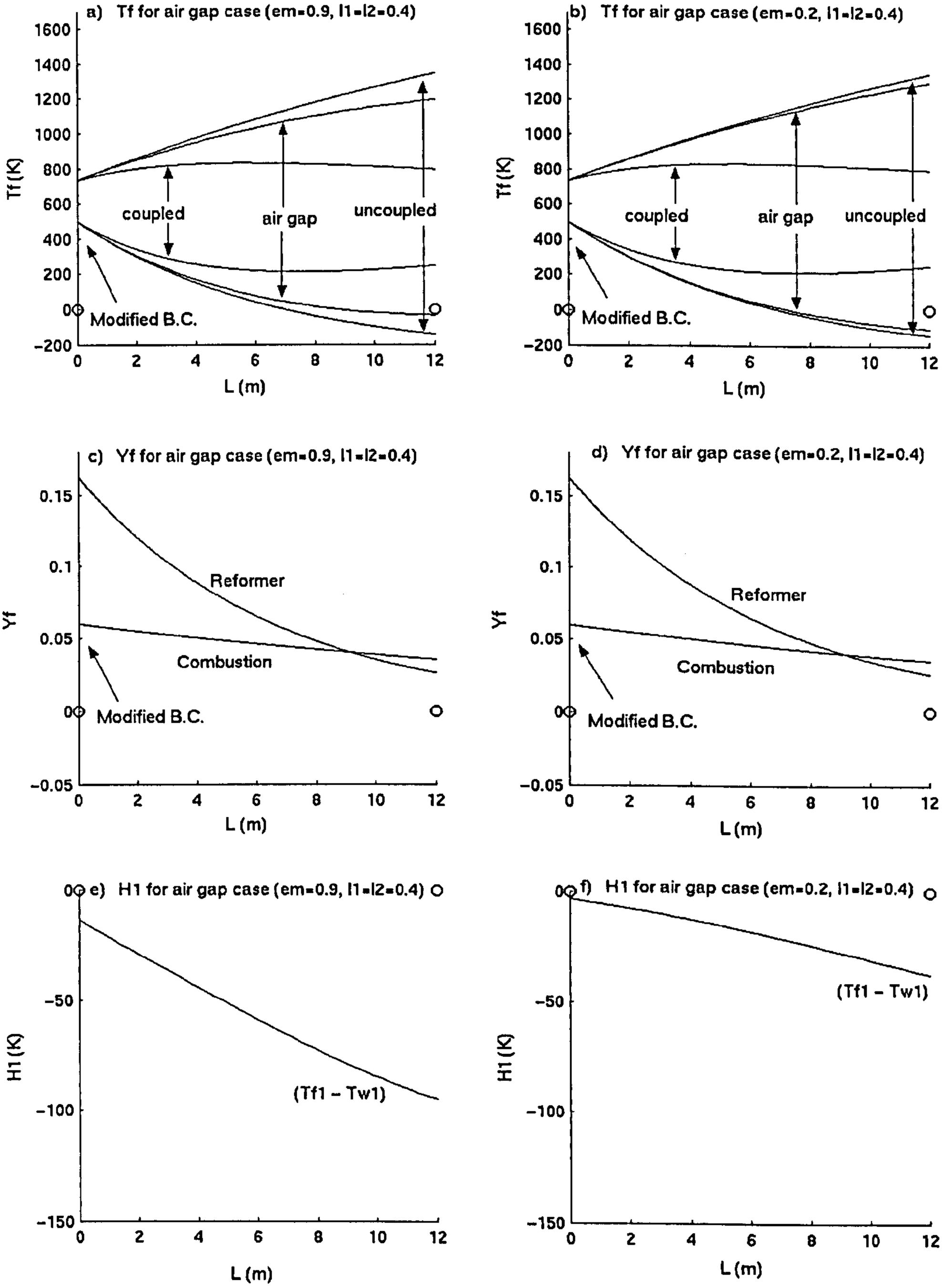

Figure 4.6: Graphs showing the fluid temperature and concentration distributions when $T_f^{(1)}(0)$ and $T_s^{(1)}(0)$ are changed to 500 K and $Y_f^{(2)}(0)$ is changed to 0.06. (Top two graphs: Upper plots = Combustion side, Lower plots = Reformer side.)

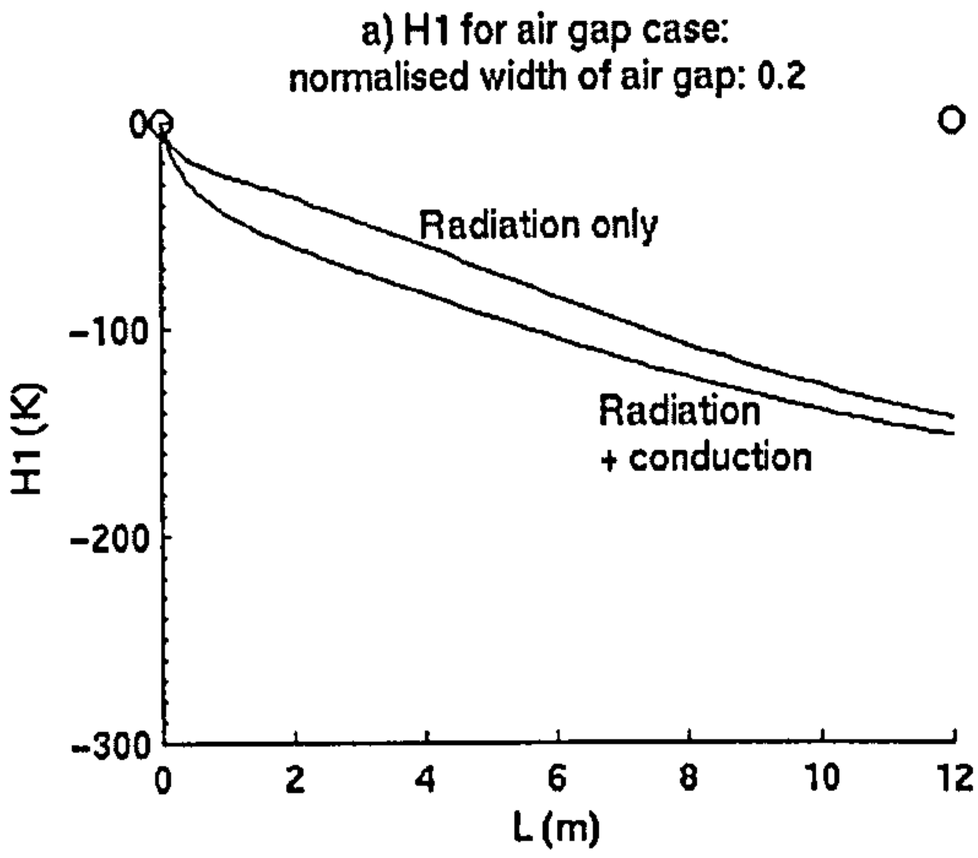

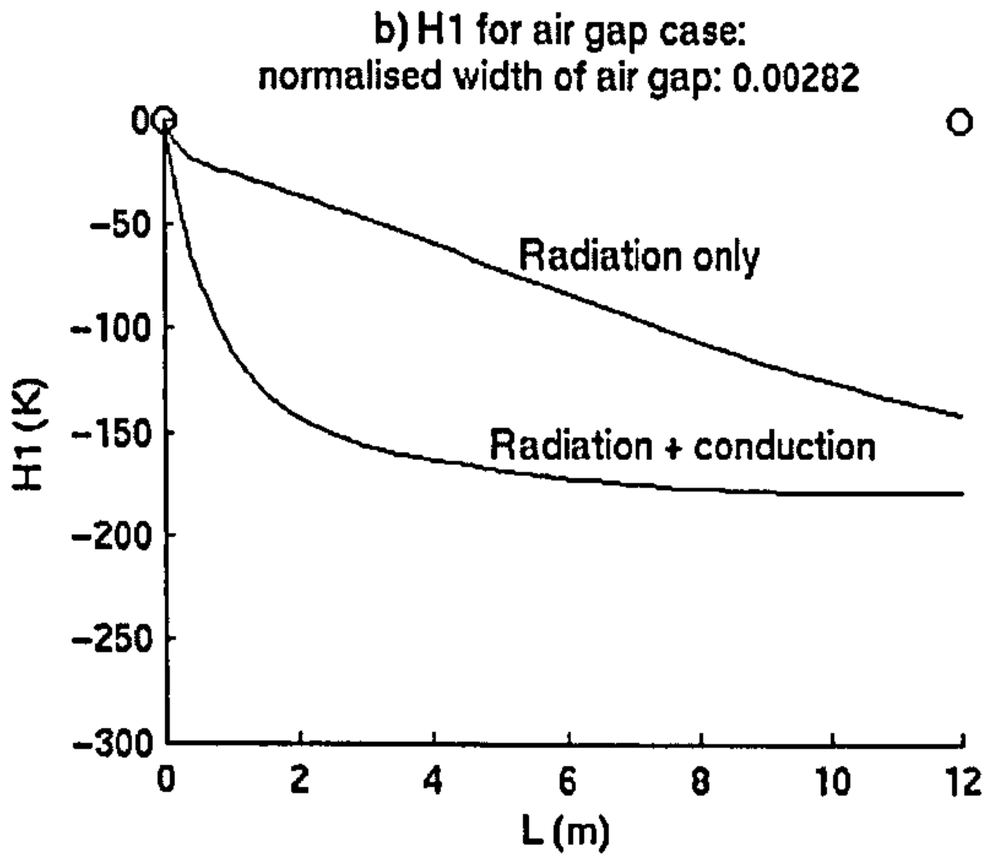

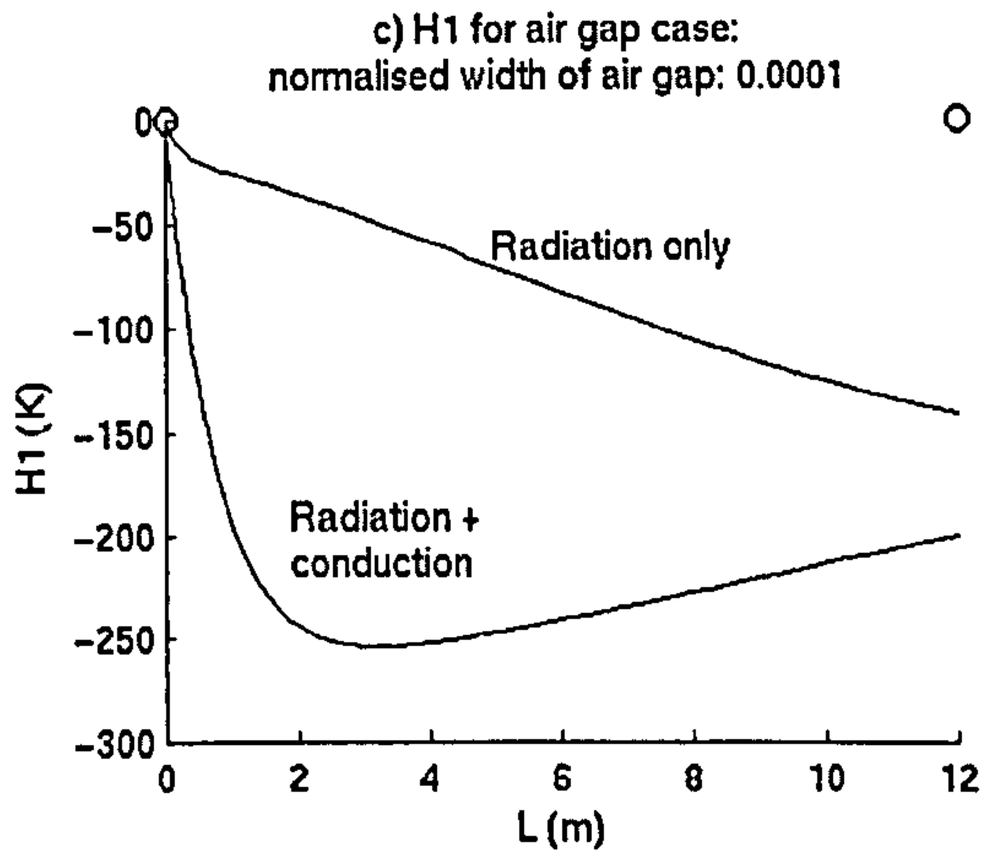

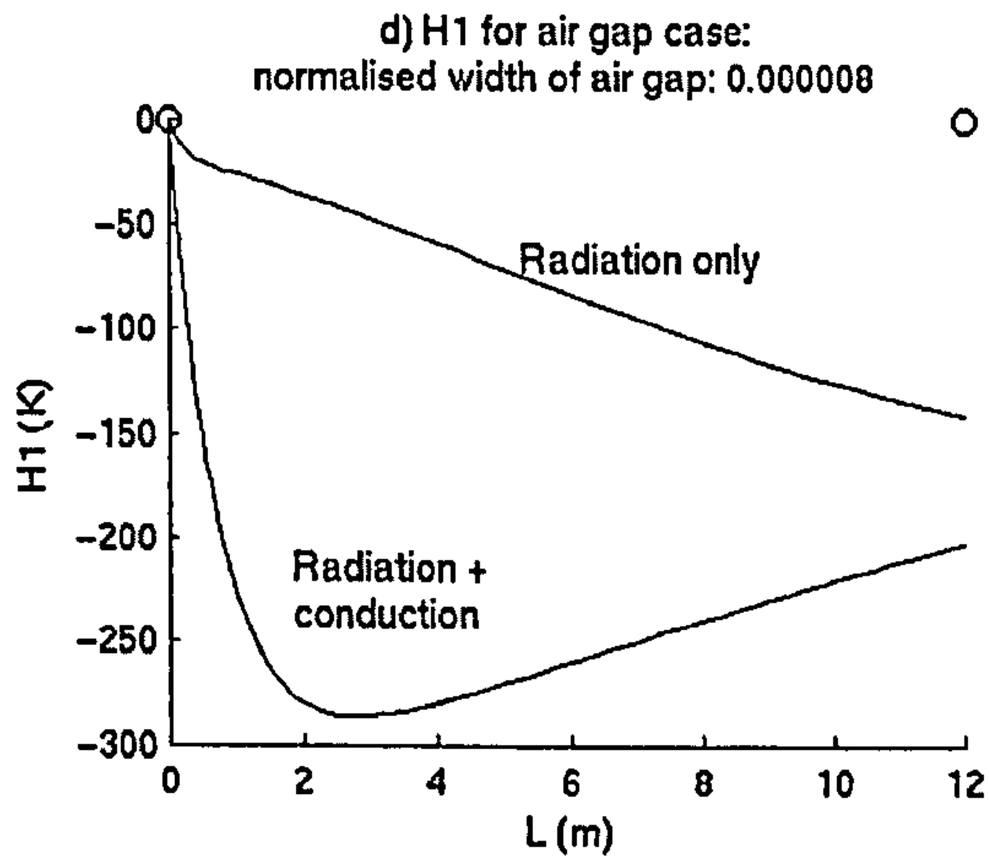

Figure 4.7: Graphs showing the increasing effect on the coupling term of heat transfer by conduction as the width of the air gap approaches zero.

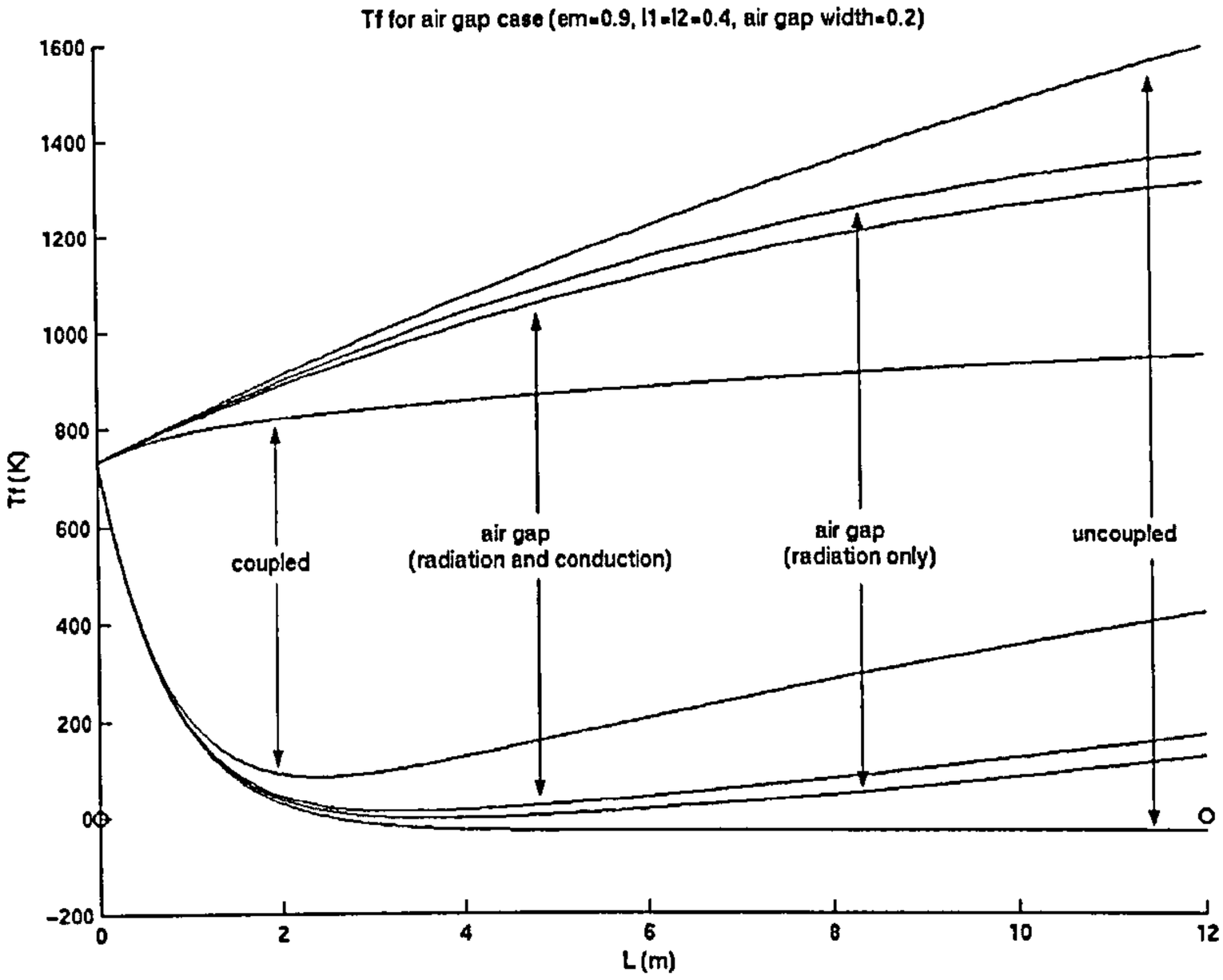

Figure 4.8: Graphs showing the effect of conduction (as well as radiation) on the temperature distribution when the width of the air gap is of the same order of magnitude as the widths of the outer layers of the wall.

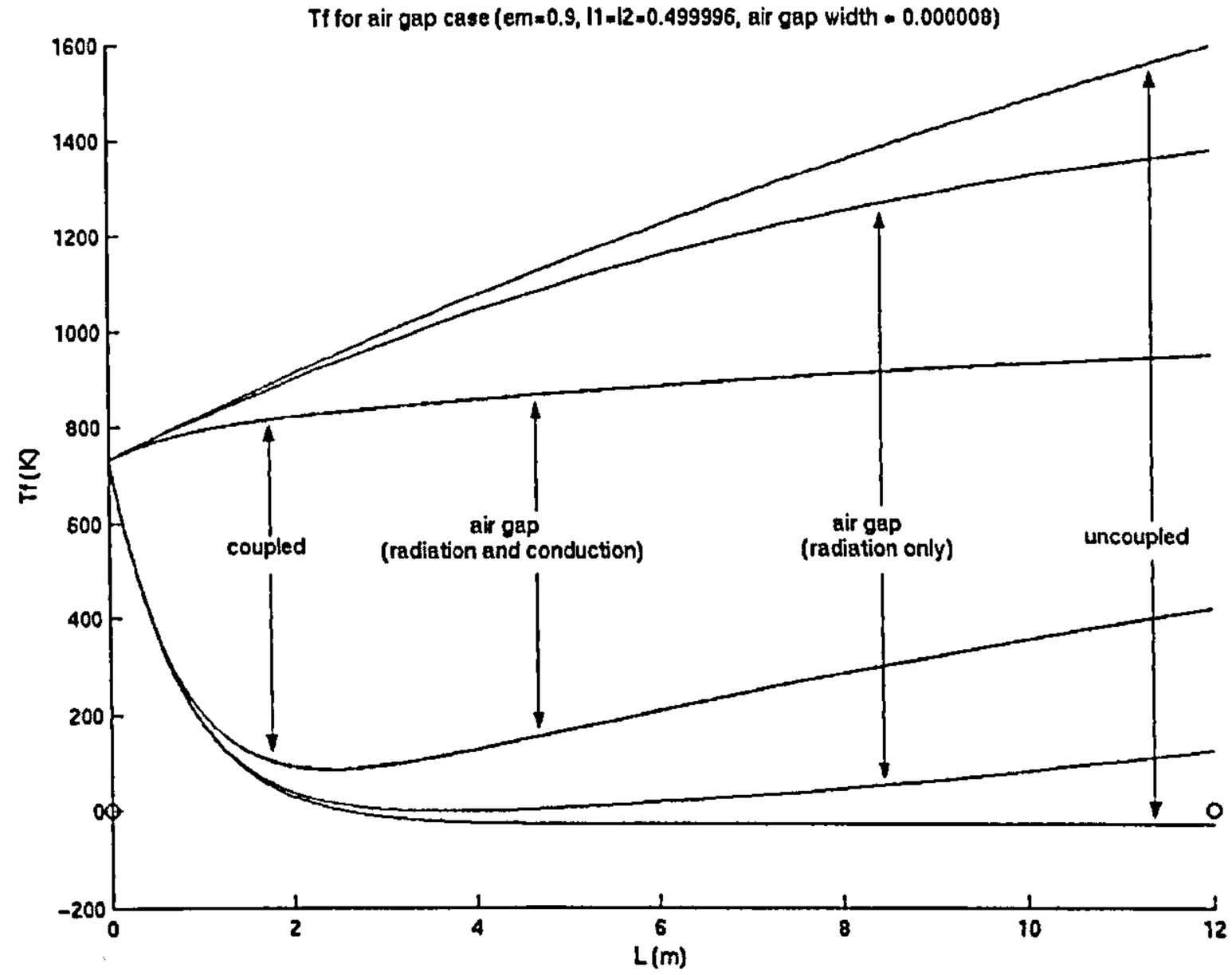

Figure 4.9: Graphs showing the effect of conduction (as well as radiation) on the temperature distribution when the width of the air gap approaches zero.

Chapter 5

Asymptotic analysis of the equations associated with a catalytic reformer

Our nonlinear coupled system of second order differential equations with constant coefficients, first introduced in Chapter 3, where $i = 1, 2$, is given below. This system represents reforming and combustion chemical reactions taking place in a catalytic reformer, where the reaction rate is taken in the Arrhenius form. As before, we pose Dirichlet boundary conditions at the inlet and Neumann boundary conditions at the outlet.

5.1 Full system of equations

Fluid mole balance equations

$$a_3^{(i)} \frac{d^2 Y_f^{(i)}}{dx^2}(x) = a_4^{(i)} \frac{dY_f^{(i)}}{dx}(x) + a_5^{(i)} Y_f^{(i)}(x) \left(1 - \frac{a_1^{(i)}}{a_1^{(i)} + a_2^{(i)} \mathcal{A}^{(i)} e^{\left(\frac{-E^{(i)}}{R_g T_s^{(i)}(x)}\right)}}\right).$$

Solid energy balance equations

$$a_{10}^{(i)}\frac{d^2T_s^{(i)}}{dx^2}(x) = a_8^{(i)}(T_s^{(i)}(x)-T_f^{(i)}(x)) + a_1^{(i)}a_{11}^{(i)}Y_f^{(i)}(x)\left(1-\frac{a_1^{(i)}}{a_1^{(i)}+a_2^{(i)}\mathcal{A}^{(i)}e^{\left(\frac{-E^{(i)}}{R_gT_s^{(i)}(x)}\right)}}\right). \quad (5.1.1)$$

Fluid energy balance equations

$$a_6^{(1)}\frac{d^2T_f^{(1)}}{dx^2}(x) = a_7^{(1)}\frac{dT_f^{(1)}}{dx}(x) - a_8^{(1)}(T_s^{(1)}(x)-T_f^{(1)}(x)) + a_9^{(1)}\left(\frac{\gamma^{(2)}(T_f^{(1)}(x)-T_f^{(2)}(x))}{\gamma^{(1)}+\gamma^{(2)}+\gamma^{(1)}\gamma^{(2)}}\right), \quad (5.1.2)$$

$$a_6^{(2)}\frac{d^2T_f^{(2)}}{dx^2}(x) = a_7^{(2)}\frac{dT_f^{(2)}}{dx}(x) - a_8^{(2)}(T_s^{(2)}(x)-T_f^{(2)}(x)) - a_9^{(2)}\left(\frac{\gamma^{(1)}(T_f^{(1)}(x)-T_f^{(2)}(x))}{\gamma^{(1)}+\gamma^{(2)}+\gamma^{(1)}\gamma^{(2)}}\right), \quad (5.1.3)$$

where

$$\begin{aligned}
a_1^{(1)} &= 2426.51\ \text{mol}/(\text{m}^3\ \text{s}),\quad a_2^{(1)} = 604.70\ \text{kg}_{\text{cat}}/\text{m}^3,\\
a_3^{(1)} &= 0.0053\ \text{m}^2/\text{s},\quad a_4^{(1)} = 2.47\ \text{m/s},\quad a_5^{(1)} = 6.06\ \text{s}^{-1},\\
a_6^{(1)} &= 0.061\ \text{W}/(\text{m K}),\quad a_7^{(1)} = 43515.47\ \text{W}/(\text{m}^2\ \text{K}),\\
a_8^{(1)} &= 76513.19\ \text{W}/(\text{m}^3\ \text{K}),\quad a_9^{(1)} = 6777.22\ \text{W}/(\text{m}^3\ \text{K}),\\
a_{10}^{(1)} &= 0.22\ \text{W}/(\text{m K}),\quad a_{11}^{(1)} = 206000\ \text{J/mol},\quad \gamma^{(1)} = 0.799,\\
\mathcal{A}^{(1)} &= 0.778\ \text{mol}/(\text{kg}_{\text{cat}}\ \text{s}),\quad E^{(1)}/R_g = 4416.65\ \text{K}^{-1},
\end{aligned}$$

$$
\begin{aligned}
a_1^{(2)} &= 2136.21 \text{ mol/(m}^3 \text{ s)}, \quad a_2^{(2)} = 604.70 \text{ kg}_{\text{cat}}/\text{m}^3, \\
a_3^{(2)} &= 0.0048 \text{ m}^2/\text{s}, \quad a_4^{(2)} = 2.24 \text{ m/s}, \quad a_5^{(2)} = 5.34 \text{ s}^{-1}, \\
a_6^{(2)} &= 0.054 \text{ W/(m K)}, \quad a_7^{(2)} = 28700.67 \text{ W/(m}^2 \text{ K)}, \\
a_8^{(2)} &= 68722.95 \text{ W/(m}^3 \text{ K)}, \quad a_9^{(2)} = 7834.57 \text{ W/(m}^3 \text{ K)}, \\
a_{10}^{(2)} &= 0.22 \text{ W/(m K)}, \quad a_{11}^{(2)} = -802000 \text{ J/mol}, \quad \gamma^{(2)} = 0.985, \\
\mathcal{A}^{(2)} &= 0.0794 \text{ mol/(kg}_{\text{cat}} \text{ s)}, \quad E^{(2)}/R_g = 132.31 \text{ K}^{-1},
\end{aligned}
$$

and

$$
a_1^{(i)} = \frac{k_m^{(i)} a_v^{(i)} F_t^{(i)}}{A_c^{(i)} v_x^{(i)}}, \quad a_2^{(i)} = \xi^{(i)} \rho_c^{(i)} (1 - \phi^{(i)}), \quad a_3^{(i)} = D_e^{(i)}, \quad a_4^{(i)} = v_x^{(i)},
$$

$$
a_5^{(i)} = k_m^{(i)} a_v^{(i)}, \quad a_6^{(i)} = k_f^{(i)}, \quad a_7^{(i)} = \rho_f^{(i)} C_p^{(i)} v_x^{(i)}, \quad a_8^{(i)} = h_{fs}^{(i)} a_v^{(i)},
$$

$$
a_9^{(i)} = U_a^{(i)} a_f^{(i)}, \quad a_{10}^{(i)} = k_s^{(i)}, \quad a_{11}^{(i)} = (\Delta H_R^{(i)}), \; i = 1, 2,
$$

with the boundary conditions

$$
\begin{aligned}
& Y_f^{(1)}(0) = 0.163, \; T_f^{(1)}(0) = 733 \text{ K}, \; T_s^{(1)}(0) = 733 \text{ K}, \\
& Y_f^{(2)}(0) = 0.0836, \; T_f^{(2)}(0) = 733 \text{ K}, \; T_s^{(2)}(0) = 733 \text{ K}, \qquad (5.1.4) \\
& \frac{dY_f^{(1)}}{dx}(12) = 0, \quad \frac{dT_f^{(1)}}{dx}(12) = 0, \quad \frac{dT_s^{(1)}}{dx}(12) = 0, \\
& \frac{dY_f^{(2)}}{dx}(12) = 0, \quad \frac{dT_f^{(2)}}{dx}(12) = 0, \quad \frac{dT_s^{(2)}}{dx}(12) = 0.
\end{aligned}
$$

Due to large differences in the magnitudes of the coefficients involved in the above equations, we normalise this system (by dividing each equation by the coefficient which multiplies the second order derivative, and then multiplying each equation by a small parameter δ, where $\delta = 7 \times 10^{-7}$). The normalised system of equations, in terms of δ, has the following form:

Normalised boundary value problem

Fluid mole balance equations

$$\delta \frac{d^2 Y_f^{(1)}}{dx^2}(x) = c_1^{(1)} \frac{dY_f^{(1)}}{dx}(x) + c_2^{(1)} Y_f^{(1)}(x)\zeta_1(x),$$

$$\delta \frac{d^2 Y_f^{(2)}}{dx^2}(x) = c_1^{(2)} \frac{dY_f^{(2)}}{dx}(x) + c_2^{(2)} Y_f^{(2)}(x)\zeta_2(x).$$

Solid energy balance equations

$$\delta \frac{d^2 T_s^{(1)}}{dx^2}(x) = c_{10}^{(1)} (T_s^{(1)}(x) - T_f^{(1)}(x)) + c_{11}^{(1)} Y_f^{(1)}(x)\zeta_1(x),$$

$$\delta \frac{d^2 T_s^{(2)}}{dx^2}(x) = c_{10}^{(2)} (T_s^{(2)}(x) - T_f^{(2)}(x)) - c_{11}^{(2)} Y_f^{(2)}(x)\zeta_2(x).$$

Fluid energy balance equations

$$\delta \frac{d^2 T_f^{(1)}}{dx^2}(x) = c_6^{(1)} \frac{dT_f^{(1)}}{dx}(x) + c_7^{(1)} T_f^{(1)}(x) - c_8^{(1)} T_f^{(2)}(x) - c_9^{(1)} T_s^{(1)}(x),$$

$$\delta \frac{d^2 T_f^{(2)}}{dx^2}(x) = c_6^{(2)} \frac{dT_f^{(2)}}{dx}(x) - c_7^{(2)} T_f^{(1)}(x) + c_8^{(2)} T_f^{(2)}(x) - c_9^{(2)} T_s^{(2)}(x), \quad (5.1.5)$$

where

$$\zeta_1(x) = \left(1 - \frac{c_3^{(1)}}{c_3^{(1)} + c_4^{(1)} e^{-\left(\frac{c_5^{(1)}}{T_s^{(1)}(x)}\right)}}\right),$$

$$\zeta_2(x) = \left(1 - \frac{c_3^{(2)}}{c_3^{(2)} + c_4^{(2)} e^{-\left(\frac{c_5^{(2)}}{T_s^{(2)}(x)}\right)}}\right),$$

and

$$\begin{aligned}
c_1^{(1)} &= 0.0003262264,\ c_2^{(1)} = 0.0008004377,\ c_3^{(1)} = 2426.51,\\
c_4^{(1)} &= 470.4566,\ c_5^{(1)} = 4416.65,\ c_6^{(1)} = 0.4993578525,\\
c_7^{(1)} &= 0.9078157705,\ c_8^{(1)} = 0.0297955574,\ c_9^{(1)} = 0.8780202131,\\
c_{10}^{(1)} &= 0.2434510591,\ c_{11}^{(1)} = 1590.467009, \qquad (5.1.6)\\
c_1^{(2)} &= 0.0003266667,\ c_2^{(2)} = 0.00077875,\ c_3^{(2)} = 2136.21,\\
c_4^{(2)} &= 48.01318,\ c_5^{(2)} = 132.31,\ c_6^{(2)} = 0.3720457222,\\
c_7^{(2)} &= 0.0315618333,\ c_8^{(2)} = 0.9224148889,\ c_9^{(2)} = 0.8908530556,\\
c_{10}^{(2)} &= 0.2186639318,\ c_{11}^{(2)} = 5451.219518,\quad \delta = 0.0000007.
\end{aligned}$$

For the normalised system the boundary conditions (5.1.4) remain unchanged.

In order to solve the above singularly perturbed[1] system of equations (5.1.4) - (5.1.6) analytically, we first look at the linear problem by setting the temperatures in the reaction rates[2] as the temperatures at the inlet, similar to Chapters 2 to 4.

5.2 Singular perturbation - linear case

To solve the linear problem analytically we use a method known in the literature as the compound asymptotic expansions technique (see, for example, [7], [55], [65], [67], [70], [83] and [90]). This method is used to solve singularly perturbed boundary value problems where the solution is written as a series in powers of the small coefficient (in this case δ). First, we solve the problem in the case when this small coefficient is zero. This is known as the limit solution. The next step

[1]By singularly perturbed we mean that small coefficients appear in front of the highest order derivatives.

[2]The reaction rates in the equations are present in the terms $\zeta_1(x)$ and $\zeta_2(x)$ and depend exponentially on the solid temperature.

is to compensate for any discrepancies at the boundaries caused by this limit solution, i.e. we construct boundary layers in the regions where there are rapid changes in the functions. We introduce the following notations

$$\begin{aligned}
\mathbf{Y}^{(1)}(x) &= (Y_f^{(1)}(x),\ Y_f^{(2)}(x),\ T_f^{(1)}(x),\ T_f^{(2)}(x))^T, \\
\mathbf{Y}^{(2)}(x) &= (T_s^{(1)}(x),\ T_s^{(2)}(x))^T.
\end{aligned}$$

Therefore, system (5.1.5) can be written as:

$$\delta \frac{d^2\mathbf{Y}^{(1)}}{dx^2}(x) = D^{(1)}\frac{d\mathbf{Y}^{(1)}}{dx}(x) + D^{(2)}\mathbf{Y}^{(1)}(x) + D^{(3)}\mathbf{Y}^{(2)}(x), \qquad (5.2.7)$$

$$\delta \frac{d^2\mathbf{Y}^{(2)}}{dx^2}(x) = D^{(4)}\mathbf{Y}^{(1)}(x) + D^{(5)}\mathbf{Y}^{(2)}(x), \qquad (5.2.8)$$

where $D^{(i)},\ i = 1, ..., 5$, are all constant matrices of the form:

$$D^{(1)} = \begin{pmatrix} c_1^{(1)} & 0 & 0 & 0 \\ 0 & c_1^{(2)} & 0 & 0 \\ 0 & 0 & c_6^{(1)} & 0 \\ 0 & 0 & 0 & c_6^{(2)} \end{pmatrix}, \quad D^{(2)} = \begin{pmatrix} c_2^{(1)}\zeta_1 & 0 & 0 & 0 \\ 0 & c_2^{(2)}\zeta_2 & 0 & 0 \\ 0 & 0 & c_7^{(1)} & -c_8^{(1)} \\ 0 & 0 & -c_7^{(2)} & c_8^{(2)} \end{pmatrix},$$

$$D^{(3)} = \begin{pmatrix} 0 & 0 \\ 0 & 0 \\ -c_9^{(1)} & 0 \\ 0 & -c_9^{(2)} \end{pmatrix}, \quad D^{(4)} = \begin{pmatrix} c_{11}^{(1)}\zeta_1 & 0 & -c_{10}^{(1)} & 0 \\ 0 & -c_{11}^{(2)}\zeta_2 & 0 & -c_{10}^{(2)} \end{pmatrix},$$

$$D^{(5)} = \begin{pmatrix} c_{10}^{(1)} & 0 \\ 0 & c_{10}^{(2)} \end{pmatrix},$$

and $c_j^{(i)},\ i = 1, 2,\ j = 1, ..., 11$, are given explicitly in (5.1.6).

We now denote by $\mathbf{Z}$ the vector $(\mathbf{Y}(x)^{(1)}, \mathbf{Y}(x)^{(2)})^T$. Using equations (5.2.7) and (5.2.8) we thus obtain the following overall equation for the system:

$$\delta \frac{d^2\mathbf{Z}}{dx^2}(x) = A^{(1)} \frac{d\mathbf{Z}}{dx}(x) + A^{(2)}\mathbf{Z}(x), \tag{5.2.9}$$

where

$$A^{(1)} = \begin{pmatrix} D^{(1)} & 0 \\ 0 & 0 \end{pmatrix},$$

$$A^{(2)} = \begin{pmatrix} D^{(2)} & D^{(3)} \\ D^{(4)} & D^{(5)} \end{pmatrix},$$

and $A^{(1)}, A^{(2)}$ are 6×6 matrices. We assume that the solution of equation (5.2.9) has the form:

$$\mathbf{Z} = \sum_{j=1}^{12} \mathcal{R}_j \mathbf{w}_j e^{\lambda_j x},$$

where λ_j are the eigenvalues of the differential system, $\mathbf{w}_j$ are the corresponding eigenvectors of the differential system, and $\mathcal{R}_j$, $j = 1, ..., 12$, are constants which are determined from the boundary conditions (5.1.4). Substituting this solution into (5.2.9) gives

$$\left[\delta\lambda_j^2 I - \begin{pmatrix} D^{(1)} & 0 \\ 0 & 0 \end{pmatrix}\lambda_j - \begin{pmatrix} D^{(2)} & D^{(3)} \\ D^{(4)} & D^{(5)} \end{pmatrix}\right] \sum_{j=1}^{12} \mathcal{R}_j \mathbf{w}_j e^{\lambda_j x} = 0, \tag{5.2.10}$$

where I is the 6×6 identity matrix. (A detailed explanation of the general solutions of homogeneous linear differential systems with constant coefficients can be found in Section 7.5 of [31].)

We first consider the limit problem by setting $\delta = 0$ in equation (5.2.10). For a non-trivial solution, we find the eigenvalues and eigenvectors of the remaining matrix, that is, we want this matrix to be non-invertible.

5.2.1 Limit problem

Setting $\delta = 0$ in equation (5.2.10) we denote the remaining matrix by $\mathcal{P}$,

$$\mathcal{P} = \begin{pmatrix} -D^{(1)}\tilde{\lambda}_j - D^{(2)} & -D^{(3)} \\ -D^{(4)} & -D^{(5)} \end{pmatrix},$$

where $\tilde{\lambda}_j,\ j = 3, ..., 6$, denotes the eigenvalues of the limit problem of the differential system. Setting the determinant of the above matrix $\mathcal{P}$ equal to zero, we obtain the following:

$$\begin{aligned} 0 &= (c_1^{(1)}\tilde{\lambda}_j + c_2^{(1)}\zeta_1) \times (c_1^{(2)}\tilde{\lambda}_j + c_2^{(2)}\zeta_2) \\ &\times \det \begin{pmatrix} -c_6^{(1)}\tilde{\lambda}_j - c_7^{(1)} & c_8^{(1)} & c_9^{(1)} & 0 \\ c_7^{(2)} & -c_6^{(2)}\tilde{\lambda}_j - c_8^{(2)} & 0 & c_9^{(2)} \\ c_{10}^{(1)} & 0 & -c_{10}^{(1)} & 0 \\ 0 & c_{10}^{(2)} & 0 & -c_{10}^{(2)} \end{pmatrix}, \end{aligned} \tag{5.2.11}$$

which, in turn, gives the following equation for $\tilde{\lambda}_j,\ j = 3, ..., 6$:

$$0 = \tilde{\lambda}_j(c_1^{(1)}\tilde{\lambda}_j + c_2^{(1)}\zeta_1)(c_1^{(2)}\tilde{\lambda}_j + c_2^{(2)}\zeta_2)(C_1\tilde{\lambda}_j + C_2), \tag{5.2.12}$$

where

$$\begin{aligned} C_1 &= c_6^{(1)}c_6^{(2)}, \\ C_2 &= c_6^{(1)}(c_8^{(2)} - c_9^{(2)}) + c_6^{(2)}(c_7^{(1)} - c_9^{(1)}). \end{aligned}$$

From (5.2.12) we obtain the four eigenvalues for the limit problem,

$$\tilde{\lambda}_3 = -\frac{C_2}{C_1} = -0.14450, \quad \tilde{\lambda}_4 = -\frac{c_2^{(2)}\zeta_2}{c_1^{(2)}} = -0.04391,$$

$$\tilde{\lambda}_5 = -\frac{c_2^{(1)}\zeta_1}{c_1^{(1)}} = -0.00115, \quad \tilde{\lambda}_6 = 0.$$

The four corresponding eigenvectors of the system, $\mathbf{w}_j$, $j = 3, ..., 6$, are as follows:

$$\mathbf{w_3} = \begin{pmatrix} 0 \\ 0 \\ \dfrac{c_8^{(1)}}{c_6^{(1)}\tilde{\lambda}_3 + c_7^{(1)} - c_9^{(1)}} \\ 1 \\ \dfrac{c_8^{(1)}}{c_6^{(1)}\tilde{\lambda}_3 + c_7^{(1)} - c_9^{(1)}} \\ 1 \end{pmatrix} = \begin{pmatrix} 0 \\ 0 \\ -0.7033536146 \\ 1 \\ -0.7033536146 \\ 1 \end{pmatrix},$$

$$\mathbf{w_4} = \begin{pmatrix} 0 \\ \dfrac{c_{10}^{(2)}\tilde{\lambda}_4(C_1\tilde{\lambda}_4 + C_2)}{c_8^{(1)}c_9^{(1)}c_{11}^{(2)}\zeta_2} \\ 1 \\ \dfrac{c_6^{(1)}\tilde{\lambda}_4 + c_7^{(1)} - c_9^{(1)}}{c_8^{(1)}} \\ 1 \\ \dfrac{C_1\tilde{\lambda}_4^2 + C_3\tilde{\lambda}_4 + C_4}{c_8^{(1)}c_9^{(2)}} \end{pmatrix} = \begin{pmatrix} 0 \\ -0.0000673279 \\ 1 \\ 0.2641245090 \\ 1 \\ 0.2332100239 \end{pmatrix},$$

$$\mathbf{w_5} = \begin{pmatrix} \dfrac{c_{10}^{(1)}\tilde{\lambda}_5(C_1\tilde{\lambda}_5 + C_2)}{c_9^{(1)}c_{11}^{(1)}c_7^{(2)}\zeta_1} \\ 0 \\ \dfrac{c_6^{(2)}\tilde{\lambda}_5 + c_8^{(2)} - c_9^{(2)}}{c_7^{(2)}} \\ 1 \\ \dfrac{C_1\tilde{\lambda}_5^2 + C_5\tilde{\lambda}_5 + C_6}{c_7^{(2)}c_9^{(1)}} \\ 1 \end{pmatrix} = \begin{pmatrix} 0.0003609175 \\ 0 \\ 0.9864566218 \\ 1 \\ 0.9853524460 \\ 1 \end{pmatrix},$$

$$\mathbf{w}_6 = \begin{pmatrix} 0 \\ 0 \\ \dfrac{c_8^{(1)}}{c_7^{(1)} - c_9^{(1)}} \\ 1 \\ \dfrac{c_8^{(1)}}{c_7^{(1)} - c_9^{(1)}} \\ 1 \end{pmatrix} = \begin{pmatrix} 0 \\ 0 \\ 1 \\ 1 \\ 1 \\ 1 \end{pmatrix},$$

where

$$C_3 = c_6^{(2)}(c_7^{(1)} - c_9^{(1)}) + c_6^{(1)}c_8^{(2)}, \quad C_4 = c_8^{(2)}(c_7^{(1)} - c_9^{(1)}) - c_7^{(2)}c_8^{(1)},$$
$$C_5 = c_6^{(1)}(c_8^{(2)} - c_9^{(2)}) + c_6^{(2)}c_7^{(1)}, \quad C_6 = c_7^{(1)}(c_8^{(2)} - c_9^{(2)}) - c_7^{(2)}c_8^{(1)}.$$

Therefore, the solution of the limit problem is:

$$\mathbf{Z} = \sum_{j=3}^{6} \mathcal{R}_j \mathbf{w}_j e^{\tilde{\lambda}_j x}, \tag{5.2.13}$$

where $\mathbf{w}_j$, $j = 3, ..., 6$, are given above and $\mathcal{R}_j$, $j = 3, ..., 6$, are constants which we determine from the Dirichlet boundary conditions (5.1.4) at the inlet, $x = 0$, for the vector $\mathbf{Z}$. When $\delta = 0$, the system of six differential equations becomes a system of four differential equations and two algebraic equations (which is why we obtain only four eigenvalues for the limit problem):

$$c_1^{(1)} \frac{dY_f^{(1)}}{dx}(x) + c_2^{(1)} Y_f^{(1)}(x)\zeta_1(x) = 0,$$
$$c_1^{(2)} \frac{dY_f^{(2)}}{dx}(x) + c_2^{(2)} Y_f^{(2)}(x)\zeta_2(x) = 0,$$

$$c_6^{(1)} \frac{dT_f^{(1)}}{dx}(x) + c_7^{(1)} T_f^{(1)}(x) - c_8^{(1)} T_f^{(2)}(x) - c_9^{(1)} T_s^{(1)}(x) = 0,$$
$$c_6^{(2)} \frac{dT_f^{(2)}}{dx}(x) - c_7^{(2)} T_f^{(1)}(x) + c_8^{(2)} T_f^{(2)}(x) - c_9^{(2)} T_s^{(2)}(x) = 0,$$

$$c_{10}^{(1)}(T_s^{(1)}(x) - T_f^{(1)}(x)) + c_{11}^{(1)} Y_f^{(1)}(x)\zeta_1(x) = 0, \tag{5.2.14}$$

$$c_{10}^{(2)}(T_s^{(2)}(x) - T_f^{(2)}(x)) - c_{11}^{(2)} Y_f^{(2)}(x)\zeta_2(x) = 0. \tag{5.2.15}$$

Therefore, we satisfy the conditions at the inlet for the first four components of $\mathbf{Z}$: $Y_f^{(1)}$, $Y_f^{(2)}$, $T_f^{(1)}$ and $T_f^{(2)}$, and thus find the constants $\mathcal{R}_3, ..., \mathcal{R}_6$. Using the eigenvectors above along with the inlet conditions in (5.1.4) we deduce that

$$\begin{aligned} \mathcal{R}_3 &= -540.01838, \quad \mathcal{R}_4 = -1241.68521, \\ \mathcal{R}_5 &= 451.62672, \quad \mathcal{R}_6 = 1149.35116. \end{aligned} \tag{5.2.16}$$

By substituting $Y_f^{(i)}(0), T_f^{(i)}(0)$, $i = 1, 2$ into equations (5.2.14) and (5.2.15) we find that,

$$T_s^{(1)}(0) = 732.50132 \text{ K}, \quad T_s^{(2)}(0) = 771.38606 \text{ K}. \tag{5.2.17}$$

This implies that there is a boundary layer region near the inlet since the original conditions, $T_s^{(i)}(0) = 733$ K, i $= 1, 2$, are not satisfied. In order to find these boundary layers we look at the full linear system, (5.2.9) and (5.2.10), when δ has the finite value 7×10^{-7} and we denote by $\mathcal{Q}$ the full matrix.

5.2.2 Boundary layer at the inlet

When δ is finite, we consider the full problem given in (5.2.10). To obtain a non-trivial solution we have

$$\det \mathcal{Q} = \det \begin{pmatrix} \delta\lambda_j^2 - D^{(1)}\lambda_j - D^{(2)} & -D^{(3)} \\ -D^{(4)} & \delta\lambda_j^2 - D^{(5)} \end{pmatrix} = 0. \tag{5.2.18}$$

Equation (5.2.18) gives the following (compare with (5.2.11) for the limit case):

$$\begin{aligned} 0 &= (\delta\lambda_j^2 - c_1^{(1)}\lambda_j - c_2^{(1)}\zeta_1) \times (\delta\lambda_j^2 - c_1^{(2)}\lambda_j - c_2^{(2)}\zeta_2) \\ &\times \det \begin{pmatrix} \delta\lambda_j^2 - c_6^{(1)}\lambda_j - c_7^{(1)} & c_8^{(1)} & c_9^{(1)} & 0 \\ c_7^{(2)} & \delta\lambda_j^2 - c_6^{(2)}\lambda_j - c_8^{(2)} & 0 & c_9^{(2)} \\ c_{10}^{(1)} & 0 & \delta\lambda_j^2 - c_{10}^{(1)} & 0 \\ 0 & c_{10}^{(2)} & 0 & \delta\lambda_j^2 - c_{10}^{(2)} \end{pmatrix}. \end{aligned}$$

This gives twelve eigenvalues $\lambda_j,\ j = 1, ..., 12$, of the differential system. Four of these eigenvalues are the roots of quadratic polynomials (the first two factors of the right hand side of the above equation):

$$\lambda_4 = \frac{c_1^{(2)} - \sqrt{(c_1^{(2)})^2 + 4\delta c_2^{(2)}\zeta_2}}{2\delta} = -0.0439039012,$$

$$\lambda_5 = \frac{c_1^{(1)} - \sqrt{(c_1^{(1)})^2 + 4\delta c_2^{(1)}\zeta_1}}{2\delta} = -0.0011489254, \qquad (5.2.19)$$

$$\lambda_7 = \frac{c_1^{(1)} + \sqrt{(c_1^{(1)})^2 + 4\delta c_2^{(1)}\zeta_1}}{2\delta} = 466.0388848,$$

$$\lambda_8 = \frac{c_1^{(2)} + \sqrt{(c_1^{(2)})^2 + 4\delta c_2^{(2)}\zeta_2}}{2\delta} = 466.7105706,$$

and the other eight are the roots of the following polynomial

$$\lambda(\mathcal{C}_7\lambda^7 + \mathcal{C}_8\lambda^6 + \mathcal{C}_9\lambda^5 + \mathcal{C}_{10}\lambda^4 + \mathcal{C}_{11}\lambda^3 + \mathcal{C}_{12}\lambda^2 + \mathcal{C}_{13}\lambda + \mathcal{C}_{14}) = 0, \qquad (5.2.20)$$

where

$$\mathcal{C}_7 = \delta^4, \quad \mathcal{C}_8 = -\delta^3(c_6^{(1)} + c_6^{(2)}),$$
$$\mathcal{C}_9 = (c_6^{(1)}c_6^{(2)} - \delta(c_8^{(2)} + c_{10}^{(2)} + c_7^{(1)} + c_{10}^{(1)})\delta^2,$$

$$\begin{aligned}
\mathcal{C}_{10} &= (c_6^{(2)}c_{10}^{(2)} + c_6^{(1)}c_8^{(2)} + c_6^{(1)}c_{10}^{(2)} + c_7^{(1)}c_6^{(2)} + c_6^{(1)}c_{10}^{(1)} + c_6^{(2)}c_{10}^{(1)})\delta^2, \\
\mathcal{C}_{11} &= ((c_8^{(2)}c_{10}^{(2)} - c_9^{(1)}c_{10}^{(1)} - c_9^{(2)}c_{10}^{(2)} + c_7^{(1)}c_8^{(2)} + c_7^{(1)}c_{10}^{(2)} - c_8^{(1)}c_7^{(2)} + c_8^{(2)}c_{10}^{(1)} \\
&\quad + c_{10}^{(1)}c_{10}^{(2)} + c_{10}^{(1)}c_7^{(1)})\delta - c_6^{(1)}c_6^{(2)}c_{10}^{(2)} - c_6^{(1)}c_6^{(2)}c_{10}^{(1)})\delta, \\
\mathcal{C}_{12} &= (c_6^{(2)}c_9^{(1)}c_{10}^{(1)} + c_6^{(1)}c_9^{(2)}c_{10}^{(2)} - c_6^{(1)}c_8^{(2)}c_{10}^{(2)} - c_6^{(1)}c_8^{(2)}c_{10}^{(1)} - c_7^{(1)}c_6^{(2)}c_{10}^{(2)} \\
&\quad - c_7^{(1)}c_6^{(2)}c_{10}^{(1)} - c_6^{(1)}c_{10}^{(1)}c_{10}^{(2)} - c_6^{(2)}c_{10}^{(1)}c_{10}^{(2)})\delta,
\end{aligned}$$

$$
\begin{aligned}
C_{13} &= (c_9^{(1)}c_{10}^{(1)}c_8^{(2)} + c_9^{(1)}c_{10}^{(1)}c_{10}^{(2)} - c_7^{(1)}c_8^{(2)}c_{10}^{(2)} + c_7^{(1)}c_9^{(2)}c_{10}^{(2)} + c_7^{(2)}c_8^{(1)}c_{10}^{(2)} \\
&\quad - c_8^{(2)}c_{10}^{(1)}c_{10}^{(2)} + c_9^{(2)}c_{10}^{(1)}c_{10}^{(2)} - c_7^{(1)}c_8^{(2)}c_{10}^{(1)} - c_7^{(1)}c_{10}^{(1)}c_{10}^{(2)} + c_7^{(2)}c_8^{(1)}c_{10}^{(1)})\delta \\
&\quad + c_6^{(1)}c_6^{(2)}c_{10}^{(1)}c_{10}^{(2)} \\
C_{14} &= (c_6^{(1)}c_8^{(2)} - c_6^{(2)}c_9^{(1)} - c_6^{(1)}c_9^{(2)} + c_6^{(2)}c_7^{(1)})c_{10}^{(1)}c_{10}^{(2)}.
\end{aligned}
$$

Solving equation (5.2.20) numerically we obtain

$$
\begin{aligned}
\lambda_1 &= -590.61404, \quad \lambda_2 = -560.10445, \\
\lambda_3 &= -0.14450, \quad \lambda_6 = 0, \\
\lambda_9 &= 557.70998, \quad \lambda_{10} = 588.85575, \\
\lambda_{11} &= 531496.3682, \quad \lambda_{12} = 713370.1786.
\end{aligned} \tag{5.2.21}
$$

We note that the eigenvalues of the limit problem, $\tilde{\lambda}_j,\ j = 3, ..., 6$, (see Section 5.2.1) are similar to the eigenvalues $\lambda_j,\ j = 3, ..., 6$, of the full system (the system generated from matrix $\mathcal{Q}$ above) as expected. The first two eigenvalues, λ_1 and λ_2, are large and negative suggesting that these eigenvalues are associated with boundary layers at the inlet since they represent a solution that decays as x increases. The corresponding eigenvectors $\mathbf{w}_1$ and $\mathbf{w}_2$ are

$$
\mathbf{w}_1 = \begin{pmatrix} 0 \\ 0 \\ -0.0029837828 \\ 0.0000004454 \\ 1 \\ -0.0000038176 \end{pmatrix}, \quad \mathbf{w}_2 = \begin{pmatrix} 0 \\ 0 \\ 0.0000004438 \\ -0.0042895127 \\ 0.0001458757 \\ 1 \end{pmatrix}.
$$

From $\mathbf{w}_1,\ \mathbf{w}_2$ and (5.2.17) we find the constants $\mathcal{R}_1$ and $\mathcal{R}_2$, that is,

$$
\mathcal{R}_1 = 0.5042748792, \quad \mathcal{R}_2 = -38.38605704.
$$

Therefore, the boundary layer

$$
\mathcal{R}_1\mathbf{w}_1 e^{\lambda_1 x} + \mathcal{R}_2\mathbf{w}_2 e^{\lambda_2 x}
$$

compensates for the discrepancies in the boundary conditions at the inlet for the functions $T_s^{(1)}$ and $T_s^{(2)}$. (We note that there are other terms in the vectors $\mathbf{w}_1$ and $\mathbf{w}_2$ above but, when multiplied by $\mathcal{R}_1$ and $\mathcal{R}_2$ respectively, they only result in a small insignificant error in the other four boundary conditions.) The solution so far, which satisfies all the equations and the boundary conditions at the inlet, has the form

$$\mathbf{Z} = \underbrace{\sum_{j=3}^{6} \mathcal{R}_j \mathbf{w}_j e^{\tilde{\lambda}_j x}}_{\text{Limit solution}} + \underbrace{\sum_{j=1}^{2} \mathcal{R}_j \mathbf{w}_j e^{\lambda_j x}}_{\text{Boundary layer at the inlet}} \tag{5.2.22}$$

5.2.3 Boundary layer at the outlet

Differentiating (5.2.22) and evaluating its components at the outlet of the channel, $x = 12$, gives the following non-zero values

$$\frac{d\mathbf{Z}}{dx}(12) = \begin{pmatrix} -0.0001847110 \\ -0.0021673151 \\ 21.99433120 \\ 21.76919076 \\ 21.99489708 \\ 20.77403902 \end{pmatrix}.$$

This shows that solution (5.2.22) produces discrepancies in all boundary conditions at the outlet, where we want zero flux in all functions. To compensate for these discrepancies we use the eigenvectors corresponding to the eigenvalues λ_7,..., λ_{12}, in (5.2.19) and (5.2.21) to form a boundary layer for $\mathbf{Z}$ at the outlet. The eigenvalues $\lambda_7, ..., \lambda_{12}$ are large and positive, and therefore, they contribute to a decaying boundary layer near the outlet, which is represented in the form:

$$\text{Boundary Layer at the outlet} = \sum_{j=7}^{12} \hat{\mathcal{R}}_j \mathbf{w}_j e^{\lambda_j (x-12)}. \tag{5.2.23}$$

This boundary layer solution decays as x moves away from the outlet. The eigenvectors for the large positive eigenvalues have the following form

$$\mathbf{w}_7 = \begin{pmatrix} 0.2242192966 \\ 0 \\ 1 \\ -0.0145476210 \\ 0.8363006046 \\ -0.0477423151 \end{pmatrix}, \quad \mathbf{w}_8 = \begin{pmatrix} 0 \\ 0.0006481304 \\ 0.0000006575 \\ 0.0051078795 \\ 0.1759499685 \\ 1 \end{pmatrix},$$

$$\mathbf{w}_9 = \begin{pmatrix} 0 \\ 0 \\ 0.0000004707 \\ 0.0042788681 \\ 0.0000044545 \\ 1 \end{pmatrix}, \quad \mathbf{w}_{10} = \begin{pmatrix} 0 \\ 0 \\ 0.0029792197 \\ 0.0000004127 \\ 1 \\ -0.0000037502 \end{pmatrix},$$

$$\mathbf{w}_{11} = \begin{pmatrix} 0 \\ 0 \\ 0.0000004403 \\ 1 \\ 0 \\ -0.0000011058 \end{pmatrix}, \quad \mathbf{w}_{12} = \begin{pmatrix} 0 \\ 0 \\ 1 \\ -0.0000003475 \\ -0.0000006834 \\ 0 \end{pmatrix}.$$

Differentiating the sum of (5.2.22) and (5.2.23) and setting each derivative equal to zero at $x = 12$ gives the following values for the constants $\mathcal{R}_7, ..., \mathcal{R}_{12}$:

$$\mathcal{R}_7 = 0.0000017677, \quad \mathcal{R}_8 = 0.0071649313,$$

$$\mathcal{R}_9 = -0.0432447976, \quad \mathcal{R}_{10} = -0.0373573516,$$

$$\mathcal{R}_{11} = -0.0000407963, \quad \mathcal{R}_{12} = -0.0000307408.$$

The overall analytical solution for the singularly perturbed problem given by (5.2.10) is thus of the form:

$$\mathbf{Z} = \underbrace{\sum_{j=3}^{6} \mathcal{R}_j \mathbf{w}_j e^{\tilde{\lambda}_j x}}_{\text{Limit solution}} + \underbrace{\sum_{j=1}^{2} \mathcal{R}_j \mathbf{w}_j e^{\lambda_j x}}_{\text{Boundary layer at the inlet}} + \underbrace{\sum_{j=7}^{12} \hat{\mathcal{R}}_j \mathbf{w}_j e^{\lambda_j (x-12)}}_{\text{Boundary layer at the outlet}}. \quad (5.2.24)$$

5.3 Results and discussion

Figures 5.1 - 5.13 show the distributions of temperatures and concentrations along the two channels for the linear model. For each case, we present two graphs: the first shows the distribution for the limit case (described by (5.2.13)) and the second shows the distribution for the solution that includes the boundary layers (as described in (5.2.24)). We note that, in each case, the two figures are almost identical and this is due to the fact that the boundary layers are only associated with small regions close to the ends. For the fluid temperature given in Figures 5.1 - 5.4, the boundary layer lies near the outlet of the channels only. Figures 5.3 and 5.4 are presented to show how these temperatures behave in a magnified region near the outlet. Figures 5.5 - 5.9 show how the solid temperature changes along the channels. Since there are boundary layers at both the inlet and the outlet for this case, in both the reformer side and the combustion side, Figures 5.7 - 5.9 are presented to show the behaviour in magnified regions near both ends. Figures 5.10 - 5.13 show the distribution of the fluid concentration. The boundary layer in this case only appears at the outlet and compensates for only a small error in the limit case; this is shown by the fact that, in order to see the change in the concentrations at the outlet, we need to use a small range for the vertical axes, see Figures 5.12 and 5.13.

The analysis in the first three sections of this chapter shows why the graphical

results for the industrial examples given in Chapters 3 and 4 do not appear to satisfy the zero flux condition at the outlet. (The same would have applied for the Dirichlet conditions at the inlet in the graphs for the solid temperature distribution had they been presented.) From the numerical package (in this case we used Femlab) we obtained the limit solution - the solution in the middle region of the channel. The numerical package does not, however, construct the boundary layers in the regions where the functions vary rapidly. Also, numerical packages had difficulties solving this nonlinear problem. Therefore in the following sections of this chapter we consider an asymptotic approximation for the solution of the nonlinear problem, following a similar method to the sections above for the main part of the channel.

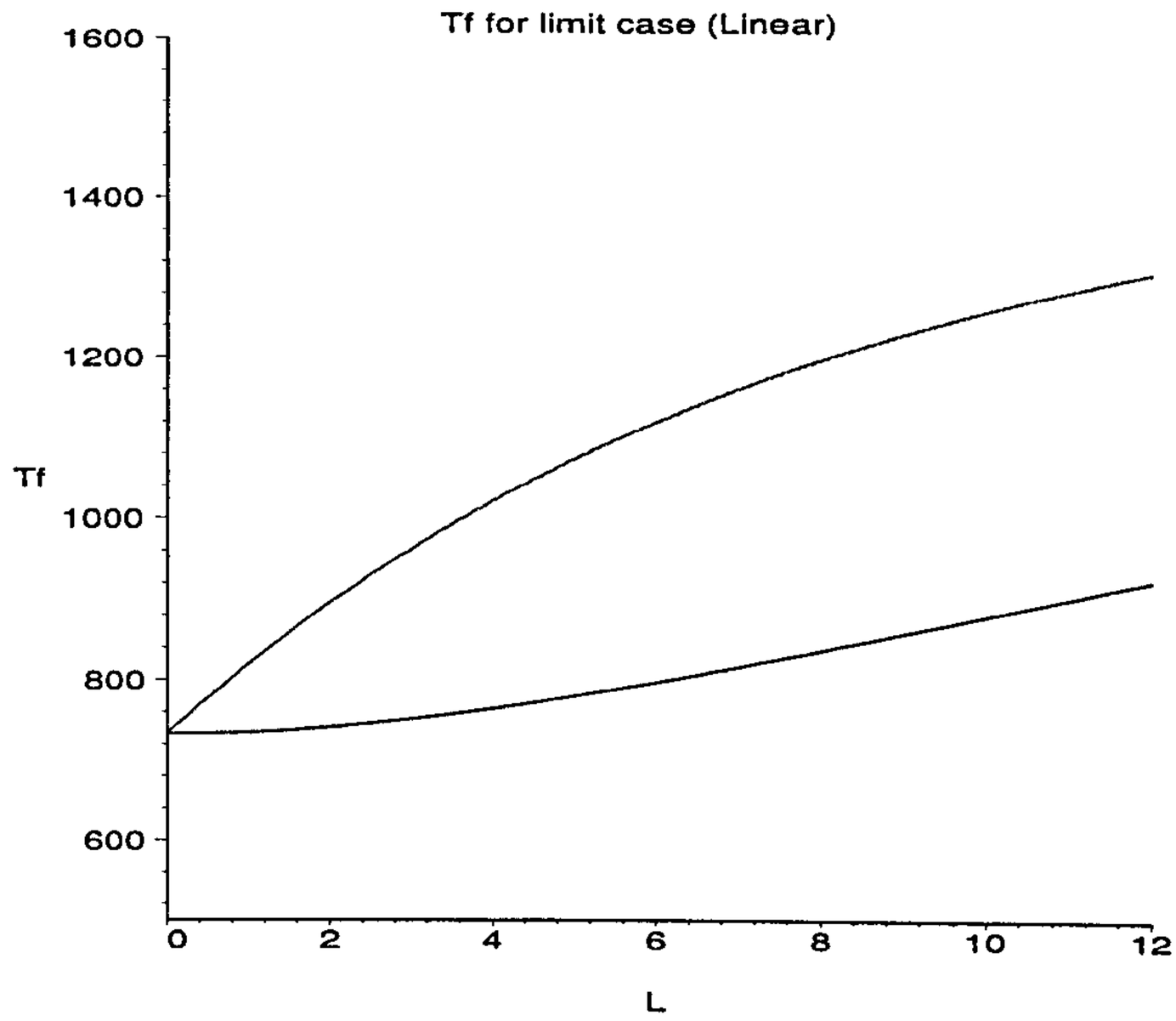

Figure 5.1: Limit problem for the temperature of the fluid in both channels (see (5.2.13)). Upper plot = Combustion side, Lower plot = Reformer side.

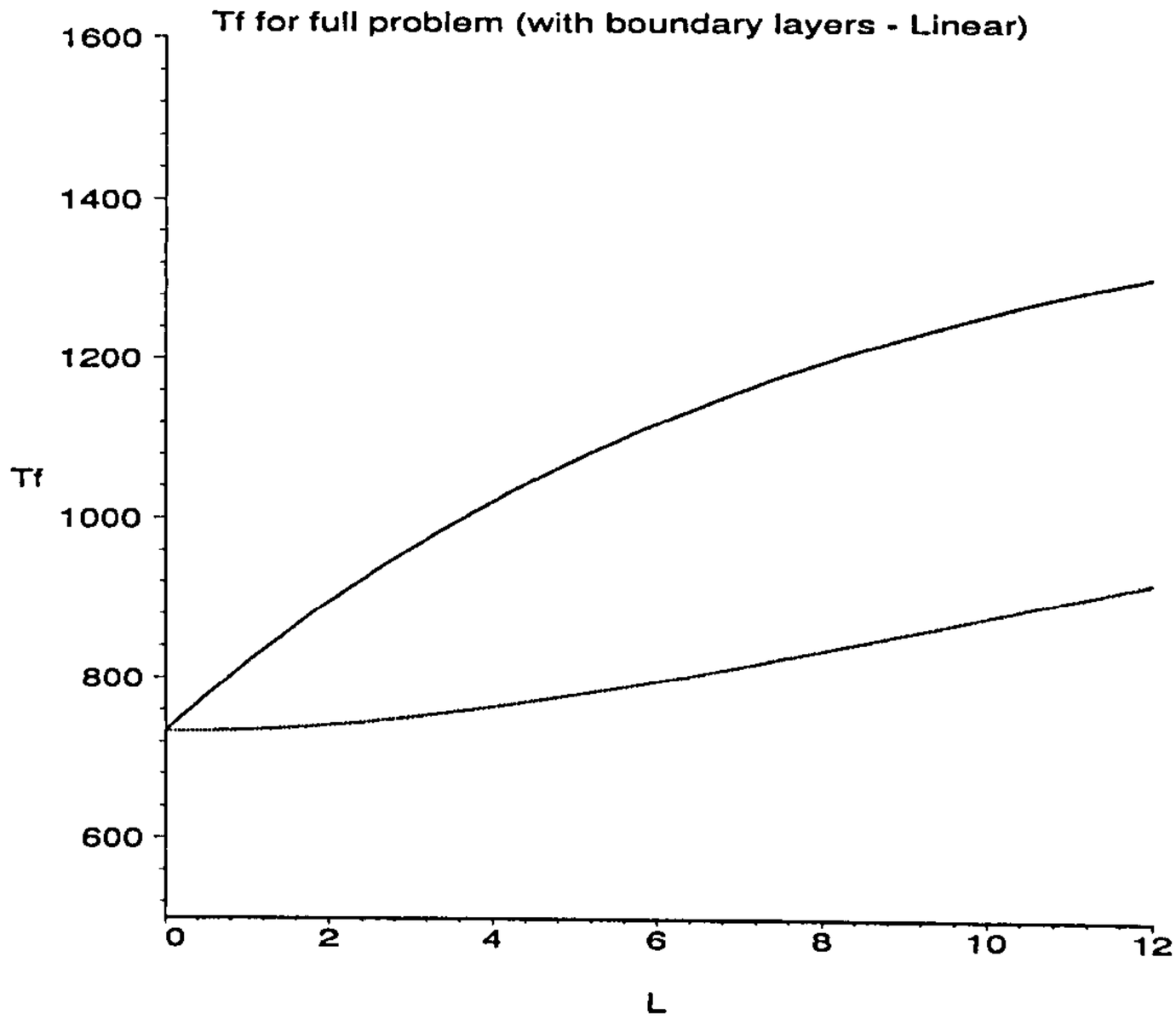

Figure 5.2: Full problem (with boundary layers) for the temperature of the fluid in both channels (see (5.2.24)). Upper plot = Combustion side, Lower plot = Reformer side.

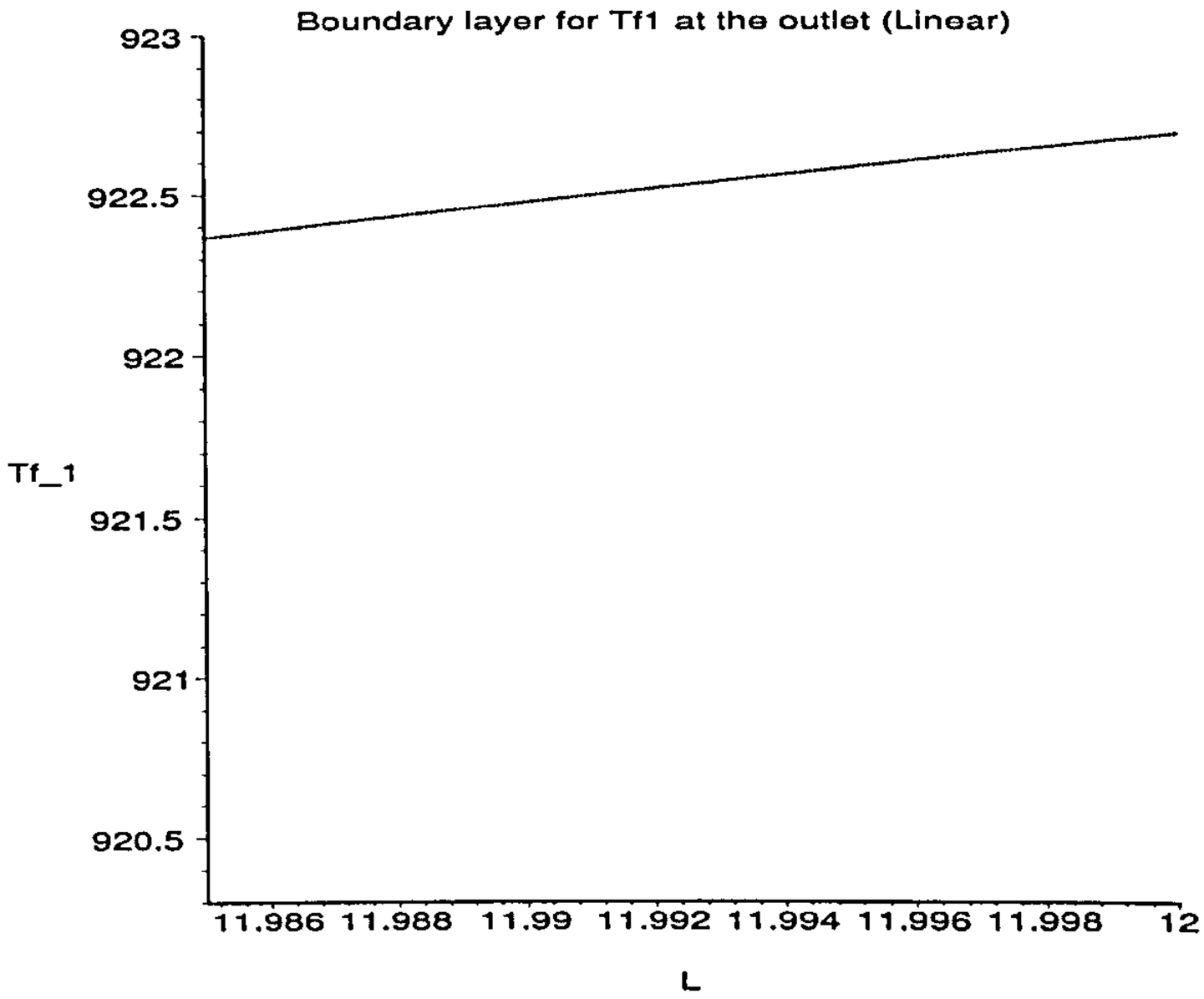

Figure 5.3: Boundary layer for the fluid temperature at the outlet of the reformer channel.

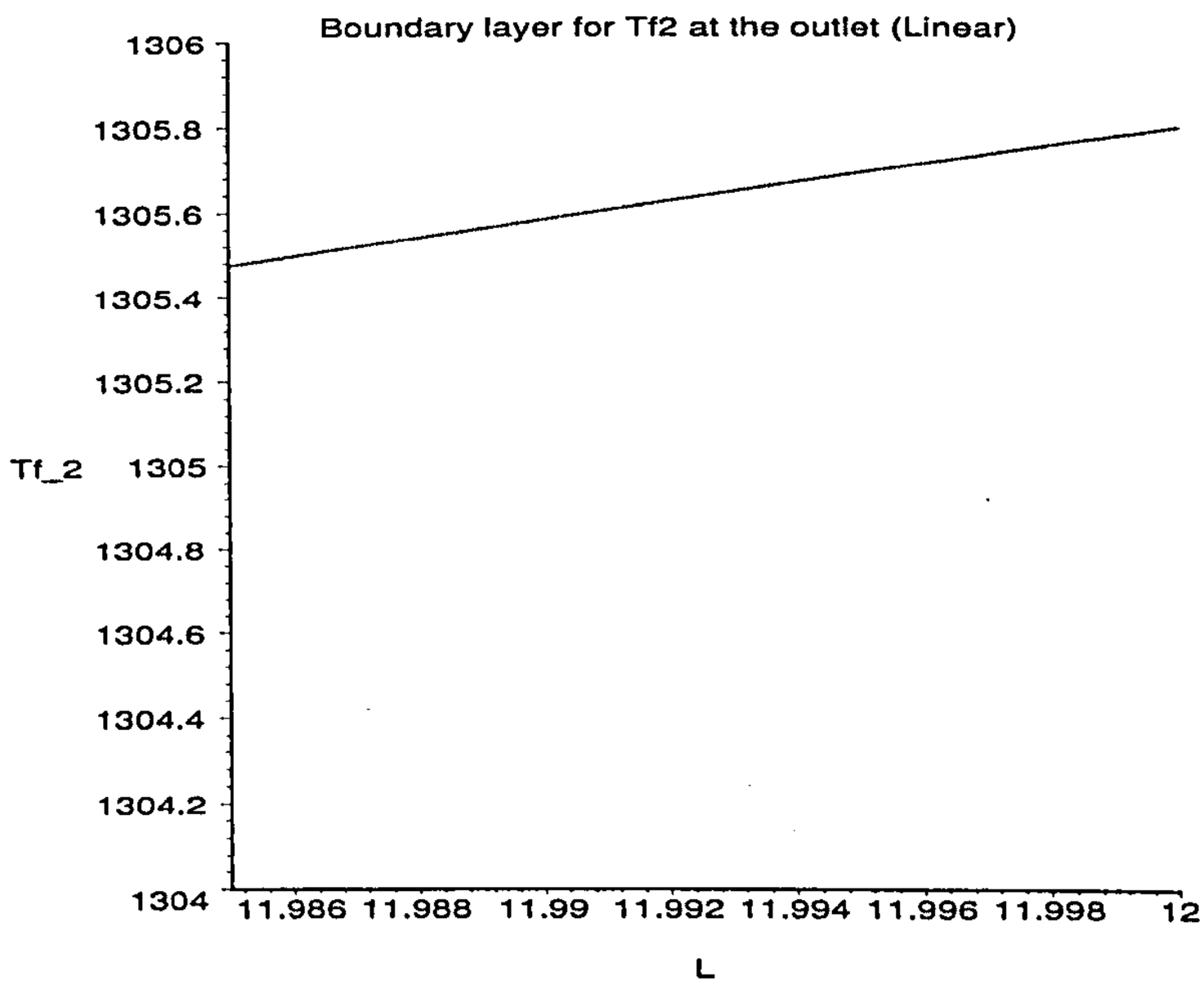

Figure 5.4: Boundary layer for the fluid temperature at the outlet of the combustion channel.

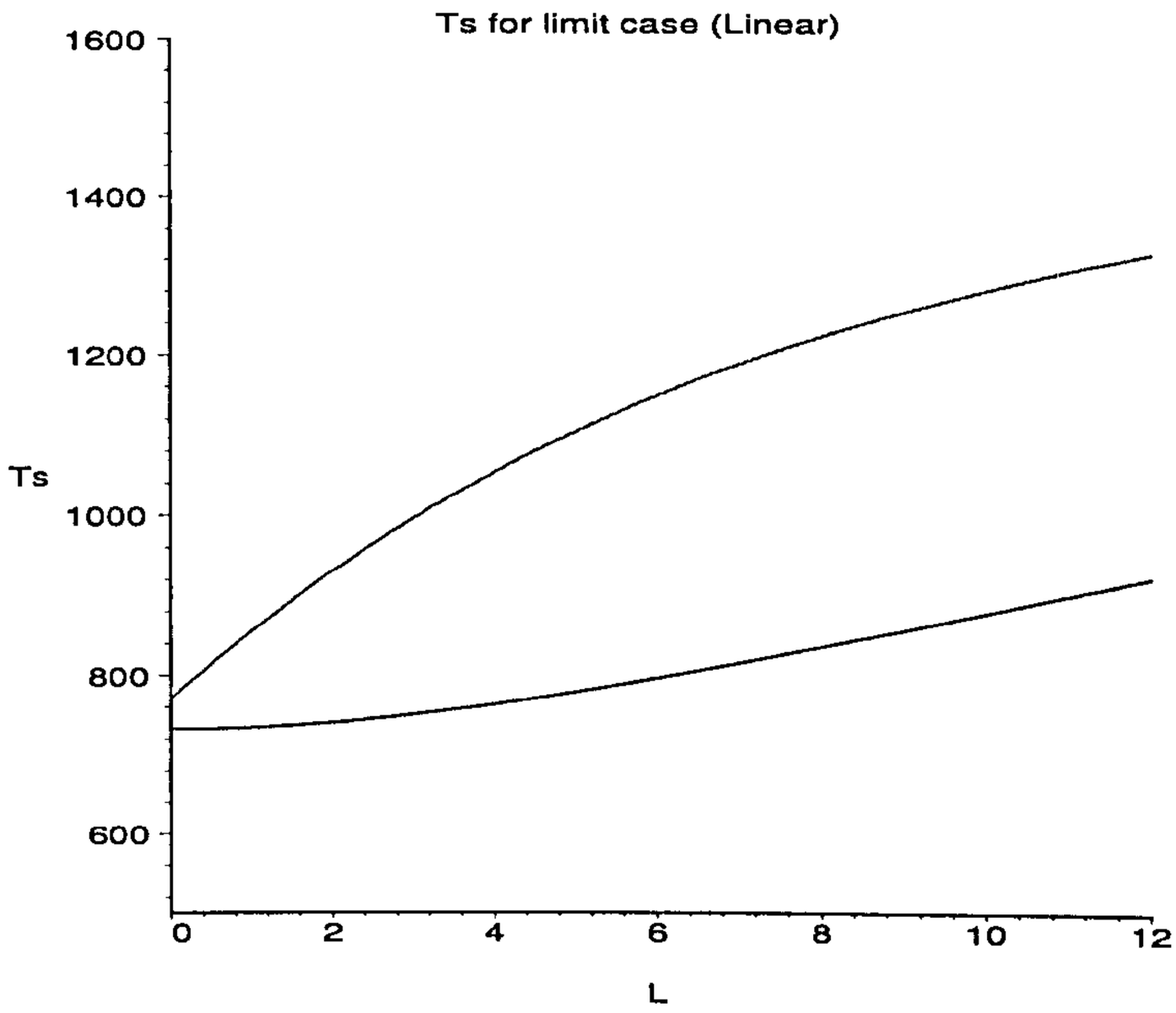

Figure 5.5: Limit problem for the temperature of the solid in both channels (see (5.2.13)). Upper plot = Combustion side, Lower plot = Reformer side.

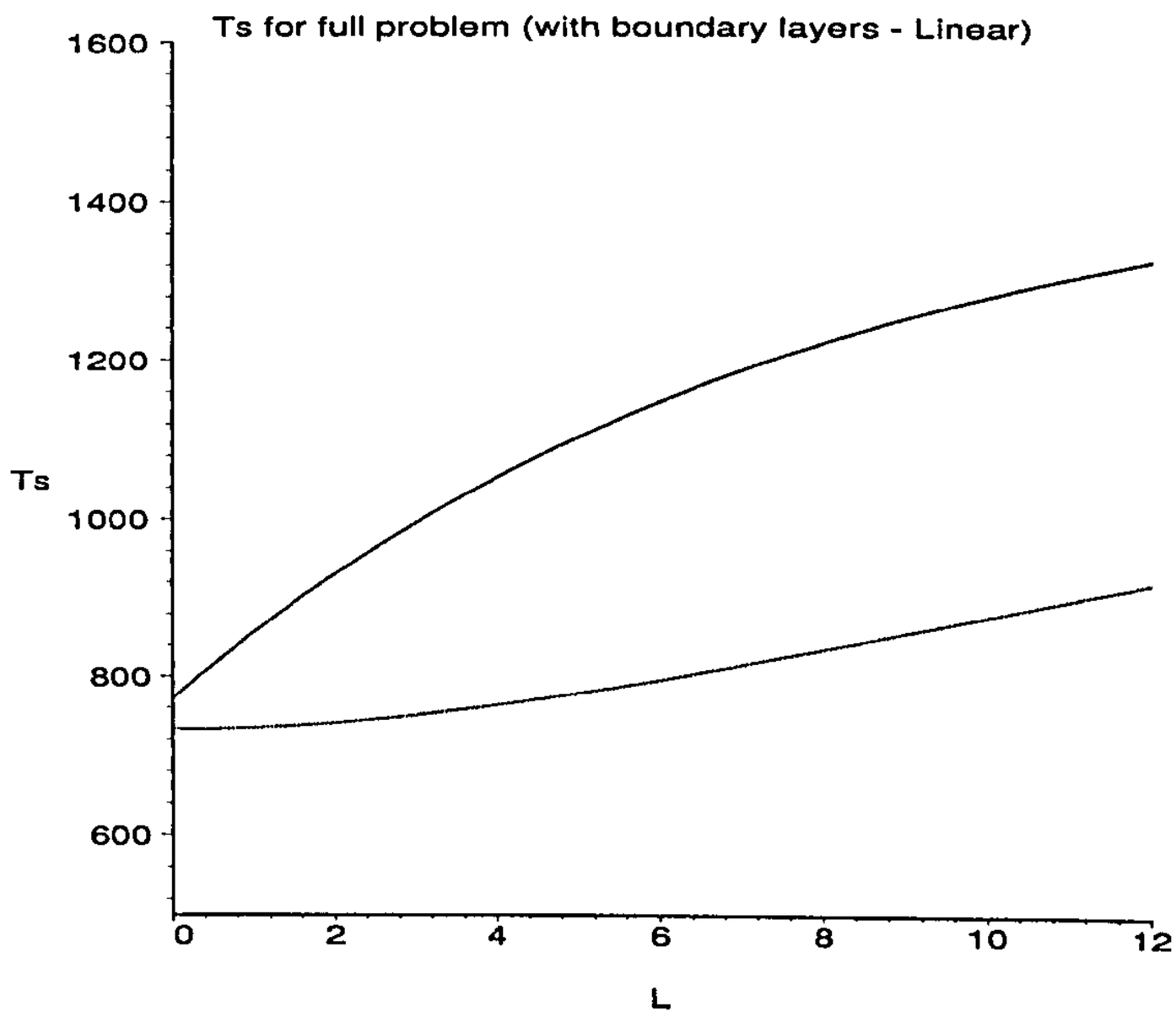

Figure 5.6: Full problem (with boundary layers) for the temperature of the solid in both channels (see (5.2.24)). Upper plot = Combustion side, Lower plot = Reformer side.

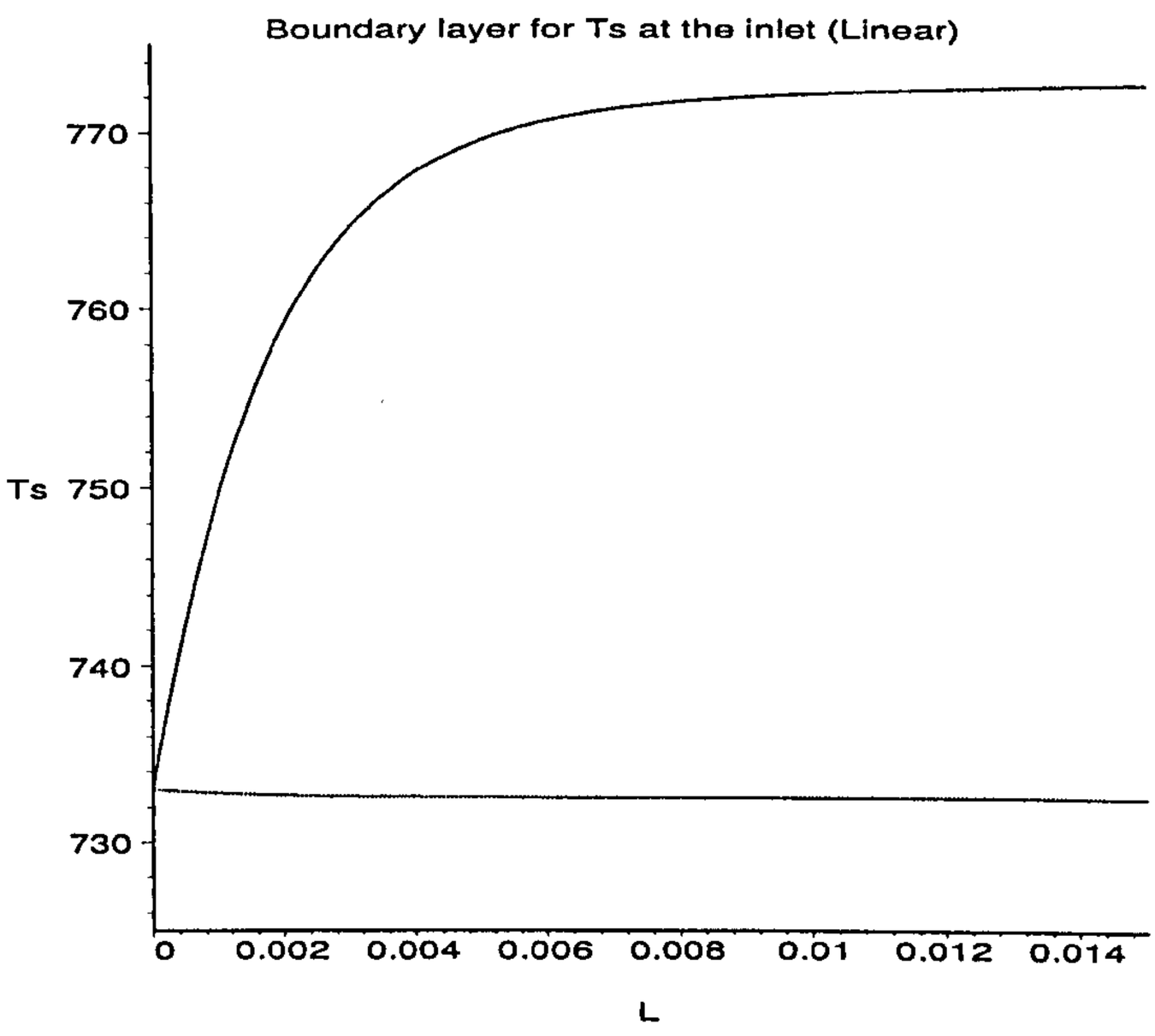

Figure 5.7: Boundary layer for the solid temperature at the inlet of the channels. (Upper plot = Combustion side, Lower plot = Reformer side.)

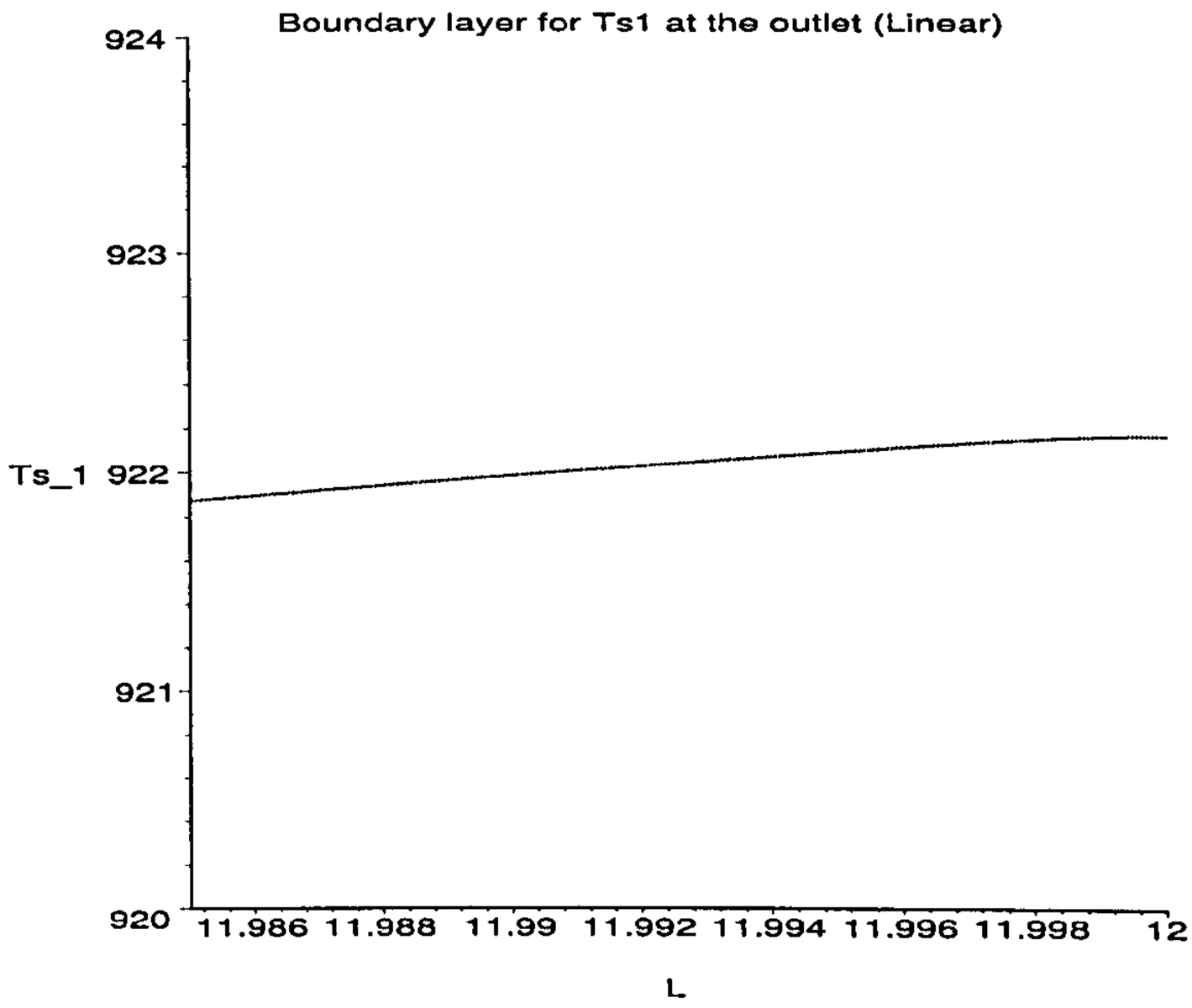

Figure 5.8: Boundary layer for the solid temperature at the outlet of the reformer channel.

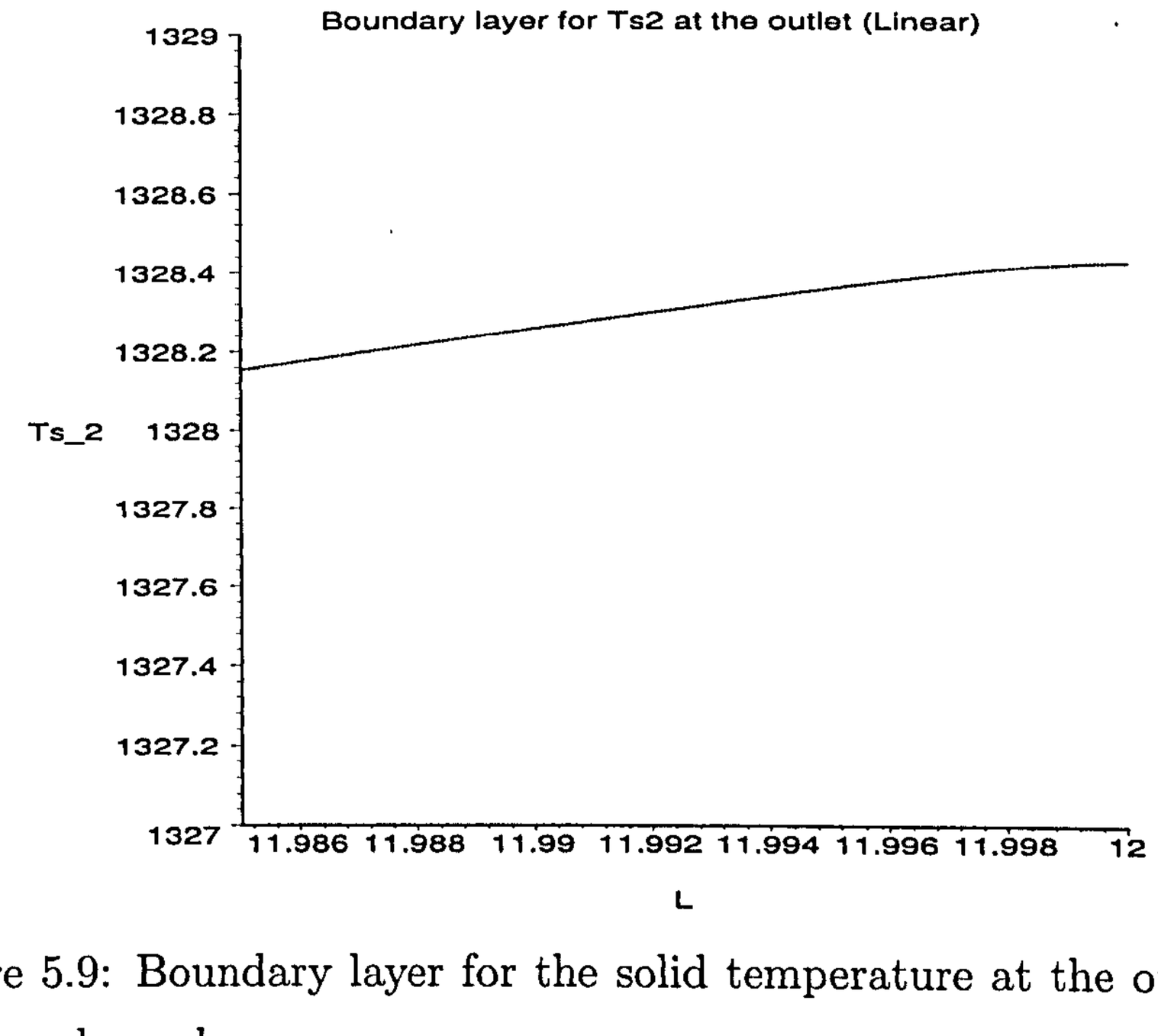

Figure 5.9: Boundary layer for the solid temperature at the outlet of the combustion channel.

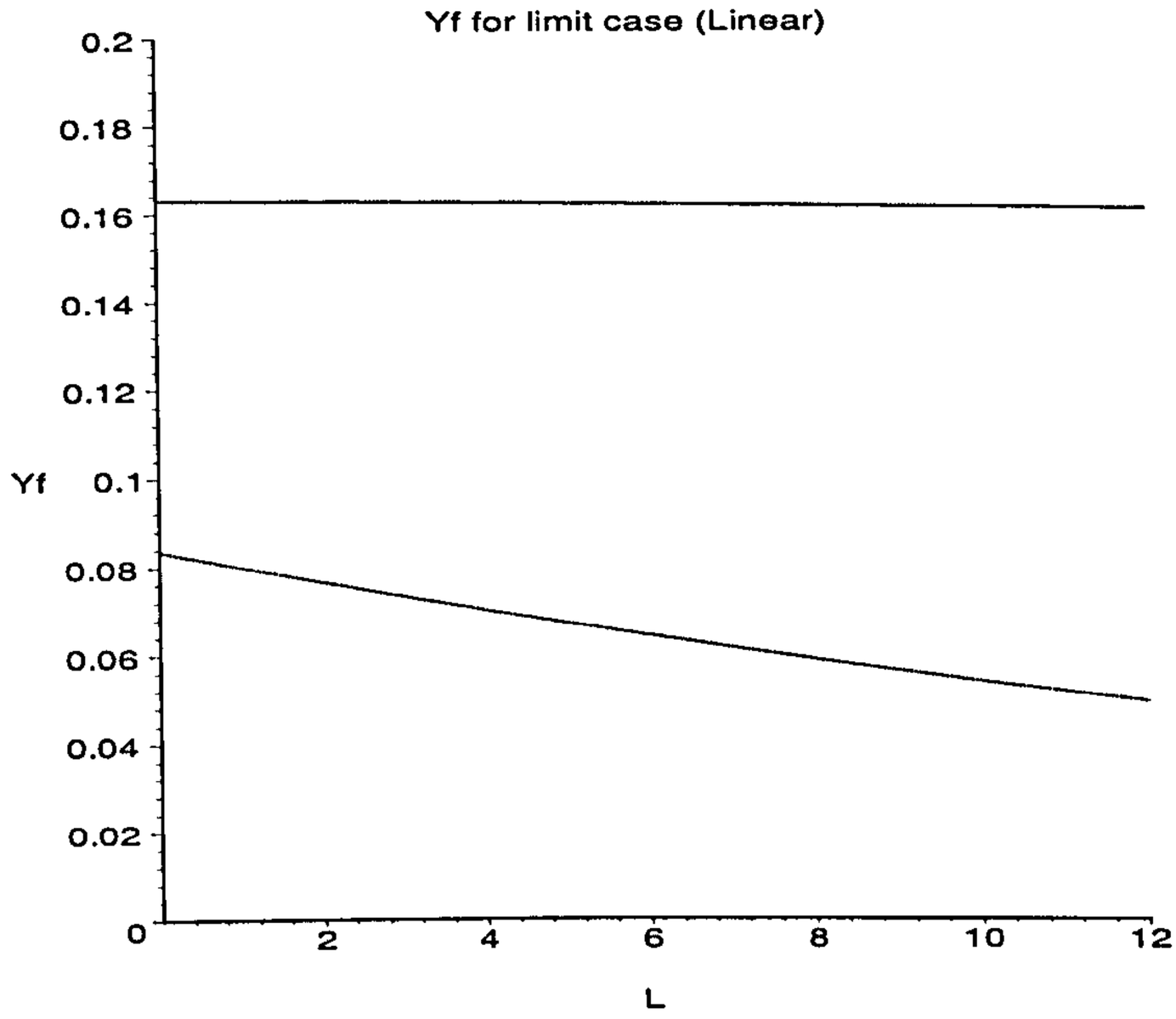

Figure 5.10: Limit problem for the concentration of the fluid in both channels (see (5.2.13)). Upper plot = Reformer side, Lower plot = Combustion side.

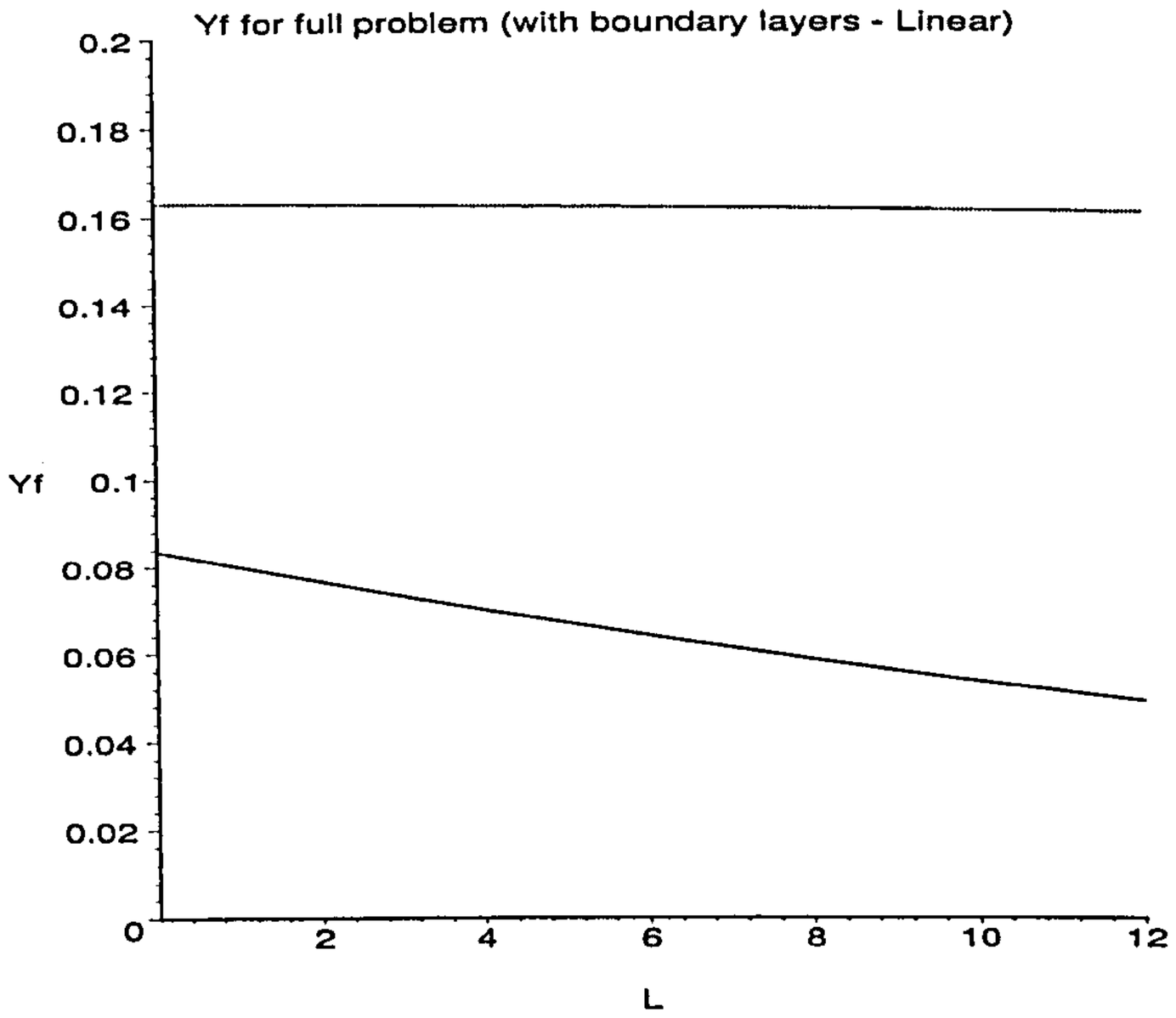

Figure 5.11: Full problem (with boundary layers) for the concentration of the fluid in both channels (see (5.2.24)). Upper plot = Reformer side, Lower plot = Combustion side.

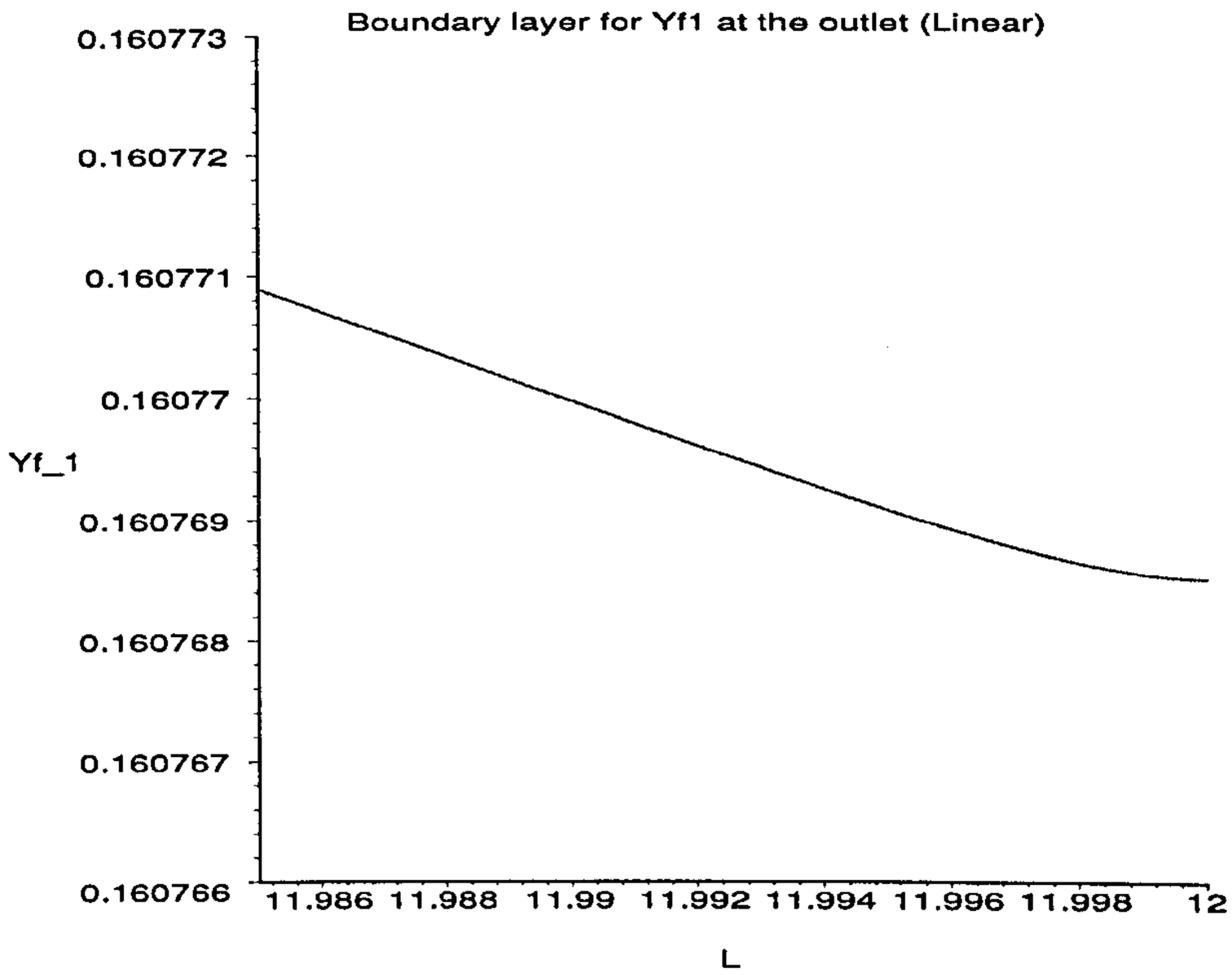

Figure 5.12: Boundary layer for the fluid concentration at the outlet of the reformer channel.

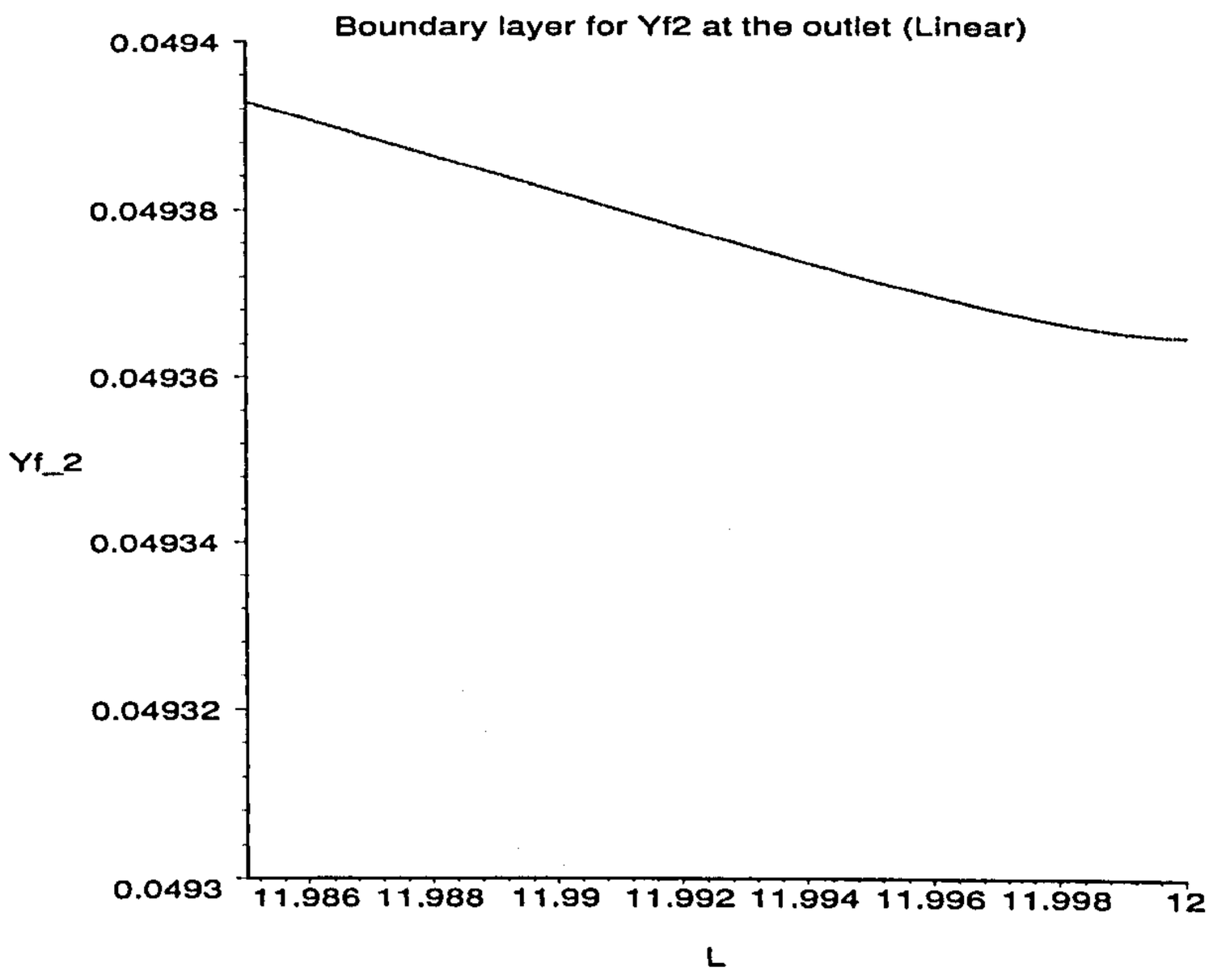

Figure 5.13: Boundary layer for the fluid concentration at the outlet of the combustion channel.

5.4 Singular perturbation - nonlinear case

In this section we present an approximation to the nonlinear case. For the nonlinear problem the reaction rates depend on the solid temperature $T_s^{(j)}(x)$, $j = 1, 2$. Here we use a *matching* procedure, that is, we obtain *outer* expansions using the original variables and then *inner* expansions, for magnified variables, in the regions where the functions change rapidly. Then the solutions are matched (see [59]). The method is used as follows: The channels are divided into three regions, and the equations are modified and solved separately for each region. For the *matching* we assume continuity of temperature along the length of the channel. We choose these regions in such a way that the boundary layers are taken into account, that is, the first is the region close to $x = 0$, associated with the boundary layer at the inlet, the second is the main part of the channel, the middle region, and the third is the region associated with the boundary layer at the outlet, the region close to $x = 12$. (Available numerical packages have difficulty in dealing with this nonlinear singularly perturbed problem in the entire channel, and give errors due to the small coefficients in front of the second order derivatives.)

5.4.1 Region 1: Boundary layer at the inlet

Consider the region near the inlet $x = 0$

From the linear problem we recall that the functions which change rapidly near the inlet are $T_s^{(1)}(x)$ and $T_s^{(2)}(x)$. Since the other four functions behave smoothly and do not change significantly in this region, their derivatives are small and we can assume that their second order derivatives are negligible. Consequently, the system of six equations takes the form:

$$0 = c_1^{(1)} \frac{dY_f^{(1)}}{dx}(x) + c_2^{(1)} Y_f^{(1)}(x)\zeta_1(x),$$

$$0 = c_1^{(2)} \frac{dY_f^{(2)}}{dx}(x) + c_2^{(2)} Y_f^{(2)}(x)\zeta_2(x),$$

$$0 = c_6^{(1)} \frac{dT_f^{(1)}}{dx}(x) + c_7^{(1)} T_f^{(1)}(x) - c_8^{(1)} T_f^{(2)}(x) - c_9^{(1)} T_s^{(1)}(x),$$

$$0 = c_6^{(2)} \frac{dT_f^{(2)}}{dx}(x) - c_7^{(2)} T_f^{(1)}(x) + c_8^{(2)} T_f^{(2)}(x) - c_9^{(2)} T_s^{(2)}(x),$$

$$\delta \frac{d^2 T_s^{(1)}}{dx^2}(x) = c_{10}^{(1)} (T_s^{(1)}(x) - T_f^{(1)}(x)) + c_{11}^{(1)} Y_f^{(1)}(x) \zeta_1(x), \qquad (5.4.25)$$

$$\delta \frac{d^2 T_s^{(2)}}{dx^2}(x) = c_{10}^{(2)} (T_s^{(2)}(x) - T_f^{(2)}(x)) - c_{11}^{(2)} Y_f^{(2)}(x) \zeta_2(x), \qquad (5.4.26)$$

where

$$\zeta_1(x) = \left(1 - \frac{c_3^{(1)}}{c_3^{(1)} + c_4^{(1)} e^{-\left(\frac{c_5^{(1)}}{T_s^{(1)}(x)}\right)}}\right),$$

$$\zeta_2(x) = \left(1 - \frac{c_3^{(2)}}{c_3^{(2)} + c_4^{(2)} e^{-\left(\frac{c_5^{(2)}}{T_s^{(2)}(x)}\right)}}\right),$$

and the constants $c_j^{(i)}$, $i = 1, 2$, $j = 1, ..., 11$, are given by (5.1.6). The first region is small ($x = 0$ to $x = 0.015$), and all functions except for $T_s^{(1)}(x)$ and $T_s^{(2)}(x)$ do not change significantly in this region. Therefore, we deal only with the equations for $T_s^{(1)}(x)$ and $T_s^{(2)}(x)$ and we assume that all other functions are constant in this interval. Also since the region is small, we introduce a scaled variable of the form $\varrho = \frac{x}{\sqrt{\delta}}$. The new functions which depend on the new variable ϱ are denoted here by $\hat{T}_s^{(1)}$, $\hat{T}_s^{(2)}$ and $\hat{\zeta}_i$, $i = 1, 2$. Thus, in this new coordinate, equations (5.4.25) and (5.4.26) can be written as

$$\frac{d^2 \hat{T}_s^{(1)}}{d\varrho^2}(\varrho) = c_{10}^{(1)} (\hat{T}_s^{(1)}(\varrho) - 733) + 0.163\, c_{11}^{(1)} \hat{\zeta}_1(\varrho),$$

$$\frac{d^2 \hat{T}_s^{(2)}}{d\varrho^2}(\varrho) = c_{10}^{(2)} (\hat{T}_s^{(2)}(\varrho) - 733) - 0.0836\, c_{11}^{(2)} \hat{\zeta}_2(\varrho), \qquad (5.4.27)$$

where $T_f^{(i)}$ and $Y_f^{(i)}$, $i = 1, 2$, are replaced by their values at the inlet. Each second order differential equation in (5.4.27) requires two boundary conditions. From (5.1.4) we have one condition for each function at the inlet. At the point $\varrho = 0.015/\sqrt{\delta}$ we assume that the conditions are the same as those obtained for the linear case (5.2.24) at $x = 0.015$, that is, we say

$$\hat{T}_s^{(1)}(\varrho = 0.015/\sqrt{\delta}) = 732.4889 \text{ and } \hat{T}_s^{(2)}(\varrho = 0.015/\sqrt{\delta}) = 772.7295.$$

(Table 5.1 shows similar results for how $T_s^{(i)}$ and $\hat{T}_s^{(i)}$, $i = 1, 2$, change between $x = 0$ and $x = 0.015$ (or $\varrho = 0$ and $\varrho = 0.015/\sqrt{\delta}$) so this assumption provides a good approximation for the values at the right end of this first region).

Summary for the region near the inlet $x = 0$:

The functions $Y_f^{(j)}(x)$ and $T_f^{(j)}(x)$, $j = 1, 2$, are approximated by constants for this small interval, $x = 0$ to $x = 0.015$. The nonlinear equations (5.4.27) are solved numerically for $\hat{T}_s^{(1)}(\varrho)$ and $\hat{T}_s^{(2)}(\varrho)$, together with the Dirichlet conditions at both ends. The results in Table 5.1 show the behaviour of the solid temperatures in the small region near the inlet.

5.4.2 Region 2: Middle section

Consider the middle part of the channel

From the linear case, we know that the functions $T_s^{(1)}$ and $T_s^{(2)}$ have large derivatives in the region close to the inlet and all the functions have large derivatives in the region close to the outlet. As a consequence, the derivatives of ζ_1 and ζ_2 are also large in the regions close to the inlet and the outlet, since these functions depend upon $T_s^{(1)}$ and $T_s^{(2)}$, respectively, that is

$$\zeta^{(j)} = \left(1 - \frac{c_3^{(j)}}{c_3^{(j)} + c_4^{(j)} e^{-\left(\frac{c_5^{(j)}}{T_s^{(j)}(x)}\right)}}\right), \; j = 1, 2.$$

x	$T_s^{(1)}$ (linear) (from (5.2.24))	$\hat{T}_s^{(1)}$ (nonlinear) (from (5.4.27))	$T_s^{(2)}$ (linear) (from (5.2.24))	$\hat{T}_s^{(2)}$ (nonlinear) (from (5.4.27))
0	733	733	733	733
0.001	732.7766	732.7155	749.5521	749.8487
0.002	732.6525	732.6247	759.0445	759.4434
0.003	732.5834	732.5647	764.5048	764.7792
0.004	732.5448	732.5332	767.6620	767.4850
0.005	732.5230	732.5195	769.5040	767.2132
0.006	732.5015	732.5109	770.5947	770.7631
0.007	732.5033	732.5076	771.2563	770.0508
0.008	732.4990	732.5054	771.6729	767.2717
0.009	732.4961	732.5052	771.9494	766.2980
0.01	732.4942	732.5034	772.1460	768.9262
0.011	732.4928	732.5028	772.2969	771.6853
0.012	732.4916	732.5020	772.4217	771.7927
0.013	732.4906	732.5000	772.5316	771.6964
0.014	732.4897	732.4998	772.6330	772.3012
0.015	732.4889	732.4889	772.7295	772.7295

Table 5.1: Comparison of the functions $T_s^{(1)}$, $\hat{T}_s^{(1)}$, $T_s^{(2)}$ and $\hat{T}_s^{(2)}$ for the linear and nonlinear cases.

However, in the middle part of the channel - the region not associated with the boundary layers - all functions are smooth and continuous and their derivatives are small. As a consequence ζ_1 and ζ_2 do not change significantly in the middle region. For the particular industrial data used in this thesis, the derivative of the term ζ_2, for example, is 0.01126 in the region $x = 0$ to $x = 0.015$ and 0.00012 in the region $x = 0.015$ to $x = 11$. Therefore, as an approximation to the nonlinear case, for this second region, we assume that the system can be approximated as being linear, that is, we assume no $T_s^{(i)}$ dependence on the terms $\zeta_i,\ i = 1, 2$, and we use the same method as before (see Section 5.2) for solving the linear system. We set 'new' boundary conditions at the 'new' left end ($x = 0.015$ instead of $x = 0$). Here $\mathbf{Z}$ satisfies the equation

$$\delta \frac{d^2\mathbf{Z}}{dx^2} = A^{(1)} \frac{d\mathbf{Z}}{dx} + A^{(2)}\mathbf{Z}, \tag{5.4.28}$$

where the 6×6 matrices $A^{(1)}$ and $A^{(2)}$ are similar to those given in Section 5.2 with ζ_1 and ζ_2 modified accordingly to account for the 'new' inlet conditions

$$T_s^{(1)}(0.015) = 732.4889 \text{ K} \quad \text{and} \quad T_s^{(2)}(0.015) = 772.7295 \text{ K}.$$

For the limit case, we obtain the solution in the form

$$\mathbf{Z} = \sum_{j=3}^{6} \mathcal{K}_j \mathbf{w}_j e^{\tilde{\lambda}_j x},$$

where $\mathcal{K}_j,\ j = 3, ..., 6$, are constants which we determine from the boundary conditions at $x = 0.015$, and the limit eigenvalues $\tilde{\lambda}_j,\ j = 3, ..., 6$, are computed as

$$\tilde{\lambda}_3 = -\frac{C_2}{C_1} = -0.144501, \quad \tilde{\lambda}_4 = -\frac{c_2^{(2)}\zeta_2}{c_1^{(2)}} = -0.0443098,$$

$$\tilde{\lambda}_5 = -\frac{c_2^{(1)}\zeta_1}{c_1^{(1)}} = -0.001144, \quad \tilde{\lambda}_6 = 0, \tag{5.4.29}$$

where, as before,

$$\begin{aligned} \mathcal{C}_1 &= c_6^{(1)} c_6^{(2)}, \\ \mathcal{C}_2 &= c_6^{(1)}(c_8^{(2)} - c_9^{(2)}) + c_6^{(2)}(c_7^{(1)} - c_9^{(1)}). \end{aligned}$$

The four corresponding eigenvectors are given by

$$\mathbf{w}_3 = \begin{pmatrix} 0 \\ 0 \\ \dfrac{c_8^{(1)}}{c_6^{(1)}\tilde{\lambda}_3 + c_7^{(1)} - c_9^{(1)}} \\ 1 \\ \dfrac{c_8^{(1)}}{c_6^{(1)}\tilde{\lambda}_3 + c_7^{(1)} - c_9^{(1)}} \\ 1 \end{pmatrix}, \quad \mathbf{w}_4 = \begin{pmatrix} 0 \\ \dfrac{c_{10}^{(2)}\tilde{\lambda}_4(\mathcal{C}_1\tilde{\lambda}_4 + \mathcal{C}_2)}{c_8^{(1)} c_9^{(1)} c_{11}^{(2)} \zeta_2} \\ 1 \\ \dfrac{c_6^{(1)}\tilde{\lambda}_4 + c_7^{(1)} - c_9^{(1)}}{c_8^{(1)}} \\ 1 \\ \dfrac{\mathcal{C}_1\tilde{\lambda}_4^2 + \mathcal{C}_3\tilde{\lambda}_4 + \mathcal{C}_4}{c_8^{(1)} c_9^{(2)}} \end{pmatrix},$$

$$\mathbf{w}_5 = \begin{pmatrix} \dfrac{c_{10}^{(1)}\tilde{\lambda}_5(\mathcal{C}_1\tilde{\lambda}_5 + \mathcal{C}_2)}{c_9^{(1)} c_{11}^{(1)} c_7^{(2)} \zeta_1} \\ 0 \\ \dfrac{c_6^{(2)}\tilde{\lambda}_5 + c_8^{(2)} - c_9^{(2)}}{c_7^{(2)}} \\ 1 \\ \dfrac{\mathcal{C}_1\tilde{\lambda}_5^2 + \mathcal{C}_5\tilde{\lambda}_5 + \mathcal{C}_6}{c_7^{(2)} c_9^{(1)}} \\ 1 \end{pmatrix}, \quad \mathbf{w}_6 = \begin{pmatrix} 0 \\ 0 \\ \dfrac{c_8^{(1)}}{c_7^{(1)} - c_9^{(1)}} \\ 1 \\ \dfrac{c_8^{(1)}}{c_7^{(1)} - c_9^{(1)}} \\ 1 \end{pmatrix}.$$

Substituting the limit eigenvalues (5.4.29) and the constants (5.1.6) we have

$$\mathbf{w}_3 = \begin{pmatrix} 0 \\ 0 \\ -0.7033536146 \\ 1 \\ -0.7033536146 \\ 1 \end{pmatrix}, \quad \mathbf{w}_4 = \begin{pmatrix} 0 \\ -0.0000670589 \\ 1 \\ 0.2573909091 \\ 1 \\ 0.2263181478 \end{pmatrix},$$

$$\mathbf{w}_5 = \begin{pmatrix} 0.0003609297 \\ 0 \\ 0.9865134162 \\ 1 \\ 0.9854138338 \\ 1 \end{pmatrix}, \quad \mathbf{w}_6 = \begin{pmatrix} 0 \\ 0 \\ 1 \\ 1 \\ 1 \\ 1 \end{pmatrix},$$

where C_i, $i = 1, ..., 6$, are given in Section 5.2. Using the above eigenvectors together with the boundary conditions for the functions $Y_f^{(j)}$ and $T_f^{(j)}$, $j = 1, 2$, at $x = 0.015$ we obtain the constants $\mathcal{K}_3, ..., \mathcal{K}_6$:

$$\mathcal{K}_3 = -548.269683, \quad \mathcal{K}_4 = -1247.493387,$$
$$\mathcal{K}_5 = 451.619287, \quad \mathcal{K}_6 = 1149.351165. \tag{5.4.30}$$

In this case, substituting these four constants into the functions for $T_s^{(1)}(x)$ and $T_s^{(2)}(x)$ shows that the boundary conditions for the last two components of the vector $\mathbf{Z}$ are approximately satisfied. Therefore, to a satisfactory degree of accuracy, all the boundary conditions at the inlet are satisfied.

Summary for the middle region:

The analytical representations for the six components of $\mathbf{Z}$ in the middle region

of the channels between $x = 0.015$ and $x = 11$ are

$$\begin{aligned}
Y_f^{(1)}(x) &= 0.00036\mathcal{K}_5\, e^{\tilde{\lambda}_5 x}, \\
Y_f^{(2)}(x) &= -0.00007\mathcal{K}_4\, e^{\tilde{\lambda}_4 x}, \\
T_f^{(1)}(x) &= -0.70335\mathcal{K}_3 e^{\tilde{\lambda}_3 x} + \mathcal{K}_4 e^{\tilde{\lambda}_4 x} + 0.98651\mathcal{K}_5 e^{\tilde{\lambda}_5 x} + \mathcal{K}_6 e^{\tilde{\lambda}_6 x}, \\
T_f^{(2)}(x) &= \mathcal{K}_3\, e^{\tilde{\lambda}_3 x} + 0.25739\mathcal{K}_4\, e^{\tilde{\lambda}_4 x} + \mathcal{K}_5\, e^{\tilde{\lambda}_5 x} + \mathcal{K}_6\, e^{\tilde{\lambda}_6 x}, \qquad (5.4.31) \\
T_s^{(1)}(x) &= -0.70335\mathcal{K}_3 e^{\tilde{\lambda}_3 x} + \mathcal{K}_4 e^{\tilde{\lambda}_4 x} + 0.98541\mathcal{K}_5 e^{\tilde{\lambda}_5 x} + \mathcal{K}_6 e^{\tilde{\lambda}_6 x}, \\
T_s^{(2)}(x) &= \mathcal{K}_3\, e^{\tilde{\lambda}_3 x} + 0.22632\mathcal{K}_4\, e^{\tilde{\lambda}_4 x} + \mathcal{K}_5\, e^{\tilde{\lambda}_5 x} + \mathcal{K}_6\, e^{\tilde{\lambda}_6 x},
\end{aligned}$$

where the constants $\mathcal{K}_j$ and the eigenvalues $\tilde{\lambda}_j$, $j = 3, ..., 6$, are all given explicitly in (5.4.29) and (5.4.30).

5.4.3 Region 3: Boundary layer at the outlet

Consider the region near the outlet $x = 12$

From the linear case described in Section 5.2 we know that the limit problem does not satisfy the zero flux conditions at the outlet. The same applies to the nonlinear case. When the functions given by (5.4.31) are differentiated and computed at the point $x = 12$ we have the following

$$\frac{d\mathbf{Z}}{dx}(12) = \begin{pmatrix} -0.000184 \\ -0.002178 \\ 22.13786 \\ 21.83962 \\ 22.13842 \\ 20.83037 \end{pmatrix}.$$

So the solution at the outlet must compensate for this discrepancy. We assume that the solution is made up of two parts - one which depends on a slow variable

and compensates for the fact that we have taken a linear approximation in the middle of the channel, and the other which depends on fast variables and compensates for the discrepancy in the boundary conditions. We take this solution in the form

$$\mathbf{Z}^{\mathbf{r}} = \mathbf{Z} + \mathbf{Z}^{\mathbf{F}},$$

where $\mathbf{Z}$ depends on x and $\mathbf{Z}^{\mathbf{F}}$ depends on two scaled coordinates

$$\varphi = \frac{12-x}{\sqrt{\delta}} \quad \text{and} \quad \breve{\varphi} = \frac{12-x}{\delta}.$$

The functions $Y_f^{(i)}$ and $T_s^{(i)}$, $i = 1, 2$, depend on φ, and $T_f^{(i)}$, $i = 1, 2$, depend on $\breve{\varphi}$. The conditions on $\mathbf{Z}^{\mathbf{r}}$ are

$$\mathbf{Z}^{\mathbf{r}} = \mathbf{Z} \quad \text{at } x = 11 \quad \text{and} \quad \frac{d\mathbf{Z}^{\mathbf{F}}}{dx} + \frac{d\mathbf{Z}}{dx} = 0 \quad \text{at } x = 12.$$

The full system of equations for the six components of $\mathbf{Z}^{\mathbf{r}}$ is written as

$$\begin{aligned}
\delta R_{11}^* \quad + \quad & \frac{d^2 Y_f^{(1)F}}{d\varphi^2}(\varphi) = c_1^{(1)} R_1^* - \frac{c_1^{(1)}}{\sqrt{\delta}} \frac{dY_f^{(1)F}}{d\varphi}(\varphi) \\
+ \quad & c_2^{(1)} (Y_f^{(1)}(x) + Y_f^{(1)F}(\varphi)) \zeta_1(\varphi), \qquad (5.4.32) \\
\delta R_{22}^* \quad + \quad & \frac{d^2 Y_f^{(2)F}}{d\varphi^2}(\varphi) = c_1^{(2)} R_2^* - \frac{c_1^{(2)}}{\sqrt{\delta}} \frac{dY_f^{(2)F}}{d\varphi}(\varphi) \\
+ \quad & c_2^{(2)} (Y_f^{(2)}(x) + Y_f^{(2)F}(\varphi)) \zeta_2(\varphi), \qquad (5.4.33) \\
\delta R_{33}^* \quad + \quad & \frac{1 d^2 T_f^{(1)F}}{\delta \quad d\breve{\varphi}^2}(\breve{\varphi}) = c_6^{(1)} R_3^* - \frac{c_6^{(1)}}{\delta} \frac{dT_f^{(1)F}}{d\breve{\varphi}}(\breve{\varphi}) + c_7^{(1)} (T_f^{(1)}(x) + T_f^{(1)F}(\breve{\varphi})) \\
- \quad & c_8^{(1)} (T_f^{(2)}(x) + T_f^{(2)F}(\breve{\varphi})) - c_9^{(1)} (T_s^{(1)}(x) + T_s^{(1)F}(\varphi), \qquad (5.4.34)
\end{aligned}$$

$$\delta R_{44}^* + \frac{1}{\delta}\frac{d^2T_f^{(2)F}}{d\breve{\varphi}^2}(\breve{\varphi}) = c_6^{(2)}R_4^* - \frac{c_6^{(2)}}{\delta}\frac{dT_f^{(2)F}}{d\breve{\varphi}}(\breve{\varphi}) - c_7^{(2)}(T_f^{(1)}(x)+T_f^{(1)F}(\breve{\varphi}))$$
$$+ c_8^{(2)}(T_f^{(2)}(x)+T_f^{(2)F}(\breve{\varphi})) - c_9^{(2)}(T_s^{(2)}(x)+T_s^{(2)F}(\varphi), \tag{5.4.35}$$

$$\delta R_{55}^* + \frac{d^2T_s^{(1)F}}{d\varphi^2}(\varphi) = c_{10}^{(1)}(T_s^{(1)}(x)+T_s^{(1)F}(\varphi)) - c_{10}^{(1)}(T_f^{(1)}(x)+T_f^{(1)F}(\breve{\varphi}))$$
$$+ c_{11}^{(1)}(Y_f^{(1)}(x)+Y_f^{(1)F}(\varphi))\zeta_1(\varphi), \tag{5.4.36}$$

$$\delta R_{66}^* + \frac{d^2T_s^{(2)F}}{d\varphi^2}(\varphi) = c_{10}^{(2)}(T_s^{(2)}(x)+T_s^{(2)F}(\varphi)) - c_{10}^{(2)}(T_f^{(2)}(x)+T_f^{(2)F}(\breve{\varphi}))$$
$$- c_{11}^{(2)}(Y_f^{(2)}(x)+Y_f^{(2)F}(\varphi))\zeta_2(\varphi), \tag{5.4.37}$$

where

$$R_{11}^* = \frac{d^2Y_f^{(1)}}{dx^2}(x), \quad R_1^* = \frac{dY_f^{(1)}}{dx}(x), \quad R_{22}^* = \frac{d^2Y_f^{(2)}}{dx^2}(x), \quad R_2^* = \frac{dY_f^{(2)}}{dx}(x),$$

$$R_{33}^* = \frac{d^2T_f^{(1)}}{dx^2}(x), \quad R_3^* = \frac{dT_f^{(1)}}{dx}(x), \quad R_{44}^* = \frac{d^2T_f^{(2)}}{dx^2}(x), \quad R_4^* = \frac{dT_f^{(2)}}{dx}(x),$$

$$R_{55}^* = \frac{d^2T_s^{(1)}}{dx^2}(x), \quad R_5^* = \frac{dT_s^{(1)}}{dx}(x), \quad R_{66}^* = \frac{d^2T_s^{(1)}}{dx^2}(x), \quad R_6^* = \frac{dT_s^{(1)}}{dx}(x),$$

and

$$\zeta_i(\varphi) = \left(1 - \frac{c_3^{(i)}}{c_3^{(i)} + c_4^{(i)}e^{\left(\frac{-c_5^{(i)}}{T_s^{(i)}(0.015)+T_s^{(i)F}(\varphi)}\right)}}\right), \; i = 1, 2.$$

All functions which depend on the slow variable x are known from the middle region, see (5.4.31), and are substituted into the above system. The system is difficult to treat numerically because we have two independent variables and a large difference in the coefficients for the fluid temperature equations (5.4.34) and

(5.4.35). We consider the leading order terms for these two equations, giving

$$\frac{1}{\delta}\frac{d^2T_f^{(1)F}}{d\breve{\varphi}^2}(\breve{\varphi}) + \frac{c_6^{(1)}}{\delta}\frac{dT_f^{(1)F}}{d\breve{\varphi}}(\breve{\varphi}) = 0,$$
$$\frac{1}{\delta}\frac{d^2T_f^{(2)F}}{d\breve{\varphi}^2}(\breve{\varphi}) + \frac{c_6^{(2)}}{\delta}\frac{dT_f^{(2)F}}{d\breve{\varphi}}(\breve{\varphi}) = 0.$$

Consequently these two equations for $T_f^{(1)F}(\breve{\varphi})$ and $T_f^{(2)F}(\breve{\varphi})$ can be solved separately, with the conditions

$$T_f^{(1)F}\left(\breve{\varphi} = \frac{1}{\delta}\right) = 0; \quad \left.\frac{dT_f^{(1)F}}{d\breve{\varphi}}\right|_{\breve{\varphi}=0} = \delta\left.\frac{dT_f^{(1)}}{dx}\right|_{x=12},$$
$$T_f^{(2)F}\left(\breve{\varphi} = \frac{1}{\delta}\right) = 0; \quad \left.\frac{dT_f^{(2)F}}{d\breve{\varphi}}\right|_{\breve{\varphi}=0} = \delta\left.\frac{dT_f^{(2)}}{dx}\right|_{x=12},$$

which gives

$$T_f^{(1)F}(\breve{\varphi}) = -0.000031e^{-596.85\breve{\varphi}} + 0.000031e^{-596846.8}, \qquad (5.4.38)$$
and $$T_f^{(2)F}(\breve{\varphi}) = -0.000041e^{-444.68\breve{\varphi}} + 0.000041e^{-444679.7}. \qquad (5.4.39)$$

Using the fact that $\breve{\varphi} = \varphi/\sqrt{\delta}$, we thus substitute solutions (5.4.38) and (5.4.39) into the remaining system (5.4.32), (5.4.33), (5.4.36) and (5.4.37) to find the four functions $Y_f^{(i)F}$ and $T_s^{(i)F}$, $i = 1, 2$, whose boundary conditions are

$$Y_f^{(i)F}\left(\varphi = \frac{1}{\sqrt{\delta}}\right) = 0; \quad \left.\frac{dY_f^{(i)F}}{d\varphi}\right|_{\varphi=0} = \sqrt{\delta}\left.\frac{dY_f^{(i)}}{dx}\right|_{x=12},$$
$$T_s^{(i)F}\left(\varphi = \frac{1}{\sqrt{\delta}}\right) = 0; \quad \left.\frac{dT_s^{(i)F}}{d\varphi}\right|_{\varphi=0} = \sqrt{\delta}\left.\frac{dT_s^{(i)}}{dx}\right|_{x=12}, \quad i = 1, 2.$$

Summary for the region $x = 11$ to $x = 12$:

The numerical results for the components of $\mathbf{Z^r}$, where $\mathbf{Z^r} = \mathbf{Z} + \mathbf{Z^F}$ and $\mathbf{Z^r}$ is the solution in the region near the outlet of the channels, are given in Figures

5.16, 5.17, 5.21, 5.22, 5.25 and 5.26. The solution at the outlet is a combination of the slow varying part $\mathbf{Z}$, given by (5.4.31), and the fast varying part, given by the solution of the system (5.4.32) - (5.4.37).

5.4.4 Results and discussion

In Figures 5.14 - 5.26 we present the solutions in the two channels for the nonlinear model. The graphs show the temperature and the concentration distributions for the entire length of the channels, and the results for the magnified regions near the inlet and outlet separately. For each case, we have matched the three regions by assuming continuity in temperature and concentration along the channel. The solutions are a combination of the results given in Table 5.1, the functions given in (5.4.31), and the solution to the system (5.4.32) - (5.4.37). Figures 5.14 - 5.17 show the distribution of the fluid temperature; Figures 5.14 and 5.15 show the full solution when we have constant fluid temperature in a small region near the inlet, the solution for the fluid temperature that is obtained from the modified limit problem in the middle section of the channel, and the change in the fluid temperature near the outlet. Figures 5.16 and 5.17 are presented to show this small change at the outlet in more detail in each channel. We present the results for the solid temperature in Figures 5.18 - 5.22. Figures 5.20 - 5.22 show the boundary layer regions at the inlet and outlet in detail. Figures 5.23 - 5.26 contain the distributions for the fluid concentration, which is approximated by a constant in the small region near the inlet, satisfies equation (5.4.31) for the middle section of the channel, and changes slightly in the region near the outlet, as shown in Figures 5.25 and 5.26.

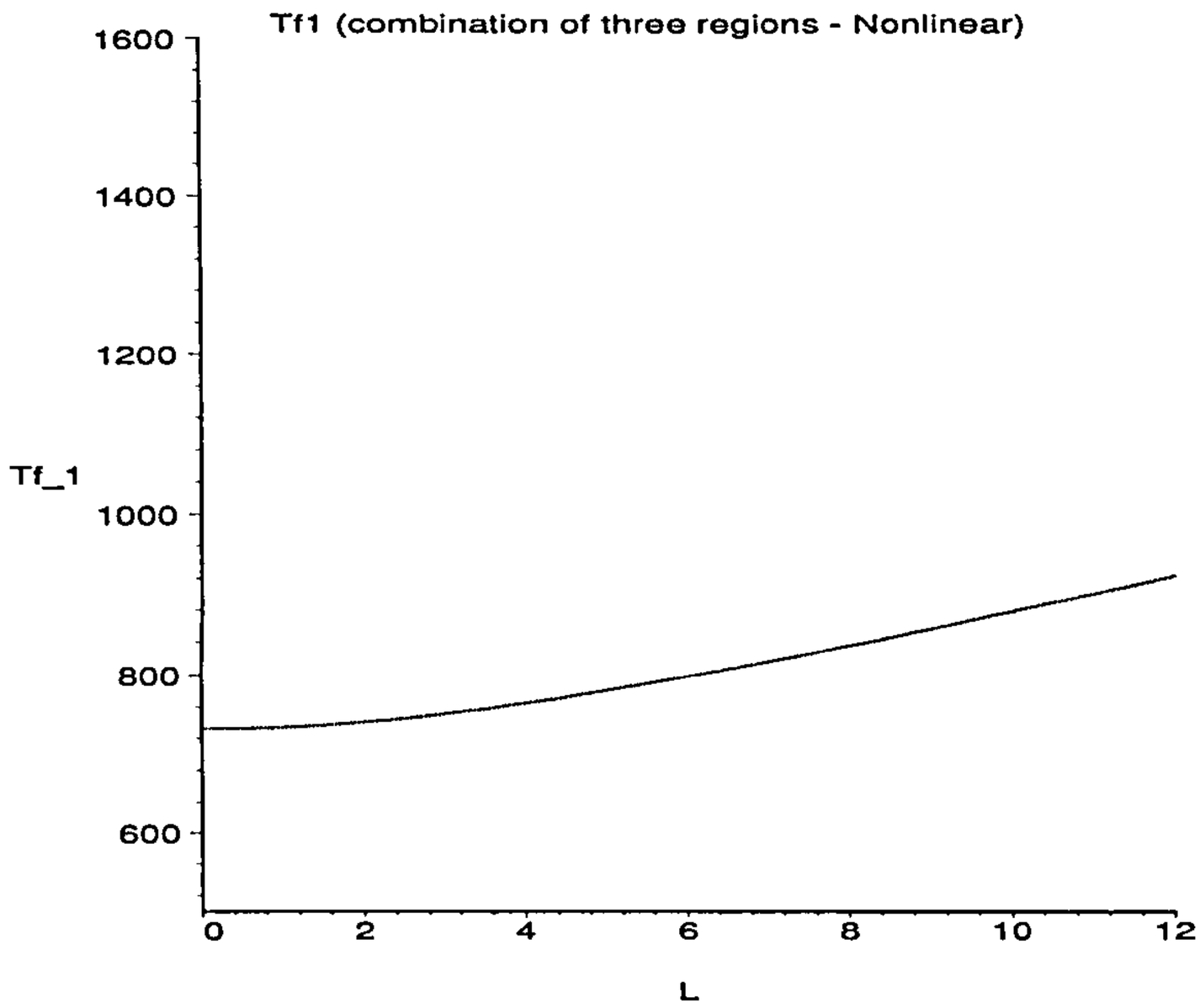

Figure 5.14: Full problem (combination of the results in region 1, region 2 and region 3) for the temperature of the fluid in the reformer channel.

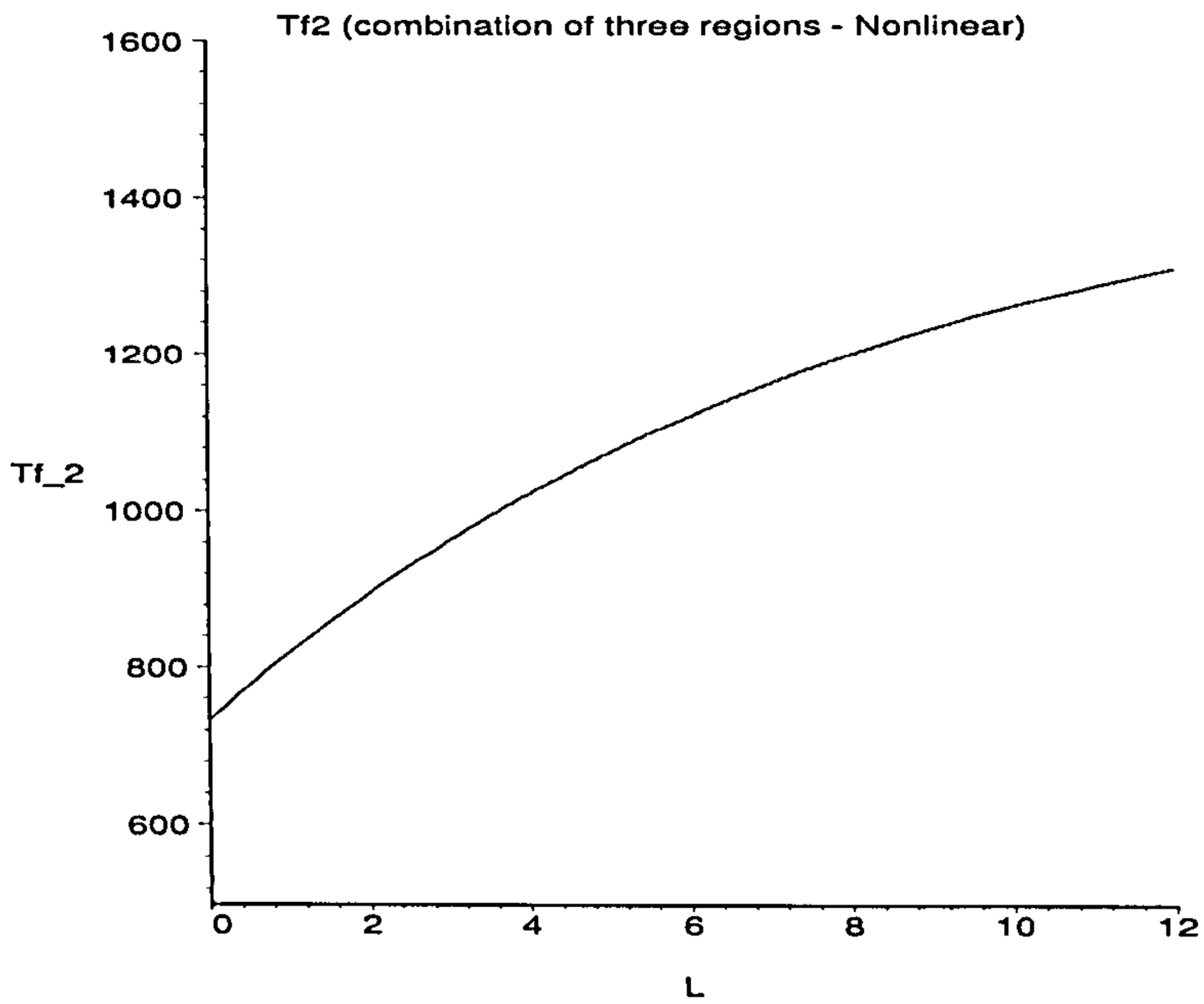

Figure 5.15: Full problem (combination of the results in region 1, region 2 and region 3) for the temperature of the fluid in the combustion channel.

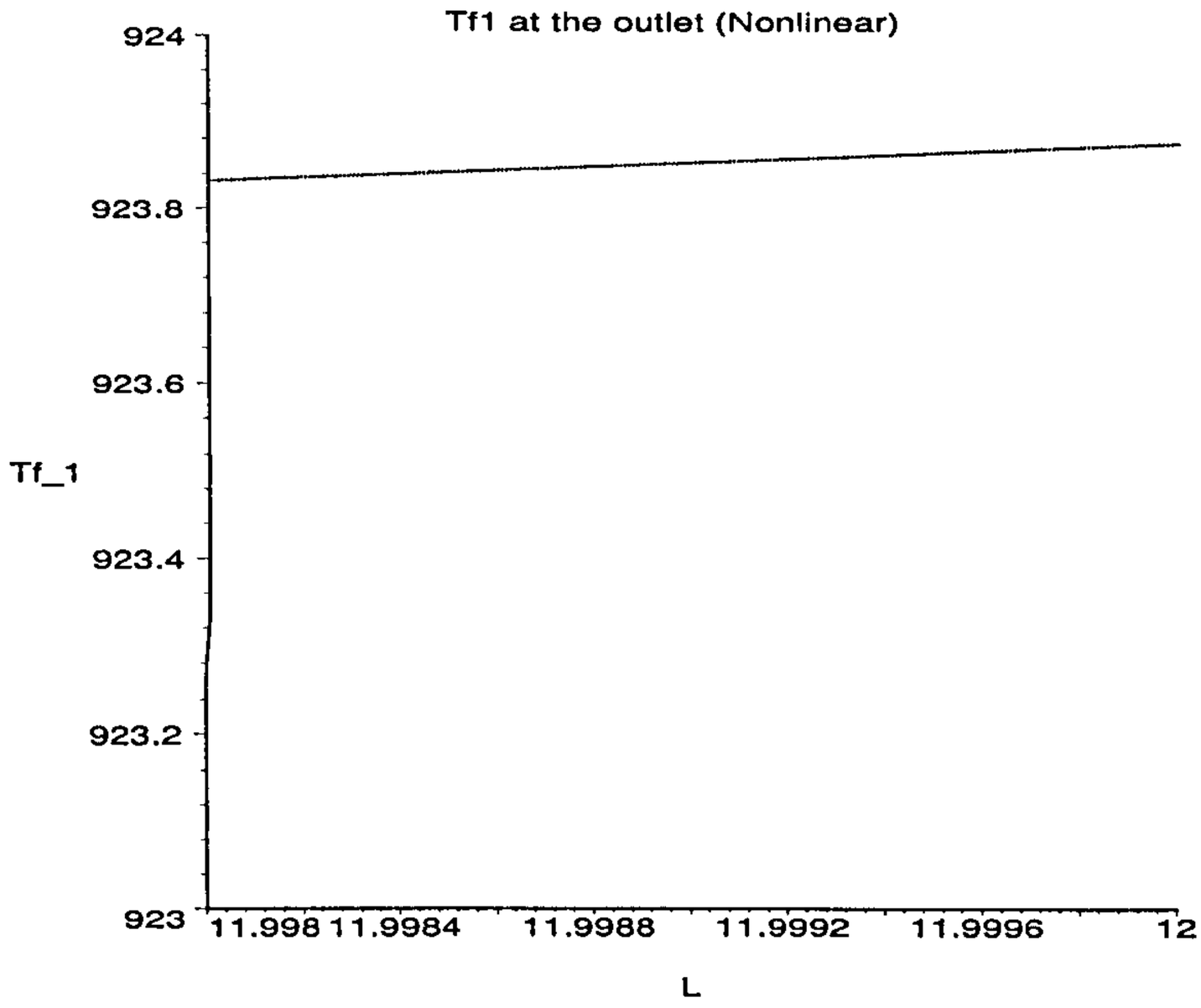

Figure 5.16: Boundary layer for the fluid temperature at the outlet of the reformer channel.

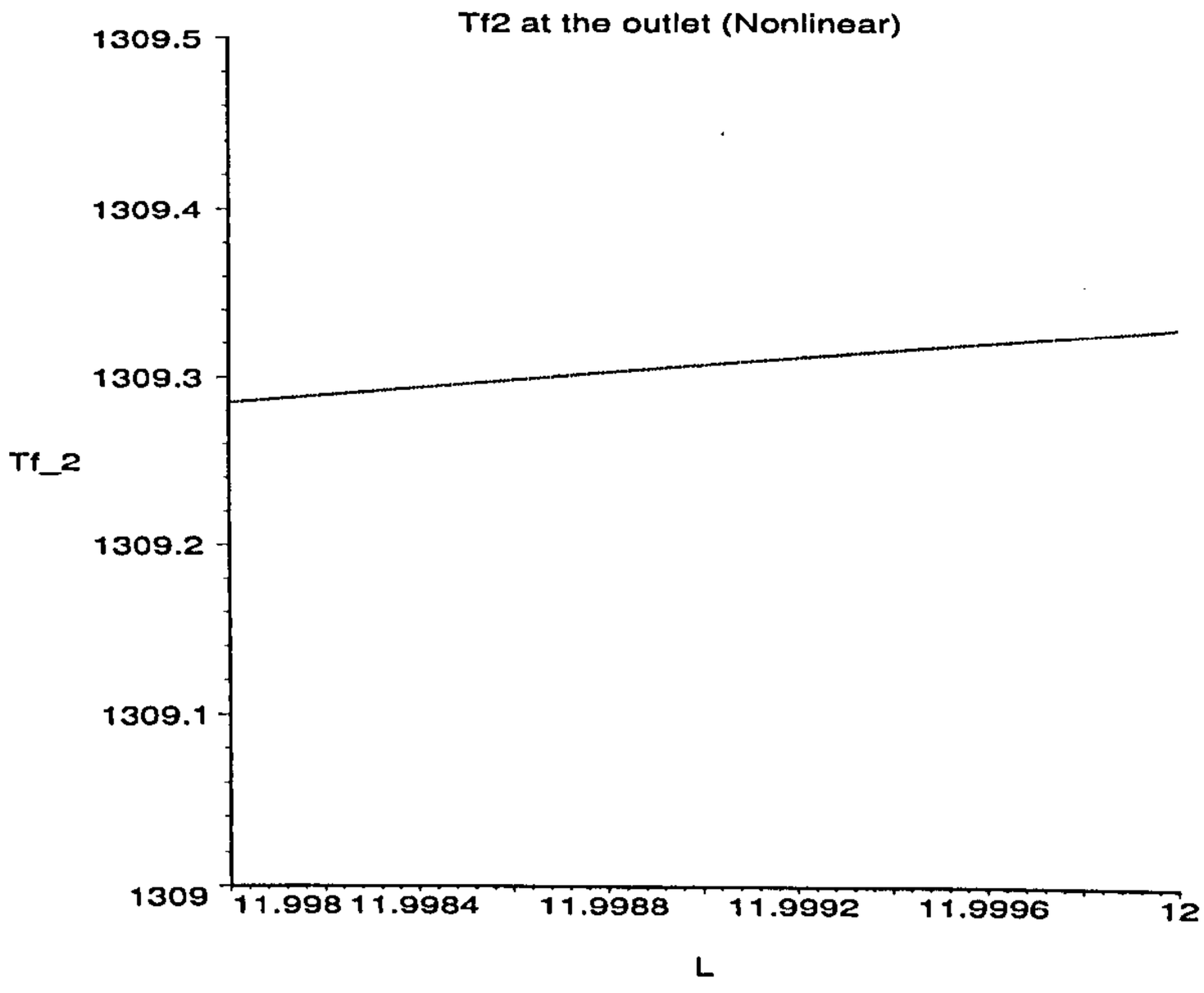

Figure 5.17: Boundary layer for the fluid temperature at the outlet of the combustion channel.

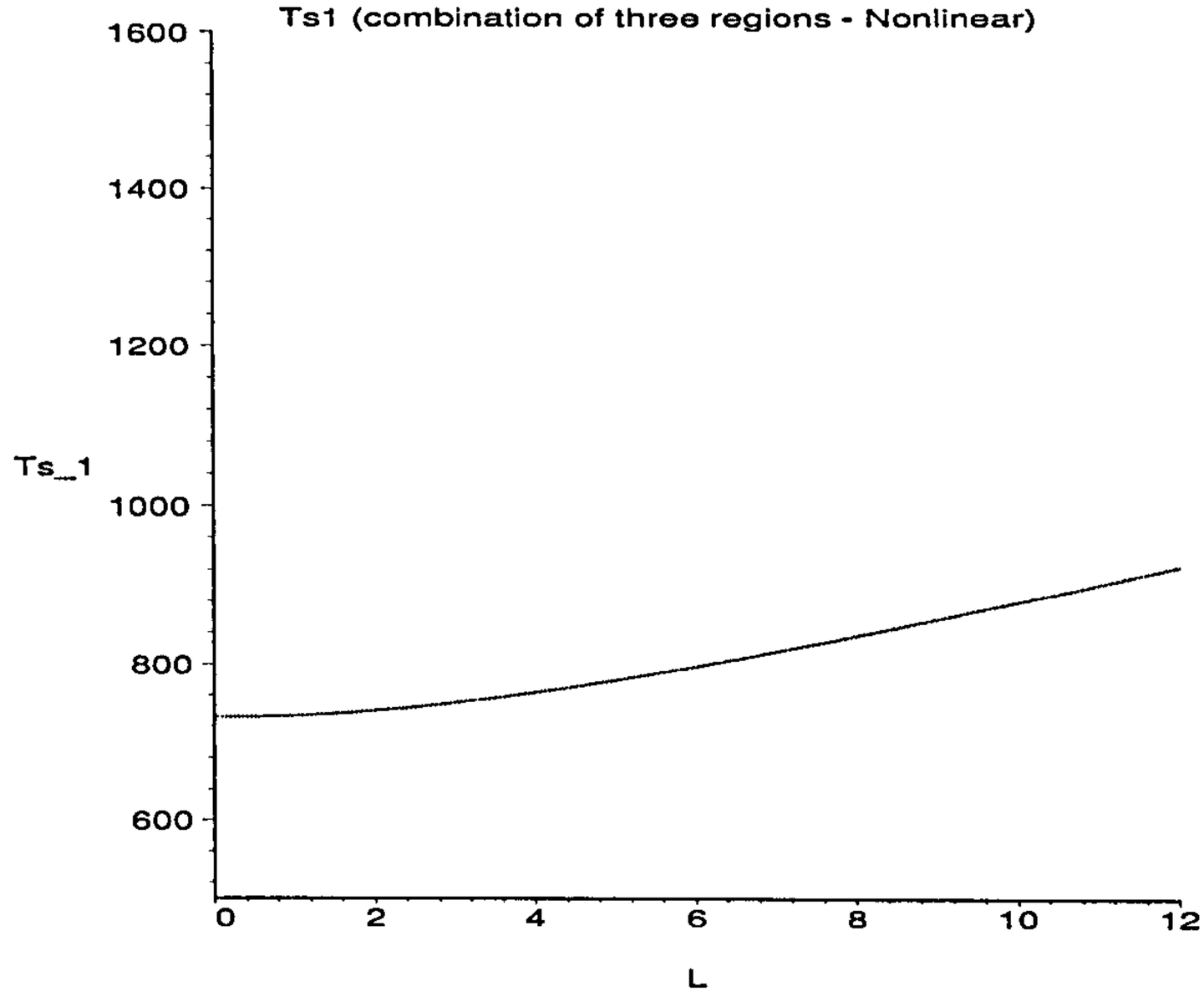

Figure 5.18: Full problem (combination of the results in region 1, region 2 and region 3) for the temperature of the solid in the reformer channel.

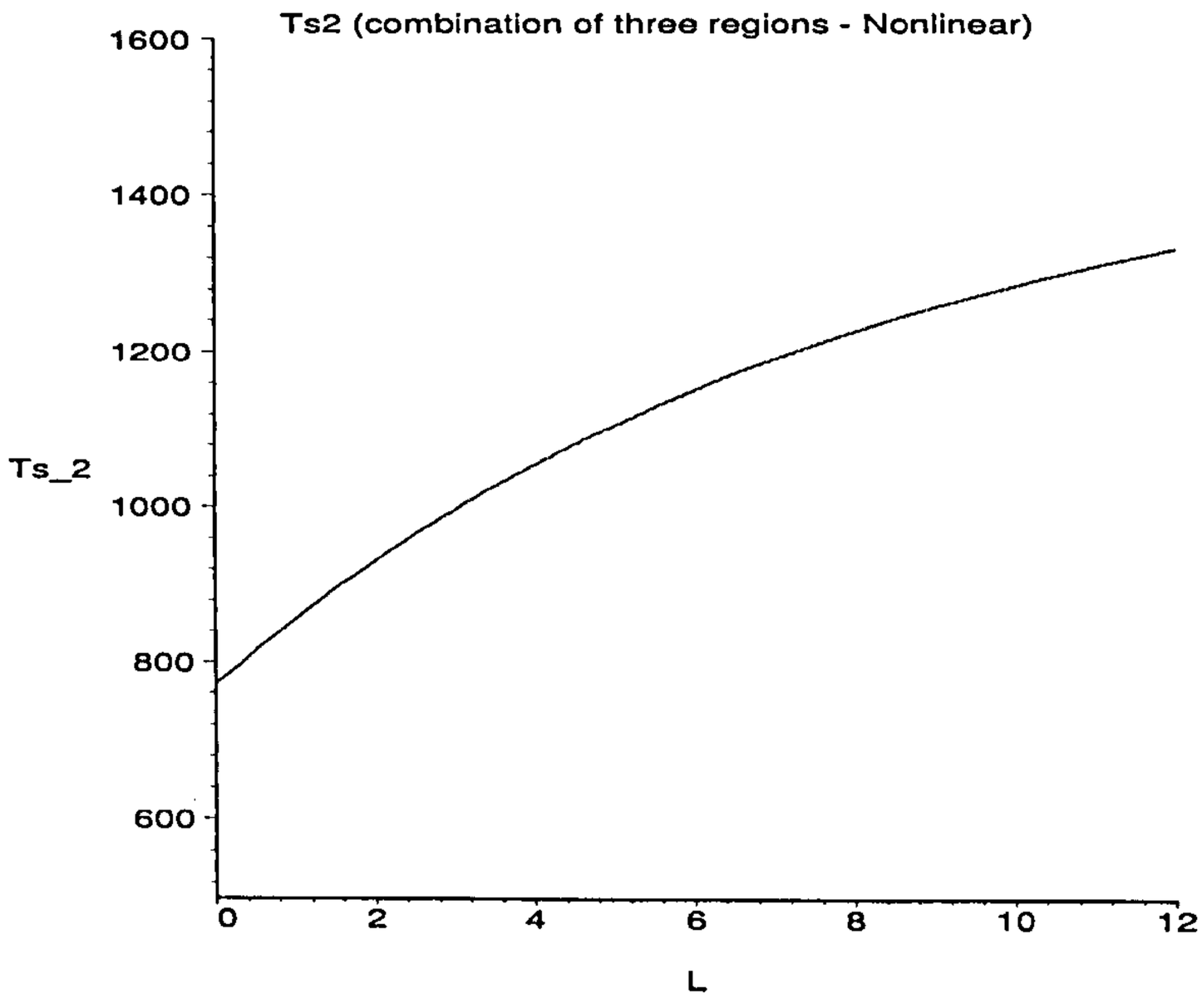

Figure 5.19: Full problem (combination of the results in region 1, region 2 and region 3) for the temperature of the solid in the combustion channel.

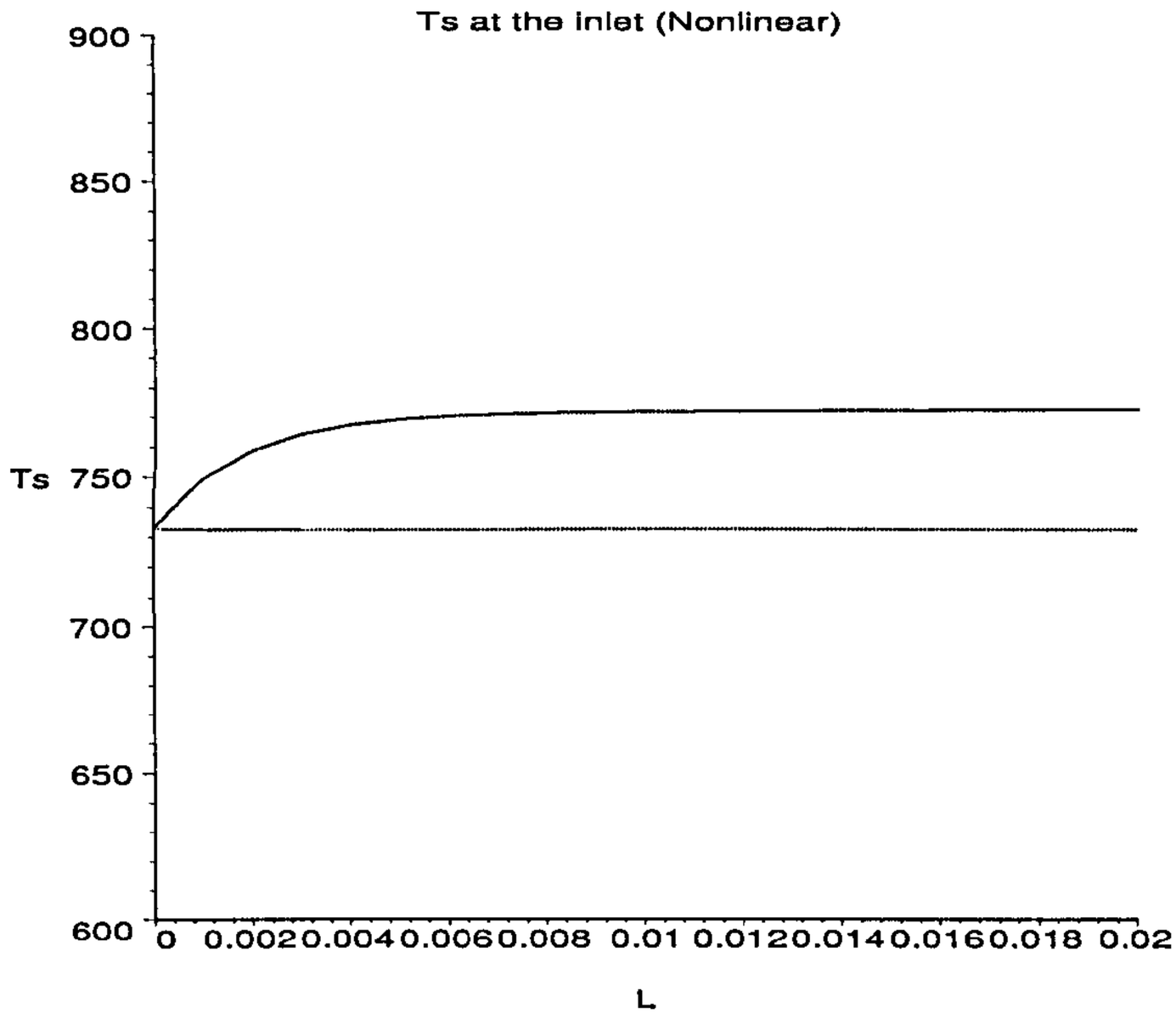

Figure 5.20: Boundary layer for the solid temperature at the inlet of both channels. Upper plot = Combustion side, Lower plot = Reformer side.

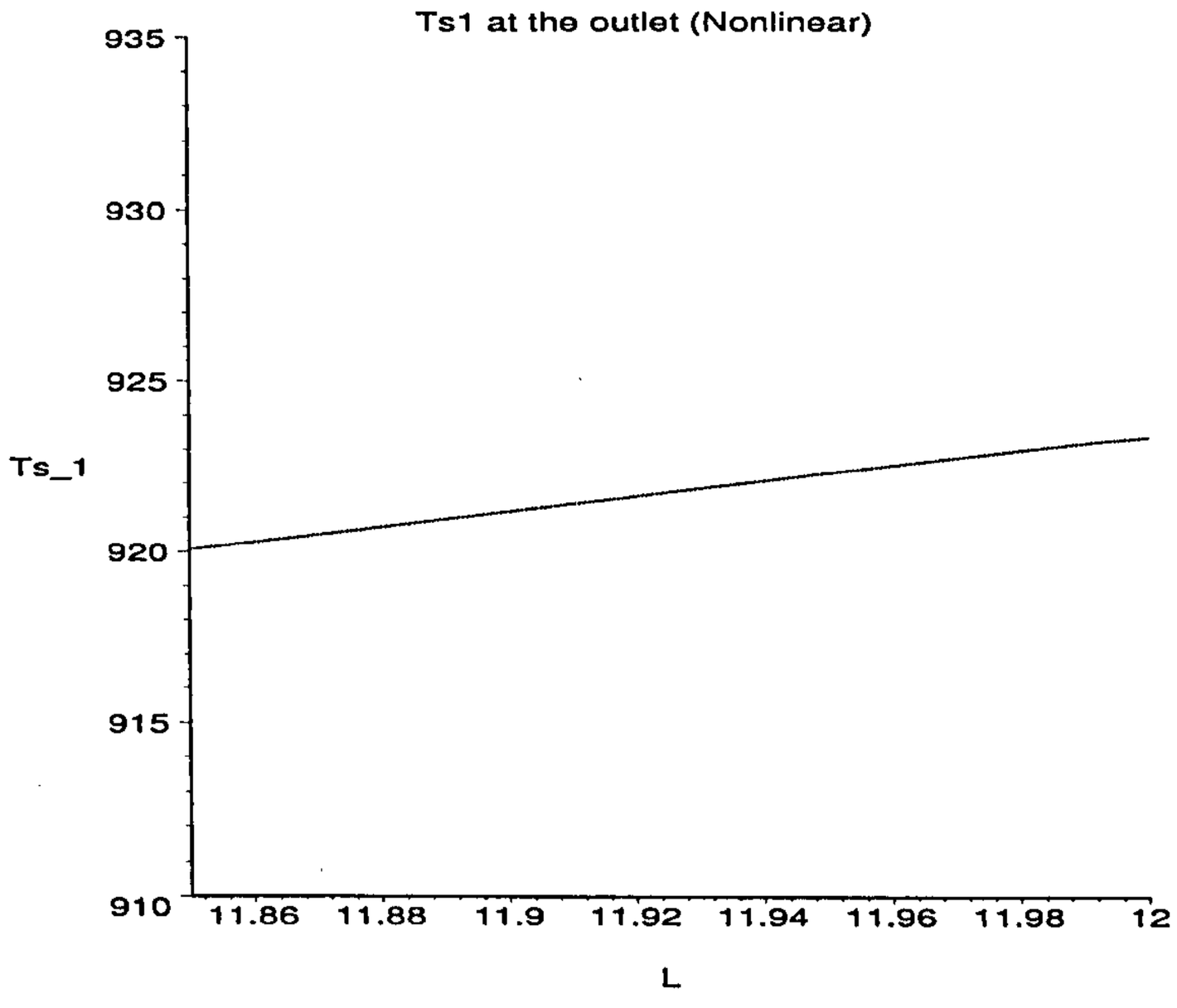

Figure 5.21: Boundary layer for the solid temperature at the outlet of the reformer channel.

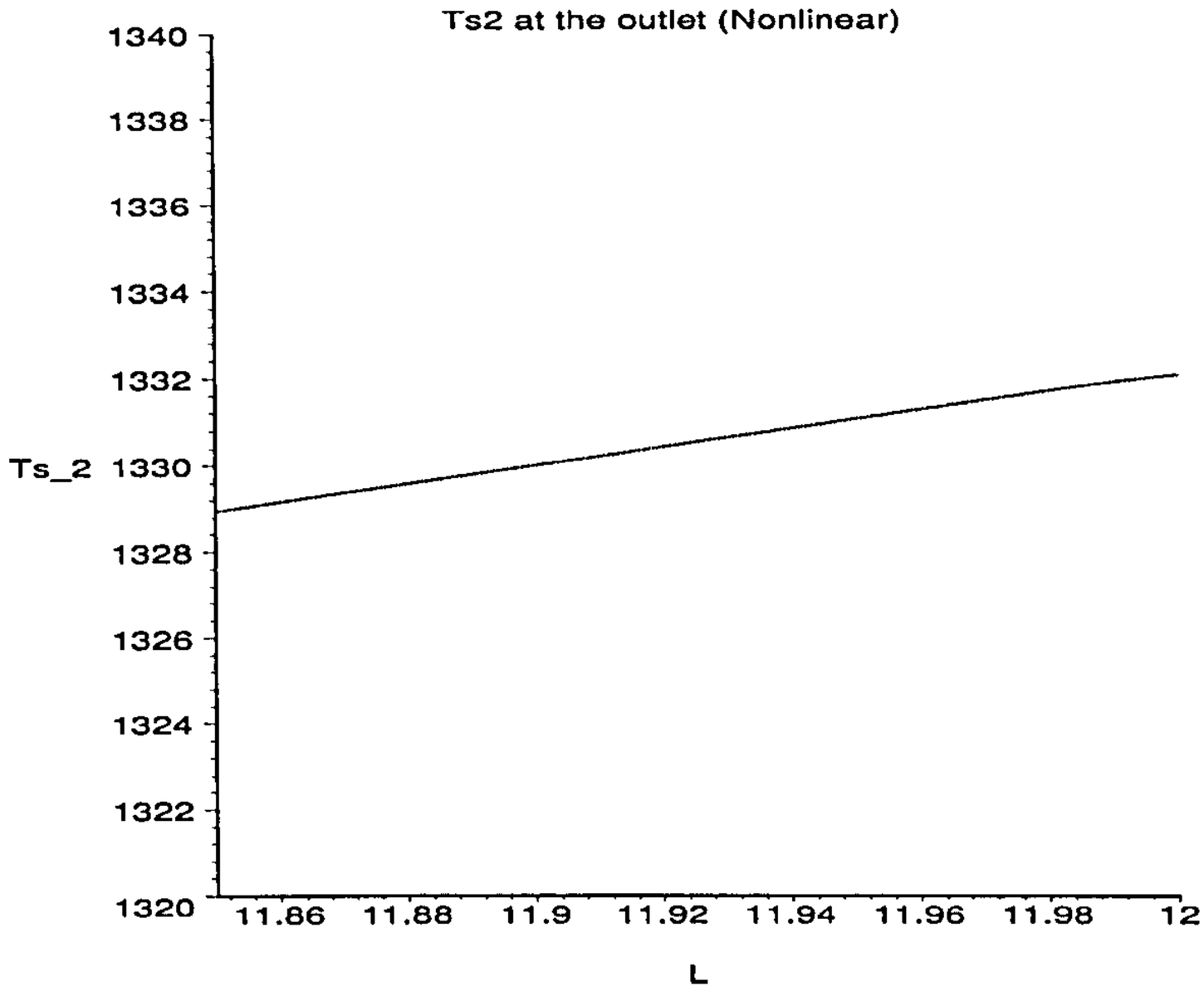

Figure 5.22: Boundary layer for the solid temperature at the outlet of the combustion channel.

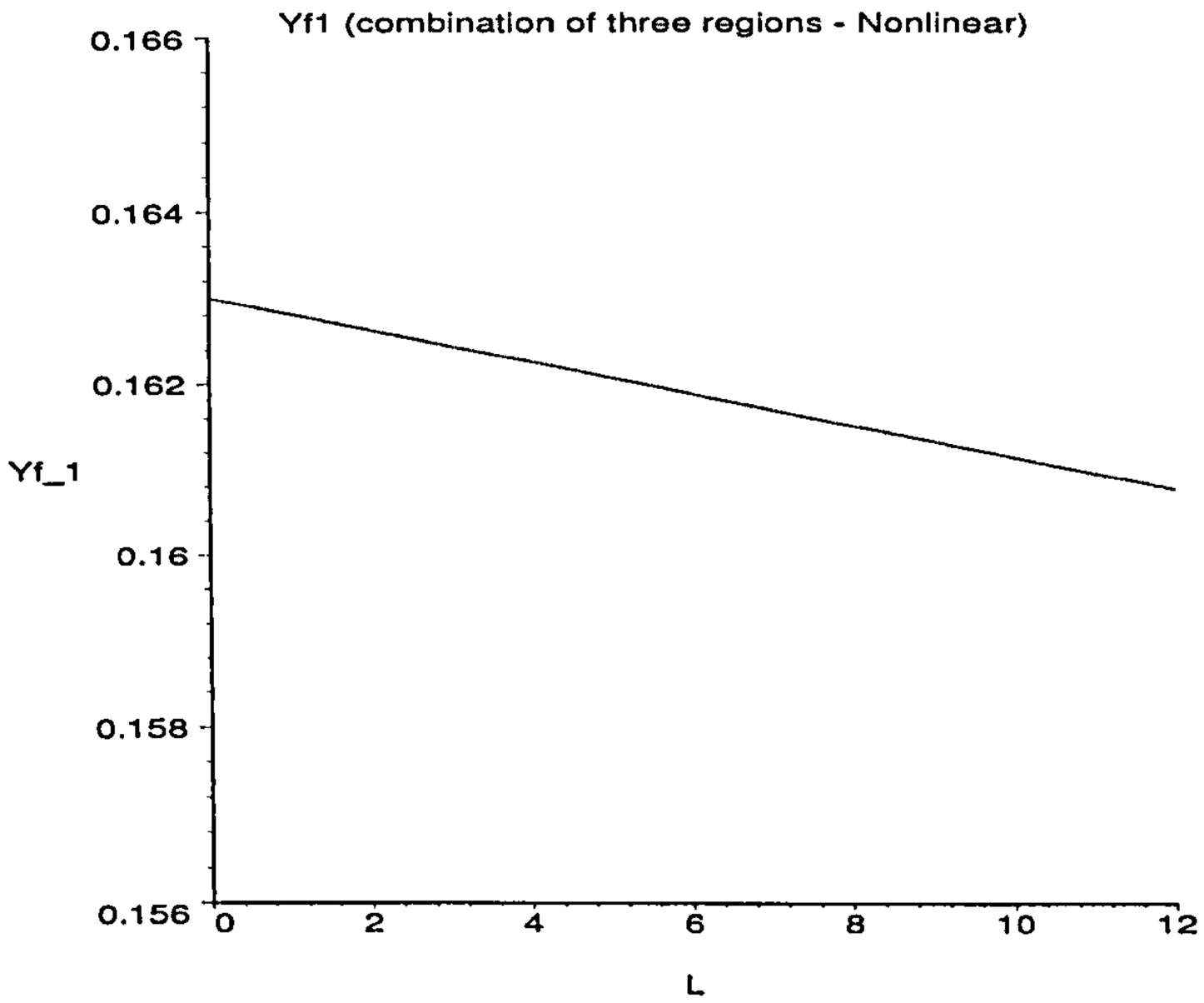

Figure 5.23: Full problem (combination of the results in region 1, region 2 and region 3) for the concentration of the fluid in the reformer channel.

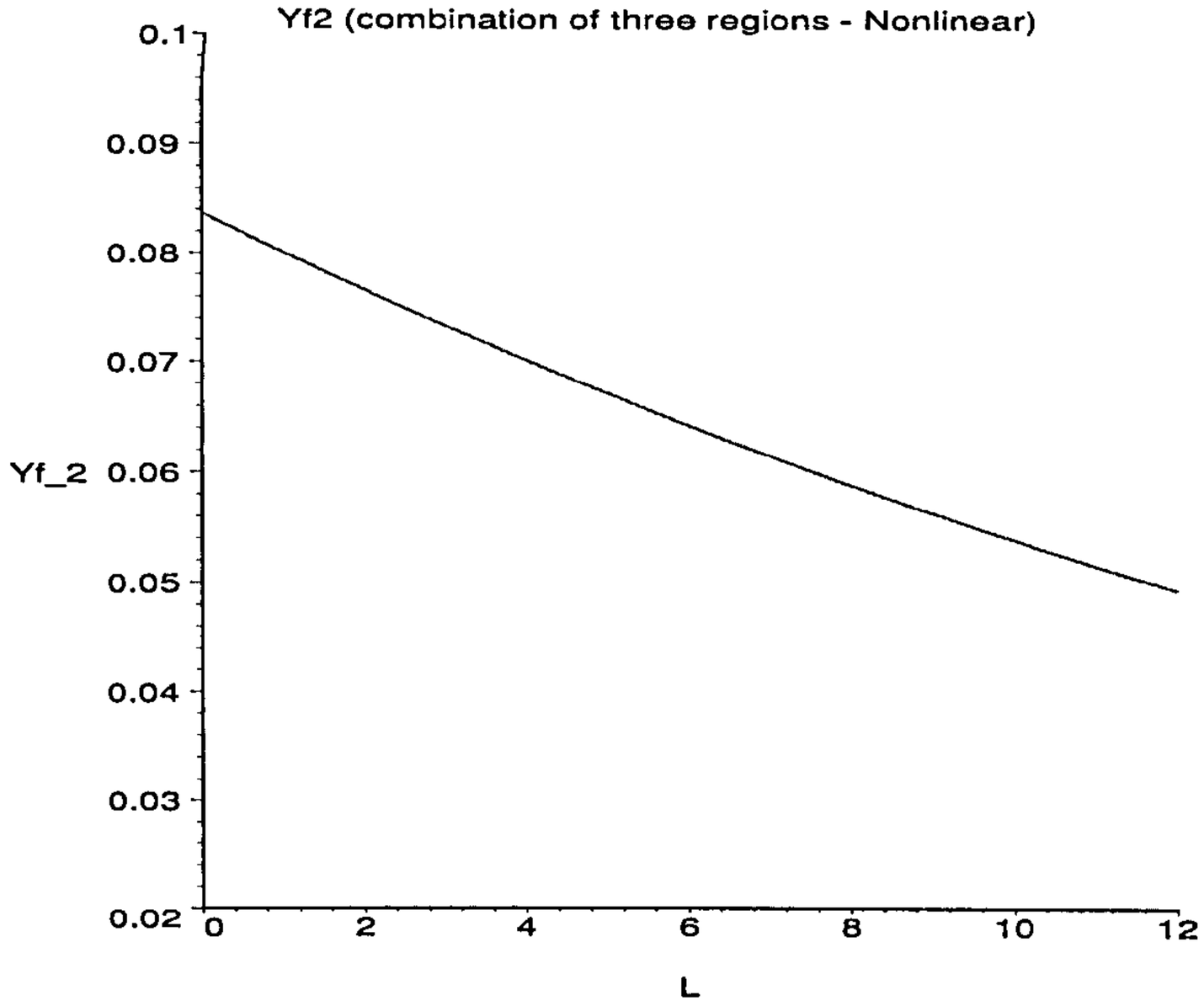

Figure 5.24: Full problem (combination of the results in region 1, region 2 and region 3) for the concentration of the fluid in the combustion channel.

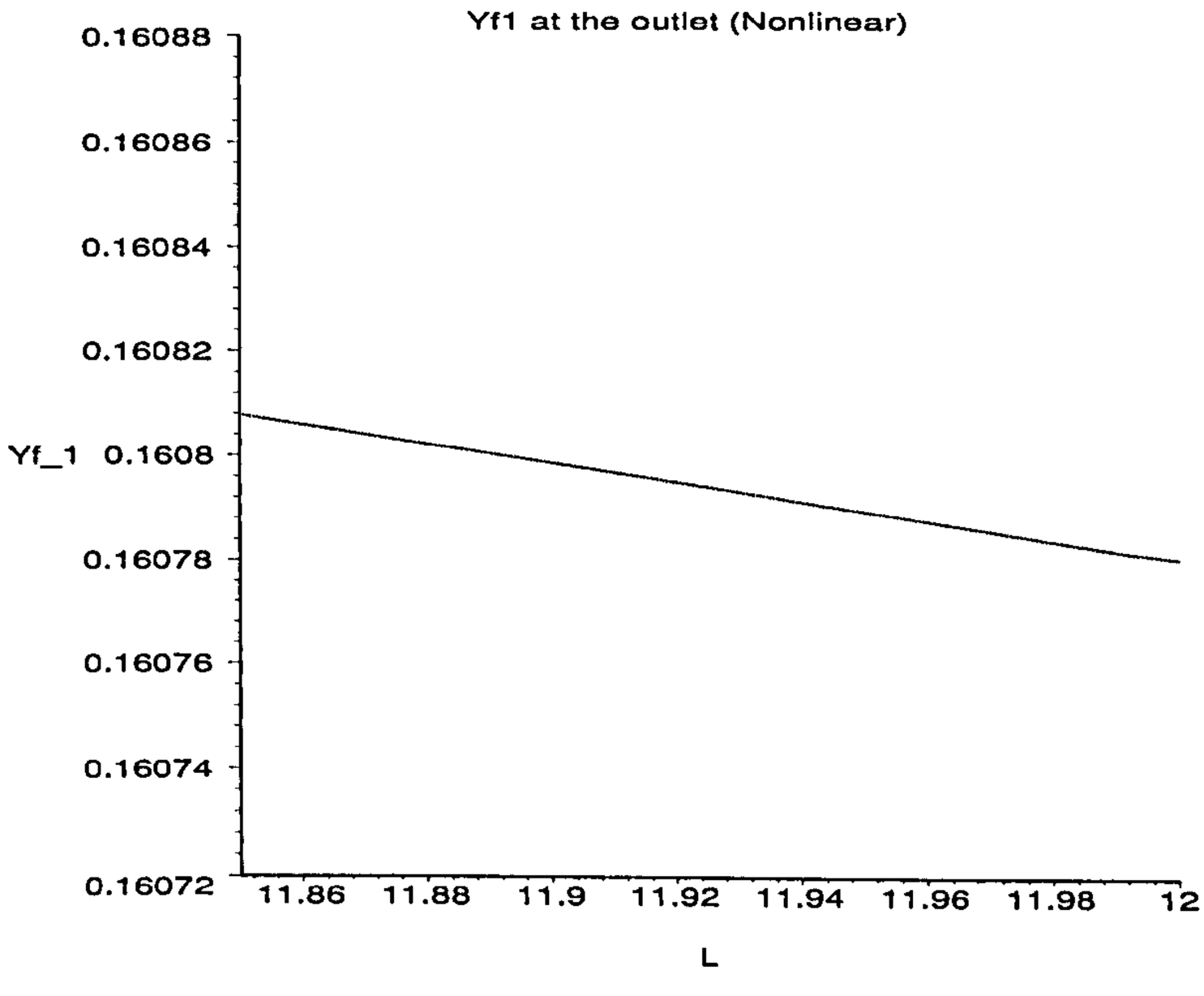

Figure 5.25: Boundary layer for the fluid concentration at the outlet of the reformer channel.

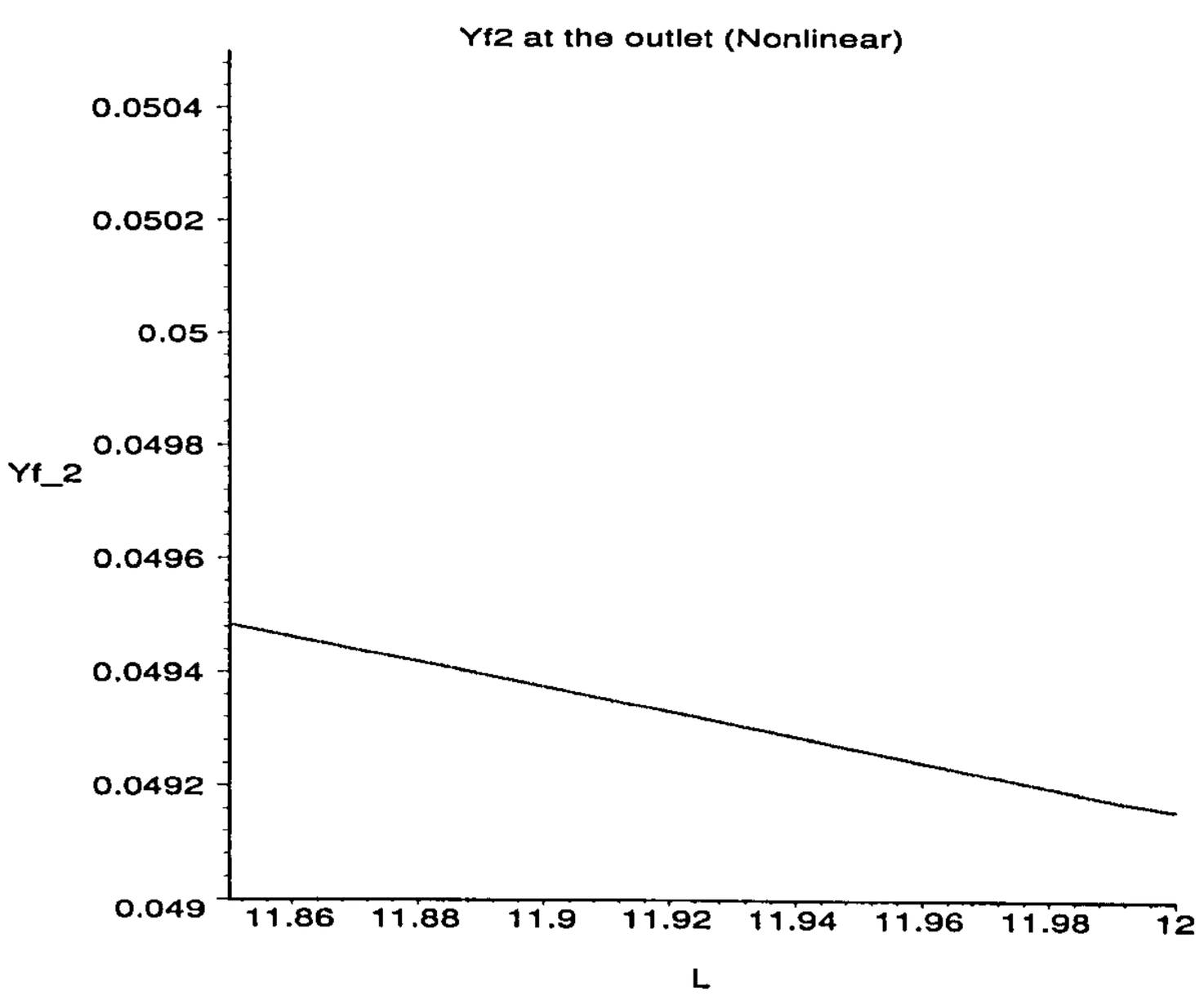

Figure 5.26: Boundary layer for the fluid concentration at the outlet of the combustion channel.

Chapter 6

Modelling a fluid flow through a packed bed channel of a catalytic reformer

6.1 Introduction

The purpose of the present chapter is to model in more detail the fluid flowing through the packed bed - we describe how the fluid flows through a channel that is randomly packed with pellets, see Figure 6.1, where the pellets are covered in a catalyst, which promotes the reaction taking place inside the channel. As before, we assume that the normalised thickness of the channel is ε, where $\varepsilon = D_w/D_C$, and D_w and D_C are the widths (in metres) of the wall and the channel respectively. First, our aim is to obtain averaged or what is known in the literature as *homogenised* (see, for example, [11], [12] and [50]) equations of motion for a fluid with averaged (*effective*) properties flowing through an 'unobstructed' channel. The model is such that the equations describe a real fluid flowing through a channel packed with pellets. To achieve this we consider two models: one that describes the real fluid (the properties of which we know) with a

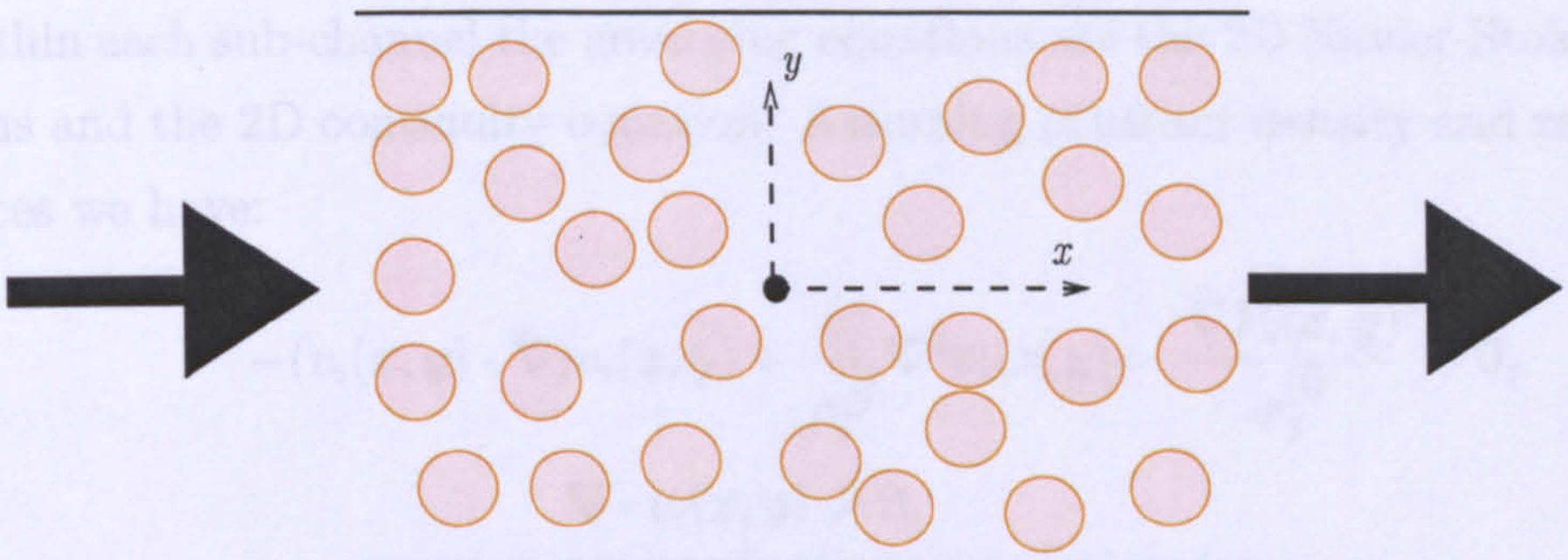

Figure 6.1: Fluid flow through a bed packed with catalytic pellets.

certain arrangement of pellets, and the other that describes a fluid with effective properties flowing in an unobstructed channel. We link the two models by assuming that the average velocity predicted by either model is the same for every cross-section of the channel. We then use an asymptotic technique, expanding the velocity and the pressure, to obtain an expression for the leading order terms of the averaged velocity across the homogenised channel. This allows us to write the homogenised equations of motion, and thus specify the effective properties, in terms of the properties of the real fluid.

6.2 Model 1: Real fluid, with a certain arrangement of pellets

Let the normalised thickness of the packed channel be ε. We assume that instead of having the pellets arranged as in Figure 6.1, they can be arranged to form N sub-channels of thickness $\varepsilon\alpha_i,\ i = 1, ..., N,\ \alpha_i < 1$, where the sub-channels are separated by horizontal layers of pellets. The fluid flows through the N sub-channels, i.e. the fluid passes between the layers, see Figure 6.2.

The 2D velocity of the fluid in each sub-channel is denoted by

$$v_i = (v_{1i}, v_{2i}),\ i = 1, ..., N.$$

Within each sub-channel the governing equations are the 2D Navier-Stokes equations and the 2D continuity equation. Assuming constant density and zero body forces we have:

$$-(v_i(x,y)\cdot\nabla)v_i(x,y)+\frac{\eta_i^*}{\rho_f^{(i)}}\nabla^2 v_i(x,y)-\frac{\nabla P_i(x,y)}{\rho_f^{(i)}}=0, \qquad (6.2.1)$$

$$\nabla\cdot v_i(x,y)=0, \qquad (6.2.2)$$

$$i=1,...,N, \quad -\infty<x<\infty, \quad y_i\in\left(-\frac{\varepsilon\alpha_i}{2},\frac{\varepsilon\alpha_i}{2}\right),$$

where the viscosity η_i^* of the fluid in each sub-channel is small ($\eta_i^*=\varepsilon^2\eta_i$, η_i is of order $O(1)$), and in each sub-channel $\rho_f^{(i)}$ is the fluid density and P_i is the pressure of the fluid, $i=1,...,N$. We introduce a scaled variable τ_i in each sub-channel

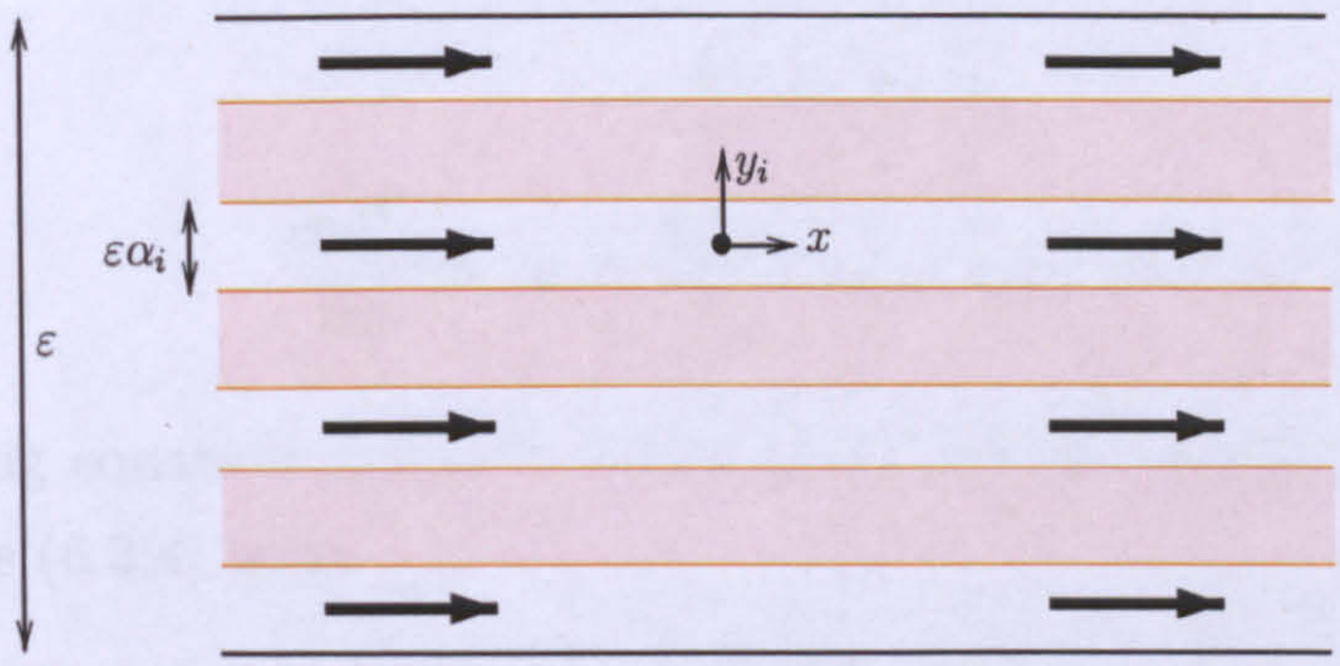

Figure 6.2: Pellets arranged to form horizontal 'obstacles' in the flow.

such that

$$\tau_i=\frac{y_i}{\varepsilon},\ \tau_i\in\left(-\frac{\alpha_i}{2},\ \frac{\alpha_i}{2}\right),\ i=1,...,N.$$

We also assume non-slip boundary conditions (zero velocity) which, in the scaled variable, gives

$$v_i\left(x,\frac{\alpha_i}{2}\right)=v_i\left(x,-\frac{\alpha_i}{2}\right)=0. \qquad (6.2.3)$$

We expand the velocity and the pressure asymptotically as follows:

$$v_i(x,\tau_i) = v_i^{(0)}(x,\tau_i) + \varepsilon v_i^{(1)}(x,\tau_i) + \varepsilon^2 v_i^{(2)}(x,\tau_i) + \dots ,$$
$$P(x,\tau_i) = P^{(0)}(x,\tau_i) + \varepsilon P^{(1)}(x,\tau_i) + \varepsilon^2 P^{(2)}(x,\tau_i) + \dots , \quad i = 1, \dots, N. \tag{6.2.4}$$

Rewriting the continuity equation (6.2.2) in terms of the scaled coordinate τ_i gives

$$\nabla \cdot v_i(x,\tau_i) = \frac{\partial v_{1i}}{\partial x}(x,\tau_i) + \frac{1}{\varepsilon}\frac{\partial v_{2i}}{\partial \tau_i}(x,\tau_i), \quad i = 1, \dots, N. \tag{6.2.5}$$

Substituting the expansion for the velocity from (6.2.4) into (6.2.5) and the boundary conditions (6.2.3), for the first two terms of the asymptotic expansion of the velocity we obtain

$$v_{2i}^{(0)}(x,\tau_i) \equiv 0, \tag{6.2.6}$$

$$\frac{\partial v_{1i}^{(0)}}{\partial x}(x,\tau_i) + \frac{\partial v_{2i}^{(1)}}{\partial \tau_i}(x,\tau_i) = 0, \quad i = 1, \dots, N. \tag{6.2.7}$$

Rewriting equation (6.2.1) in terms of the scaled variable, and substituting expansions (6.2.4) gives

$$-\Big[(v_i^{(0)}(x,\tau_i) + \varepsilon v_i^{(1)}(x,\tau_i) + \dots) \cdot \Big(\frac{\partial}{\partial x}, \frac{1}{\varepsilon}\frac{\partial}{\partial \tau_i}\Big)\Big](v_i^{(0)}(x,\tau_i) + \varepsilon v_i^{(1)}(x,\tau_i) + \dots)$$
$$+ \frac{\varepsilon^2 \eta_i}{\rho_f^{(i)}}\Big(\frac{\partial^2}{\partial x^2} + \frac{1}{\varepsilon^2}\frac{\partial^2}{\partial \tau_i^2}\Big)(v_i^{(0)}(x,\tau_i) + \varepsilon v_i^{(1)}(x,\tau_i) + \dots)$$
$$-\frac{1}{\rho_f^{(i)}}\Big(\frac{\partial}{\partial x}, \frac{1}{\varepsilon}\frac{\partial}{\partial \tau_i}\Big)(P_i^{(0)}(x,\tau_i) + \varepsilon P_i^{(1)}(x,\tau_i) + \dots) = 0, \quad i = 1, \dots, N.$$

Equating coefficients and using (6.2.6) we obtain, for the leading order term,

$$-\frac{1}{\rho_f^{(i)}}\frac{\partial P_i^{(0)}}{\partial \tau_i}(x,\tau_i) = 0,$$

which implies that $P_i^{(0)}$ does not depend on τ_i, $i = 1, ..., N$. For the term of order $O(1)$ we have

$$-v_{1i}^{(0)}(x,\tau_i)\frac{\partial v_{1i}^{(0)}}{\partial x}(x,\tau_i)\mathbf{e}^{(1)} - v_{2i}^{(1)}(x,\tau_i)\frac{\partial v_{1i}^{(0)}}{\partial \tau_i}(x,\tau_i)\mathbf{e}^{(1)}$$
$$+\frac{\eta_i}{\rho_f^{(i)}}\frac{\partial^2 v_{1i}^{(0)}}{\partial \tau_i^2}(x,\tau_i)\mathbf{e}^{(1)} - \frac{1}{\rho_f^{(i)}}\frac{\partial P_i^{(0)}}{\partial x}(x)\mathbf{e}^{(1)} - \frac{1}{\rho_f^{(i)}}\frac{\partial P_i^{(1)}}{\partial \tau_i}(x,\tau_i)\mathbf{e}^{(2)} = 0,$$

where $\mathbf{e}^{(j)}$, $j = 1, 2$, are unit vectors parallel to the $x-$ and $y-$ axes. We therefore obtain the following relationships

$$P_i^{(0)} = P_i^{(0)}(x), \qquad P_i^{(1)} = P_i^{(1)}(x),$$
$$v_{1i}^{(0)}(x,\tau_i)\frac{\partial v_{1i}^{(0)}}{\partial x}(x,\tau_i) + v_{2i}^{(1)}(x,\tau_i)\frac{\partial v_{1i}^{(0)}}{\partial \tau_i}(x,\tau_i)$$
$$-\frac{\eta_i}{\rho_f^{(i)}}\frac{\partial^2 v_{1i}^{(0)}}{\partial \tau_i^2}(x,\tau_i) + \frac{1}{\rho_f^{(i)}}\frac{dP_i^{(0)}}{dx}(x) = 0, \ i = 1, ..., N. \tag{6.2.8}$$

6.2.1 Linearised Navier-Stokes equation

From the governing equations (6.2.1) and (6.2.2) we obtained equations (6.2.7) and (6.2.8). We assume that the velocity and any derivatives of the velocity are small, i.e. any product of v_i and its derivatives is negligible. This implies that the term $[-(v_i(x,\tau_i)\cdot\nabla)v_i(x,\tau_i)]$ in equation (6.2.1) can be neglected. As a consequence, equation (6.2.7) and the modified form of (6.2.8) are given by

$$\frac{\partial v_{2i}^{(1)}}{\partial \tau_i}(x,\tau_i) = -\frac{\partial v_{1i}^{(0)}}{\partial x}(x,\tau_i),$$
$$\frac{\partial^2 v_{1i}^{(0)}}{\partial \tau_i^2}(x,\tau_i) = \frac{1}{\eta_i}\frac{dP_i^{(0)}}{dx}(x), \ i = 1, ..., N. \tag{6.2.9}$$

Solving (6.2.9) gives

$$v_{1i}^{(0)}(x,\tau_i) = \frac{\Lambda_i(x)}{2}\tau_i^2 + S_i^A(x)\tau_i + S_i^B(x), \ i = 1, ..., N.$$

Here

$$\Lambda_i(x) = \frac{1}{\eta_i}\frac{dP_i^{(0)}}{dx},\ i = 1, ..., N.$$

The functions $S_i^A(x)$ and $S_i^B(x)$ are obtained from the non-slip conditions (6.2.3) on the boundaries of each sub-channel, giving

$$v_{1i}^{(0)}(x, \tau_i) = \frac{\Lambda_i(x)}{8}(4\tau_i^2 - \alpha_i^2),\ i = 1, ..., N.$$

Therefore, to leading order, the vertical component of the velocity in each sub-channel is zero and the horizontal component has a parabolic profile (compare with experimental studies on catalytic reactors by Hayes and Kolaczkowski [45], Zanfir [95] and Zanfir *et al.* [96]). Our objective is to compare the average velocities across the entire channel in the two models. The average velocity, denoted by $\tilde{v}_{1i}^{(0)}(x, \tau_i),\ i = 1, ..., N$, in each sub-channel, is

$$\tilde{v}_{1i}^{(0)}(x, \tau_i) = \frac{1}{\alpha_i}\int_{-\alpha_i/2}^{\alpha_i/2}\frac{\Lambda_i(x)}{8}(4\tau_i^2 - \alpha_i^2)d\tau_i = -\frac{\Lambda_i(x)\alpha_i^2}{12}, \qquad (6.2.10)$$

$$\Lambda_i(x) = \frac{1}{\eta_i}\frac{dP_i^{(0)}}{dx}(x),\quad i = 1, ..., N.$$

The average velocity, across the entire channel denoted by $\tilde{V}$, is obtained from the following:

$$\text{Normalised width} \cdot \tilde{V}(x, \tau_i) = 1 \cdot \tilde{V}(x, \tau_i) = \sum_{i=1}^{N}\tilde{v}_{1i}^{(0)}(x, \tau_i)\alpha_i. \qquad (6.2.11)$$

We assume that all sub-channels are of equal widths, with identical flow in each one of them. In what follows we use the notations

$$\tilde{v}_{1i}^{(0)} = \tilde{v},\quad \alpha_i = \tilde{\alpha},\quad \Lambda_i(x) = \tilde{\Lambda}(x),\quad \eta_i = \tilde{\eta},\quad P_i^{(0)} = \tilde{P}\ \ \forall\, i,\ i = 1, ..., N.$$

Therefore, equation (6.2.10) becomes

$$\tilde{v}(x, \tau_i) = -\frac{\tilde{\Lambda}(x)\ \tilde{\alpha}^2}{12},\quad \tilde{\Lambda}(x) = \frac{1}{\tilde{\eta}}\frac{d\tilde{P}}{dx}, \qquad (6.2.12)$$

where the pressure gradient along the channel is negative. This gives the average (flat) velocity profile across each sub-channel. This means that the average velocity across the entire channel, using (6.2.11), is

$$1 \cdot \tilde{V}(x,\tau_i) = \sum_{i=1}^{N} \tilde{v}_{1i}^{(0)}(x,\tau_i)\alpha_i = N\tilde{v}(x,\tau_i)\tilde{\alpha} = -\frac{N\tilde{\Lambda}(x)\,\tilde{\alpha}^3}{12}, \qquad (6.2.13)$$

giving

$$\tilde{V}(x,\tau_i) = -\frac{N\tilde{\Lambda}(x)\tilde{\alpha}^3}{12}, \quad \tilde{\Lambda}(x) = \frac{1}{\tilde{\eta}}\frac{d\tilde{P}}{dx} \quad \text{where} \quad \frac{d\tilde{P}}{dx} < 0.$$

6.3 Model 2: Homogenised fluid

We now consider the flow of fluid through an infinite channel of thickness ε. We assume that the flow in the channel is 'homogenised', see Figure 6.3, in such a way that the Navier-Stokes equation of motion has an extra term to account for the presence of the pellets (see, for example, [3], [4], [12], [16], [24], [44] and [62]). The fluid is described as an incompressible Newtonian fluid. The governing

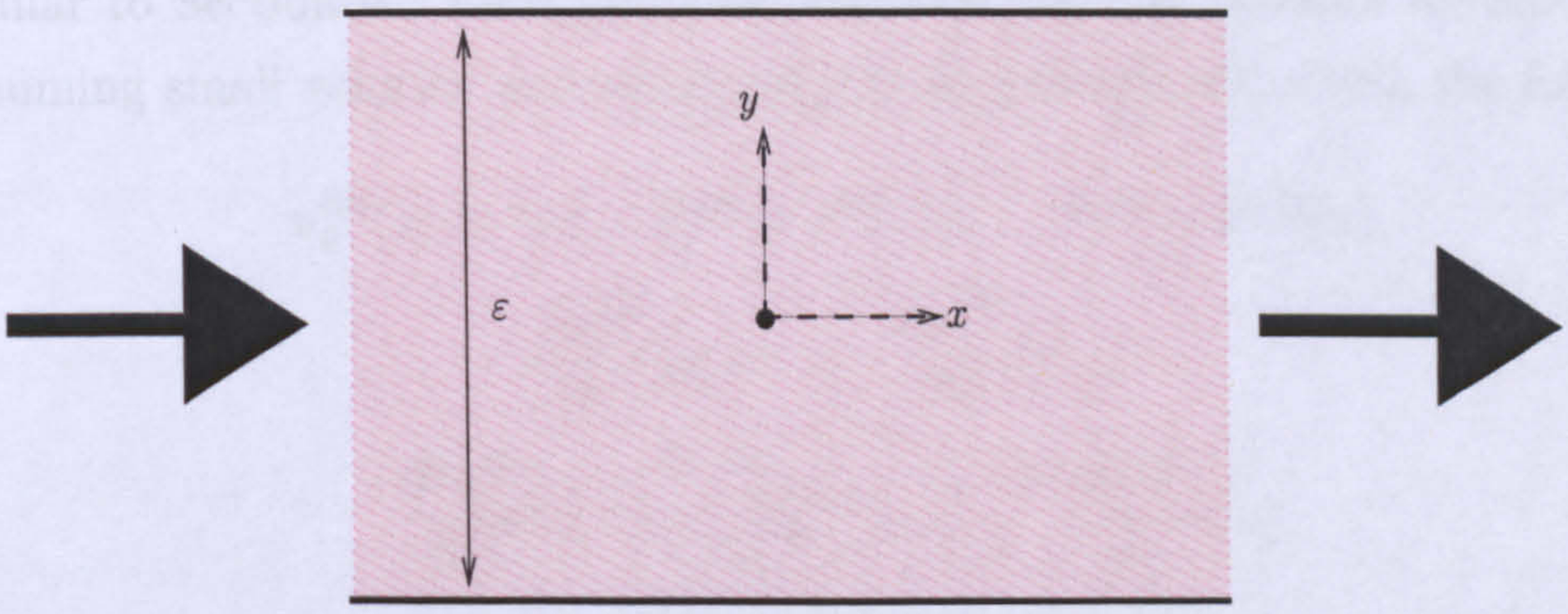

Figure 6.3: 'Homogenised' channel.

equations are the continuity equation and the modified Navier-Stokes equation.

Here $u = (u_1, u_2)$ represents the velocity in the 'homogenised' channel:

$$-(u(x,y)\cdot\nabla)u(x,y)+\frac{\eta^*}{\rho_f}\nabla^2 u(x,y)-\frac{\nabla P(x,y)}{\rho_f}-\frac{\eta^* u(x,y)}{\rho_f\ \kappa^*}=0, \quad (6.3.14)$$

$$\nabla\cdot u(x,y)=0, \quad (6.3.15)$$

$$-\infty < x < \infty, \quad y \in \left(-\frac{\varepsilon}{2}, \frac{\varepsilon}{2}\right),$$

where the viscosity η^* and the permeability κ^* of the fluid are both assumed to be small ($\eta^* = \varepsilon^2\eta$, $\kappa^* = \varepsilon^2\kappa$, where η and κ are of order $O(1)$), ρ_f is the density and P is the pressure of the fluid. We introduce a scaled variable, τ, such that,

$$\tau = \frac{y}{\varepsilon},\ \tau \in \left(-\frac{1}{2},\ \frac{1}{2}\right).$$

We also assume non-slip boundary conditions (zero velocity) which in the scaled variable is

$$u\left(x, \frac{1}{2}\right) = u\left(x, -\frac{1}{2}\right) = 0. \quad (6.3.16)$$

Similar to Section 6.2 we expand the velocity and the pressure asymptotically. Assuming small velocity and small velocity derivatives we obtain the following:

$$u_2^{(0)}(x,\tau)\equiv 0, \quad P^{(0)} = P^{(0)}(x), \quad P^{(1)} = P^{(1)}(x),$$

$$\frac{\partial u_2^{(1)}}{\partial\tau}(x,\tau) = -\frac{\partial u_1^{(0)}}{\partial x}(x,\tau),$$

$$\frac{\partial^2 u_1^{(0)}}{\partial\tau^2}(x,\tau) - \frac{1}{\kappa}u_1^{(0)}(x,\tau) = \frac{1}{\eta}\frac{dP^{(0)}}{dx}(x). \quad (6.3.17)$$

Assuming that the pressure gradient is given (and negative), we write equation (6.3.17) as

$$\frac{\partial^2 u_1^{(0)}}{\partial\tau^2}(x,\tau) - a u_1^{(0)}(x,\tau) = \Lambda(x), \qquad a = \frac{1}{\kappa}, \quad \Lambda(x) = \frac{1}{\eta}\frac{dP^{(0)}}{dx}(x), \quad (6.3.18)$$

where a is a constant, and $\Lambda(x)$ is a known function of x.
For large a, the second term in equation (6.3.18) is dominant in the main part of the channel far from the boundaries, and for such a case we have

$$u_1^{(0)}(x,\tau) = -\frac{\Lambda(x)}{a}, \quad \Lambda(x) = \frac{1}{\eta}\frac{dP^{(0)}}{dx}(x), \quad a = \frac{1}{\kappa}. \tag{6.3.19}$$

This directly corresponds to *Darcy's law.* (For a discussion on Darcy's law see Section 1.4.3.) When a is large we have a singularly perturbed problem (with a small coefficient in front of the second order term), such that

$$\frac{1}{a}\frac{\partial^2 u_1^{(0)}}{\partial \tau^2}(x,\tau) - u_1^{(0)}(x,\tau) = \frac{\Lambda(x)}{a}. \tag{6.3.20}$$

For a non-trivial solution the function in equation (6.3.19) is not enough on its own as the complete solution of (6.3.18) because it does not satisfy the boundary conditions (6.3.16). The solution of equation (6.3.20), regardless of the magnitude of a, with the non-slip boundary conditions is

$$u_1^{(0)}(x,\tau) = -\frac{\Lambda(x)}{a}\left[1 - \frac{\cosh(\sqrt{a}\tau)}{\cosh(\frac{\sqrt{a}}{2})}\right]. \tag{6.3.21}$$

This shows that away from the boundaries of the channel, to leading order, we have a flat velocity profile, corresponding to Darcy's law. Close to the boundaries the velocity changes exponentially in order to satisfy the non-slip conditions and the full result is given by (6.3.21).

For Hartmann flow (see Section 1.4.2 and [22], [57] and [66]), that is, for the flow between parallel plates of a magnetic fluid, where the space between the parallel plates is long and thin, the solution of the system corresponds exactly to the solution we have derived here for the velocity in the homogenised channel, given by (6.3.21). For a large Hartmann number there is an exponential decay in the velocity and the induced magnetic field near the plates. This is equivalent to solution (6.3.21) when the constant a is increased.

Using equation (6.3.21) we write the expression for the average velocity $\tilde{u}_1^{(0)}$, such that,

$$\tilde{u}_1^{(0)}(x,\tau) = \int_{-1/2}^{1/2} u_1^{(0)}(x,\tau)d\tau = \int_{-1/2}^{1/2} -\frac{\Lambda(x)}{a}\Big[1 - \frac{\cosh(\sqrt{a}\tau)}{\cosh(\frac{\sqrt{a}}{2})}\Big]d\tau$$

$$= -\frac{\Lambda(x)}{a}\Big[\tau - \frac{\sinh(\sqrt{a}\tau)}{\sqrt{a}\cosh(\frac{\sqrt{a}}{2})}\Big]_{-1/2}^{1/2} = -\frac{\Lambda(x)}{a} = -\frac{\kappa}{\eta}\frac{dP^{(0)}}{dx}(x). \quad (6.3.22)$$

In the scaled coordinate τ, the thickness of the channel is 1. Therefore the average velocity across each cross-section for the 'homogenised' channel is

$$\tilde{u}_1^{(0)}(x,\tau)\cdot 1 = -\frac{\kappa}{\eta}\frac{dP^{(0)}}{dx}. \quad (6.3.23)$$

6.4 Link between Model 1 and Model 2

Comparing (6.2.13) and (6.3.23) we can now write

$$\tilde{u}_1^{(0)}(x,\tau) = -\frac{\kappa}{\eta}\frac{dP^{(0)}}{dx} = \tilde{V}(x,\tau) = -\frac{N\tilde{\Lambda}(x)\ \tilde{\alpha}^3}{12}, \quad (6.4.24)$$

and therefore,

$$\frac{\kappa}{\eta} = \frac{N\tilde{\Lambda}(x)\ \tilde{\alpha}^3}{12\frac{dP^{(0)}}{dx}}, \qquad \tilde{\Lambda}(x) = \frac{1}{\tilde{\eta}}\frac{d\tilde{P}}{dx}. \quad (6.4.25)$$

If we assume that the pressure gradient for the homogenised fluid is equal to that of the real fluid, i.e.

$$\frac{dP^{(0)}}{dx} = \frac{d\tilde{P}}{dx}$$

then equation (6.4.25) can be rewritten as

$$\frac{\kappa}{\eta} = \frac{N\tilde{\alpha}^3}{12\tilde{\eta}}. \quad (6.4.26)$$

The quantities on the right hand side of equation (6.4.26) are given for the real fluid. Thus, we have computed the constant in Darcy's law. For the full solution we still need to compute the constant a. In order to find this constant we assume that the viscosity of the homogenised fluid is equal to that of the real fluid, that is,

$$\eta_i^* = \varepsilon^2 \eta_i = \varepsilon^2 \tilde{\eta} = \eta^* = \varepsilon^2 \eta. \tag{6.4.27}$$

Using (6.4.26) and (6.4.27) we rewrite equation (6.3.21), the leading order term of the horizontal component of the 'homogenised' velocity, as follows:

$$u_1^{(0)}(x,\tau) = -\frac{N\tilde{\alpha}^3}{12\tilde{\eta}} \frac{d\tilde{P}}{dx} \left[1 - \frac{\cosh(\sqrt{a}\tau)}{\cosh(\sqrt{a}/2)}\right], \tag{6.4.28}$$

where

$$\sqrt{a} = 2\sqrt{\frac{3}{N\tilde{\alpha}^3}}.$$

We also find that the linearised form of the equation of motion for the 'homogenised' channel (equation (6.3.14) without the $[-(u(x,y)\cdot\nabla)u(x,y)]$ term), can be rewritten in terms of the given properties of the real fluid, such that,

$$\tilde{\eta^*}\nabla^2 u(x,\tau) - \nabla\tilde{P}(x) - \frac{\tilde{\eta}^* u(x,\tau)}{\varepsilon^2\left(\frac{N\tilde{\alpha}^3}{12}\right)} = 0, \; y \in \left(-\frac{\varepsilon}{2}, \frac{\varepsilon}{2}\right), \; (-\infty < x < \infty). \tag{6.4.29}$$

Therefore equation (6.4.29) gives the final form of the linearised equation of motion with its solution, given by (6.4.28), in terms of known properties, which describes a flat velocity profile in the main part of the homogenised channel, with exponentially decreasing velocity at the boundaries.

6.4.1 Extension to Model 1:

Sub-channels of different widths

In this section we generalise Model 1 (discussed in Section 6.2), to the case when sub-channels have different widths. We analyse the effect of this modification on

the constant in Darcy's law associated with the homogenised channel (discussed in Sections 6.3 and 6.4). We denote this constant in Darcy's law for the case when all the sub-channels are of equal width (compare with (6.4.26)) by

$$\left(\frac{\kappa}{\eta}\right)^* = \frac{N\tilde{\alpha}^3}{12\tilde{\eta}}. \tag{6.4.30}$$

We now assume that we have two sets of sub-channels: n sub-channels of width $\tilde{\Pi}$ and $N-n$ sub-channels of width $\tilde{\alpha}$ (see Figure 6.4 for an arrangement of this type). Here $\tilde{\alpha}$ is the same as in the previous sections: the width of a sub-channel in the case when all the sub-channels are of equal width.

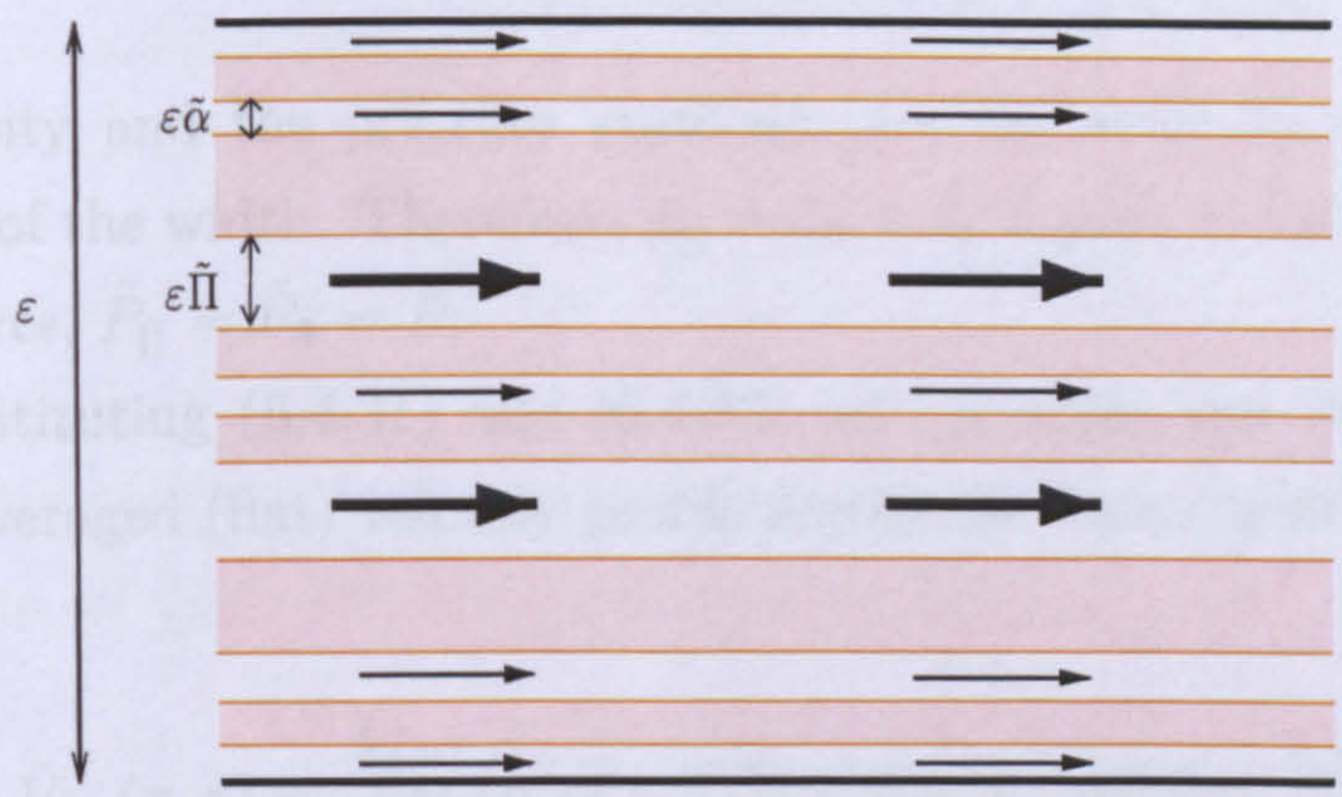

Figure 6.4: Pellets arranged to form horizontal 'obstacles' in the flow (pellets of different sizes).

We assume that all the sub-channels of equal width have identical flow in each one of them.

Similar to Section 6.2 we obtain the following for the average velocities across the entire channel:

Average velocity across a sub-channel of width $\tilde{\Pi}$:

$$\tilde{v}_{\tilde{\Pi}}(x,\tau) = -\frac{\tilde{\Lambda}_{\tilde{\Pi}}(x)\ \tilde{\Pi}^2}{12}, \quad \tilde{\Lambda}_{\tilde{\Pi}}(x) = \frac{1}{\tilde{\eta}_{\tilde{\Pi}}}\frac{d\tilde{P}_{\tilde{\Pi}}}{dx}, \tag{6.4.31}$$

Average velocity across a sub-channel of width $\tilde{\alpha}$:

$$\tilde{v}_{\tilde{\alpha}}(x,\tau) = -\frac{\tilde{\Lambda}_{\tilde{\alpha}}(x)\,\tilde{\alpha}^2}{12}, \quad \tilde{\Lambda}_{\tilde{\alpha}}(x) = \frac{1}{\tilde{\eta}_{\tilde{\alpha}}}\frac{d\tilde{P}_{\tilde{\alpha}}}{dx}, \tag{6.4.32}$$

where, as before, the pressure gradients are negative.

Therefore, the average velocity across the entire channel, $\tilde{V}_{\tilde{\Pi}\tilde{\alpha}}$ is, (compare with (6.2.11) and (6.2.13)),

$$\begin{aligned} 1 \cdot \tilde{V}_{\tilde{\Pi}\tilde{\alpha}}(x,\tau) &= \sum_{i=1}^{n} \tilde{v}^{(0)}_{\tilde{\Pi}i}(x,\tau)\Pi_i + \sum_{j=n}^{N} \tilde{v}^{(0)}_{\tilde{\alpha}j}(x,\tau)\alpha_j \\ &= n \cdot \tilde{\Pi}\tilde{v}_{\tilde{\Pi}}(x,\tau) + (N-n)\cdot\tilde{\alpha}\tilde{v}_{\tilde{\alpha}}(x,\tau). \end{aligned} \tag{6.4.33}$$

The viscosity and the pressure gradients are the same in every sub-channel, regardless of the width. Therefore, $\tilde{\eta}_{\tilde{\Pi}} = \tilde{\eta}_{\tilde{\alpha}} = \tilde{\eta}$, $\tilde{\Lambda}_{\tilde{\Pi}}(x) = \tilde{\Lambda}_{\tilde{\alpha}}(x) = \tilde{\Lambda}(x)$, and for the pressures, $\tilde{P}_{\tilde{\Pi}} = \tilde{P}_{\tilde{\alpha}} = \tilde{P}$.

Thus, substituting (6.4.31) and (6.4.32) into (6.4.33) and rearranging we find that the averaged (flat) velocity profile across the entire width of the channel is given by

$$\tilde{V}_{\tilde{\Pi}\tilde{\alpha}}(x,\tau) = \frac{\tilde{\Lambda}(x)}{12}(n(\tilde{\alpha}^3 - \tilde{\Pi}^3) - N\tilde{\alpha}^3), \quad \tilde{\Lambda}(x) = \frac{1}{\tilde{\eta}}\frac{d\tilde{P}}{dx}. \tag{6.4.34}$$

Now we compare the average velocity across the homogenised channel and the average velocity when there are sub-channels of different widths, by equating (6.3.23) and (6.4.34). We also assume that the pressure gradient for the homogenised channel is the same as that for the real fluid, similar to (6.4.26), and we find that

$$\frac{\kappa}{\eta} = \frac{1}{12\tilde{\eta}}(n(\tilde{\Pi}^3 - \tilde{\alpha}^3) + N\tilde{\alpha}^3). \tag{6.4.35}$$

This is the modified version of the constant involved in Darcy's law (compare with (6.4.30), the constant for the case when all the widths are the same.)

From (6.4.35) we see that, provided the pressure gradient stays the same, if sub-channels of width $\tilde{\alpha}$ are paired with sub-channels of a larger (smaller) width, then the constant in Darcy's law is larger (smaller) than the corresponding constant for the case when all the sub-channels are of equal width, that is

$$\text{For} \quad \tilde{\Pi} > \tilde{\alpha} \; : \quad \frac{\kappa}{\eta} > \left(\frac{\kappa}{\eta}\right)^*;$$

$$\text{For} \quad \tilde{\Pi} < \tilde{\alpha} \; : \quad \frac{\kappa}{\eta} < \left(\frac{\kappa}{\eta}\right)^*.$$

It is also worth noting that this particular work shows that the constant in Darcy's law is independent of the arrangement of the sub-channels: only the size of the sub-channels influences the constant in Darcy's law and the different sized sub-channels can be arranged in any arbitrary way.

Similarly, for sub-channels of three different widths, say n_1 sub-channels of width $\tilde{\mathcal{I}}$, n_2 sub-channels of width $\tilde{\mathcal{H}}$, and $N-(n_1+n_2)$ sub-channels of width $\tilde{\alpha}$, where the viscosity and (negative) pressure gradient are the same in every sub-channel, the constant in Darcy's law takes the modified form

$$\frac{\kappa}{\eta} = \frac{1}{12\tilde{\eta}}(n_1(\tilde{\mathcal{I}}^3 - \tilde{\alpha}^3) + n_2(\tilde{\mathcal{H}}^3 - \tilde{\alpha}^3) + N\tilde{\alpha}^3). \tag{6.4.36}$$

The criterion for this constant to be the same as the constant in the case when the sub-channels are of equal width (see Section 6.2), is given below

$$n_1\tilde{\mathcal{I}}^3 + n_2\tilde{\mathcal{H}}^3 = (n_1+n_2)\tilde{\alpha}^3. \tag{6.4.37}$$

Therefore,

$$\text{for} \quad \tilde{\mathcal{I}} > \tilde{\alpha} \text{ and } \tilde{\mathcal{H}} > \tilde{\alpha} \; : \quad \frac{\kappa}{\eta} > \left(\frac{\kappa}{\eta}\right)^*;$$

$$\text{for} \quad \tilde{\mathcal{I}} < \tilde{\alpha} \text{ and } \tilde{\mathcal{H}} < \tilde{\alpha} \; : \quad \frac{\kappa}{\eta} < \left(\frac{\kappa}{\eta}\right)^*;$$

and if equation (6.4.37) holds, for sub-channels of width $\tilde{\alpha}$ together with sub-channels of larger width and sub-channels of thinner width

$$\frac{\kappa}{\eta} = \left(\frac{\kappa}{\eta}\right)^*.$$

6.4.2 Discussion of the results

In this chapter we modelled the fluid flow through a packed bed channel and, for the 2D case, we obtained the homogenised equations of motion and the effective properties in terms of the known properties of a real fluid. We obtained an expression for the average velocity across the channel, which directly related to Darcy's law with an additional exponential term; this term corresponded to decaying boundary layers near the sides of the channel, in order to satisfy the non-slip boundary conditions. We also showed how this concept is directly related to Hartmann flow. We then discussed in detail the effect on the constant in Darcy's law of having different-sized pellets, and we showed that the change in this constant is independent of the arrangement of the layers of pellets.

In the next chapter we consider the effect of time dependence on the 1D system discussed in the earlier chapters. We plot the temperature and concentration distributions along the channels at several different time intervals. We present the example associated with the industrial case described in Chapter 3 as well as additional simulations to show the sensitivity to the initial and inlet boundary conditions.

Chapter 7

Time-dependent model

The full time dependent system of equations for the temperatures and the concentrations, which describes the energy and molar balances for the fluid and the solid phases is given below.

7.1 Transient equations

Fluid mole balance equations

$$a_3^{(i)}\frac{\partial^2 Y_f^{(i)}}{\partial x^2}(x,t) = a_4^{(i)}\frac{\partial Y_f^{(i)}}{\partial x}(x,t) + a_5^{(i)}Y_f^{(i)}(x,t)\left(1-\frac{a_1^{(i)}}{a_1^{(i)}+a_2^{(i)}\mathcal{A}^{(i)}e^{-\left(\frac{E^{(i)}}{R_g T_s^{(i)}(x,t)}\right)}}\right),$$

Fluid energy balance equations

$$a_6^{(i)}\frac{\partial^2 T_f^{(i)}}{\partial x^2}(x,t)-a_7^{(i)}\frac{\partial T_f^{(i)}}{\partial x}(x,t) + a_8^{(i)}(T_s^{(i)}(x,t)-T_f^{(i)}(x,t)) + a_9^{(i)}(T_w^{(i)}(x,t)-T_f^{(i)}(x,t))=0, \quad (7.1.1)$$

Solid energy balance equations

$$a_{10}^{(i)}\frac{\partial^2 T_s^{(i)}}{\partial x^2}(x,t) \quad - \quad a_{12}^{(i)}\frac{\partial T_s^{(i)}}{\partial t}(x,t) = a_8^{(i)}(T_s^{(i)}(x,t) - T_f^{(i)}(x,t))$$

$$+ \quad a_1^{(i)}a_{11}^{(i)}Y_f^{(i)}(x,t)\Big(1 - \frac{a_1^{(i)}}{a_1^{(i)} + a_2^{(i)}\mathcal{A}^{(i)}e^{-\left(\frac{E^{(i)}}{R_g T_s^{(i)}(x,t)}\right)}}\Big),$$

Equation for the temperature inside the wall

$$a_{13}\nabla^2 T^{(0)}(x,y,t) - a_{14}\frac{\partial T^{(0)}}{\partial t}(x,y,t) = 0. \tag{7.1.2}$$

The transient system of equations contains the time derivative in the equations for the solid temperatures but not in the equations for the fluid temperatures. The reason for this is that the speed of response of the fluid is several orders of magnitude higher than that for the solid (see, for example, [45]). Therefore the transient terms in the fluid phases are ignored and the corresponding equations are written in the steady state form. Inside the wall the temperature satisfies the heat equation. The industrial data used for the numerical simulations, the constants $a_j^{(i)}$, $i = 1, 2$, $j = 1, ..., 14$, and the coefficients in the reaction rates

$$(-R)_s^{(i)} = \mathcal{A}^{(i)}e^{\left(\frac{-E^{(i)}}{R_g T_s^{(i)}(x,t)}\right)}Y_s^{(i)}(x,t)$$

are given below. Inside the channels we have

$$\begin{aligned}
a_1^{(1)} &= 2426.51 \text{ mol/(m}^3 \text{ s)}, \quad a_2^{(1)} = 604.70 \text{ kg}_{\text{cat}}/\text{m}^3, \\
a_3^{(1)} &= 0.0053 \text{ m}^2/\text{s}, \quad a_4^{(1)} = 2.47 \text{ m/s}, \quad a_5^{(1)} = 6.06 \text{ s}^{-1}, \\
a_6^{(1)} &= 0.061 \text{ W/(m K)}, \quad a_7^{(1)} = 43515.47 \text{ W/(m}^2 \text{ K)}, \\
a_8^{(1)} &= 76513.19 \text{ W/(m}^3 \text{ K)}, \quad a_9^{(1)} = 6777.22 \text{ W/(m}^3 \text{ K)}, \\
a_{10}^{(1)} &= 0.22 \text{ W/(m K)}, \quad a_{11}^{(1)} = 206000 \text{ J/mol}, \\
a_{12}^{(1)} &= \rho_{cat}^{(1)}C_{p_{cat}}^{(1)} = 118150 \text{ J/(m}^3 \text{ K)}, \\
\mathcal{A}^{(1)} &= 0.778 \text{ mol/(kg}_{\text{cat}} \text{ s)}, \quad E^{(1)}/R_g = 4416.65 \text{ K}^{-1},
\end{aligned}$$

$$
\begin{aligned}
a_1^{(2)} &= 2136.21 \text{ mol}/(\text{m}^3 \text{ s}), \quad a_2^{(2)} = 604.70 \text{ kg}_{\text{cat}}/\text{m}^3, \\
a_3^{(2)} &= 0.0048 \text{ m}^2/\text{s}, \quad a_4^{(2)} = 2.24 \text{ m/s}, \quad a_5^{(2)} = 5.34 \text{ s}^{-1}, \\
a_6^{(2)} &= 0.054 \text{ W}/(\text{m K}), \quad a_7^{(2)} = 28700.67 \text{ W}/(\text{m}^2 \text{ K}), \\
a_8^{(2)} &= 68722.95 \text{ W}/(\text{m}^3 \text{ K}), \quad a_9^{(2)} = 7834.57 \text{ W}/(\text{m}^3 \text{ K}), \\
a_{10}^{(2)} &= 0.22 \text{ W}/(\text{m K}), \quad a_{11}^{(2)} = -802000 \text{ J/mol}, \\
a_{12}^{(2)} &= \rho_{cat}^{(2)} C_{p_{cat}}^{(2)} = 3037050 \text{ J}/(\text{m}^3 \text{ K}), \\
\mathcal{A}^{(2)} &= 0.0794 \text{ mol}/(\text{kg}_{\text{cat}} \text{ s}), \quad E^{(2)}/R_g = 132.31 \text{ K}^{-1}, \qquad (7.1.3)
\end{aligned}
$$

and inside the wall we have

$$
a_{13} = k_w = 1.5 \text{ W}/(\text{m K}), \quad a_{14} = \rho_w C_{p_w} = (79)(5.82) = 459.78 \text{ J}/(\text{m}^3 \text{ K}). \quad (7.1.4)
$$

7.1.1 Boundary conditions

The boundary conditions remain the same as those in the steady state case (see Chapters 3 - 5):

$$
\begin{aligned}
&Y_f^{(1)}(0,t) = 0.163, \; T_f^{(1)}(0,t) = 733 \text{ K}, \; T_s^{(1)}(0,t) = 733 \text{ K}, \\
&Y_f^{(2)}(0,t) = 0.0836, \; T_f^{(2)}(0,t) = 733 \text{ K}, \; T_s^{(2)}(0,t) = 733 \text{ K}, \qquad (7.1.5)
\end{aligned}
$$

$$
\begin{aligned}
&\frac{dY_f^{(1)}}{dx}(12,t) = 0, \; \frac{dT_f^{(1)}}{dx}(12,t) = 0, \; \frac{dT_s^{(1)}}{dx}(12,t) = 0, \\
&\frac{dY_f^{(2)}}{dx}(12,t) = 0, \; \frac{dT_f^{(2)}}{dx}(12,t) = 0, \; \frac{dT_s^{(2)}}{dx}(12,t) = 0.
\end{aligned}
$$

7.1.2 Initial conditions

This transient problem also requires initial conditions. In this chapter we consider only those solutions which have a uniform distribution at time $t = 0$. For

convenience, we assume that the conditions at $t = 0$ are the same as the conditions at $x = 0$, that is,

$$Y_f^{(1)}(x,0) = 0.163,\ T_f^{(1)}(x,0) = 733\ \text{K},\ T_s^{(1)}(x,0) = 733\ \text{K},$$
$$Y_f^{(2)}(x,0) = 0.0836,\ T_f^{(2)}(x,0) = 733\ \text{K},\ T_s^{(2)}(x,0) = 733\ \text{K}.$$

7.2 Scaled variable and asymptotic approximations

Similar to Chapter 3, we introduce a dimensionless scaled variable $\tau_0 = y/(\varepsilon D_C)$. Here, as in the steady state case, the small parameter ε denotes the ratio of the width of the wall to the width of the channel, $\varepsilon = D_w/D_C$, where D_w and D_C are 0.00159 m and 0.0795 m respectively (see Chapter 3). Thus, in the new coordinate, equation (7.1.2) can be written as

$$\frac{\partial^2 T^{(0)}}{\partial x^2}(x,\tau_0) + \frac{1}{\varepsilon^2 D_C^2}\frac{\partial^2 T^{(0)}}{\partial \tau_0^2}(x,\tau_0) - \frac{a_{14}}{a_{13}}\frac{\partial T^{(0)}}{\partial t}(x,\tau_0,t) = 0, \quad (7.2.6)$$
$$x \in (0,12),\ \ \tau_0 \in \Big(-\frac{1}{2},\frac{1}{2}\Big).$$

We assume ideal thermal contact (continuity in temperature and heat flux) between the wall and the channels, that is,

$$\text{at } \tau_0 = \frac{1}{2}: \qquad T^{(0)}\Big(x,\frac{1}{2}\Big) = T_w^{(1)}(x), \quad (7.2.7)$$
$$k_w\frac{\partial T^{(0)}}{\partial n}\Big(x,\frac{1}{2}\Big) = h_w^{(1)}(T_f^{(1)}(x) - T_w^{(1)}(x)), \quad (7.2.8)$$

$$\text{at } \tau_0 = -\frac{1}{2}: \qquad T^{(0)}\Big(x,-\frac{1}{2}\Big) = T_w^{(2)}(x), \quad (7.2.9)$$
$$k_w\frac{\partial T^{(0)}}{\partial n}\Big(x,-\frac{1}{2}\Big) = h_w^{(2)}(T_f^{(2)}(x) - T_w^{(2)}(x)), \quad (7.2.10)$$

where k_w is the thermal conductivity of the wall, $h_w^{(i)}$, $i = 1, 2$, is the heat transfer coefficient between the fluid and the wall, and n is the outward normal. From (7.2.6) it follows that, for the leading order term for the temperature, we have

$$\frac{\partial^2 T_0^{(0)}}{\partial \tau_0^2}(x, \tau_0) = 0, \quad x \in (0, 12), \quad \tau_0 \in \Big(-\frac{1}{2}, \frac{1}{2}\Big),$$

since the constant a_{14}/a_{13}, multipying the time derivative, is of order $O(\varepsilon^{-1})$. This implies that $T_0^{(0)}$ is linear in τ_0, as in the time independent case. Similar to Chapter 3, using conditions (7.2.7) and (7.2.9) we find that the leading order term for the temperature can be written as

$$T_0^{(0)}(x, \tau_0) = \frac{1}{2}(T_w^{(1)}(x) + T_w^{(2)}(x)) + (T_w^{(1)}(x) - T_w^{(2)}(x))\tau_0. \tag{7.2.11}$$

From (7.2.8), (7.2.10) and (7.2.11) it follows that

$$\gamma^{(1)}(T_f^{(1)} - T_w^{(1)}) = T_w^{(1)} - T_w^{(2)} \text{ and } -\gamma^{(2)}(T_f^{(2)} - T_w^{(2)}) = T_w^{(1)} - T_w^{(2)}, \tag{7.2.12}$$

where, $\gamma^{(i)} = \dfrac{h_w^{(i)} \varepsilon D_C}{k_w} = \dfrac{h_w^{(i)} D_w}{k_w}$, $i = 1, 2$, which we assume to be of order $O(1)$.

We use the relationships given in (7.2.12) to obtain the following coupling terms:

$$T_f^{(1)} - T_w^{(1)} = \frac{\gamma^{(2)}(T_f^{(1)} - T_f^{(2)})}{\gamma^{(1)} + \gamma^{(2)} + \gamma^{(1)}\gamma^{(2)}}, \tag{7.2.13}$$

$$T_f^{(2)} - T_w^{(2)} = -\frac{\gamma^{(1)}(T_f^{(1)} - T_f^{(2)})}{\gamma^{(1)} + \gamma^{(2)} + \gamma^{(1)}\gamma^{(2)}}. \tag{7.2.14}$$

These coupling terms[1] are substituted back into the fluid energy balance equations (7.1.1) giving

$$a_6^{(1)}\frac{d^2 T_f^{(1)}}{dx^2} - a_7^{(1)}\frac{dT_f^{(1)}}{dx} + a_8^{(1)}(T_s^{(1)} - T_f^{(1)}) - a_9^{(1)}\frac{\gamma^{(2)}(T_f^{(1)} - T_f^{(2)})}{\gamma^{(1)} + \gamma^{(2)} + \gamma^{(1)}\gamma^{(2)}} = 0, \tag{7.2.15}$$

[1]The coupling terms obtained here are the same as those obtained for the steady state case (see Chapter 3).

$$a_6^{(2)}\frac{d^2T_f^{(2)}}{dx^2} - a_7^{(2)}\frac{dT_f^{(2)}}{dx} + a_8^{(2)}(T_s^{(2)} - T_f^{(2)}) + a_9^{(2)}\frac{\gamma^{(1)}(T_f^{(1)} - T_f^{(2)})}{\gamma^{(1)} + \gamma^{(2)} + \gamma^{(1)}\gamma^{(2)}} = 0. \quad (7.2.16)$$

We take the linear form of the Arrhenius reaction rate, introduced in Chapter 2,

$$(-R)_s^{(i_0)} = \mathcal{A}^{(i)} e^{-\left(\frac{E^{(i)}}{R_g T_s^{(i)}(0)}\right)} Y_s^{(i)}(x,t),$$

that is, we set the temperatures in the reaction rates to be the temperatures at the inlet. Consequently, the time dependent model describing the solid and fluid mass and energy balance equations is solved numerically and the results are presented in Figures 7.1 - 7.3.

7.3 Discussion of the results

We run the transient numerical simulations over a sufficiently large time interval until the solution evolves into a steady state. We present the temperature and concentration distributions for different times t within this interval. Figures 7.1 and 7.2 show the coupled and uncoupled temperature distributions for different t between 0 and 3000 seconds. The steady state solution is obtained between 2000 and 3000 seconds. For comparison we also present the solution from Chapter 3 for the corresponding time independent problem. The bottom two graphs in Figure 7.2 are identical, which shows that, for the particular set of solutions considered, the solution of the steady state problem is exactly the solution that the transient problem evolves to. Figure 7.3 shows that the concentration does not change significantly over time. Again the solution of the time independent problem is presented to show that the transient problem evolves to the corresponding solution of the steady state problem. Another important factor to consider is the sensitivity of the solution to the initial and boundary conditions at the inlet.

Functions at $t = 0$, $x = 0$	Original BCs and ICs	Figures 7.4c) and 7.4d)	Figures 7.4e) and 7.4f)	Figures 7.6c) and 7.6d)	Figures 7.6e) and 7.6f)
$T_f^{(1)}, T_s^{(1)}$	733 K	550 K	850 K	733 K	733 K
$T_f^{(2)}, T_s^{(2)}$	733 K	733 K	733 K	720 K	850 K
$Y_f^{(1)}$	0.163	0.163	0.163	0.163	0.163
$Y_f^{(2)}$	0.0836	0.0836	0.0836	0.0836	0.0836

Table 7.1: Modified inlet boundary and initial conditions associated with Figures 7.4 and 7.6.

Functions at $t = 0$, $x = 0$	Original BCs and ICs	Figures 7.5c) and 7.5d)	Figures 7.5e) and 7.5f)	Figures 7.7c) and 7.7d)	Figures 7.7e) and 7.7f)
$T_f^{(1)}, T_s^{(1)}$	733 K	733 K	733 K	733 K	733 K
$T_f^{(2)}, T_s^{(2)}$	850 K	733 K	733 K	733 K	733 K
$Y_f^{(1)}$	0.163	0.1	0.2	0.163	0.163
$Y_f^{(2)}$	0.0836	0.0836	0.0836	0.06	0.15

Table 7.2: Modified inlet boundary and initial conditions associated with Figures 7.5 and 7.7.

For the original inlet boundary and initial conditions given in Sections 7.1.1 and 7.1.2 we have shown that the temperature and the concentration profiles for the transient problem evolve to a steady state which is the same solution obtained from the corresponding time independent problem. We modify the inlet boundary and initial conditions according to Tables 7.1 and 7.2, and we present the graphs for each case when t is large, and the solution has reached its steady state. For the coupled temperature distributions in the numerical experiments mentioned above, a decrease in values for $T_f^{(1)}$ and $T_s^{(1)}$ set at $x = 0, t = 0$ results in a slight decrease in the coupling effect compared to that for the original conditions. The opposite is true for an increase in the values of $T_f^{(1)}$ and $T_s^{(1)}$ set at $x = 0, t = 0$ (see Figure 7.4). Figure 7.5 shows that slightly increasing or decreasing the values of $Y_f^{(1)}$ at $x = 0, t = 0$ has no significant effect on the temperature distribution. Decreasing (increasing) the values at the inlet for $T_f^{(2)}$ and $T_s^{(2)}$ results in a slight decrease (increase) in the coupling effect (see Figure 7.6). The temperature distribution is very sensitive to the conditions for the concentration on the combustion side (see Figure 7.7). Decreasing the boundary and initial condition at $t = 0, x = 0$ from 0.0836 to 0.06 results in a substantial increase in the coupling effect, and increasing the conditions from 0.0836 to 0.15 gives a substantial decrease in the coupling effect.

The main result in this final chapter is that, for the set of solutions in which the temperature at time $t = 0$ is assumed to be uniform, the solution of the time dependent problem converges to that of the corresponding steady state problem for the industrial data and conditions given in (7.1.3), (7.1.4) and (7.1.5). The same is true when the initial and boundary conditions at the inlet are those given in Tables 7.1 and 7.2. This confirms that the results in Chapters 3 - 5 are valid for the physical problem.

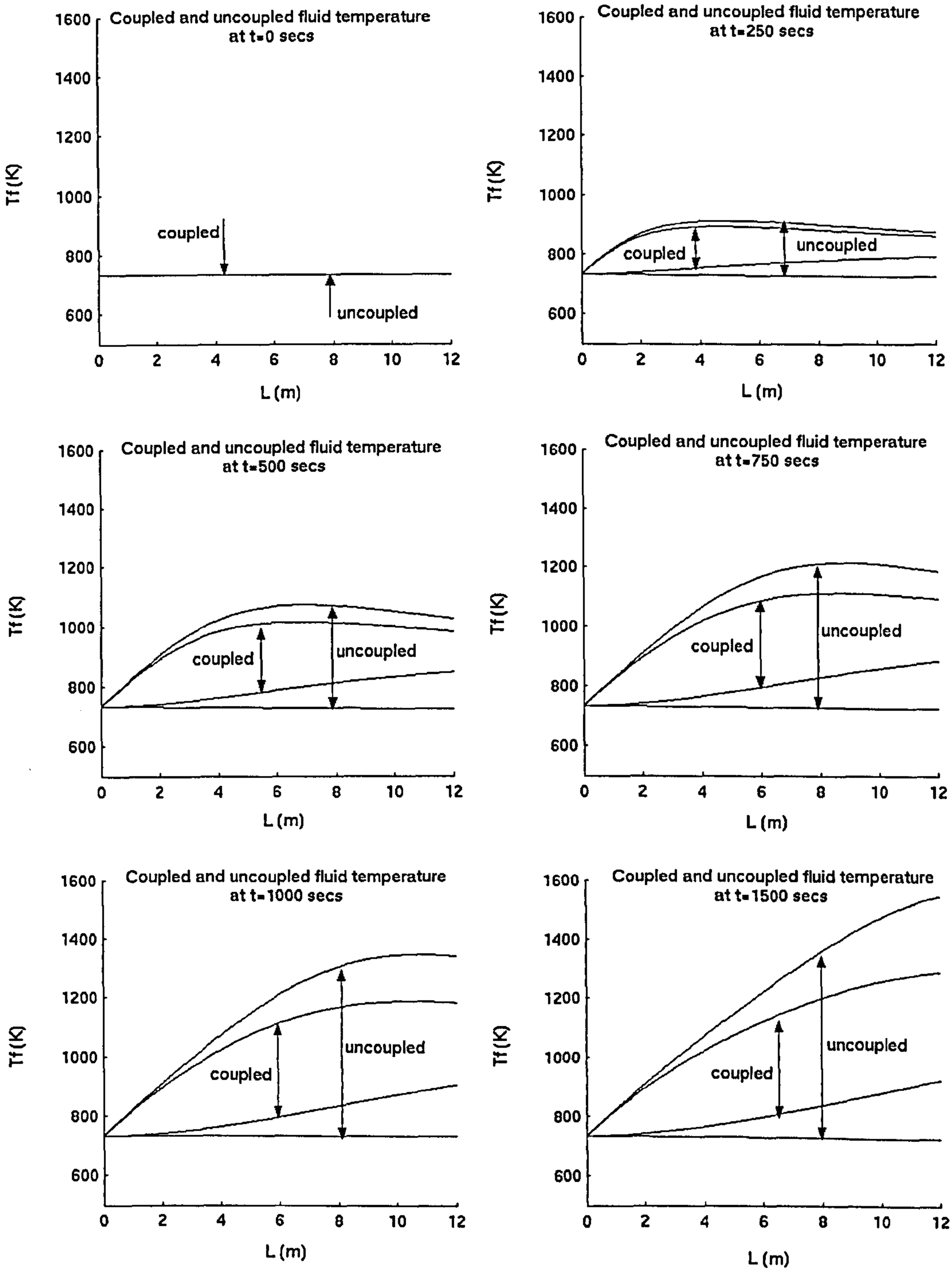

Figure 7.1: Uncoupled and coupled fluid temperatures at increasing time intervals between $t = 0$ and $t = 3000$ seconds (Part 1): Upper plots = Combustion side; Lower plots = Reformer side.

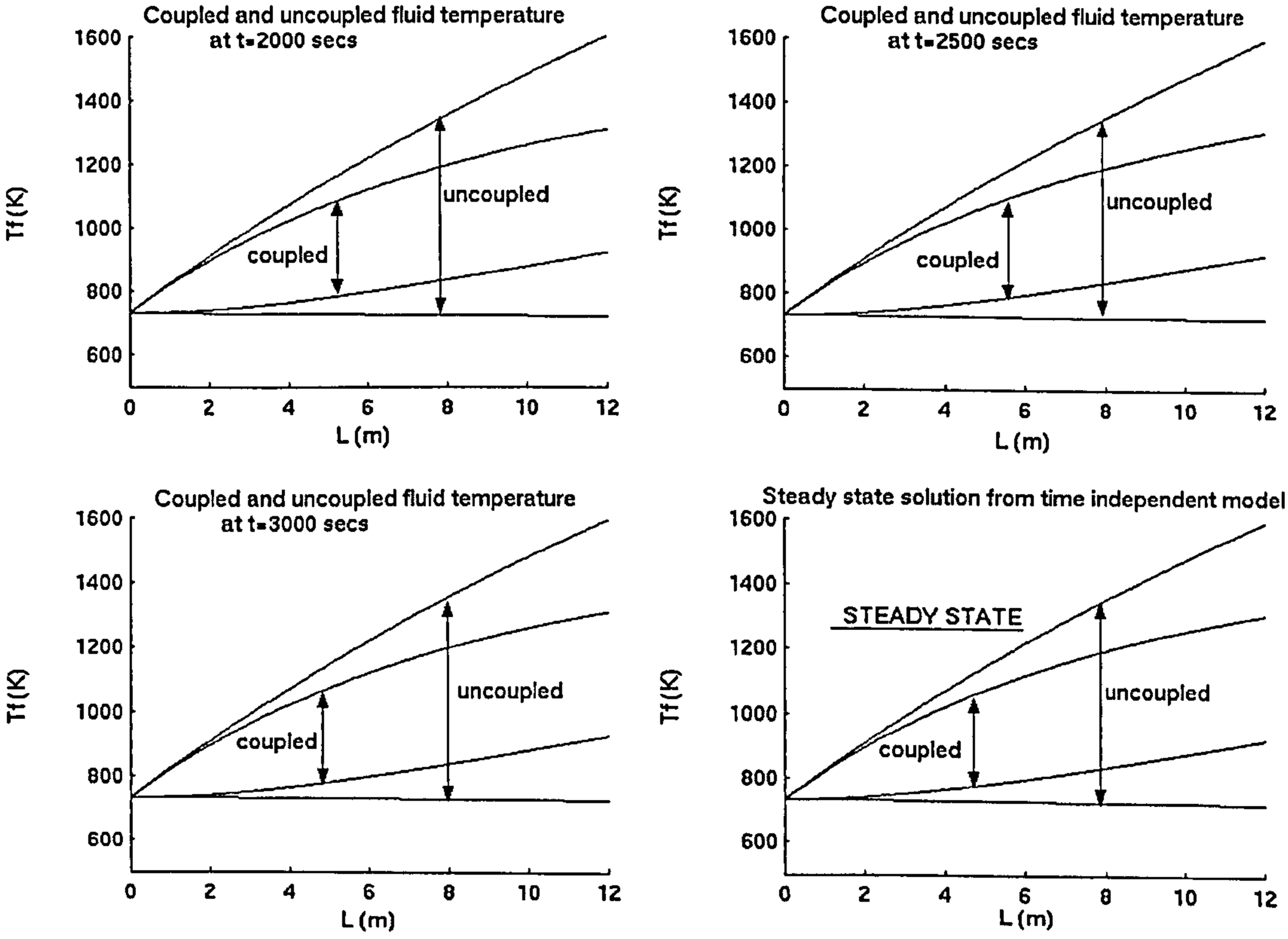

Figure 7.2: Uncoupled and coupled fluid temperatures at increasing time intervals between $t = 0$ and $t = 3000$ seconds (Part 2): the bottom right hand figure shows the corresponding steady state solution for comparison. Upper plots = Combustion side; Lower plots = Reformer side.

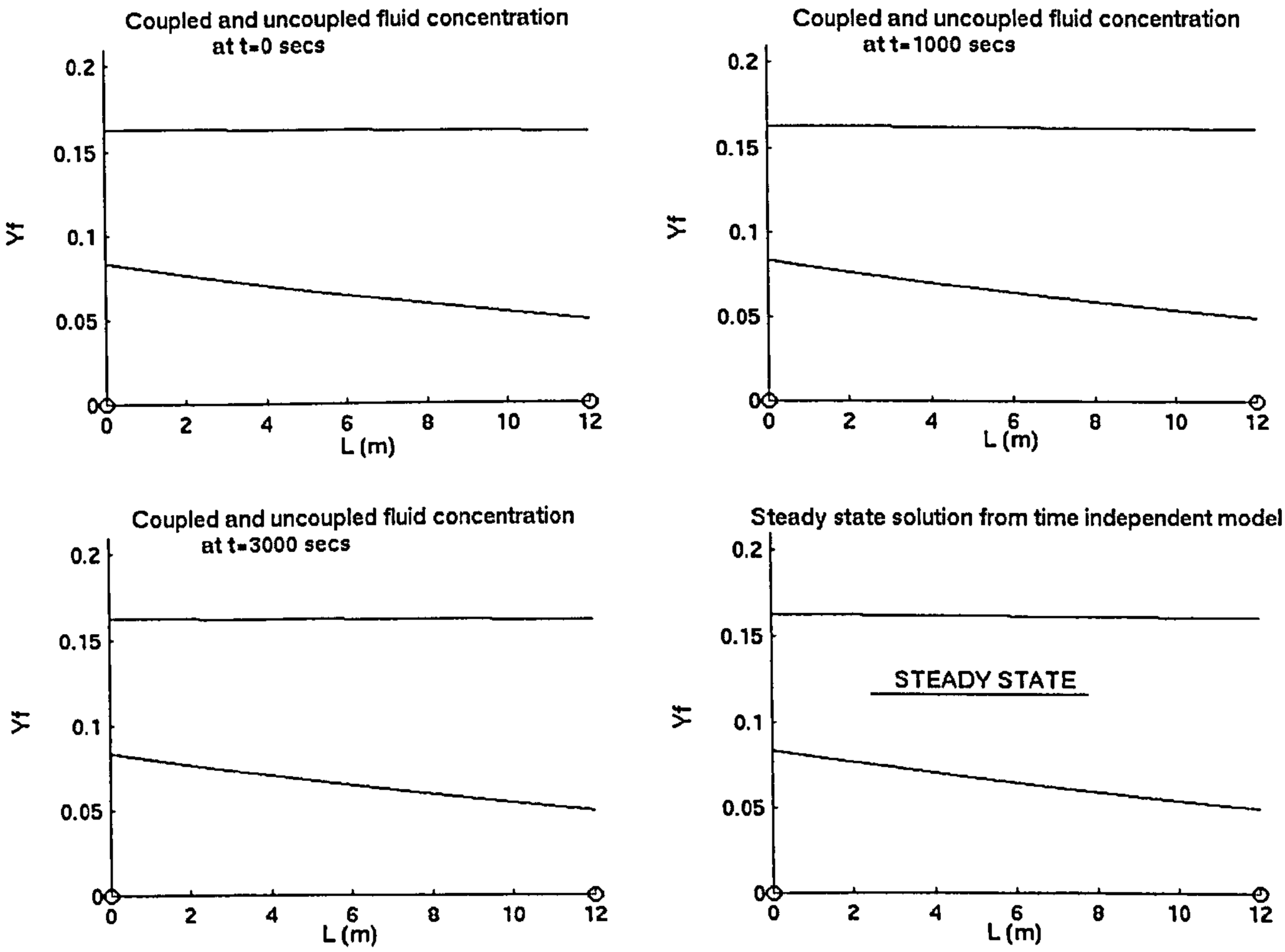

Figure 7.3: Uncoupled and coupled fluid concentrations at increasing time intervals between $t = 0$ and $t = 3000$ seconds; the bottom right hand figure shows the corresponding steady state solution for comparison. Upper plot = Reformer side; Lower plot = Combustion side.

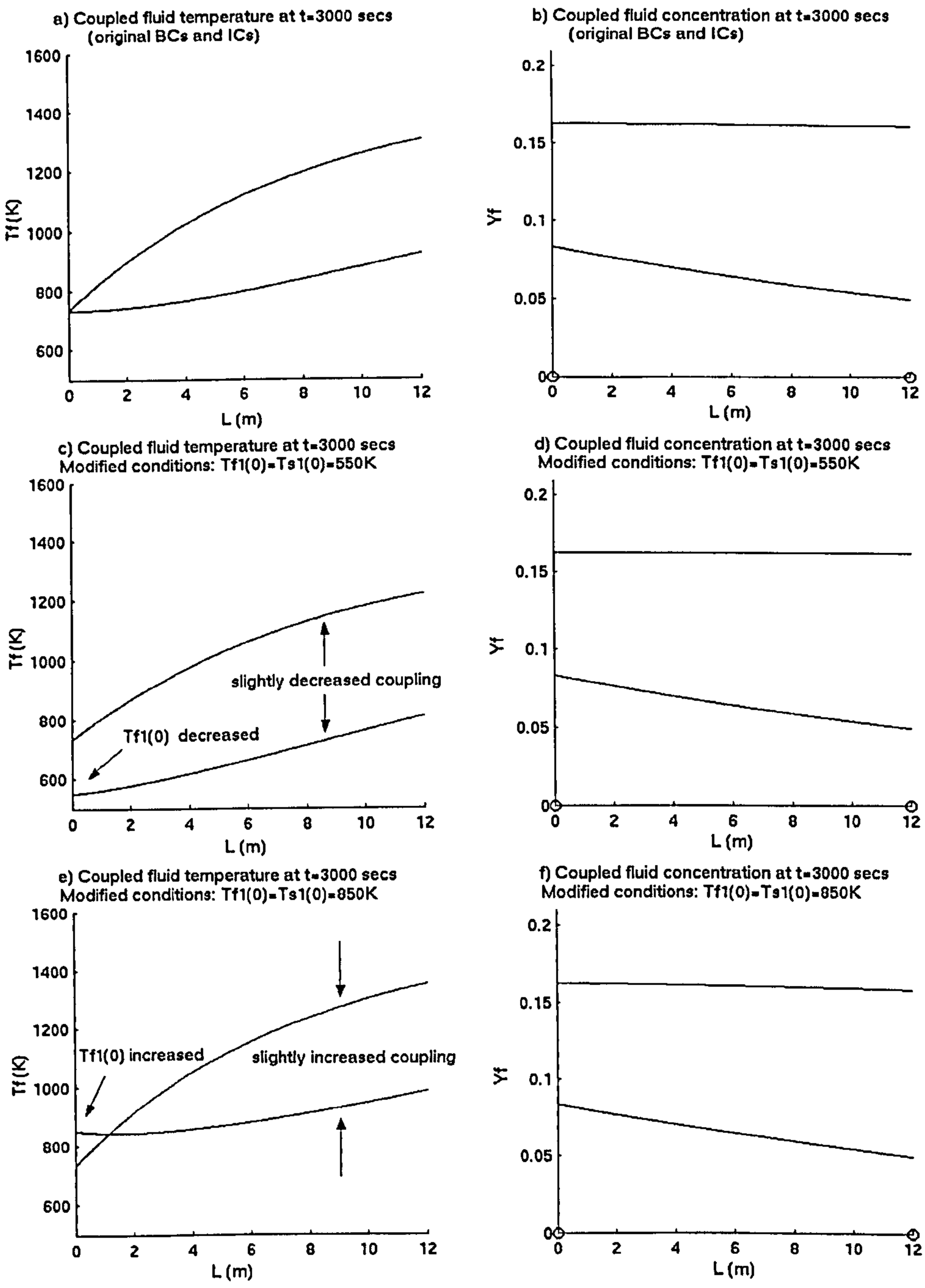

Figure 7.4: Coupled fluid temperatures and concentrations for the cases when the inlet boundary and initial conditions for $T_f^{(1)}$ and $T_s^{(1)}$ are modified. The case with the original boundary conditions is given for comparison. (These graphs are the temperature and concentration distributions that the transient cases evolve to.)

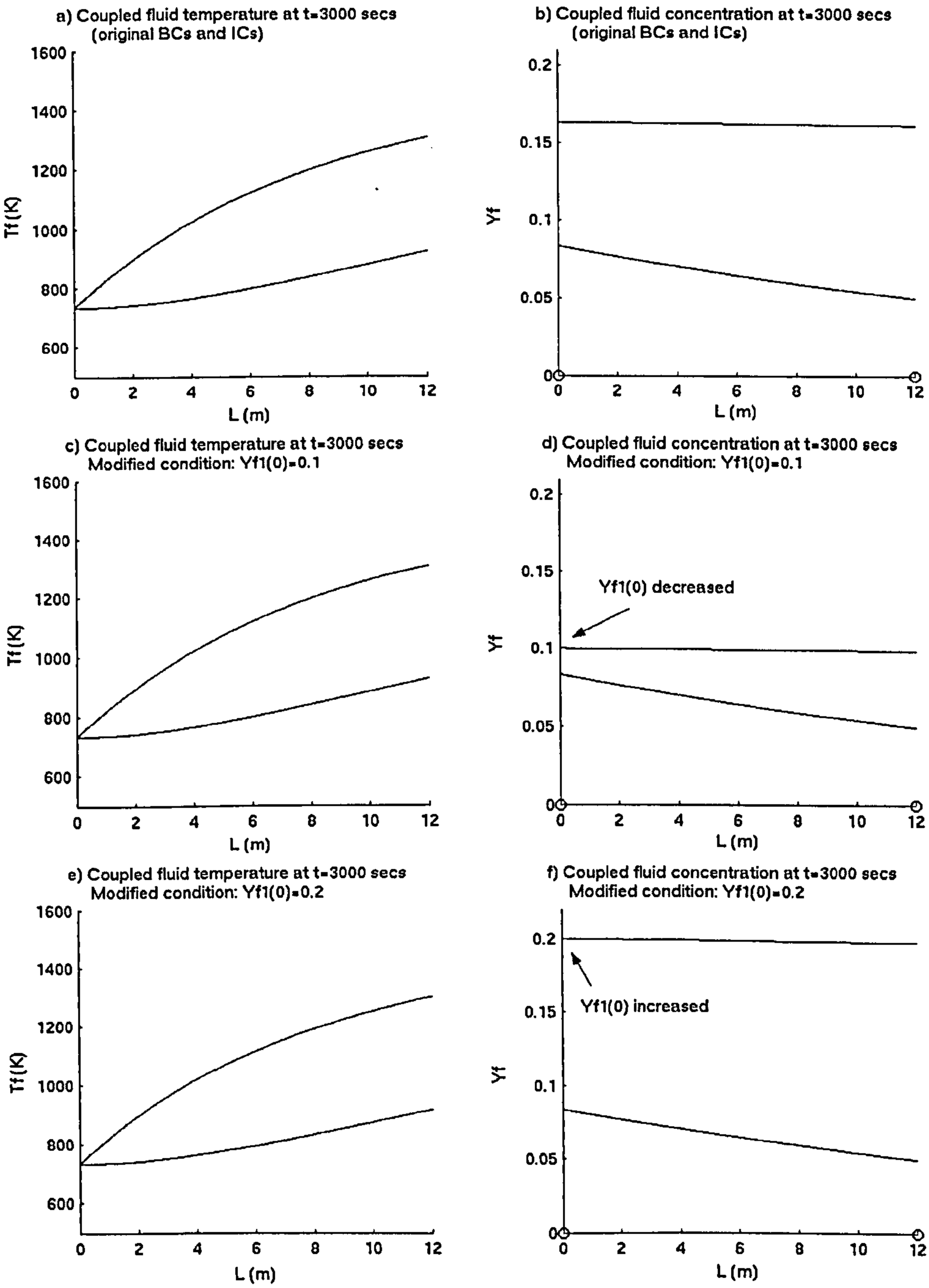

Figure 7.5: Coupled fluid temperatures and concentrations for the cases when the inlet boundary and initial condition for $Y_f^{(1)}$ is modified. The case with the original boundary conditions is given for comparison. (These graphs are the temperature and concentration distributions that the transient cases evolve to.)

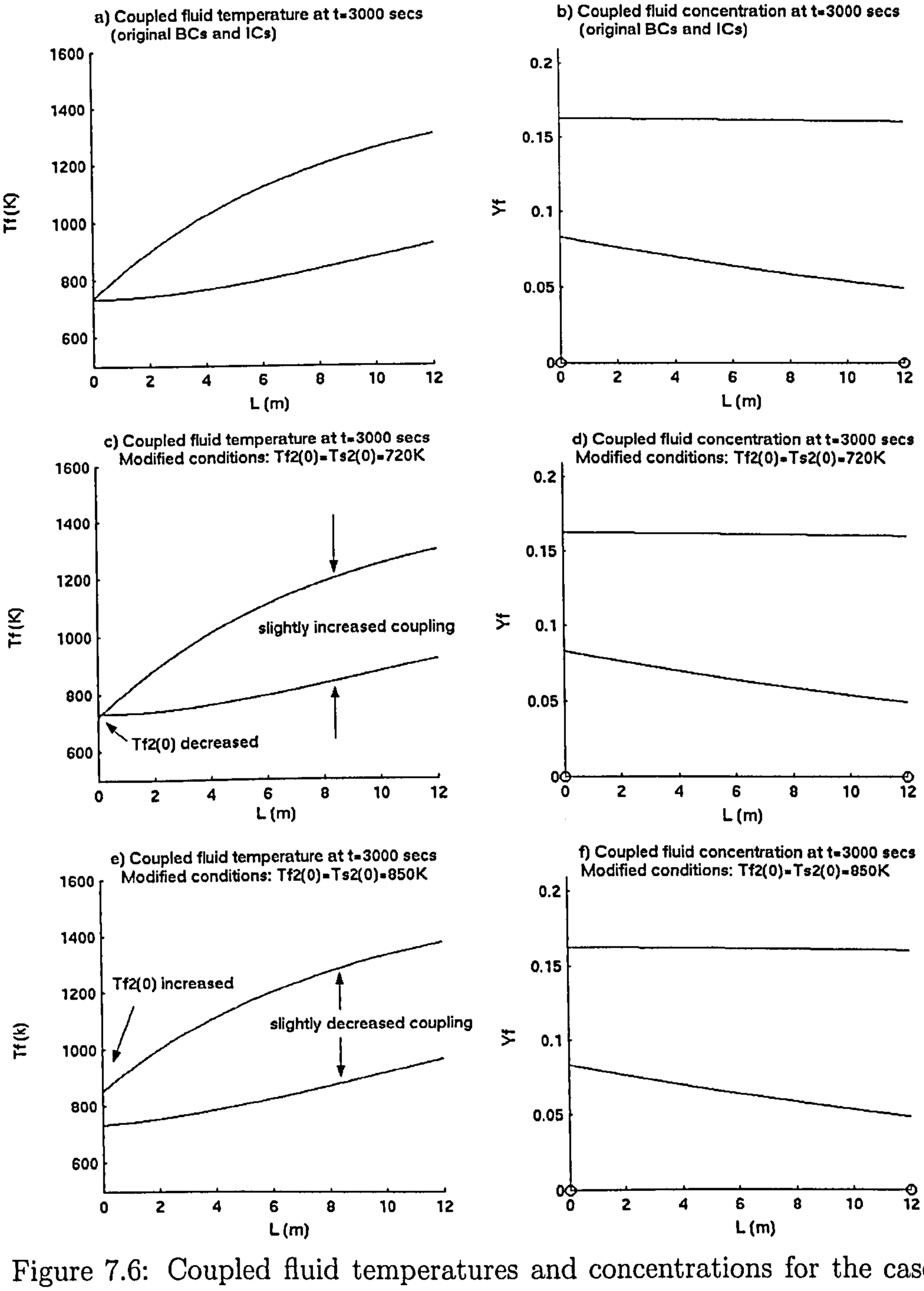

Figure 7.6: Coupled fluid temperatures and concentrations for the cases when the inlet boundary and initial conditions for $T_f^{(2)}$ and $T_s^{(2)}$ are modified. The case with the original boundary conditions is given for comparison. (These graphs are the temperature and concentration distributions that the transient cases evolve to.)

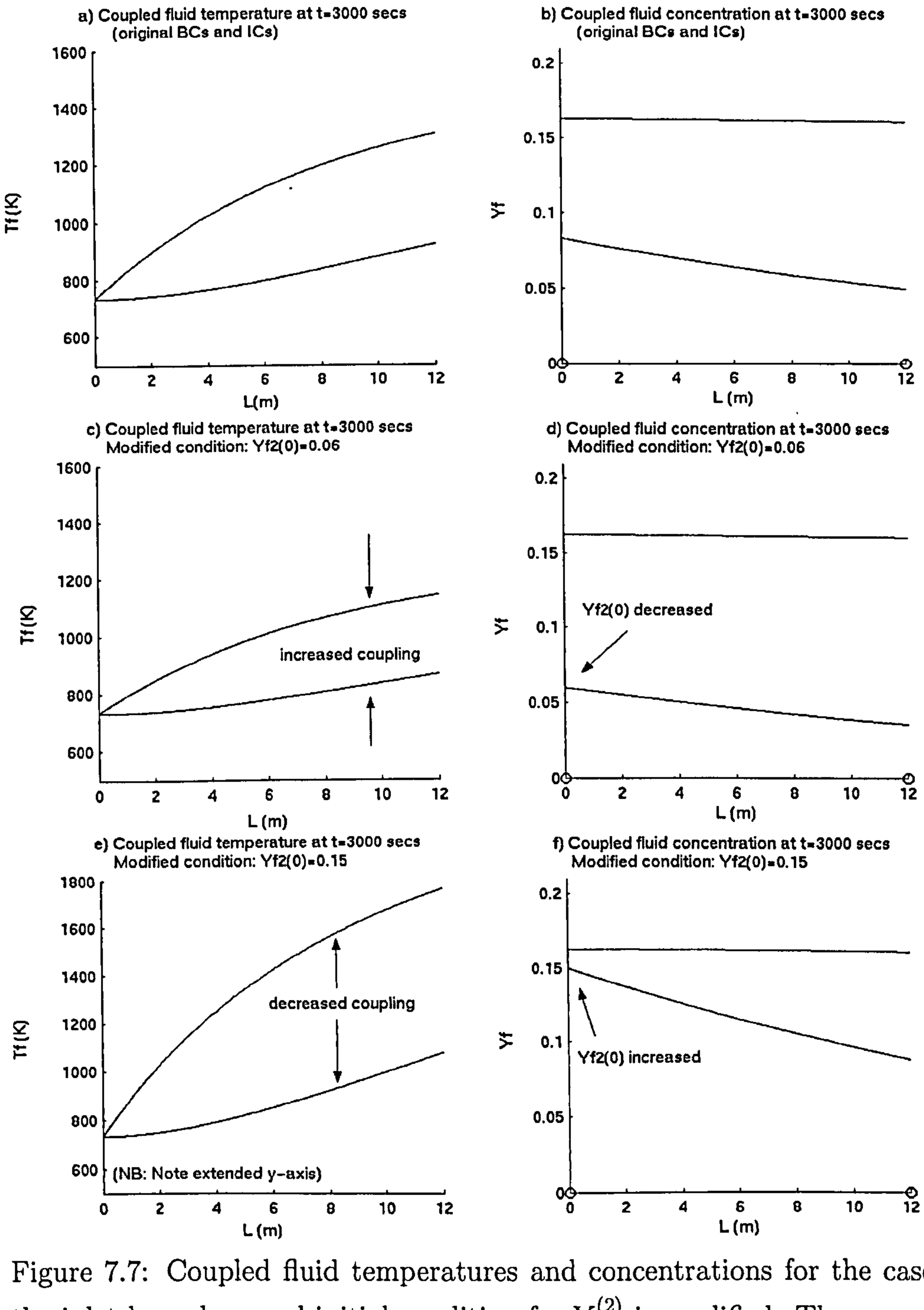

Figure 7.7: Coupled fluid temperatures and concentrations for the cases when the inlet boundary and initial condition for $Y_f^{(2)}$ is modified. The case with the original boundary conditions is given for comparison. (These graphs are the temperature and concentration distributions that the transient cases evolve to.)

Chapter 8

Conclusions *and future* work

In this thesis we developed a mathematical model for a problem that engineers have faced for many years. Our model described a new design for a catalytic reformer - a reactor which is used in industry to produce hydrogen. Conventional combustion and reforming of methane is essential for this purpose, but the disadvantages of existing plants is that they are very large, and they cause substantial pollution through reactions with nitrogen in the air. The new design consists of long adjacent channels with combustion and reforming reactions taking place in parallel rather than in series: heat exchange between the two processes takes place across thin conducting walls that separate the channels. The idea of combining catalytic combustion and reforming was first introduced in the early 1980's and since then many works of an experimental nature have followed, because the new design would overcome the problems caused by the existing reactors.

In the work presented here, we have shown how one could use an asymptotic method to accurately describe the theoretical concepts associated with this new reactor. We analysed the heat transfer across a thin conducting wall, which resulted in a coupling of the two processes taking place in the adjacent channels. We have shown how the energy generated by the combustion reaction is used

to heat the reforming reaction. This is of great industrial importance for many reasons: a large fire box is no longer required to provide energy for the reforming reaction, thus reducing size and peak temperatures - polluting oxides of nitrogen are no longer produced. Also, the difference between the outlet temperatures of the two reactions is reduced dramatically; this can remove problems associated with high temperature differences, for example, cracks in the reactor, hot and cold spots, regions of high pressure and breakdown of the reactor.

The effect of the structure of the wall was investigated in Chapters 3 and 4 where we studied two cases: one where the wall was made of different layers of different widths and thermal conductivities, and the other where the wall contained an air gap. Changing the structure of the wall can be used to provide thermal barriers, which control the amount of heat transferred from one channel to the other. Experimentalists believe that having such thermal barriers is one of the key factors in avoiding failure of the system as it provides a tool to prevent the endothermic reaction from taking too much heat and consequently extinguishing the exothermic reaction. We have presented the results of numerical computations for the temperature and concentration distributions along the channels: these results have indicated that an air gap would be more efficient for the purpose of temperature control, as the main mechanism of heat transfer shifts from conduction to radiation, (we gave an asssessment of when this is the case), thus raising the temperature on the combustion side. We have shown that, in the limiting case, as the width of the air gap approaches zero, heat transfer via conduction, as well as radiation, also needs to be taken into account. Further work on this model could involve the analysis of air gaps where the air is at different temperatures, and the addition of heat transfer by convection as well as radiation and conduction across the gap.

In this thesis we gave a detailed description and a asymptotic approximation of the solution including the boundary layer regions near the inlet and outlet of the

reactor. Numerical packages have difficulties in dealing with singularly perturbed boundary value problems and tend to only give the limit outer solution. In Chapter 5 we have shown that the limit outer solution is sufficiently accurate in the main part of the channel, but near the inlet and outlet, where functions change rapidly, additional boundary layer fields needed to be constructed. A future direction would be to develop a code that would generate the numerical solution along the entire length of the channel, automatically incorporating the limit outer solution, as well as the asymptotic approximation for the rapidly varying functions in the small regions near the ends.

Although we have dealt with a simple model of the problem, where we first considered 1D equations in the channels and 2D equations in the wall, we have provided a sufficiently accurate analysis of the physical phenomenon associated with the design of this industrial reactor. We have shown how the temperatures are coupled and how this coupling can be controlled. In Chapter 6 we also analysed how one could model the structure of the pellets in the channels in more detail. We derived a direct relationship to Darcy's law for the main part of the cross-section of the channel, with exponentially decaying solutions near the walls. This is similar to Hartmann flow for fluids in a magnetic field. Future work could involve an alternative way of modelling the pellets which are packed randomly in the bed. Additionally, one could also model a catalytic plate reactor, where there are no pellets and the catalyst is present on the sides of the walls. The simplest model for such a case would include at least 2D equations, as the temperature profile would change across as well as along the channels.

Finally, we considered the time dependent model and showed that for the set of solutions with uniform temperature distribution at time $t = 0$, our steady state solutions were exactly those that the transient problem evolved to. Further work on the transient case would involve an investigation of how the temperature changes at the inlet, that is, when $t = 0$, and how the heating up of the solid

phase would affect the result. Also, an increase in the dimensions of the system and a generalisation to multi-channel interactions could be considered. Additionally one could analyse the optimal design for the catalytic reactor, for example, how many channels are required and what is the best arrangement (combustion or reforming channels at the ends), how do certain parameters depend on temperature, flow rate etc. and how would this affect the results, and what is the optimal outlet temperature for the reactor to be most efficent.

Bibliography

[1] Aiken, R.C., Lapidus, L. (1974) An effective numerical integration method for typical stiff systems. *A.I.Ch.E. Journal*, **20**, No. 2, 368-375.

[2] Akers, W.W., Camp, D.P. (1955) Kinetics of the methane steam reaction. *A.I.Ch.E. Journal*, **1**, No. 4, 471-473.

[3] Allaire, G. (1991) Homogenization of the Navier-Stokes Equations in Open Sets Perforated with Tiny Holes 1. Abstract Framework, a Volume Distribution of Holes. *Arch. Rational Mech. Anal.*, **113**, 209-259.

[4] Allaire, G. (1991) Homogenization of the Navier-Stokes Equations in Open Sets Perforated with Tiny Holes 2. Non-Critical Sizes of the Holes for a Volume Distribution and a Surface Distribution of Holes. *Arch. Rational Mech. Anal.*, **113**, 261-298.

[5] Antipov, Y.A., Kolaczkowski, S.T., Movchan, A.B., Spence, A. (1999) Asymptotic analysis for cracks in a catalytic monolith combustor. *Int. J. of Solids Structures*, **37**, 1899-1930.

[6] Avci, A.K., Trimm, D.L., Ilsen Onsan, Z. (2001) Heterogeneous reactor modelling for simulation of catalytic oxidation and steam reforming of methane. *Chem. Eng. Sci.*, **56**, 641-649.

[7] Avila-Pozos, O. (1999) Mathematical models of layered structures with an imperfect interface and delamination cracks. *PhD Thesis*, Chpt. 2, University of Bath.

[8] Balforth, N.J., Craster, R.V., Malham, S.J.A. (1999) Unsteady fronts in an autocatalytic system. *Proc. R. Soc. London*, A**455**, 1401-1433.

[9] Baxter, S.C., Horgan, C.O. (1995) End effects for anti-plane shear deformations of sandwich structures. *Journal of Elasticity*, **40**, 123-164.

[10] Baxter, S.C., Horgan, C.O. (1997) Anti-plane shear deformations of anisotropic sandwich structures: end effects. *Int. J. Solids Structures*, **34**, No. 1, 79-98.

[11] Bachmat, Y., Bear, J. (1986) Macroscopic Modelling of Transport Phenomena in Porous Media 1: The Continuum Approach. *Transport in Porous Media*, **1**, 213-240.

[12] Bear, J., Bachmat, Y. (1991) *Introduction to modelling of transport phenomena in porous media*, Kluwer Academic Publishers.

[13] Benveniste, Y., Miloh, T. (1998) Composites with superconducting interfaces. *Continuum models and discrete systems: Proc. of the 9th Int. Symp.*, 100-108.

[14] Berlyand, L., Goncharenko, M.V. (1990) The averaging of the diffusion equation in a porous medium with weak absorption. *Teoriya Funktsional'nyi Analiz i Ikh Prelozheniya*, **52**, 113-122.

[15] Berlyand, L., Kolpakov, A. (2001) Network Approximation in the limit of small interparticle distance of the effective properties of a high-contrast random dispersed composite. *Arch. Rational Mech. Anal.*, **159**, 179-227.

[16] Bird, R.B., Stewart, W.E., Lightfoot, E.N. (1960) *Transport Phenomena*, John Wiley and Sons, Inc.

[17] Blouza, A., Coquel, F., Hamel, F. (1998) Algorithmic reduction process for kinetic stiff systems. *Comptes Rendus de l'Academie des Sciences Serie 1-Mathematique*, **327**, No. 12, 979-984.

[18] Borcea, L. Asymptotic Analysis of Quasi-Static Transport in High Contrast Conductive Media. *SIAM J. Appl. Math.*, **59**, No. 2, 597-635.

[19] Borcea, L., Papanicolaou, G.C. (1998) Network approximation for transport properties of high contrast materials. *SIAM J. Appl. Math.*, **58**, No. 2, 501-539.

[20] Branch, C.A., Tomlinson, D. (1995) A stability study of the catalytic plate reactor when reforming an endothermic reaction. *Proceedings of the first international conference on science, engineering and technology of intensive processing, Nottingham.*

[21] Brezis, H., Lions, J.L. (1982) Un terme etrange venu d'ailleurs. *Nonlinear Partial Differential Equations and their Applications, College de France Seminar*, **60** and **70**, 98-138 and 154-178.

[22] Cabannes, H. (1970) *Theoretical Magnetofluiddynamics*, Academic Press, New York. (Translated by Maurice Holt.)

[23] Carroni, R., Griffin, T., Mantzaras, J., Reinke, M. (2003) High-pressure experiments and modeling of methane/air catalytic combustion for power-generation applications. *Catalysis today*, **83**, 157-170.

[24] Chapman, A.J. (1960) *Heat Transfer*, The MacMillan Company.

[25] Charlesworth, R.J. (1996) The steam reforming and combustion of methane on micro-thin catalyst for use in a catalytic plate reactor. *PhD Thesis*, University of Newcastle upon Tyne.

[26] Charlesworth, R., Gough, A., Ramshaw, C. (1995) Combustion and steam reforming of methane on thin layer catalysts for use in catalytic plate reactors. *4th UK National Conference on Heat Transfer: IMECHE Conference Transactions*, **2**, 85-89.

[27] Choi, I., Horgan, C.O. (1978) Saint-Venant end effects for plane deformation of sandwich strips. *Int. J. Solids Structures*, **14**, 187-195.

[28] Curtiss, C. F., Hirschfelder, J.O. (1952) Integration of stiff equations. *Proc. Nat. Acad. Sci. U.S.A.*, **38**, 235-243.

[29] De Wasch, A.P., Froment, G.F. (1970) A two-dimensional heterogeneous model for fixed bed catalytic reactors. *Chem. Eng. Sci.*, **26**, 629-634.

[30] De Wasch, A.P., Froment, G.F. (1972) Heat transfer in packed beds. *Chem. Eng. Sci.*, **27**, 567-576.

[31] Boyce, W.E., DiPrima, R.C. (1992) *Elementary Differential Equations and Boundary Value Problems*, John Wiley and Sons, Inc.

[32] Dixon, A.G., Cresswell, D.L. (1979) Theoretical prediction of effective heat transfer parameters in packed beds. *A.I.Ch.E. Journal*, **25**, No. 4, 663-672.

[33] Do, D.D., Rice, R.G. (1995) *Applied mathematics and modelling for chemical engineers*, John Wiley and Sons, Inc.

[34] Dullien, F.A.L. (1979) *Fluid Transport and Pore Structure*. Academic Press.

[35] Elnashaie, S.S., Adris, A.M., Soliman, M.A., Al-Ubaid, A.S. (1992) Digital simulation of industrial steam reformers for natural gas using heterogeneous models. *Can. J. Chem. Eng.*, **70**, 789, Table 1.

[36] Foss, B.A., Wasbo, S.O. (2001) An integration scheme for stiff solid-gas reactor models. *Modelling Identification and Control*, **22**, No. 2, 103-118.

[37] Frankel, N.A., Acrivos, A. (1967) On the viscosity of a concentrated suspension of solid spheres. *Chem. Eng. Sci.*, **22**, 847-853.

[38] Frauhammer, J., Eigenberger, G., von Hippel, L., and Arntz, D. (1999) A new reactor concept for endothermic high-temperature reactions. *Chem. Eng. Sci.*, **54**, 3661-3670.

[39] Froment, G.F., Bischoff, K.B. (1990) *Chemical Reactor Design and Analysis*, 2nd Edition, Wiley Series in Chemical Engineering.

[40] Gerenrot, D., Berlyand, L., Phillips, J. (2003) Random network model for heat transfer in high contrast composite materials. *IEEE Trans. on Adv. Packaging*, **26**, No. 4, 410-416.

[41] Gioia, G., Ortiz, M. (1996) The two-dimensional structure of dynamic boundary layers and shear bands in thermoviscoplastic solids. *J. Mech. Phys. Solids*, **44**, No. 2, 251-292.

[42] Guenneau, S., Movchan, A.B., Poulton C.G., Nicolet, A. (2004) Coupling between electromagnetic and mechanical vibrations of thin-walled structures. *Q. J. Mech. Appl. Math.*, **57**, Part 3, 407-428.

[43] Hawkins, S.C. (2000) Iterative methods for the large sparse eigenvalue problem. *PhD Thesis*, Chpt. 6, University of Bath.

[44] Hayes, R.E., Afacan, A., Boulanger, B. (1995) An Equation of Motion for an Incompressible Newtonian Fluid in a Packed Bed. *Transport in Porous Media*, **18**, 185-198.

[45] Hayes, R.E., Kolaczkowski, S.T. (1997) *Introduction to Catalytic Combustion*, Gordon and Breach Publishers.

[46] Hayes, R.E., Kolaczkowski, S.T., Thomas, W.J., Titiloye, J. (1995) Intraphase diffusion and interphase mass-transfer effects during the catalytic-oxidation of CO in a tube wall reactor. *Proc. R. Soc. London*, A**448**, 321-334.

[47] Hayes, R.E., Tanguy, P.A. (1987) Solution of stiff convection-diffusion differential equations using Marquardt's method. *Can. J. Chem. Eng.*, **65**, 522-525.

[48] Heinemann, R.F., Poore, A.B. (1981) Multiplicity, stability and oscillatory dynamics of the tubular reactor. *Chem. Eng. Sci.*, **36**, 1411-1419.

[49] Hunter, J.B., McGuire, G. (1980) Method and apparatus for catalytic heat exchange. *US Patent 4,214,867.*

[50] Hornung, U. (1997) *Homogenization and porous media*, Springer-Verlag, New York.

[51] Iordanidis, A.A., Annaland, M.V., Kronberg, A.E., Kuipers, J.A.M. (2004) A numerical method for the solution of the wave model and convection dominated diffusion type models for catalytic packed bed reactors. *Comp. Chem. Eng.*, **28**, No. 11, 2337-2349.

[52] Jamal, Y., Wyszynski, M.L. (1994) On board generation of hydrogen-rich gaseous fuels - a review. *Int. J. Hydrogen Energy*, **19**, No. 7, 557-572.

[53] Khanna, R., Seinfeld, J.H. (1987) Mathematical modeling of a packed bed reactor: numerical solutions and control development. *Adv. Chem. Eng.*, **13**, 113-191.

[54] Kolaczkowsi, S.T., Lin, P., Movchan, A.B., Serkov, S.K., Spence, A. (1999) Thermal stress analysis and homogenisation for catalytic combustor monoliths. *Euro. J. Appl. Maths.*, **10**, Part 2, 185-220.

[55] Kozlov, V.A., Maz'ya V.G., Movchan, A.B. (1999) *Asymptotic Analysis of Fields in Multi-Structures*, Oxford University Press.

[56] Kvernfold, O., Tyvand, P.A. (1979) Nonlinear thermal convection in anisotropic porous media. *J. Fluid Mech.*, **90**, Part 4, 609-624.

[57] Landau, L.D., Lifshitz, E.M. (1984) *Electrodynamics of continuous media*, **8**, Chpt. 8, Pergamon Press.

[58] Landau, L.D., Lifshitz, E.M. (1959) *Fluid mechanics*, Pergamon Press Ltd.

[59] Leach, J.A., Needham, D.J. (2004) *Matched Asymptotic Expansions in Reaction-Diffusion Theory*, Springer-Verlag London.

[60] Li, C.H., Finlayson, B.A. (1977) Heat transfer in packed beds - A reevaluation. *Chem. Eng. Sci.*, **32**, 1055-1066.

[61] Liniger, W., Willoughby, R.A. (1970) Efficient integration methods for stiff systems of ordinary differential equations. *SIAM J. Num. Analysis*, **7**, No. 1, 47-66.

[62] List, J. (1968) A 2-D sink in a density stratified porous medium. *J. Fluid Mech.*, **33**, part 3, 529-543.

[63] McCabe, P.M., Leach, J.A., Needham, D.J. (2002) On an initial-boundary-value problem for a coupled, singular reaction-diffusion system arising from a model of fractional-order chemical autocatalysis with decay. *Q. J. Mech. Appl. Math.*, **55**, No. 4, 511-560.

[64] Miranker, W.L. (1973) Numerical methods of boundary layer type for stiff systems of differential equations. *Computing*, **11**, 221-234.

[65] Movchan, A.B., Movchan, N.V. (1985) *Mathematical modelling of solids with nonregular boundaries*, CRC Press.

[66] Muller, U., Buhler, L. (2002) *Magneto-Hydraulics*, Springer-Verlag, New York.

[67] Murray, J.D. (1984) *Asymptotic Analysis*, Springer-Verlag, New York.

[68] Needham, D. J., Barnes, A.N. (1999) Reaction-diffusion and phase waves occurring in a class of scalar reaction-diffusion equations. *Nonlinearity*, **12**, 41-58.

[69] Needham, D.J., King, C. (2002) The evolution of travelling waves in the weakly hyperbolic generalized Fisher model. *Proc. R. Soc. London*, A448, 1055-1088.

[70] Ockendon, H., Ockendon, J.R. (1995) *Viscous Flow*, Cambridge University Press.

[71] Ockendon, H., Tayler A.B. (1983) *Inviscid Fluid Flows*, Springer-Verlag, New York.

[72] Parker, J., Boggs, J., Blick, E. (1969) *Introduction to fluid mechanics and heat transfer*, Addison Wesley Publishing Company.

[73] Parulekar, S.J., Ramkrishna, D. (1982) A spectral-theoretical view of axial dispersion models. *Residence time distribution theory in chemical engineering*, Verlag Chemie, Weinheim.

[74] Plehiers, P.M., Froment, G.F. (1989) Coupled simulation of heat transfer and reaction in a steam-reforming furnace. *Chem. Eng. Technol.*, **12**, 20-26.

[75] Polubarinova-Kochina, P. Ya., Falkovich, S.B. (1947) Theory of Filtration of Liquids in Porous Media. *P.P.M.*, **11**, 153-225. (Translated by D.R. Mazkevich.)

[76] Prigent, M. (1997) On board hydrogen generation for fuel cell powered electric cars. *Revue de l'Institut Francais du Petrole*, **52**, No. 3, 349-360.

[77] Prieur Du Plessis, J., Masliyah, J.H. (1991) Flow through isotropic granular porous media. *Transport in Porous Media*, **6**, 207-221.

[78] Rajesh, J.K., Gupta, S.K., Rangaiah, G.P., Ray, A.K. (2000) Multiobjective Optimization of Steam Reformer Performance Using Genetic Algorithm. *Ind. Eng. Chem.*, **39**, 706-717.

[79] Rose, L.M. (1974) *The Application of Mathematical Modelling to Process Development and Design*, Applied Science Publishers.

[80] Schlunder, E.U. (1978) Transport phenomena in packed bed reactors. *Chemical Reaction Engineering Reviews*, 4, 110-161.

[81] Selsil, A., Movchan, A.B., Movchan, N.V. (2003) Asymptotic Analysis of Heat Transfer in a System of Channels Connected by Thin Conducting Walls. *Asymptotics, Singularities and Homogenisation in Problems of Mechanics: Proc. of the IUTAM Symp.*, 455-465.

[82] Selsil, A., Movchan, A.B., Movchan, N.V., Kolaczkowski, S.T. Mathematical Modelling of Heat Transfer in a Catalytic Reformer. *IMA. J. Appl. Math.*, to appear in volume **7**, 2005.

[83] Selsil, O. (2000) Asymptotic models of multi-structures. *PhD Thesis*, University of Liverpool.

[84] Slattery, J.C. (1969) Single-Phase Flow through Porous Media. *A.I.Ch.E. Journal*, **15**, No. 6, 866-873.

[85] Slattery, J.C. (1972) *Momentum, Energy and Mass Transfer in Continua*, McGraw-Hill Book Company.

[86] Spence, A., Worth, D.J., Kolaczkowski, S.T., Crumpton, P.I. (1993) Modelling catalytic combustion in a monolith reactor: A numerical algorithm for varying solid phase Peclet numbers. *Comp. Chem. Engng.*, **17**, No. 11, 1057-1066.

[87] Streeter, V.L., Wylie, E.B. (1983) *Fluid Mechanics: First SI Metric Edition*, McGraw-Hill Book Company.

[88] Uppal, A., Ray, W.H., Poore, A.B. (1974) On the dynamic behaviour of continuous stirred tank reactors. *Chem. Eng. Sci.*, **29**, 967-985.

[89] Uppal, A., Ray, W.H., Poore, A.B. (1976) The classification of the dynamic behaviour of continuous stirred tank reactors - influence of reactor residence time. *Chem. Eng. Sci.*, **31**, 205-214.

[90] Van Dyke, M.D. (1975) *Perturbation methods in fluid mechanics*, Parabolic Press, Stanford.

[91] Wakao, N., Yagi, S. (1959) Heat and mass transfer from wall to fluid in packed beds. *A.I.Ch.E. Journal*, **5**, No. 1, 79-85.

[92] Wehner, J.F., Wilhelm, R.H. (1956) Boundary conditions of flow reactor. *Chem. Eng. Sci.*, **6**, 89-98.

[93] Worth, D.J., Kolaczkowski, S.T., Spence, A. (1993) Modeling channel interaction in a catalytic monolith reactor. *Chem Eng. Research and Design*, **71**, 331-333.

[94] Xu, J., Froment, G.F. (1989) Methane steam reforming: II. Diffusional limitations and reactor simulation. *A.I.Ch.E. Journal*, **35**, No. 1, 97-103.

[95] Zanfir, M. (2000) Catalytic plate reactors for exothermic-endothermic reaction coupling. *PhD Thesis*, University College London.

[96] Zanfir, M., Gavriilidis, A. (2001) Modelling of a catalytic plate reactor for dehydrogenation-combustion coupling. *Chem. Eng. Sci.*, **56**, Issue 8, 2671-2683.